

Université du Québec

INRS EMT

**TRAVELING-WAVE MULTIPLE BEAM SLOT ANTENNAS IN
SUBSTRATE INTEGRATED WAVEGUIDE**

Par

F. D. L. Peters

Thèse présentée

pour l'obtention

du grade de Philosophiae doctor (Ph.D.)

en Télécommunications

Jury d'évaluation

Président du jury

et examinateur interne

Examineur externe

Examineur externe

Directeur de recherche

Codirecteur de recherche

D. O'Shaughnessy,

INRS-EMT

Ammar Kouki,
ETS de Montréal

Cevdet Akyel,
Éc. Polytechnique de Montréal

T.A. Denidni,
INRS-EMT

S.O. Tatu,
INRS-EMT

ACKNOWLEDGEMENTS

This document is based on research in the groups of Prof. T. A. Denidni and Prof. S. O. Tatu, working both with the INRS-EMT, member of the University of Quebec. My profound thanks go to my director Prof. Denidni as well as to my Co-director Prof. Tatu for their support, guidance, patience and shared expertise. Furthermore, I would like to express my gratitude to the other members of my PhD committee, Prof. Kouki , Prof. Akyel and Prof. O'Shaughnessy.

I want to send my appreciations to the team of technicians of the ÉTS de l'Université du Québec and École Polytechnique de Montréal for the prototype preparation. In addition, I appreciate the academic support and measurement facilities provided by Prof. M. Schneider from the University of Bremen. I would also provide great recognitions to Prof. M. Purat, and Prof. em. D. Rudolph of the Beuth University of Applied Sciences Berlin, I am so grateful for having me initially prepared for this courageous step. I am also thanking the BDr GmbH for its support.

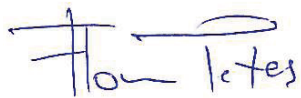
Advice and assistance during stormier days made this thesis succeed. Many thanks go to my fellow graduate students, specifically to Mu'ath Al-Hasan. Individual credits are sent to my mum and dad, U.M. and F. Peters, who provided unlimited and invaluable back up for this project. The last but not least important acknowledgments I am submitting together with this document are the most grateful words for ML to whom I owe to have stayed the course. To my closest friends and allies EP, CY and DF, MG, CT, and to my former band FM, as well as to FT and to the other uncounted amiable people of the CS and ski community of Montreal I transmit my mute thankfulness. I lack the words to describe how glad I am to have received your accompaniment during the journey to this thesis.

À la Ville de Montréal, QC

Tu es de toute beauté

ABSTRACT

This thesis presents an enhanced way of designing traveling-wave antennas built with slotted substrate integrated waveguides. A novel configuration of vias is derived for controlling the slotted element phase by $>30^\circ$. A straightforward design method that includes slot excitation from either side is set up. It is very useful specifically for high width-to-height waveguide ratios as well as both off-resonant and mismatched slots, where conventional methods have been shown to be less performing. The validation has revealed a radiation pattern with low SLL of -27 dB, and zero degree broadside beam. Measured antenna arrays yielded a low $|S_{11}| < -20$ dB. Nevertheless, the project has exposed reflections from the applied transition and fixture at the end of the array that degrade the results. The new concept has been completed with a published MATLAB design guide script. When applying the vias to steer to a particular angle, the shifted beams do reveal the same range of beam width and low SLL as the initial zero degree beam which outperforms the State-of-the-Art. A solution comprising slot antenna sub-arrays that are excited from either side is further presented in this work. Four particular beams from -20° to $+20^\circ$ - have been designed with good matching of better -10 dB reflection, and a maximum directivity of about 16 dBi, exhibiting an efficiency of nearly 70 %. A new very practical millimeter-wave transition is proposed at the end of this work. It addresses the shrinkage tolerances typically seen with LTCC material. The $\tan\delta$ and ϵ_r of the latter could have been determined through a LINE and THRU measurement. A strong dispersion of the dielectric constant from 9.9 to 6.7 has been the important outcome of this task. This solution represents the first purely intra-substrate experiment allowing to avoid the uncertainties that occur with the *effective* permittivity. The transition shows a good insertion loss < 0.7 dB and a good matching with RL < 10 dB. To sum up, a bunch of new tools has been conceived with this work to enhance the performance of very thin slotted traveling-wave-antennas substantially.



F.D.L. Peters, Student

RÉSUMÉ EN FRANÇAIS

Lorsque Heinrich Hertz a déclaré qu'il avait prouvé l'existence des ondes électromagnétiques avec le dipôle hertzien, il était peu optimiste que sa découverte soit utilisée à des fins de communication. Les longueurs d'ondes étaient, selon lui, notamment trop élevées. Hertz n'a pas atteint son 35^{ème} anniversaire, et depuis, l'application de l'héritage de ce grand ingénieur est encore réinventée et élargie chaque décennie par une forte réduction des longueurs d'ondes entre autre utilisées à des fins de communications. Hertz n'aura pas eu tort.

Hülsmeier inventa le radar en 1904 afin de détecter des bateaux bien avant que la deuxième guerre mondiale ait finalement démenti l'estimation pessimiste d'Hertz. La détection d'obstacles par le radar devint un facteur déterminant. C'est afin de dévoiler des obstacles dans un plus grand angle que l'Allemagne développa la première antenne équipée d'un déphaseur : le *Mammut 1*.

De nos jours, le radar, les techniques de RFID ainsi que d'autres applications de communication ont une sélectivité de détection directement liée aux faisceaux de radiation latéraux mineurs. Cette thèse est dédiée à une nouvelle méthode de design de l'antenne à fentes à onde progressive. Elle a comme objectif d'augmenter la précision ainsi que la liberté de design au niveau du diagramme de rayonnement pour les fentes coupées dans un guide d'onde d'une petite hauteur.

Ainsi, le sujet de cette thèse est l'étude des capacités et des techniques de trous métallisés (vias) dans les antennes à fentes à ondes progressives (TWA) pour de fins d'une plus haute précision et simplification de la procédure de design. De plus, la conception des antennes réseau et des travaux auxiliaires nécessaires pour les mesures, sont aussi sujet de ce travail. Dans le *chapitre 3*, l'élément isolé avec une fente dans sa forme originale et sa forme proposée est discuté. L'idée est développée plus en détails pour une antenne réseau *au chapitre 4*, où le concept et le design interne sont révisés par rapport à des règles classiques de conception d'antennes à ondes progressives. Ces concepts sont ensuite légèrement progressés *au chapitre 5*, avec une approche de formation de faisceaux.

Les connaissances obtenues sont ensuite apportées à deux couches dans un format différent, appelé le TWAF, dans le chapitre 6. Il est nécessaire de concevoir un dispositif mécanique et également d'étudier les caractéristiques des matériaux utilisés au chapitre 7.

Chacun des chapitres principaux se termine par une section de résultats et de conclusions, suivie par toutes les références nécessaires à cette section, ainsi que des publications. Enfin, au chapitre 8, des conclusions sont tirées sur l'ensemble du travail. L'annexe fournit des informations supplémentaires sur le script en MATLAB et quelques autres détails qui accompagnent le projet.

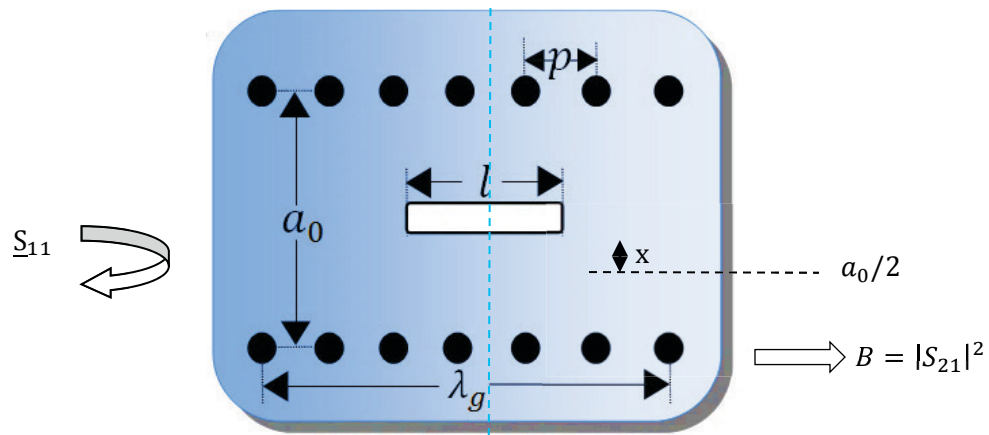


Figure 1 Procédure de la caractérisation d'un élément isolé de la longueur λ_g avec une fente de la longueur l

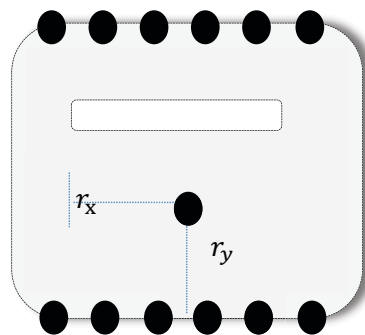


Figure 2 Élimination de la réflexion pour une fente, ($r_x = \sigma, r_y = \rho$, dans certaines Figures)

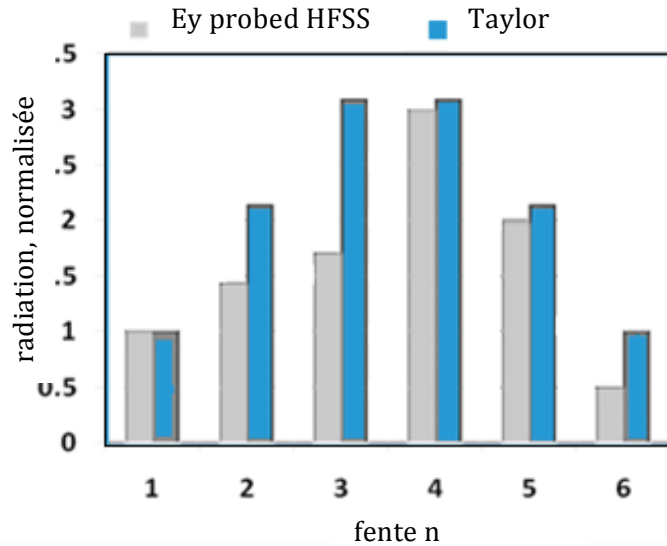


Figure 3 Comparaison entre la radiation effective et idéale (lorsque MC n'est pas prise en compte)

Figure 1 et Figure 2 montrent les éléments appliqués dans ce travail dans leur forme simple. Lors de la conception du TWA faite à partir de ces éléments, en négligeant le couplage mutuel ainsi que les réflexions inhérentes, une divergence entre le rayonnement théorique et pratique se produit. Ce problème est présenté par l'exemple dans la Figure 3. Dans cette figure, la puissance effective est comparée à la valeur attendue par la distribution de Taylor. Il est important de constater que la plus grande divergence est observée là où le plus haut rayonnement se produit.

Jusqu'à un certain point, les procédures de conception connues basées sur des paramètres S biporte du guide d'ondes à fentes peuvent être appliquées. Il est supposé que le TWA fonctionne uniquement avec des ondes de déplacement vers l'avant, ce qui simplifie considérablement la procédure de conception. Toutefois, en l'occurrence, cela ne correspond pas réellement à la réponse de la fente appliquée. Les réflexions de deux ou plusieurs fentes qui sont légèrement mal terminées par le couplage mutuel (MC) ne sont pas couvertes. Figure 4 démontre exemplairement le couplage mutuel entre deux éléments. Néanmoins, pour plusieurs raisons basées sur la caractéristique de l'élément SIW, la fente doit être considérée comme non-résonante et demande ainsi une caractérisation complexe par les paramètres S.

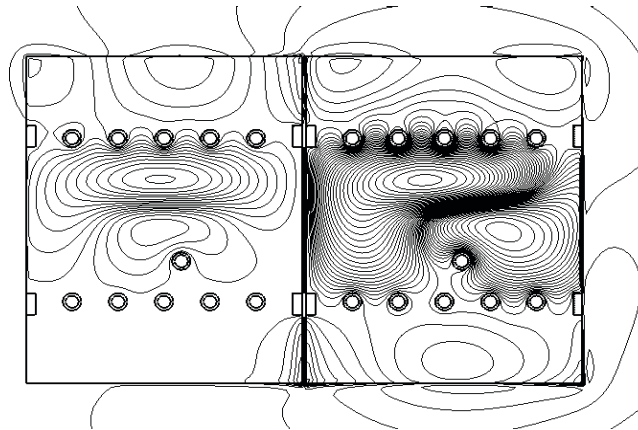


Figure 4 Couplage mutuel au sein de deux éléments

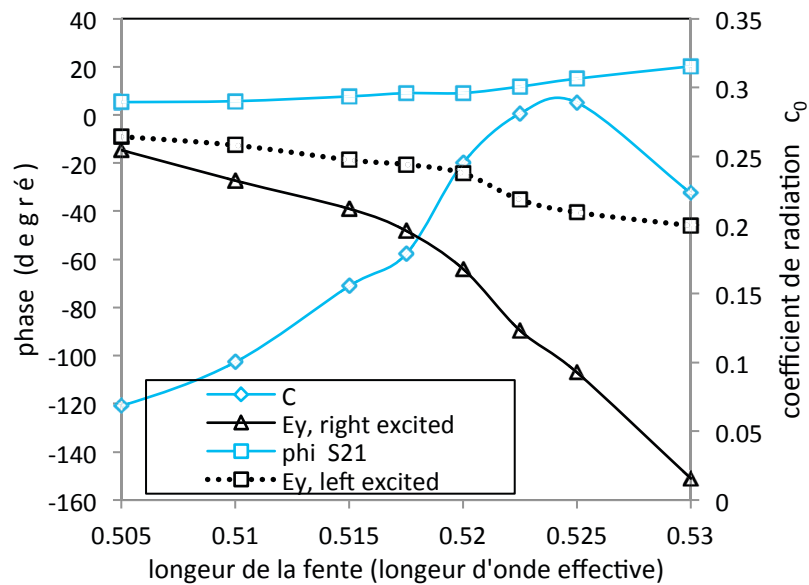


Figure 5 Impact de l'élimination de la réflexion au déphasage de la fente et de l'élément émettant

Les méthodes de conception dans la littérature qui appliquent les paramètres biportés afin de concevoir le TWA, varient la distance entre les éléments et la longueur de fente. Ainsi elles compensent itérativement les effets du couplage mutuel (MC). Enfin, cela n'est ni réalisable ni précis dans le cas des éléments de fentes fortement inadaptées à l'impédance caractéristique de la SIW.

Suite à la découverte des particularités et des limites de la fente longitudinale, observées et montrées comme exemples dans Figure 5, de nouvelles approches sophistiquées, appliquant des vias en mouvement, sont alors conçues.

Figure 6(a) illustre à nouveau l'élément à fente avec *un* via et (b) avec de multiples vias dans le deuxième cas. Par contre, le rapport des paramètres de $v_{x,y}$ qui sont définis par rapport au centre de l'élément, respectivement au mur des vias de guide d'onde intégré au substrat, diffère.

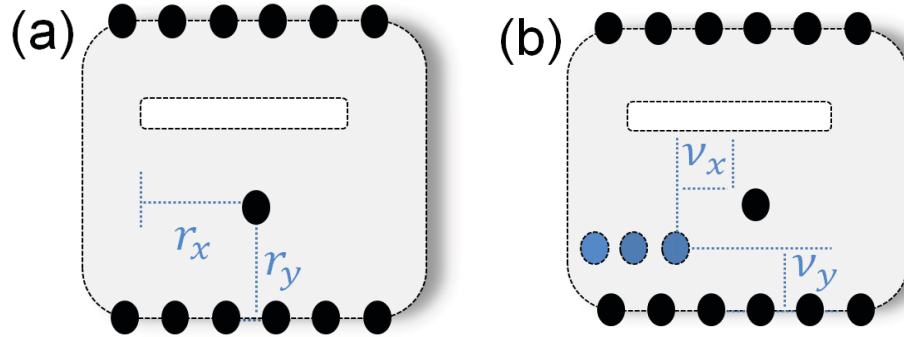


Figure 6 (a) Guide d'onde intégré avec fente et via, (b) avec quatre vias

Dans la Figure 7, les courbes de conception résultantes sont représentées pour $l = 0.5 \lambda_g$, $0.5175 \lambda_g$ et $0.52 \lambda_g$, ce qui résulte à $c_0 = 0.05 \dots 0.25$ de la puissance d'entrée. De cette manière, la phase est décalée de 30° , tandis que $|S_{11}|$ reste inférieure à -30 dB et c_0 reste constante pour une l_n particulière. Notez que le changement peut aussi être considéré comme $\pm 15^\circ$.

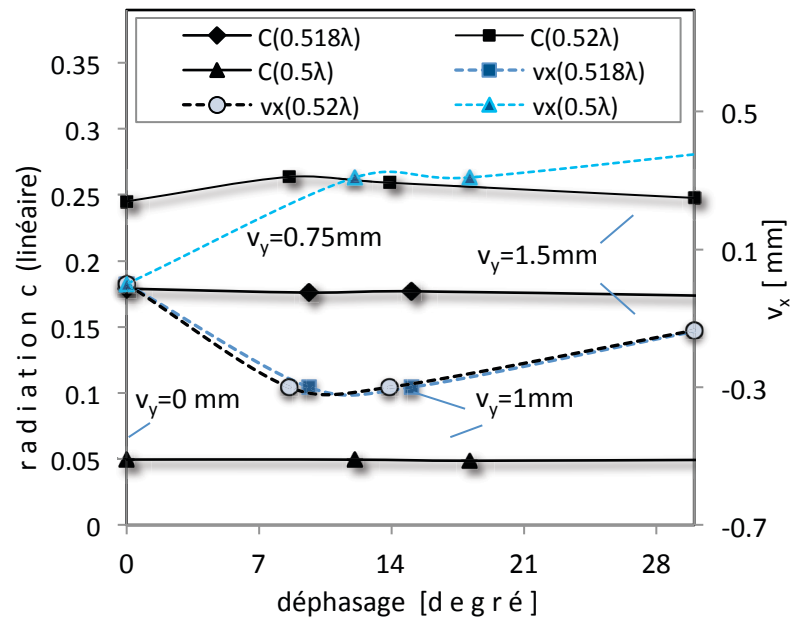


Figure 7 Résultat de la caractérisation d'un élément avec cinq vias, montré comme exemple pour trois longueurs de la fente

Par les moyens proposés, un élément devient plus polyvalent en termes de transmission et de phase de rayonnement. Cette technique a été publiée en partie en [chapitre 3, ref. 16].

Puisque que les fentes isolées ont été prises en compte dans 3 avec l'objectif de créer des réseaux d'antennes complets, le chapitre 4 propose maintenant les étapes et les règles de conception pour atteindre cet objectif.

De l'élément de fente n à l'élément $n + 1$, la relation de (1) décrit l'écart de phase à l'intérieur du TWA approximativement avec un via et sans MC entre des éléments. Par 3.3, les relations des phases sont connues de tous les éléments à fente isolée, voir Figure 8. Le déphasage causé par le MC est considéré postérieurement.

$$\Psi = \Delta\phi = (\phi S_{21}^n + \Delta\phi E_y^{n+1,n}). \quad (1)$$

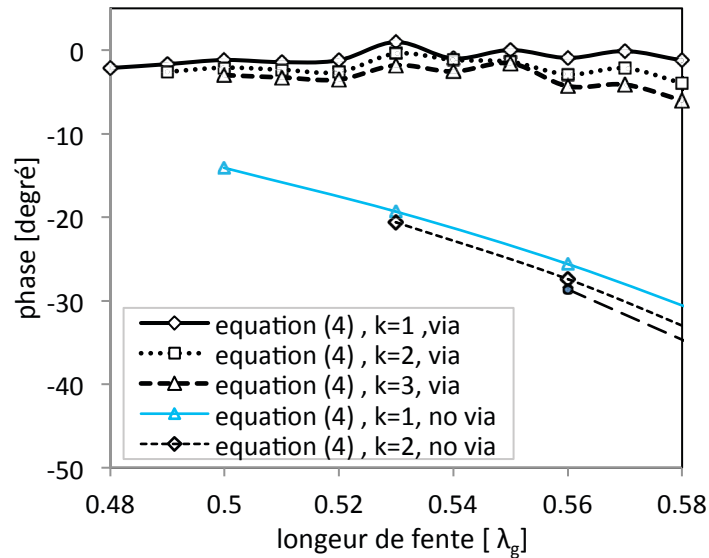


Figure 8 Déphasage partiellement équilibré, le paramètre k est défini dans (19)

$$wR_N = \frac{P_8}{rP} = C_8 / (\alpha_\lambda (1 - C_8)). \quad (2)$$

L'équation (2) décrit exemplairement la considération de la puissance P_8 rayonné par la fente $n = 8$, avec le coefficient de radiation C_8 et l'atténuation α du SIW, comme rapport wR_N entre $P_{N=8}$ et la puissance restante à la sortie rP .

La nouvelle configuration alternative d'éléments rayonnants à fente est basée sur la proposition d'un nouveau mode de calcul de P_{rad} en amplitude et en phase. L'amplitude est ensuite optimisée en modifiant seulement la longueur de la fente; tandis que la phase est réajustée autant que possible au moyen de trous métallisés, comme proposé dans la section 3.4.2 et 3.4.3. De cette manière, une conception précise des antennes à ondes progressives à fentes, y compris celles avec un rapport de largeur/hauteur élevé dans la SIW, est possible.

Figure 9 représente les coefficients typiques MC évalués pour les quatre combinaisons de longueurs possibles de la fente maximale et minimale lorsque le via est inclus dans la conception. Contrairement à certains travaux dans la littérature, on observe un fort impact de la deuxième fente d'une longueur l_2 sur les paramètres concernés. Bien que l'amplitude soit moins influencée, la phase est très affectée et donc, ces contributions MC ne peuvent être négligées.

Pour modéliser le réseau d'antennes, un diagramme de fluence (SFG) cascadié qui considère couplage mutuel externe à partir des deux éléments adjacents, est établi dans la Figure 10. Les paramètres sont définis dans Figure 11. Parce que S_{11}^0 peut être maintenu très faible en raison de la procédure et des règles de 3.4.1, il peut dès au départ être négligé.

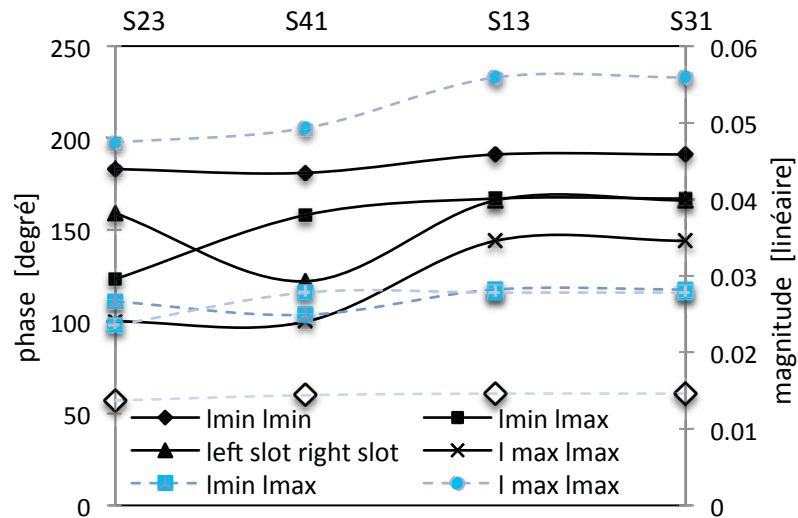


Figure 9 Coefficient du couplage mutuel pour deux fentes de longueurs différentes

Une fois résolu, le SFG aide à optimiser le réseau en faisant varier l_n (voir le script MATLAB) jusqu'à ce que suffisamment de concordance avec les amplitudes attendues soit atteinte.

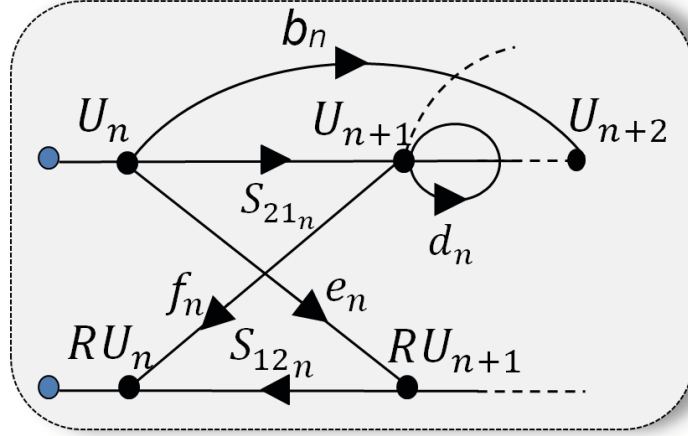


Figure 10 Diagramme de fluence pour la conception de l'antenne-réseau, les paramètres sont définis dans Figure 11, $S_{12/21}$ sont basés sur l'élément émettant isolé

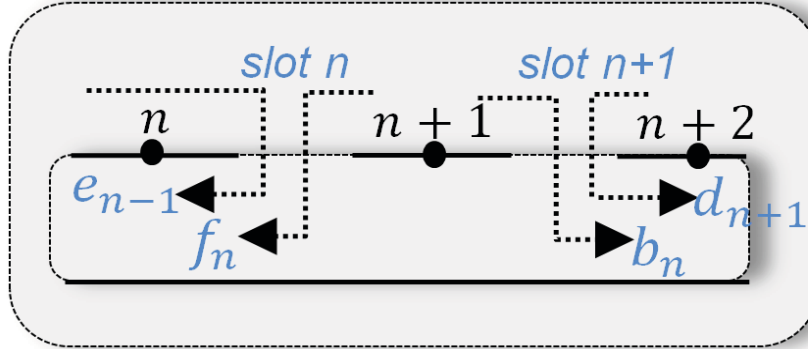


Figure 11 Définition des coefficients du couplage mutuel b_n , d_n , e_n , et f_n , comme appliqué dans le script MATLAB (voir ANNEX)

Ensuite, des déphasages sont réinitialisés comme proposé dans 3.4.3. Le SFG peut être résolu a, (abstrait)

$$RU_n = \begin{cases} 0, & \text{for } n = N + 1, (\text{terminé}) \\ S_{11}^{absorber}, & \text{for } n = N + 1 (\text{pas terminé}) \\ U_{N-1}e_{N-1}, & \text{for } n = N \\ U_{n-1}e_{n-1} + U_{n+1}f_n + S_{12}^n RU_{n+1}, & 1 < n < N \\ U_{n+1}f_n + S_{12}^n RU_{n+1}, & \text{for } n = 1 \end{cases} \quad (3)$$

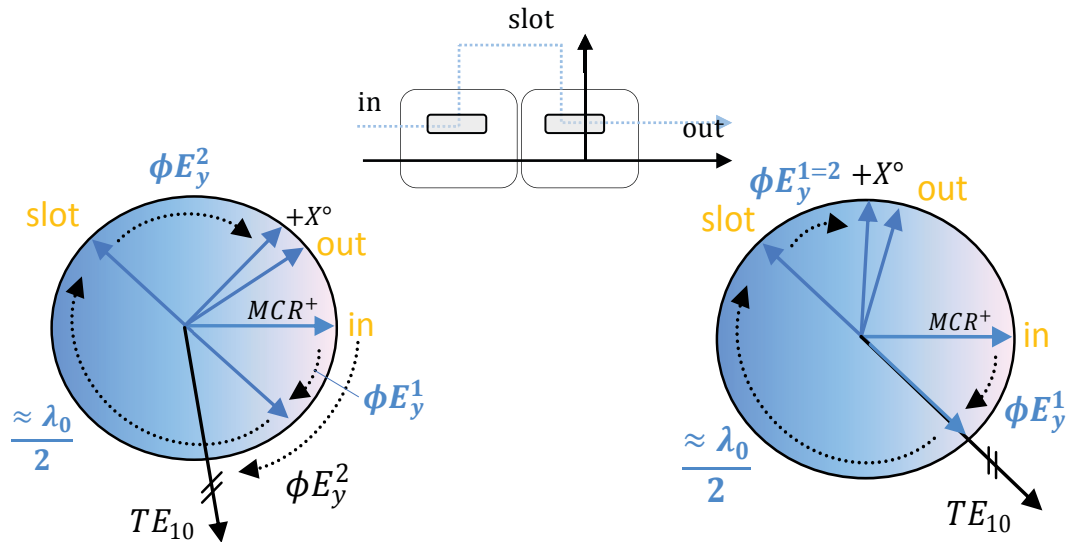


Figure 12 Relation des déphasages pour (à gauche) deux fentes d'une longueur différente, (à droite) d'une longueur identique

Les relations de phase concernées dans les équations et SFG précédentes sont illustrées pour une meilleure compréhension dans la Figure 12. La nomenclature de la Figure est la suivante: les variables en noir décrivent les déphasages internes de la propagation du mode dominant.

Les flèches bleues décrivent le déphasage d'ondes libres. 'In' décrit la phase d'entrée d'un élément. 'Slot' est la phase réelle à la 2ième fente et la phase de sortie du SIW est 'out'. La figure de gauche représente le cas de deux éléments adjacents de deux longueurs différentes et la figure à droite décrit le cas d'égalité de longueur de la fente. Il est évident que 'out' dans le premier cas, diffère de 'out' dans le 2ème cas.

La validation est faite par un réseau d'antennes de $N = 4$ qui est conçu de trois manières différentes avec l'objectif commun des amplitudes de fentes 'ideal' c'est-à-dire, attendues. Les longueurs de fente résultantes des manières de conception différentes, sont utilisées pour la simulation dans HFSS. Dans la Figure 13, la puissance effective sondée à chaque fente est comparée à la valeur 'ideal'. La procédure de conception plus simple appelée 'initial' ne tient aucunement compte de couplage mutuel, c'est à dire que la procédure dérive le rayonnement de la fente uniquement à partir la fente isolée.

Cela conduit, évidemment, à un mauvais résultat par rapport à l 'ideal' désiré. D'autre part, les deux fentes de clés centrales rayonnent comme désiré, c'est-à-dire également, lorsqu'elles sont conçues

comme proposé, (voir '*proposed*'). Par contre, elles diffèrent nettement de 2 dB lorsque l'antenne est calculée avec des simplifications des autres modèles, voir '*forward*'. Ceci est principalement lié à la forte altération par les réflexions négligées causées à la base par le couplage mutuel.

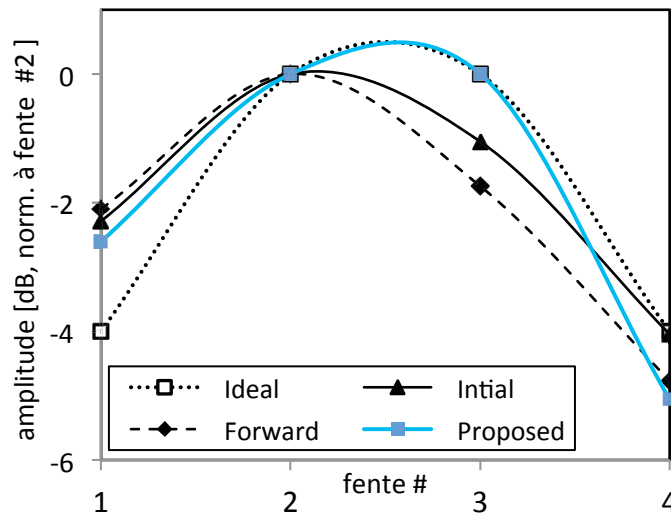


Figure 13 Validation en matière de divergence entre les amplitudes effectives et idéales

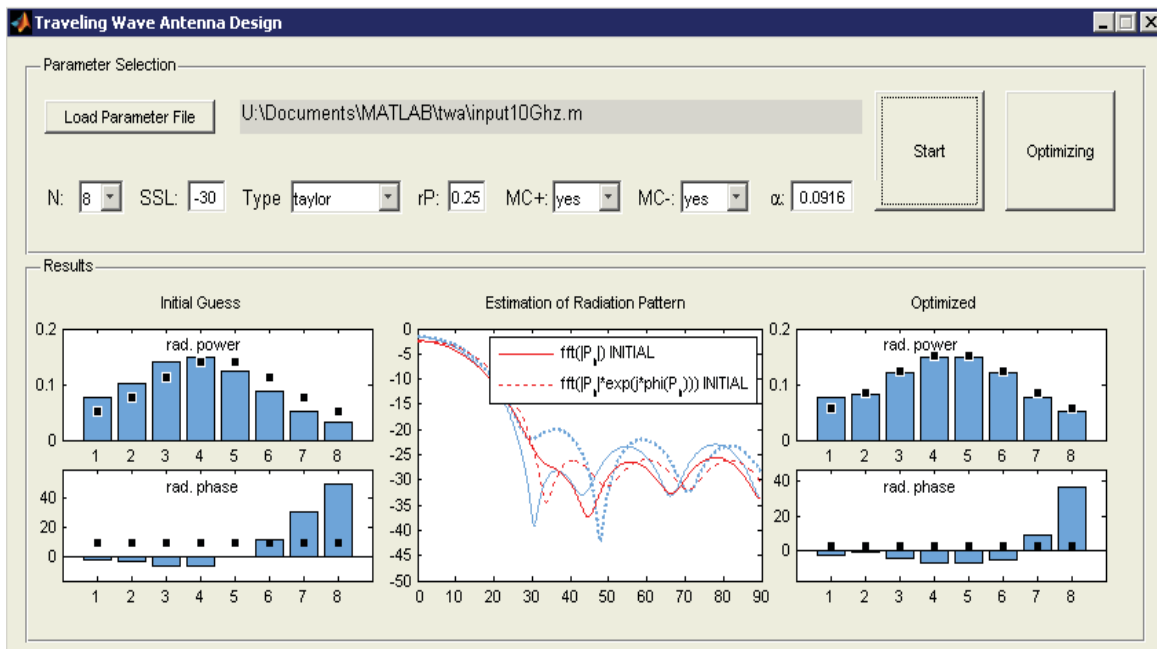


Figure 14 Interface utilisateur graphique Matlab

Une interface graphique est ajoutée pour plus de commodité, représenté dans la Figure 14. L'outil fournit une estimation approximative du diagramme de rayonnement rapport, généré par la $f f t ()$.

Pour prouver le concept et la faisabilité de la procédure de conception proposée, des circuits de réseaux d'antennes pour le 77 GHz millimètre-bande de fréquence ont été fabriquées, voir Figure 15. De plus, des simulations pour la bande de 10 GHz ont été effectuées.



Figure 15 Réseau d'antennes fabriqué avec $N = 4$, la transition conçue au chapitre 7 est appliquée sur les deux côtés

Grâce à l'optimisation de chaque élément de façon individuelle, la performance globale en termes de $|S_{11}|$ pour $N = 4$ et $N = 8$ est très bonne, malgré de nombreux vias supplémentaires introduits, présentées à la Figure 16, avec l'exemple de $N = 4$, en simulation et mesure. D'un autre côté, les limites de la conception proposée sont évidentes. La réflexion ne peut pas être réduite davantage sans autres moyens.

Le résultat de diagramme de rayonnement mesuré et simulé est représenté dans la Figure 17 pour $N = 4$ et le plan H. L'objectif principal de l'ajustement et de l'égalisation de la direction du faisceau a été adéquatement réalisé. Rappelons que sans méthode appropriée, le faisceau principal serait incliné en raison de l'écart entre les phases inhérentes et des fentes de différentes longueurs.

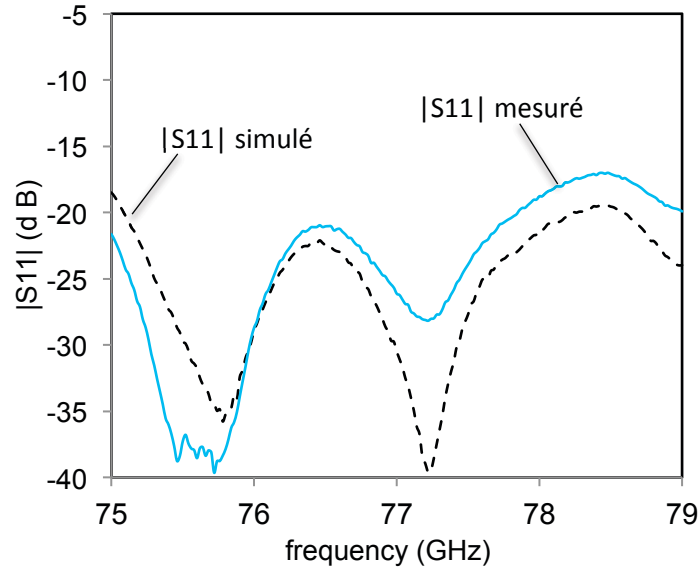


Figure 16 Coefficient de réflexion $|S_{11}|$ du circuit fabriqué ($N = 4$), mesure et simulation

Cependant, après une recherche intense, des problèmes mécaniques avec la fixation et le guide d'ondes ont été identifiés comme responsables du résultat modeste en termes de lobes latéraux mesurés. Bien que le guide se termine par un absorbeur adapté à la fin, les réflexions documentées au chapitre 4, particulièrement en fonction des vis de fixation, sont responsables de cette dégradation. Dans la Figure 17, cette dégradation est simulée en émulant la fixture réelle, c'est-à-dire avec des réflexions.

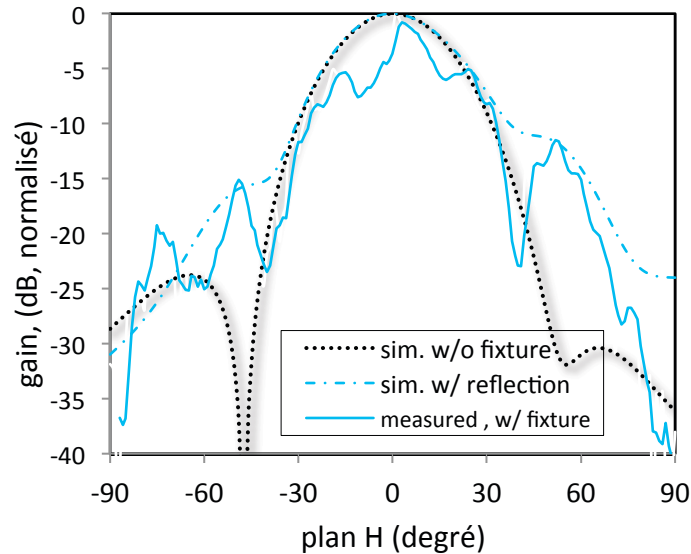


Figure 17 Diagramme de rayonnement de circuit fabriqué ($N = 4$) dans la transition et avec le dispositif proposé dans le chapitre 7

Pour la bande de 10 GHz, les diagrammes de rayonnement sont illustrés dans la Figure 18. Une fois de plus, le 'initial' et le 'forward' sont inclus. Avant toute optimisation, le concept proposé ('proposed') donne une très bonne SLL. Pour la distribution d'amplitudes choisie, il faudra un petit déphasage négatif de plus pour éliminer la cause présumée de la SL légèrement asymétrique.

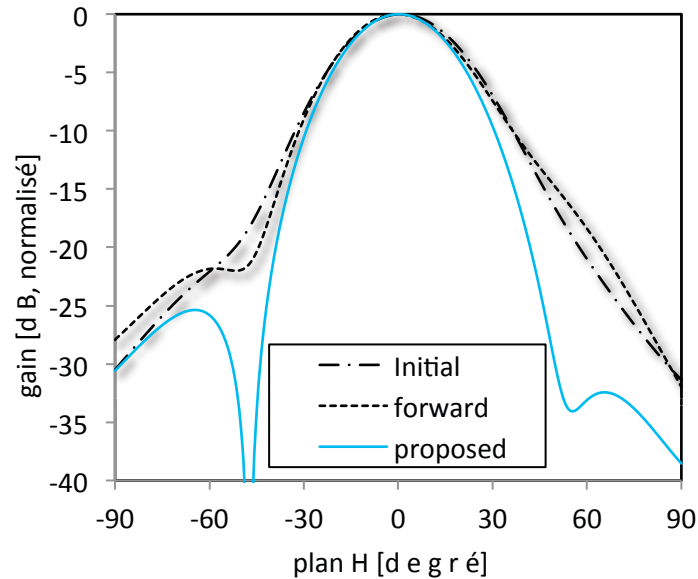


Figure 18 Comparaison de diagrammes de rayonnement à 10 GHz, «initial» est l'approche de conception qui néglige le couplage mutuel, «forward» suppose des ondes se déplaçant vers l'avant seulement

En résumé, dans les chapitres 3 et 4, un mode de configuration d'antennes de fente qui permet à décaler la phase de $> 30^\circ$ est présenté. Pour un réseau d'antennes de fente, les écarts de phase entre les fentes sont ajustés à l'intérieur, c'est à dire sans impact sur la longueur ou position de la fente elle-même. En raison de cet avantage, un procédé de conception simple qui prévoit une excitation de la fente de chaque côté, peut être proposé. La validation avec les logiciels FEM montre un bon accord avec les amplitudes souhaitées et révèle un diagramme de rayonnement à faible SLL de -27 dB avant d'autres moyens d'optimisation. Les mesures d'un circuit fabriqué ont prouvées qu'un faisceau de zéro degré peut être réalisé avec succès par cette approche. Le réseau d'antennes donne un faible $|S_{11}|$ prouvé par des mesures.

Cependant, le projet a révélé qu'un absorbeur guide d'onde intégré doit être conçu comme travail futur, car les réflexions de la transition appliquée dégradent les résultats. En résumé, les méthodes de conception proposées et la configuration de l'élément sont très pratiques et efficaces, ce qui a encore été confirmé avec un script MATLAB, également fourni en annexe. La méthode proposée est très utile en particulier pour les antennes à ondes progressives à guide d'onde intégré au substrat avec des ratios de largeur/hauteur du SIW élevés. Les autres méthodes classiques ont été présentées comme étant moins performantes.

Deux autres idées ont été développées sur la base de la technique mise au point avec le TWA et la connaissance de l'influence des vias. La première idée est destinée à l'utilisation de la technique afin de réaliser une formation de faisceaux. À chaque élément, un déphasage est ajouté expressément. Le résultat en Figure 19 démontre la faisabilité générale de cette idée. Pour la première fois, à la connaissance de l'auteur, des faisceaux arbitrairement à configurer ont été présentes pour des fentes longitudinales sans modification de distance d'élément. Les lobes littéraux restent inférieur à -20 dB, ce qui est supérieur aux résultats montrés dans la littérature pour des antennes TWA.

Quelques dégradations n'ont pas été évitées mais peuvent être réduites par une augmentation d'efforts de calculs. Ceci est à la fois un point faible du concept qui demande un grand effort de simulation de l'élément de la fente isolé.

Alors que le TWA conçu jusqu'ici comprend *une* couche rayonnante dans l'espace libre, l'approche de la deuxième élaboration de la TWA comporte une disposition de *deux* couches. Une motivation pour cette approche est d'avoir une meilleure performance dans le plan E. Ensuite, quatre faisceaux sont à réaliser pour l'utilisation dans une antenne monopulse.

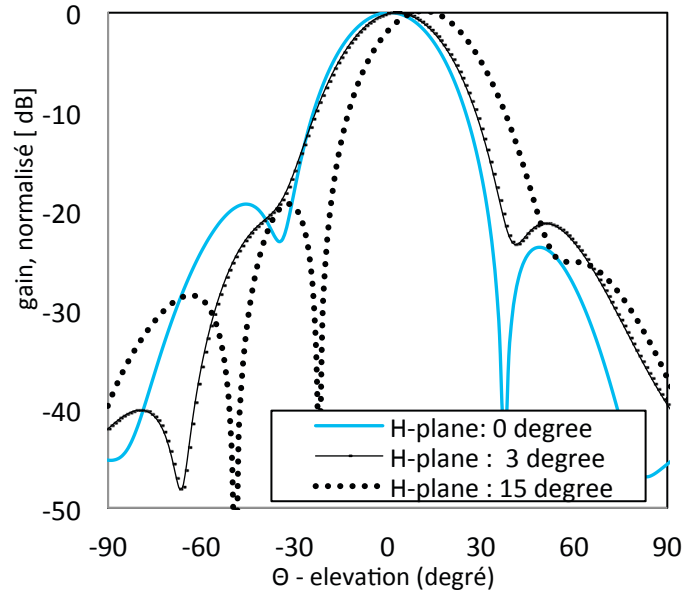


Figure 19 Diagramme de rayonnement, trois faisceaux

Quatre SIW à ondes progressives sont utilisés pour nourrir la couche supérieure de cette antenne appelée TWAF. Les quatre alimentations représentent un faisceau chacune. La couche supérieure consiste en un réseau de fentes en résonance, selon l'architecture commune décrite en 2.4.

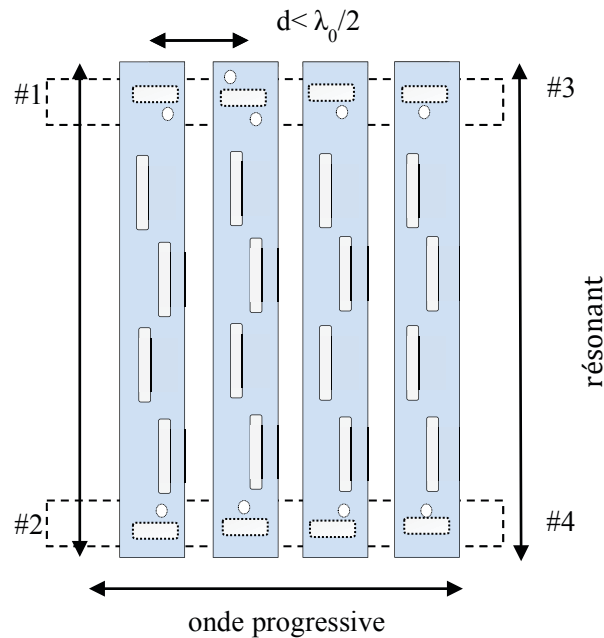


Figure 20 Une antenne résonante alimentée par quatre SIW à onde progressive, qui fait quatre faisceaux de balayage

Par conséquent, l'antenne est alimentée par le TWA. Figure 20 montre la structure globale de l'antenne. L'optimisation en logiciel de simulation est réalisée avec le guide d'onde rectangulaire conventionnel (RWG) équivalent. Avec $\epsilon_r = 9.9$, les résultats sont présentés pour les quatre portes d'excitation dans la Figure 21. Rappelant l'architecture mise en place, chaque porte ne peut pas être terminée d'une manière égale. Néanmoins, un bon compromis qui réduit tout de même la largeur de bandes a été trouvé. L'isolation est très importante entre les portes adjacentes afin de ne pas exciter le réseau de fentes résonnantes autrement. En ce qui concerne la Figure 21, l'isolation est tracée à titre d'exemple pour S_{34} , S_{23} . L'isolation des portes non excitées reste > 15 dB.

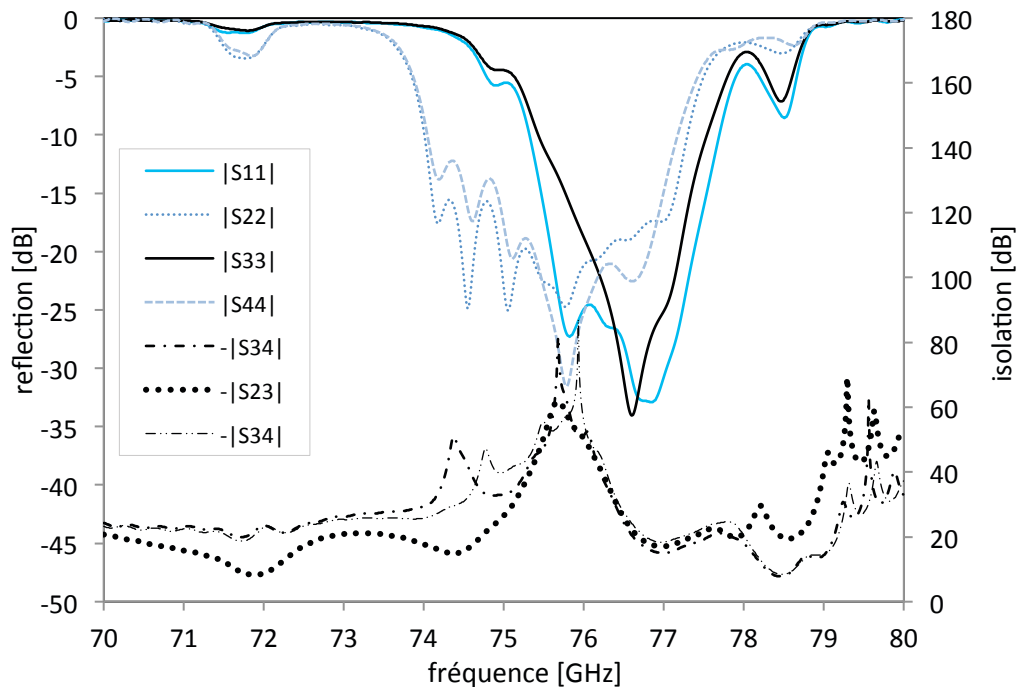


Figure 21 Paramètres S pour les quatre portes d'entrée, l'isolation entre les portes alimentées et non alimentées est également présentée

Les diagrammes de rayonnement des quatre portes #1 à #4 sont représentés dans la Figure 22. La gamme d'angles des faisceaux atteints est de -20° à $+20^\circ$. Une directivité maximale de 15,3 dBi est obtenue. En négligeant les pertes de conduction, l'efficacité est d'environ 70%, voir aussi Figure 130. D'autres diagrammes de rayonnement sont montrés dans la thèse pour le cas d'une antenne monopulse.

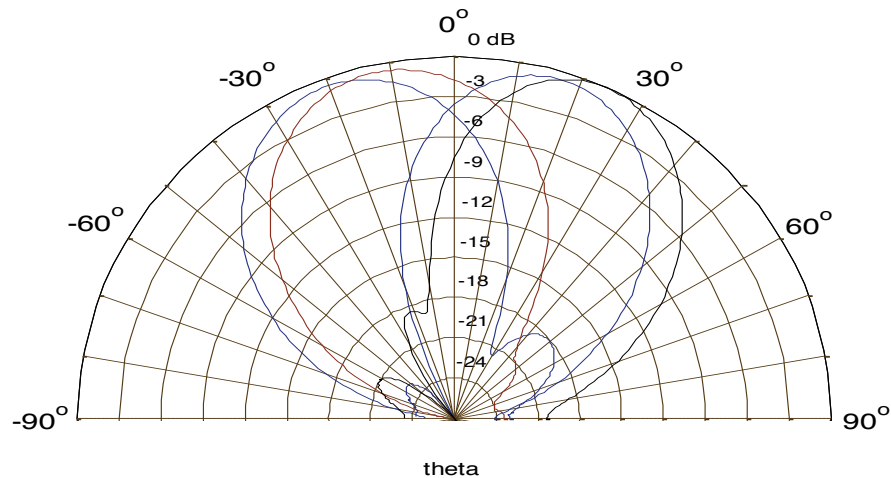


Figure 22 Diagramme de rayonnement, directivité normalisée, plan E, de gauche à droite: port # 3, # 2, # 4, # 1

Or, dans les sections 4, 5, 6, des circuits de simple et de double couches ont été élaborés et leur faisabilité a été prouvée à la fois par simulation et en partie des mesures. Bien que le réseau d'antennes de SIW du chapitre 4 soit principalement conçu pour *une* couche, il a été fabriqué également en technologie LTCC. LTCC nécessite au moins deux couches pour des raisons de stabilité. Cela implique un nouveau défi si un RWG classique d'une autre hauteur doit être connecté exclusivement à un SIW sur la couche supérieure sans transition à micro ruban (MS). Les approches existantes appliquant des lignes de transmission planaire comme MS, doivent être contournées. MS a l'inconvénient de permettre de mesurer seulement sa permittivité effective et non relative. Une transition de guide d'onde pour le couplage du mode TE pour le SIW à RWG est donc nécessaire. Cette tâche principale est résolue et présentée dans le chapitre 7.

En outre, la permittivité relative, la perte et le retrait des substrats LTCC appliqués, ne sont pas encore entièrement décrits par la littérature pour cette fréquence. Une enquête de ces paramètres est aussi traitée dans ce chapitre comme 2ième sujet.

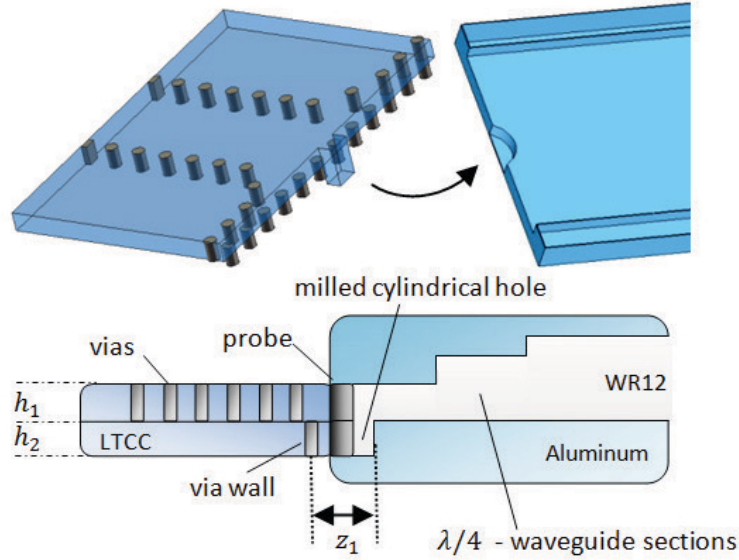


Figure 23 SIW y compris la sonde et le guide d'onde rectangulaire, vue de côté

Figure 23 montre une vue de côté de l'idée de transition. La procédure de conception en 7.4.2 traite le SIW, la taille de la sonde et la position dans le trou, ainsi que la conception de la partie RWG. Le retrait (shrinking) et le LTCC caractérisation sont décrits dans 7.6.1. Ensuite, les résultats d'une mise en œuvre complète de back-to-back sont présentés.

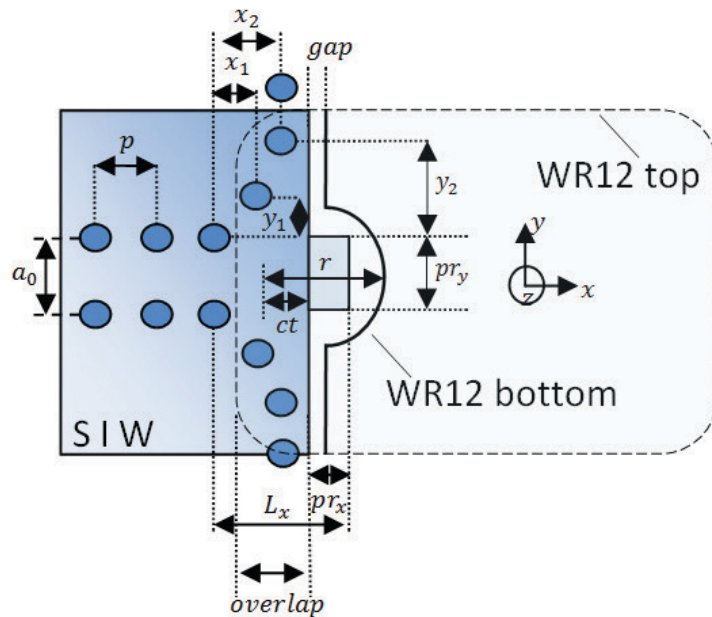


Figure 24 Aperçu de la transition, ct est défini pour l'écart de défaut

Dans la 1ère couche LTCC, le SIW est élargi pour aborder la largeur WR12, c'est-à-dire que deux vias dans sa paroi sont déplacés vers l'extérieur, comme on le voit dans la Figure 25. En outre, les réseaux d'antennes de 4, 5, and 6, et les circuits LTCC pour déterminer les paramètres du matériau, exigent une structure mécanique pour la mesure des paramètres S et de diagramme de rayonnement. Un appareil métallique est proposé pour toutes ces tâches et permet de mesurer trois chaînes d'une longueur électrique égale. La fixture est montrée dans la Figure 25. Son coefficient de réflexion et celui de transmission sont montrés dans la Figure 26.

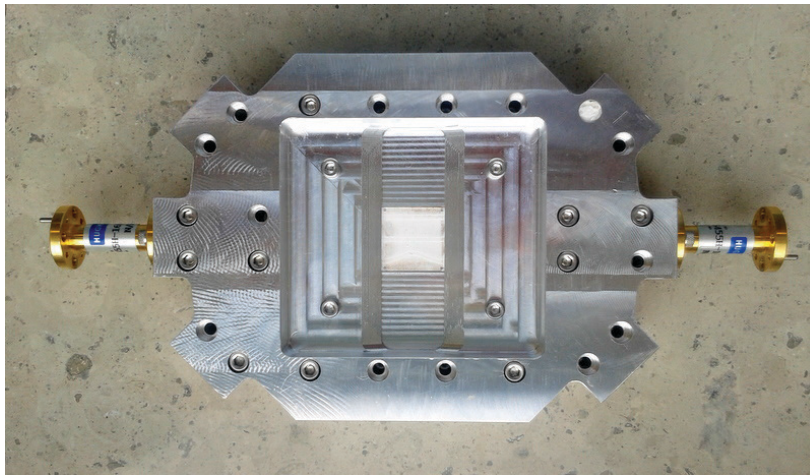


Figure 25 La fixture

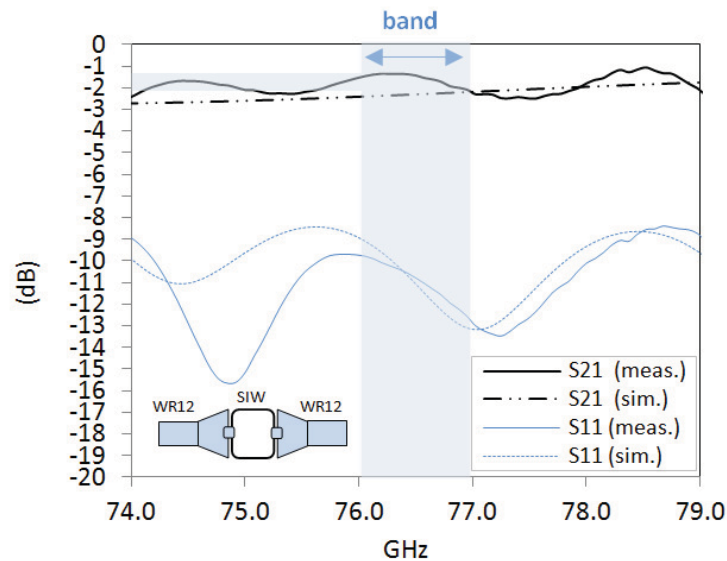


Figure 26 Réflexion et transmission, mesurées et simulées, avec une erreur de retrait de $\approx -34 \mu\text{m}$, WR12-SIW-WR12, (voir le texte pour la perte et ϵ_r)

TABLE OF CONTENTS

TITLE.....	i
ACKNOWLEDGEMENTS.....	ii
DEDICATION.....	iii
ABSTRACT.....	iv
RESUMÉ EN FRANÇAIS.....	v
TABLE OF CONTENTS.....	xxiv
TABLE OF FIGURES.....	xxix
TABLE OF TABLES.....	xxxvi
NOMENCLATURE.....	xxxvii
ABBREVIATIONS.....	xxxix
1 INTRODUCTION.....	1
1.1. Motivation.....	1
1.2. Orientation.....	4
2 BACKGROUND, STATE-OF-THE-ART, AND FUNDAMENTALS.....	7
2.1. Introduction.....	7
2.2. Fundamental Relations in Waveguides.....	7
2.2.1. Rectangular Waveguide (RWG).....	7
2.2.2. Substrate Integrated Waveguide (SIW).....	7
2.3. Radiation of the Longitudinal Slot and its Complementary Dipole.....	9
2.4. Resonant Waveguide Slot Antenna Arrays (RESA).....	9
2.5. Beam Forming Antenna Arrays Based on Matrices (BFA).....	10
2.6. Traveling Wave Slot Antenna Arrays (TWA).....	12
2.6.1. Elementary Slot Radiation Coefficient Computation.....	12
2.6.2. Particular Challenge for Complex S-parameter Usage.....	15

2.6.3. Beam Forming Capabilities of the TWA	15
2.7. Double Layer Slotted Waveguide Beam Forming Arrays (TWAFAs)	16
2.8. Conclusion and Derived Objectives	18
2.9. References	19
3 ENHANCED SLOTTED ELEMENTS IN SUBSTRATE INTEGRATED WAVEGUIDE	25
3.1. Introduction	25
3.2. Elementary Definitions of the Slot in the SIW	25
3.2.1. Traveling-Wave Propagating Direction and Phase	25
3.2.2. Radiated Power	26
3.2.3. Additional Definitions	27
3.3. Linearized Characterization of Isolated Off-Resonant Slots	27
3.3.1. Radiation, Transmission and Reflection.....	28
3.3.2. Offset and Slot Width	29
3.3.3. Impact of the Substrate Height.....	30
3.3.4. Phase of Reflection and Radiation	31
3.3.5. Discussion of Difficulties with the Linearized Longitudinal Slot	33
3.4. Study of the Impact and Capabilities of Vias in the Slotted SIW	33
3.4.1. Altering the Complex Transmission and Reflection of the Slot by Vias	35
3.4.2. Approaches of Slot Phase Shifted Elements	40
3.4.3. A Sophisticated Versatile Slot Phase Shifting Approach	49
3.5. Preconditions for the application of the designed elements in an array	53
3.5.1. SIW and RWG Equivalent Width	53
3.5.2. Full Wave Analysis Evaluation	54
3.5.3. Proof of Traveling-Wave Matched Slot.....	55
3.5.4. Dependency of Shifting Slotted Elements	56
3.5.5. Slot Phase Linearity over Bandwidth of a Fabricated Circuit	56
3.5.6. Simulation Stability of Dominant and 2 nd Mode	57
3.6. Conclusion.....	58
3.7. References	58

4 TWA DESIGN BY INTERNAL PHASE VARYING AND ENHANCED APPROPRIATE MODELING IN SIW	61
4.1. Introduction	61
4.2. Introductory Definitions and Thoughts on the Traveling-Wave Antenna	61
4.2.1. Slot Phase Consideration in the Reflection Cancelled Case.....	62
4.2.2. Radiation Coefficients Considering Losses.....	63
4.3. Alternative Configuration of the Slotted Radiating Elements in the TWA	66
4.3.1. Design and Configuration	66
4.3.2. Typical Mutual Coupling in the Array and its Compensation	67
4.3.3. Dual Excitation of the Slotted Element.....	71
4.4. Modeling of the New TWA Configuration Applying an SFG	73
4.4.1. Sequential Linear Full Model of the TWA (Rule of Mason).....	73
4.4.2. Enhanced Antenna Array Design	74
4.4.3. The Approximate Solution of the Signal Flow Chart.....	76
4.4.4. Simplifications of the TWA Model and their Limitations.....	79
4.4.5. Validation.....	80
4.5. Matlab Application with Graphical User Interface	82
4.5.1. Concept and Implemented Flow Chart.....	82
4.5.1. The Optimizer Function	82
4.5.1. Parameter File and Data Structure	84
4.5.2. Graphical User Interface	84
4.5.1. Design Example.....	85
4.6. TWA Radiation Pattern Measurement Setups.....	86
4.6.1. Impressions from the First Setup.....	86
4.6.2. Second Setup using Power Diodes.....	87
4.6.3. Power Level Diode Characterization Curves	87
4.7. Results and Discussion.....	89
4.8. Conclusion.....	96
4.9. References	96

5 FURTHER PHASE VARYING FOR MULTIPLE ARBITRARY BEAMS IN A QUASI-TWA ARCHITECTURE.....	99
5.1. Introduction	99
5.2. Attraction and Challenge of Extending the TWA for Arbitrary Beams.....	99
5.3. Enhanced Phase Shifting with Additional Vias	100
5.4. Experimental Results and Discussion	100
5.4.1. Phase Shifting in the TWA.....	100
5.4.2. Isolation between Channels	101
5.4.3. Reflection Coefficient and Pictures.....	102
5.4.4. Radiation Pattern.....	102
5.5. Fabricating Efforts and Issues	104
5.6. Conclusion.....	105
5.7. References	105
6 A TWO LAYER TWA FED FOUR-BEAM SLOT ANTENNA IN RESONANT ARCHITECTURE.....	107
6.1. Introduction	107
6.2. Background and Context of the TWAFSA.....	107
6.3. General Antenna Architecture and its Preparation for Beamforming	107
6.4. Design Procedure	109
6.4.1. Radiating Top Layer	109
6.4.2. Design of the Four Port Feeding Network and Transverse Couplers.....	109
6.5. Results and Discussion.....	114
6.6. Conclusion.....	118
6.7. References	119

7 TWO LAYER PLANAR LTCC TRANSITION AND ITS APPLICATION FOR LTCC CHARACTERIZATION.....	121
7.1. Introduction	121
7.2. Motivation for a Planar Solution and Mechanical Constraints.....	122
7.3. The LTCC Technique and the Need for Investigating its Properties	123
7.4. Design of the Novel Two Layer SIW to RWG Transition	124
7.4.1. Background and Context of this Transition	124
7.4.2. Via Configuration and Cylindrical Hole Design in the RWG	126
7.5. Design of a Three Channel Fixture Comprising the New Transition.....	129
7.6. Circuit Fabrication a. LTCC Characterization Applying the Conceived Fixture.....	131
7.6.1. Shrinkage Measurements of Micrographed LTCC circuits.....	131
7.6.1. Material Study on LTCC.....	132
7.7. Experimental Results and Discussion	135
7.8. Conclusion.....	137
7.9. References	138
8 CONCLUSIONS AND OUTLOOK.....	141
8.1. Conclusions	141
8.2. Main Contributions of this Thesis	144
8.3. Outlook and Future Work.....	144
ANNEXES.....	145

TABLE OF FIGURES

Figure 1 The Mammut 1, the first phased array	2
Figure 2 Traveling-wave antenna concept and challenge.....	3
Figure 3 (left) RFID example with multiple tags in the same field driven by one omnidirectional beam, (right) radar application w. two cars	3
Figure 4 Beamforming Network and Antenna in cascaded structure	4
Figure 5 Original picture of the so-called 'laminated waveguide', a new generation of transmission line, Figure from [6].....	8
Figure 6 Basic parameters of an SIW	8
Figure 7 Perpendicular slot and its equivalent circuit in resonance.....	10
Figure 8 Eight beam MS solutions, two layers (left) from [40] one layer from [41].....	11
Figure 9 Radiation coefficient nomenclature at each slot.....	12
Figure 10 Near field result after successful slot amplitude distribution design (Taylor) at z = 0.3 mm	13
Figure 11 Comparison between simulated probed <i>P_n</i> and perfect Taylor distribution (when MC is not taken into account)	14
Figure 12 Deviation from 0° -phase (before any means of equalization).....	14
Figure 13 Example of a bad performance of TWA beam forming [48]	15
Figure 14 Adaption of the element distance for BF with poor results [49]	16
Figure 15 The monopulse antenna of [53]	17
Figure 16 Kolak [55] proposal	17
Figure 17 A. Simmons Idea in 1963 [61]	18
Figure 18 Definition and occurrence of the different phases	26
Figure 19 Input and output variables in the simple structure, (arrays are discussed in Chapter 4). 26	
Figure 20 Y-component of the electrical field within the slot when excited from the left / right.....	27

Figure 21 Common procedure of characterization for one radiating isolated slot in a SIW segment of the length λg , (if not stated otherwise).....	28
Figure 22 Basic linearized slot characterization.....	28
Figure 23 Parameter study on slot width influence. The six Figures depict the radiation coefficient for $w_x = 0.14 \text{ mm}$ to 0.19 mm , CF=76.5 GHz.....	29
Figure 24 S_{21} as a function of offset x and length l , peaks are due to the parameter sweep resolution and MATLAB function	30
Figure 25 c_0 as a function of l and offset, there is only one maximum due to the fixed slot width and higher reflections for increased offset, (the dark region around the rising curve is a graphical error)	31
Figure 26 Slot characterization for $x = 0.05 \text{ mm}$, two different substrates at 76.5 GHz, (simulation: CST)	31
Figure 27 Phase Characterization of a single isolated slot, fixed offset x , (CST)	32
Figure 28 Phase of E-field ϕ , and reflection	32
Figure 29 The E-field, excited from either side (for $x = 0.05$, $l = 0.486 \lambda g$)	33
Figure 30 Effect of a via in the SIW	34
Figure 31 Effect of a via in the SIW, connected or not to the SIW conductive layer, (up) magnitude (below) phase	35
Figure 32 The single via in the SIW	35
Figure 33 The effect of the additional via on ϕS_{21} and ϕE_y (at c_{\max})	36
Figure 34 Effective shift of ϕS_{21} and ϕE_y as function of frequency.....	36
Figure 35 Reflection Cancelling Design for one slot, ($r_x = \sigma$, $r_y = \rho$, in some Figures)	37
Figure 36 Influence of one and no via for reflection cancelling purpose	38
Figure 37 The linearized parameters for the reflection cancelling via for a 76.5 GHz element of $a_0 = 1.074 \text{ mm}$	38
Figure 38 Reflection cancelling via position, at 10 GHz.....	39
Figure 39 Impact of the reflection cancelling on the slot and segment phase	39
Figure 40 Section of modified propagation constant with a_0' , see (17).....	41
Figure 41 Simulated phase shift compared to the predicted one from (17)	41

Figure 42 Effect of phase shifter with 6 vias in the lower part.....	42
Figure 43 Input reflection of a 6 via shift with $(\mathbf{a0} - \mathbf{a0}')/2$ from 0.01 to 0.076 mm at 76.5 Ghz center frequency	42
Figure 44 Additional via introduced after the reflection cancelling via	43
Figure 45 Effective shift of ϕS_{21} and ϕE_y as function of frequency.....	43
Figure 46 The τ -method, with two vias, approach #1.....	43
Figure 47 Influence of one, two, and no via, $\sigma = \mathbf{rx}$, $\rho = \mathbf{ry}$	44
Figure 48 The effect of the additional via on ϕS_{21} and ϕE_y (at C_{\max})	44
Figure 49 Approach #3	45
Figure 50 Approach #3, at 76.5GHz $\mathbf{a0} = 1.074$ mm	45
Figure 51 Approach #4	46
Figure 52 Results of approach #4.....	46
Figure 53 Approach #4, adjustments on first via position, at 76.5 GHz	47
Figure 54 Radiation as a function of the via position.....	47
Figure 55 Approach #5, no particular distance to the slot position is considered	48
Figure 56 Transmission and reflection coefficient as a function of the via position.....	48
Figure 57 Results of Approach #5 after re-optimization of reflection	49
Figure 58 (a) Slotted SIW element with one via, (b) with four vias.....	49
Figure 59 Impact of v_x on the radiation and reflection	50
Figure 60 Characterization results of a single element with five vias, exemplarily shown for three slot lengths, the free parameter is v_y	51
Figure 61 Impact of matching on radiation (as an example for all other dependent parameters), the results of two different pairs of \mathbf{rx}, \mathbf{y} are shown, slot l constant	52
Figure 62 Impact of an inaccurate matching on the phase of the transmission.....	52
Figure 63 Factor for \mathbf{rx}, \mathbf{y} when phase shifting by v_y , shown at 10Ghz.....	53
Figure 64 Comparison of SIW and RWG reflection and transmission coefficients; the conversion is based on (5)	54

Figure 65 Comparison between CST and HFSS for an arbitrary SIW	55
Figure 66 Proof of quasi traveling-wave condition	55
Figure 67 Shifting solely the third element, impact on ϕE_y , shift is in mm	56
Figure 68 Measured phase of a single element.....	57
Figure 69 Measured phase of a single element.....	57
Figure 70 Propagation of first and second mode, the full wave simulation is instable around the transition from complex to real propagation constant.....	58
Figure 71 Equalized phase, estimation, k according to (19).....	63
Figure 72 Radiation coefficients as a function of the slot n , parameterized for loss and rP	65
Figure 73 Typical SIW mutual coupling field produced in the first element by exciting the second. 68	
Figure 74 Mutual Coupling of two elements.....	69
Figure 75 Mutual coupling characterization: model with 2 slots and 4 ports.....	69
Figure 76 Mutual coupling coefficients for four different slots, (from left to right for each coefficient).....	69
Figure 77 Impact of mutual coupling in the frequency domain	70
Figure 78 Mutual Coupling and S_{22} along the array, magnitude.....	70
Figure 79 Mutual Coupling and S_{22} along the array, phase.....	71
Figure 80 One enhanced element excited from either side, $ S_{11} $	71
Figure 81 One element excited from both sides, transmission coefficient.....	72
Figure 82 One element excited from both sides, slot phase.....	72
Figure 83 A single isolated slot signal flow chart	73
Figure 84 Signal flow graph for the antenna array design, the parameters are defined in Figure 85, $S_{12}/21$ are based on the isolated slot characterization	74
Figure 85 Definition of mutual coupling coefficients bn , dn , en , and fn , as also used in the MATLAB script (see the ANNEX).....	75
Figure 86 Phase relation for (left) unequal slot lengths, (right) equal slot lengths.....	79
Figure 87 Model validation in terms of divergence from the ideal slot amplitudes.....	81

Figure 88 Validation #2 optimized pattern side lobes	81
Figure 89 Flow chart of the MATLAB script.....	83
Figure 90 A typical optimization procedure for $N = 4$, y-axis depicts the deviation from the optimum, ('noise' of the function suppressed).....	84
Figure 91 GUI of the Matlab Script.....	85
Figure 92 Typical result of the tool with comparable curves before and after optimization.....	85
Figure 93 Radiation pattern measurement in the anechoic chamber	86
Figure 94 Self-made radiation pattern measurement set up at the EMT-INRS.....	87
Figure 95 Low Power Curve for Diode #2k804109.....	88
Figure 96 Full range, diode #2k804111 and #2k804109 (blue).....	88
Figure 97 Entire setup with excitation and reception.....	89
Figure 98 Fixation holding the antenna, surrounded by absorber material	89
Figure 99 Produced slot antenna array with $N = 4$, the transition conceived in Chapter 7 is applied on both sides.....	90
Figure 100 Produced slot antenna array with $N = 8$, the transition conceived in Chapter 7 is applied on both sides.....	90
Figure 101 Reflection coefficient $ S_{11} $ of the fabricated circuit ($N = 4$), measurement and simulation	91
Figure 102 Radiation pattern of fabricated circuit ($N = 4$) within transition and fixture proposed in Chapter 7	91
Figure 103 Simulated gain of $N = 8$	92
Figure 104 Reflection and residual power	93
Figure 105 Radiation pattern of fabricated circuit ($N = 8$), (simulated)	93
Figure 106 Rad. pattern comparisons at 10 GHz, 'initial' is the design approach neglecting MC, 'forward' assumes forward trav. waves only according to [6].....	95
Figure 107 Result of simulated $ S_{11} $ with and without additional vias.....	95
Figure 108 ϕS_{21} , Phase shifting entity, proof of feasibility (measured)	101
Figure 109 Measured isolation between two beam channels.....	101

Figure 110 Reflection of the array, $N = 8$	102
Figure 111 Fabricated circuit (0° <i>beam</i>)	102
Figure 112 Radiation pattern, 3 beams, simulated	103
Figure 113 Radiation Pattern of zero degree, slightly erroneous ϵ_r	103
Figure 114 Photograph of the 8-element fabricated applying the transition reported in Chapter 7	104
Figure 115 Issues with this technique demonstrated with a slot.....	104
Figure 116 Issues on some LTCC circuits.....	104
Figure 117 Fabricated board of SIWs	105
Figure 118 Traveling-wave fed four beam scanning antenna, architecture, example: port #1 is excited, ports #2,#3,#4 have to be matched.....	108
Figure 119 Slot coupler design curves of coupling.....	109
Figure 120 Excitation of the resonant layer from left up and (right) near field result on top layer, slots out of phase are marked	110
Figure 121 Excitation from down left port #1 (see arrow), result dark = in phase, light = out of phase	111
Figure 122 Coupling challenges and parameters	111
Figure 123 Near field result for a four-beam Design, all slots are in phase	112
Figure 124 Resulting TE mode in upper SIW, simulation	113
Figure 125 The feeding coefficients, (shown for one side only).....	113
Figure 126 Estimated radiation pattern, as a function of different coupling factors C_r , each for high (dotted) and low efficiency (not dotted)	114
Figure 127 S-parameters for all four input ports, the isolation between fed and not fed ports is also depicted.....	115
Figure 128 Rad. pattern, normalized directivity in E-plane, from left to right: port #3, #2, #4, #1	116
Figure 129 Radiation pattern, normalized directivity in H-plane	116
Figure 130 Gain and Directivity over all ports, i.e. beams	117
Figure 131 Aperture Distribution.....	117

Figure 132 Monopulse radiation pattern for difference of #1 and #3 and sum of 1# and #3.....	118
Figure 133 Front view of the fixture holding the novel transition designed in this Chapter (slots shown exemplarily).....	122
Figure 134 Mechanical Model with one layer TWA.....	123
Figure 135 Substrate integrated waveguide including probe and rectangular waveguide, side view	125
Figure 136 SIW to WR12 transition overview, ct is defined for the default gap.....	126
Figure 137 Input reflection and transmission as a function of the air gap, at CF, simulated with CST	127
Figure 138 Three step waveguide impedance transformer.....	129
Figure 139 Horizontal cut through the fixture	130
Figure 140 The fixture.....	130
Figure 141 Fixture applied in anechoic chamber	131
Figure 142 Probe in waveguide cylindrical hole and optical calibration donut mark	132
Figure 143 Laser cut through two layer LTCC, probe and slightly impaired vias	132
Figure 144 Optical Measurement of LTTC shrinkage	132
Figure 145 Optical measurements of LTCC shrinkage result.....	133
Figure 146 TRL measurement, (left) drawn circuit (right) photographed circuit.....	134
Figure 147 Comparing $\Delta\phi_{S21}$ measurements of THRU and LINE.....	134
Figure 148 Lossless results of back-to-back SIW-WR12-SIW trans., gap=0.033mm.....	135
Figure 149 Measured and simulated reflection and transmission, with a shrinkage error of \approx -34 μ m, WR12-SIW-WR12 section, (see text for loss, ϵ_r , etc.).....	136
Figure 150 Circuit in Fixture with transition	137

TABLE OF TABLES

Table 1 Parameter Matrix Order.....	84
Table 2 List of all slotted element parameters.....	94
Table 3 Parameters of the N=4	100
Table 4 Parameters of the designed top layer antenna.....	109
Table 5 Other general parameter values of the TWAFAs.....	114
Table 6 Transition Parameters	128
Table 7 Parameter Values for the patch termination of the hybrid antenna, $\epsilon_r = 9.8$	150

NOMENCLATURE

$()_0$	The $_0$ indicates a variable associated with an isolated slotted element
$()^n$	The n indicates that the variable is linked to one certain element, $n = [1 \dots N]$
$b_n, d_n,$	Coefficients in the signal flow chart model, forward
P_{in}	Input power, by default = 1
P_{rad}	Radiated power by a slot, sometimes simply P or P_n for the slot n
Z_0	Characteristic impedance
a_0	Width of the SIW, based on the isolated single element
a_{RWG}	Width of the equivalent waveguide
e_n, f_n	Coefficients in the signal flow chart model, backward
f_c	Cut off frequency of the SIW
r_x, r_y	Reflection cancelling via position, defined with respect to the slot
σ, ρ	See r_x, r_y
ϵ_r	Relative permittivity of a substrate
N	Total number of slots in the TWA, or couplers in the TWAFAs
c	Radiation coefficient
d	Distance between the center of two radiating slots or couplers
l	Physical slot length, mostly given in guided wavelength
n	Slot index
w	Weight factor amplitudes (in MATLAB Code and text)
wth	Width to height ratio in an SIW
wx	Slot width
$\Delta\phi E_y^{n,n+1}$	Difference between slot phase of slot n and slot $n + 1$

Ψ	Auxiliary variable to discuss phase gaps between slots in the antenna array
ϕE_y	Phase of the electric field above the slot in y-direction, excited with zero phase
λ_g	Guided wavelength of the dominant mode propagating in the SIW (or MS)
$MC_{\text{left}}^{-/+}$	Dimensionless mutual coupling, subscript and superscript are defined in the text
$MC_{\text{left}}^{+/-}$	Dimensionless mutual coupling, subscript and superscript are defined in the text
p	Pitch, distance between two centers of a SIW via wall
r	Radius of the via in the SIW
h	Height of the substrate, equal to height of SIW
τ	Phase shifter dimension, with respect to $r_{x,y}$
η_{rad}	Radiation efficiency
rP	Residual power at the end of an array
RU_n	Return (backward) node in SFG
U_n	Forward nodes in SFG
x	Slot offset

ABBREVIATIONS

ACC	Automotive Cruise Control
BF	Beamforming
BFA	Beamforming Antennas fed by BF matrices
BW	Bandwidth, by default the impedance bandwidth
CF	Center Frequency
CST	CST MICROWAVE Studio, commercial full wave simulation
DFT	Discrete Fourier Transformation
HFSS	HFSS Software, commercial full wave simulation tool
HMSIW	Half Mode Substrate Integrated Waveguide
LTCC	Low Temperature Co-fired Ceramic
MC	Mutual Coupling
MS	Microstrip technology
PML	Perfectly Matched Layer (ANNEX)
RESA	Resonant Slot Antennas , conventional design
RFID	Radio Frequency Identification
RFU	Reserved for Future Use (MATLAB code and text)
RWG	Rectangular Waveguide
SIW	Substrate Integrated Waveguide
S-Parameters	Scattering Parameters
TWA	Traveling Wave Antenna
TWAFA	Traveling Wave Antenna Fed (slot) Antenna
WR 12/10	Rectangular Waveguide standards
TRL	Thru Reflection Line calibration

CHAPTER 1

INTRODUCTION

1.1. Motivation

Antennas are a fascinating implementation of electrical engineering. Antennas connect us to the world, they provide a tool in medical applications, and let us enter into a country by an RFID equipped ID-card. Though the world of communication has turned digital, antenna engineering remains an entirely analogue sub-domain. The antenna serves as the linking tool between digital ideas humans are conceiving, and the free wave propagation of these contents by electromagnetic waves. This thesis is about the design on this fascinating analogue link in the chain.

The essence of electromagnetism has not been described before Sir Maxwell set up his famous equations. The propagation of electromagnetic waves anticipated therein has been proven by means of the first antenna. Heinrich Hertz determined the induced voltage with the now called Hertzian Dipole, which led to the fascinating deduction that power *and* information can be transmitted consistently in and over the far field.

Hertz did recognize a further very promising fact along with its evidence of electromagnetic waves. He was able to measure the reflection of metallic surfaces. Hertz even discovered the wavelength and propagation velocity very close to the actual speed of light, which led to the waveguide shortly later. The radiofrequency engineer Hülsmeier applied this reflection and suitably used it as a detector for remote objects. At that time envisioned for vessels, his patent #165546 registered in Munich in 1904 might be considered as the beginning of the modernly indispensable technique of radar.

Ever since the beginning of radar, and other applications that involve directional radiation, requirements on the antennas have been high. The limiting factors of every communication system are the gain *and* the control of unintentional side radiation, named in particular '*side lobes*'.

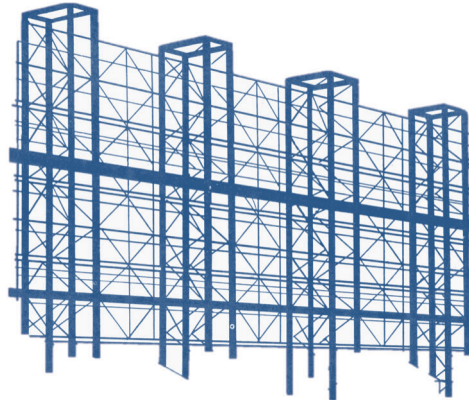


Figure 1 The Mammut 1, the first phased array ¹

To scan an extended range that is wider than the single antenna beam naturally points to, World War II triggered the development of the first phased array on the German side. The antenna *Mammut 1* exhibited multiple so-called *wave shifters* that allowed shifting the signal phase of excitation for all elements. This led to an impressive 120 degree wide span. The side lobe performance of *Mammut 1* is undocumented. It would have been noteworthy, as mutual coupling and the reflection of each element have most likely been neglected due to the lack of theory. Consequently, when shortly after *Mammut 1* the radar had to become more versatile for moving targets, a mechanical steering device composed of high gain parabolic antennas replaced it.

One solution widely used today for the latter purpose of detecting targets is the slot antenna. This waveguide fed antenna is applied particularly for its high control of the radiation pattern, e.g. to avoid false detection of targets. The slot antenna, though invented in 1938 by British Engineer A. Blumlein, was not yet available for the boom of the radar technique during WWII. Fatefully, Blumlein died during the development of the British version of the radar.

The tremendous features of the slot antenna became controllable in the 1950s and 1960s with its key particularities been published. In the first place, solely the behaviour of an isolated slot and its characterization in a rectangular waveguide have been studied. Finally in the 1980s, a full design guide became available with wide control of the radiation pattern and impedance matching of resonant slot antenna arrays.

¹ Source: US War Department [Public domain], via Wikimedia Commons

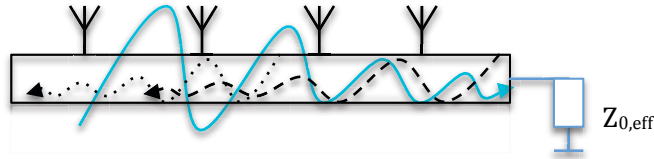


Figure 2 Traveling-wave antenna concept and challenge

Competing with the *resonant* approach operating a standing wave in the waveguide, the alternative *traveling-wave* antenna (TWA) that is terminated by a matched absorber has noteworthy advantages. Regularly, the bandwidth increases. In addition, the radiation pattern features such as beam width are further controllable by a wide freedom in the choice of the slot radiation. It is consequently appreciated in applications where the highest control of the radiation pattern is required. However, the main radiation beam is not only tilted by general inherent phase differences. Each discrete TWA involves also the risk of potential spurious radiation caused by small reflections from slightly mismatched elements, indicated in Figure 2. Though there are techniques to solve both challenges, they do not solve the latter individually. That is, reshaping the beam angle to zero intersects with the 2nd issue of mismatched elements. This represents to the author a key drawback of the slotted TWA and its improvement provides a first motivation for this work.

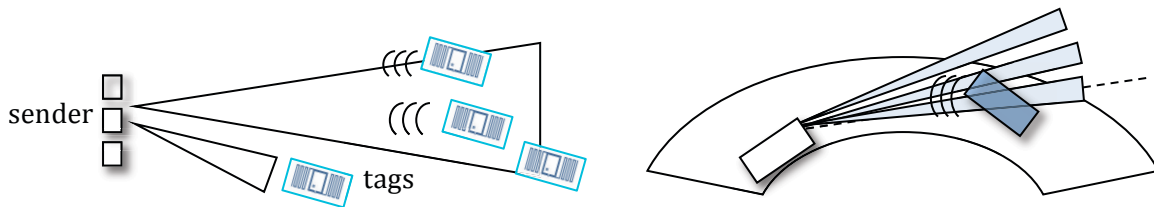


Figure 3 (left) RFID example with multiple tags in the same field driven by one omnidirectional beam, (right) radar application w. two cars

Apart from the design of the individual antenna, a future RFID or radar system requires directing its radiation towards the target, i.e. to increase its gain at a *variable* particular angle. Multiple beams are essential e.g. in RFID technologies with numerous tags in a field, see Figure 3, or vehicle guidance systems. High side lobes produce false detection of tags or targets and reduce the selectivity. So-called beamforming (BF) matrices that serve as the required preceding phase shifter exist, as indicated in Figure 4. A high space need from four beams on, and huge efforts to design low side lobes over the fed arrays are, nevertheless, some of the accompanying drawbacks.

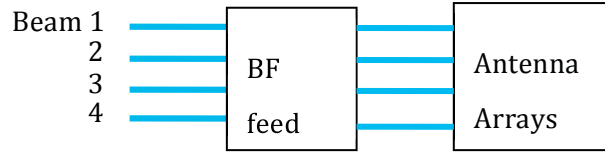


Figure 4 Beamforming Network and Antenna in cascaded structure

Naturally, in microwave and millimeter-wave bands, space is of less importance. Generating an individual set of arrays for each required beam is very appealing to fully avoid BF matrices. Recalling the initially outlined issues of the individual TWA, a simple enhancement of the TWA design procedure that allows to better control the individual slot phase might open the door for a much simpler BF solution, too. With the sole drawback of additional required space, any arbitrary beam angle would be achievable for every redesigned TWA, if a sound design process allows shaping the effective slot phase. Conventional BF matrices or frequency scanning may be applied afterwards.

Virtually no work has been published on techniques to achieve one *particular* beam of the slot TWA without altering individually the dielectric material or the distance between elements. Difficulties that rule out this approach are repeatedly cited in the literature such as the dielectric loss, mutual coupling and the complexity of phase computation. This serves as the second motivation for this thesis.

Lastly, to meet real industrial requirements, any proposed solution and enhancement of the traveling-wave antenna design shall be cost-efficiently producible. Low cost fabrication of conventional waveguides is unmanageable due to an effortful milling process and evidently high material needs. On the other hand, the so-called substrate integrated waveguide (SIW) provides almost the same features. The drawback of a vast amount of vias in the SIW is resolved with the very suitable *LTCC* technology. Due to its flexible tape before firing, any number of holes does not present a challenge. That provides in general the basis for a TWA enhancement by additional vias, however, for the application in millimeter-wave bands the so-called green tapes are poorly characterized in terms of their dielectricity. Thus, usage of this technique shall be preceded by material studies that add a third main motivation for this work.

1.2. Orientation

The leitmotif of this thesis is the study of the capabilities and techniques of vias in traveling-wave antennas, the design of the latter, and the required auxiliary work accompanying the measure-

ments. *In 3*, the isolated slotted element in its original form and its proposed enhanced form is discussed. Basic preparations are carried out in order to develop the idea further for antenna arrays *in 4*, where both the design concept and internal composition are revised with respect to conventional traveling-wave antenna design rules. These concepts are then slightly advanced *in 5* with an approach to use the same vias for beamforming features of the same antenna type. This is then further brought to two layers in a different format, called TWAFAs, *in 6*. For measurement purposes, it is necessary for these arrays to develop a mechanical fixture. In addition, a study of the material characteristics is indispensable. Both latter tasks are accomplished *in 7*. Each of the main Chapters is concluded by a *result and discussion* section, followed by conclusions and references required for the section, as well as publications. Finally *in 8*, the conclusions are drawn over the entire work. The ANNEX provides additional information on the Matlab Script and a few further accompanying details about the project.

CHAPTER 2

BACKGROUND, STATE-OF-THE-ART, AND FUNDAMENTALS

2.1. Introduction

This Chapter delivers some background of the basic design rules for the applied waveguides in 2.2. It provides a brief overview of the State-of-the-Art in resonant slot antennas in 2.4, and in traveling-wave antennas in 2.6. Subsequently, niches for two different ideas of this work are considered shortly. First, there is the beam forming traveling-wave antenna in 2.6.3. Secondly, a double layer approach based on different propagation constants is evoked in 2.7. Based on these thoughts on the current state, the main objectives are drawn in 2.8.

2.2. Fundamental Relations in Waveguides

2.2.1. Rectangular Waveguide (RWG)

Traditional rectangular waveguides are applied herein solely for measurement purposes. A mechanical waveguide structure is designed in 7. All theoretical aspects of rectangular waveguides are acquirable from [1, 2]. The textbooks [3-5] serve as further references for network parameters and RF techniques. Note that, in the RWG, only the TE_{10} mode is considered herein. Waveguide walls are treated as ideal. ANNEX - Figure 10 provides the applied RWG flunch for this work.

2.2.2. Substrate Integrated Waveguide (SIW)

Substrate integrated waveguide (SIW) technique is used in lieu of RWG for the antennas of this work. Its architecture was proposed in the original publication [6] under the name of '*laminated waveguide*', a term still widely used in Japan. The SIW has been of major interest in the last and actual decade [7], and a patent has been filed [8].

Consider Figure 5 for the original descriptive picture and Figure 6 for the parameters, as there are the pitch p , the radius r , its width a_0 and the height h . The latter is defined in accordance with RWG.

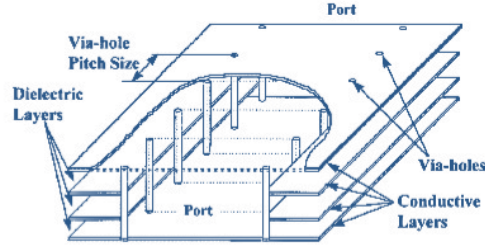


Figure 5 Original picture of the so-called ‘laminated waveguide’, a new generation of transmission line, Figure from [6]

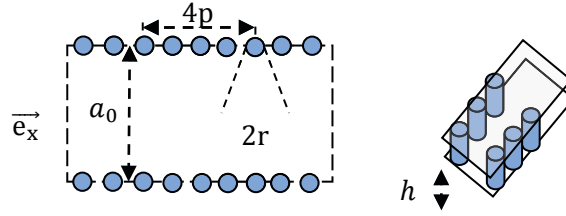


Figure 6 Basic parameters of an SIW

Comparing SIW to RWG, the equivalence in terms of width is critical for simulations and the use of existing design curves of slotted RWG in SIW. The equivalence is described in (4) from [9].

$$a_{0RWG} = a_0 - 1.8 \frac{(2r)^2}{p} + 0.1 \frac{(2r)^2}{a_0} \quad (4)$$

However, the best performance is obtained with equation (5). For further measurements on these relations and the definitions of z_1, z_2 , and z_3 of (5), see [10].

$$\frac{a_{0RWG}}{a_0} = z_1 + \frac{z_2}{\frac{p}{2r} + \frac{z_1 + z_2 - z_3}{z_3 - z_1}} \quad (5)$$

The impedance of the SIW is obtained in analogy to the RWG by (6). However, the total propagation constant slightly differs due to the unknown exact RWG equivalent width. Thus, one shall derive β from fabricated test circuits for precise computation.

$$Z_0 = \frac{k_0 \eta}{\beta} = \frac{\omega \sqrt{\mu_0 \epsilon_{eff}} \sqrt{\mu_0 / \epsilon_{eff}}}{\beta}, \quad (6)$$

Basic important design equations regarding the pitch and via radius and others are found in [11, 12] and a reliable transition from SIW to microstrip (MS) is proposed in [13]. Dispersion characteristics of the via wall have been discussed in [14].

2.3. Radiation of the Longitudinal Slot and its Complementary Dipole

For RWG, and so for SIW, the current on the upper surface F with the normal \vec{n} equals $\vec{J}_F = \vec{n} \times \vec{H}$. This equation is solved by the ideal traveling-wave of (7) where x is the direction of propagation, and y inline with the wider RWG side, where $y = 0$ is in the mid-axis of the waveguide.²

$$\vec{J}_F = H_0 \left(\vec{e}_y \frac{jk_y}{\pi/a_0} \sin \frac{\pi y}{a_0} - \vec{e}_x \cos \frac{\pi x}{a_0} \right) e^{-jk_x x} \quad (7)$$

A displacement current in y -direction excites a longitudinal slot inline with the direction of the traveling-wave, with respect to (7). The longitudinal slot has an almost omnidirectional radiation pattern similar to the dipole antenna, linked by Babinet's Principle [15]. Therein, the duality of a slot with a short metallic wire is given. The resulting slot voltage V_{slot} appears across the slot as long as $y \neq 0$ in (7) causes real currents traveling around the slot. This current distribution along the slot displays clearly the duality with the dipole. Babinet's principle also links the impedances of slot and dipole. Naturally, polarization of the slot is horizontal and the H-plane is inline with the longer side of the slot.

A slot edged to the broad side of the RWG does consequently not radiate when it is placed in the center line. Equally when it is placed very far from the center close the RWG side wall, very weak radiation is produced. On the other hand, all other locations and orientations lead to radiation.

2.4. Resonant Waveguide Slot Antenna Arrays (RESA)

Watson first explored the radiation properties of slots [16]. Stevenson, in the late forties, first stated the model of equivalent admittances for slots in resonance [17]. He consequently discovered that if the resonant slot is moved from the center line to an offset x , radiation increases. He was simplify-

² 'x' is used in the succeeding as the slot offset variable as well for legacy reasons

ing the analysis by assuming $\lambda/2$ as the resonant length and the electrical field within the slot as half-cosinusoid. Oliner in the fifties confirmed the results of Stevenson and contributed by giving explicit equations for the equivalent admittance G/Y_0 with respect to the characteristic admittance, of the RWG, for multiple different slot configurations [18]. Stegen not only improved the theory of Stevenson but also measured real slot behavior by capturing the reflection coefficients at 9.375 GHz [19].

These excellent basics led consequently to the first design procedure for resonant slot arrays by Elliot [20]. His main idea was the matching of the entire array by iteratively searching for slot admittances, which add up to the real admittance G_0 , while fulfilling the aperture distribution requirements. Mutual coupling was introduced shortly after in [21]. This milestone with its three design equations are today the most widely used in resonant arrays. Josefsson [22], Stern [23] and Park [24], in the mid-eighties, completed the design rules while also adding analysis for the effective resonant slot length different from $\lambda/2$.

To visualize the nature of the slot, for the simpler case of an assumed exact half guided wavelength slot, the Stevenson formulas can be cut down to (8). Therein, the equivalent (real part) admittance is a function of the RWG width a_0 , the wavelengths, the offset x and waveguide shorter length b . No reactance is present, as indicated in Figure 7. The simple Stevenson approach is e.g. used in [25] with acceptable results for a small array.

$$\frac{g_0}{G_{\text{RWG}}} = \left(\frac{2.09\lambda_g}{\lambda_0} \cdot \frac{a_0}{b} \cos\left(\frac{\lambda_0\pi}{2\lambda_g}\right)^2 \right) \sin^2\left(\frac{\pi x}{a_0}\right) \quad (8)$$

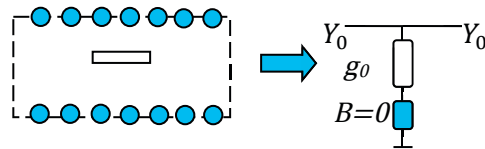


Figure 7 Perpendicular slot and its equivalent circuit in resonance

2.5. Beam Forming Antenna Arrays Based on Matrices (BFA)

As stated in the introduction, beam shaped antenna system are evidently required e.g. in future RFID industry microwave-band applications [26-34] or for automotive radar [35]. One way to

shape the radiation are lenses [36-38], and frequency scanning, see 5.2. The first requires however expensive additional material and is out of scope of this thesis.

It is straightforward to generate four beams by means of a beam forming BF matrix [39]. Invented by Butler in the 1960s, this circuit is a generic concept for feeding phase shifted arrays. A higher amount of beams is very challenging. Two examples of eight beam approaches are depicted in Figure 8 with huge complexity and space need.

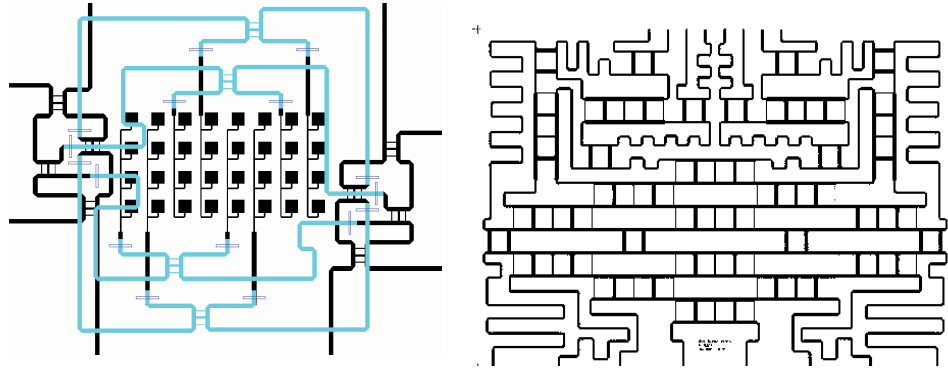


Figure 8 Eight beam MS solutions, two layers (left) from [40] one layer from [41]

Considering the very common Butler Matrix ³, the State of the Art of this technique in nearly millimeter-wave bands is well represented by recent implementations using SIW [42, 43]. Essential elements of the matrix are hybrid couplers based on [44]. Phase shifters are implemented by elongated or narrowed sections of SIW.

All these concepts share severe disadvantages. In addition to the high space requirements, a lack of a zero beam is inherent to any matrix based on the butler approach. The higher the number of input and outputs, the more important are the losses introduced just by the matrix. Even though SIW is a low loss transmission line, the losses would become significant for many couplers and dividers. Another major drawback of the Butler matrix is the lack of flexibility in achieving arbitrary angles between beams. In addition, BF networks like the Butler matrix provide much less flexibility in designing the appropriate aperture distribution. The outputs of the Butler matrix provide per defini-

³ Here, only Butler is considered, since implementations of other matrices, like Nolen or Blass Matrix [42-44] show in principal the same issues as the principal matrix.

tion equally weighted amplitudes. Several techniques are known to increase the performance of the antenna array by increasing the number of outputs artificially, e.g. [45].

It is therefore envisaged to avoid matrices by using the TWA for beam shaping. In the author's opinion, it is very likely to copy a once designed structure on the same PCB due to the low space requirements of a single TWA made from SIW. Nevertheless, high control of the phase of the slotted elements is mandatory.

2.6. Traveling Wave Slot Antenna Arrays (TWA)

2.6.1. Elementary Slot Radiation Coefficient Computation

The basic design of a TWA is shortly described in the following. Figure 9 defines the radiation coefficients at each slot n to $n = N$. c_{\max} is applied by the last element.

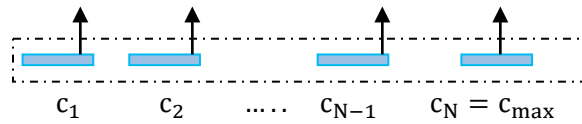


Figure 9 Radiation coefficient nomenclature at each slot

Assuming an ideal traveling-wave, each element will partly emit a fraction of the power left over from the segment $(n - 1)$ to free space. Its capability to convert the guided wave to a free wave is described by the radiation coefficient c_0^n . Along the array, the available power decreases. Thus, a *uniform* aperture distribution requires c to increase up to the element $n = N$ that exhibits the highest possible value. In order to derive all c for a desired aperture distribution, an equation system is commonly set up. This is straightforward if losses and mutual coupling are neglected, (thus the isolated c_0 is taken, not the effective c). If the radiated power for each slot P_n is given e.g. by a uniform distribution, see (9), or for a different than uniform distribution, see (10),

$$P_n = \frac{P_{in}}{N}, \quad (9)$$

$$P_n = w_n \frac{P_{in}}{N}, \quad (10)$$

where w_n are the weighting coefficients for the amplitude distribution, e.g. according to Taylor [46], then equations (11) to (13) necessitate to be solved for a particular array.

$$P_{in}C^1 = P_1 \quad (11)$$

For $k = 2 \dots N$

$$P_{in}C^k \prod_{n=2}^k (1 - C^{n-1}) = P_k \quad (12)$$

$$C_N < C_{max} \quad (13)$$

If $rP = 0$, it *must* be that at $n = N$, $c = 1$. A perfectly radiating element is not feasible, thus, the radiating coefficient will be limited to c_{max} , leading to $c_N = c_{max}$. In the ANNEX, this drawback is partly solved by a potential patch absorber. An example of a successful design of a non-uniform distribution is given in Figure 10.

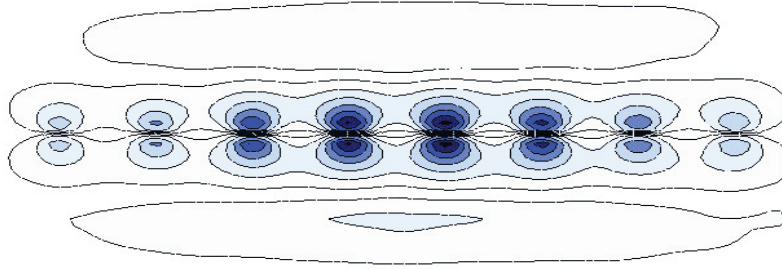


Figure 10 Near field result after successful slot amplitude distribution design (Taylor) at $z = 0.3$ mm

Conventionally, i.e. on the basis of the results discussed in 2.4, the literature derives c for the TWA by using the same deductions to obtain the equivalent admittance, followed by the simple product of slot voltage and real admittance [47].

$$P_n = |V_{slot}|^2 g_0/2 \quad (14)$$

However, when designing the TWA according to (9) to (14) neglecting the mutual coupling and inherent reflections, a divergence between the theoretical and practical slot radiation occurs. This issue is also occurring in [47] and presented by two different examples in Figure 10 and Figure 11. While in the first of both Figures the effective power is related to the desired Taylor distributed values, the subsequent Figure depicts the phase error normalized *to slot one*. It is important to observe that the highest divergence is seen where the highest radiation occurs. Thus, the assumed

mutual coupling is expected high at these slots, too. See also slot 3 in both Figures. This impact is severe and has to be compensated. The higher the desired radiation (e.g. in the range of $c = 0..0.3$), the higher is the negative impact of the MC. Therefore, the State-of-the-Art [47] indicates mainly to limit the applied radiation to 0.1 or max. 0.2 which is a restriction in the design for the TWA.

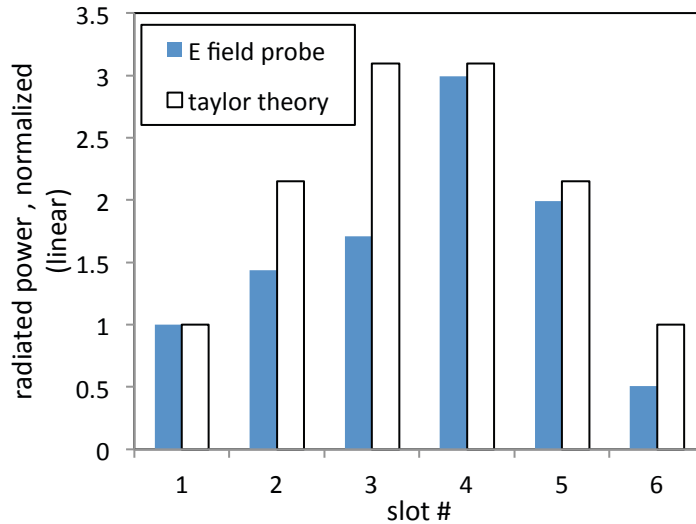


Figure 11 Comparison between simulated probed P_n and perfect Taylor distribution (when MC is not taken into account)

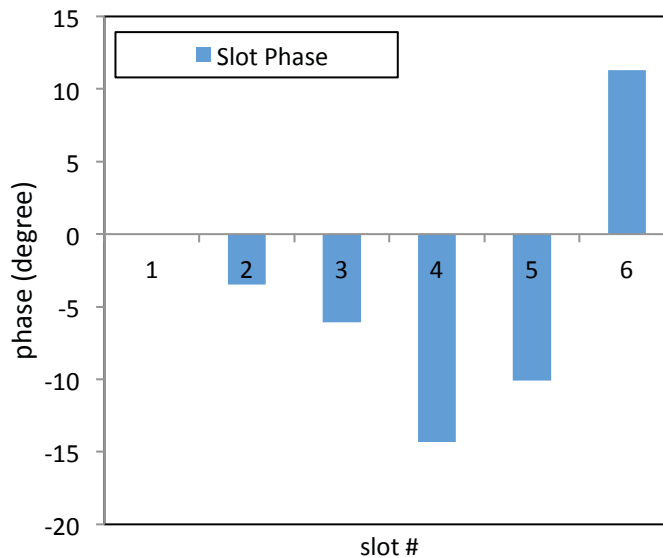


Figure 12 Deviation from 0°-phase (before any means of equalization)

Next, even if the effective phase relations are known e.g. from simulation, a matter of compensation would try to equalize them without having an impact on the total performance, [47] and 2.6.2. It is

shown later that in fact the impact is higher than expected for many slot configurations, thus, a new method of phase equalization that avoids modifying the distance, shall be conceived.

Lastly and interestingly, [47] states to not space TWA elements half a guided wavelength to not add up any reflection in phase. This is useful in case the reflection is neglected, but this is actually also true for a mismatched element from MC which is shown later in this thesis.

2.6.2. Particular Challenge for Complex S-parameter Usage

Further particular issues regarding the design based on complex S-parameters in the State-of-the-Art of a slot, instead of the methods seen in the previous sections, are described later in 4.3.

2.6.3. Beam Forming Capabilities of the TWA

Once the TWA is designed and the synthesis has yielded a broadside beam with sufficiently low side lobes, the elements might be moved to another position for an *intentional* phase gap at that new position. This yields, however, rather bad results since internal coupling might increase, the mutual coupling is no longer compensated, and other effects. One rather negative result is depicted in Figure 13 from [48].

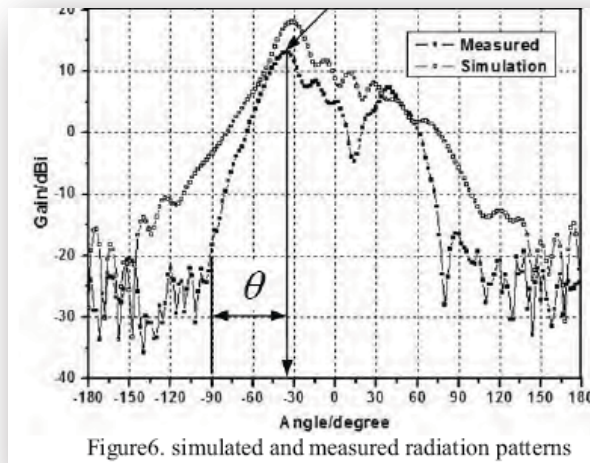


Figure 13 Example of a bad performance of TWA beam forming [48]

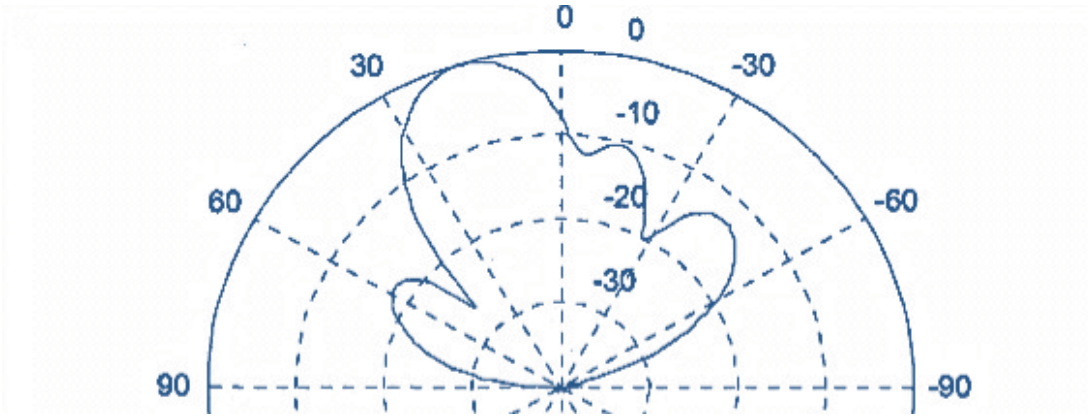


Figure 14 Adaption of the element distance for BF with poor results [49]

Another example of a failed adaption i.e. the reuse of an existing array is depicted in Figure 14 from [49]. It has not been revealed in detail whether the modified element spacing causes internal or external coupling effects not covered by the design procedure.

Frequency scanning shall be mentioned shortly as a reliable method; however, it should be seen as an asset of each TWA [50]. A smart enhancement is the addition of phase delays by meandering the waveguide [51]. That has the huge advantage of avoiding any modification to the MC distances.

The approach of altering the propagation constant or add additional phase shift by a different dielectricity is appealing since it does not necessitate to compute the entire array again. Such an approach has been patented in [52].

2.7. Double Layer Slotted Waveguide Beam Forming Arrays (TWAFAs)

To increase the total gain by improving the HPBW in the E-plane plane as well, a two-dimensional slot array shall be considered in the thesis as well. It shall provide a basic scanning feature for the envisage field of applications [35]. An easy redesign of the beam angles, low cost, and high integration with other components are key features. Some particular appliances require in addition monopulse antennas for fast sum and difference computation, which shall be possible as well.

One exemplary solution of bidirectional feeding is a patch antenna array in combination with rat race coupler in Figure 15 [53]. Another monopulse antenna is made by exiting different layers of slot antennas as shown for microstrip in [54].

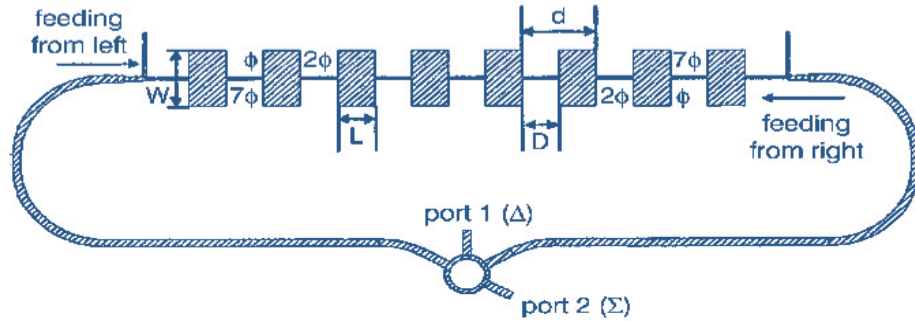


Figure 15 The monopulse antenna of [53]

However, this solution lacks additional beams. To generate supplementary beams without the use of a beamforming matrix, Kolak [55, 56] has proposed to feed patch antenna arrays by three different rectangular waveguides underneath, providing three tilted beams, see Figure 16. Instead of inserting different dielectricities in between elements, Kolak raised the idea of taking different RWGs exhibiting each a particular propagation constant for each beam. The general concept was presented but the BF aspect was actually never shown as working.

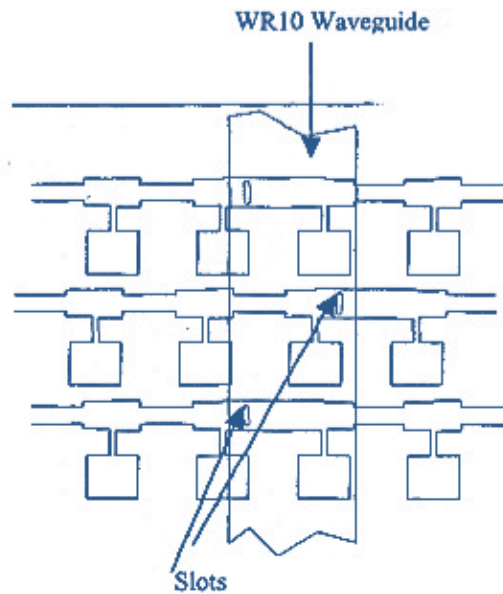


Figure 16 Kolak [55] proposal

Coupling methods involving two layers have been shown previously. [57] e.g. describes a first method of how microstrips may be coupled to SIW. Solutions in [58, 59] show a coupling junction according to [60]. These purely resonant feeding in [58, 59] excludes naturally any BF.

Thus, due to the lack of an actually working two layer beam forming antenna without any matrix and still monopulse capability, this niche shall be worked out by new design in this work. It is however important to reconsider the sole publication of this kind from the 1960s.

Simmon [61] considered two different waveguides for the same purpose of different excitation of a slotted waveguide, see Figure 17. Simmon was convinced about the versatility of ist approach, however, he did not work on the serious drawbacks coming from the reflections of each element. This in fact caused several unintended beams and degraded the absolute result substantially. Simmon was apparently not able to solve this issue with any subsequent work.

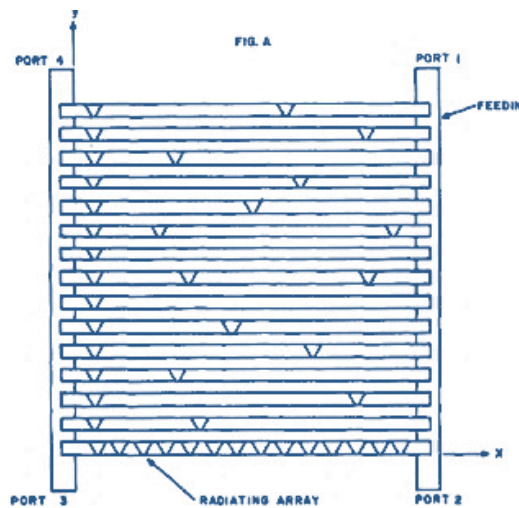


Figure 17 A. Simmons Idea in 1963 [61]

2.8. Conclusion and Derived Objectives

In this Chapter, the background for this work and its designs has been outlined. The objectives for this work are based on the latter reviewed issues and challenges, i.e.:

- Reduce the complexity in the design of slotted thin SIW arrays while keeping low side lobes
- Characterize SIW slots solely by S-parameters including MC coupling when vias are included
- Find a way to design beam shaped TWAs without modifying the distance between elements
- Design a fixture and transition that meets the challenge of LTCC material characterization
- Try to absorb any residual power at the end of an antenna array by a patch (ANNEX)

2.9. References

- [1] H. Henke, "Elektromagnetische Felder. Theorie und Anwendung", 2., neu bearb. und erg. Aufl. Berlin: Springer (Springer-Lehrbuch), 2004
- [2] D. Pozar, "Microwave engineering", 3. ed. Hoboken, NJ: Wiley, 2005
- [3] G. Gonzalez, "Microwave transistor amplifiers. Analysis and design". 2. ed. Upper Saddle River, NJ, London: Prentice Hall; Prentice Hall International, 1997
- [4] M. H. W. Hoffmann, „Hochfrequenztechnik. Ein systemtheoretischer Zugang“, Berlin: Springer (Springer-Lehrbuch), 1997
- [5] M. Hiebel, "Grundlagen der vektoriiellen Netzwerkanalyse", 2. Aufl. München: Rohde & Schwarz, 2007
- [6] H. Uchimura, T. Takenoshita, and M. Fujii, "Development of a laminated waveguide", Microwave Theory and Techniques, IEEE Trans., vol. 46, no. 12, pp. 2438–2443, 1998
- [7] M. Bozzi, A. Georgiadis, K. Wu, "Review of substrate-integrated waveguide circuits and antennas," Microwaves, Antennas & Propagation, IET , vol.5, no.8, pp.909-920, June 6 2011
- [8] F. Shigeki, "Waveguide line," (in Japanese) Japan Patent 06-053 711, Feb. 25, 1994
- [9] F. Xu and K. Wu, Guided-wave and leakage characteristics of substrate integrated waveguide, Microwave Theory and Techniques, IEEE Trans., Vol. 53, No. 1, pp. 66–73, 2005
- [10] C. H. Tseng, T.H. Chu, "Measurement of frequency-dependent equivalent width of substrate integrated waveguide", Microwave Theory and Techniques, IEEE Transactions on , "Microwave Theory and Techniques, IEEE Transactions on 54 (4), p. 1431–1437, 2006
- [11] D. Deslandes, K. Wu, "Integrated microstrip and rectangular waveguide in planar form", Microwave and Wireless Components Letters, IEEE, vol. 11, no. 2, pp. 68–70, 2001
- [12] D. Deslandes, K. Wu, "Accurate modeling, wave mechanisms, and design considerations of a substrate integrated waveguide", Microwave Theory and Techniques, IEEE Transactions on 54 (6), p. 2516–2526, 2006

- [13] D. Deslandes, "Design equations for tapered microstrip-to-Substrate Integrated Waveguide transitions", Microwave Symposium Digest (MTT), IEEE MTT-S International, p. 704–707, 2010
- [14] Y. Cassivi, L. Perregrini, et.al. , "Dispersion characteristics of substrate integrated rectangular waveguide", Microwave and Wireless Components Letters, IEEE. In: Microwave and Wireless Components Letters, IEEE , p. 333–335, 2002
- [15] H. G. Booker, "Slot aeriels and their relation to complementary wires aeriels (Babinet's Principle)", J. Inst. Elec. Eng (3-A), p. 620,1946
- [16] W. H. Watson, "Resonant Slots," IEE J., 93, pt.3A, pp. 620-626, 1946.
- [17] A. F. Stevenson, "Theory of Slots in Rectangular Wave-Guides", Journal of Applied Physics 19 (1), p. 24–38, 1948
- [18] A.A. Oliner, "The impedance properties of narrow radiating slots in the broad face of rectangular waveguide: Part I--Theory," Antennas and Propagation, IRE Transactions on , vol.5, no.1, pp.4,11, January 1957
- [19] R. J. Stegen, "Slot radiators and arrays at X-band," IEEE Transactions on Antennas and Propagation, vol. 1, pp. 62–64, 1952
- [20] R.S. Elliott, "An improved design procedure for small arrays of shunt slots", Antennas and Propagation, IEEE Transactions on, 31(1), 48-53, 1983
- [21] R.S. Elliott, W.R. Oloughlin, "The design of slot arrays including internal mutual coupling", IEEE transactions on antennas and propagation 34, p. 1149-1154, 1986
- [22] L.G. Josefsson, "Analysis of longitudinal slots in rectangular waveguides", Antennas and Propagation, IEEE Transactions on 35.12, 1351-1357, 1987
- [23] G. Stern, R. Elliot, "Resonant length of longitudinal slots and validity of circuit representation: Theory and experiment", IEEE Transactions on Antennas and Propagation, pp. 1264–1271, 1985

- [24] P. Park, G. J. Stern, R. S. Elliott, "An improved technique for the evaluation of transverse slot discontinuities in rectangular waveguide", *Antennas and Propagation, IEEE Transactions on* 31.1 , 148-154, 1983
- [25] Yong, Zi-bin Weng Rong Guo. "Design and experiment on substrate integrated waveguide resonant slot array antenna at ku-band", *Antennas, Propagation & EM Theory, 2006. ISAPE'06. 7th International Symposium on*, 2006.
- [26] P. V. Nikitin and K. V. S. Rao, "Antennas and propagation in UHF RFID systems", Las Vegas, NV, April 2008, https://www.ee.washington.edu/people/faculty/nikitin_pavel/papers/RFID_2008.pdf
- [27] Z. Tongliang; W. Feng; T. Hui, et. al., "The Performance Analysis Using Multiple Beams for RFID Warehouse Management System," *Advanced Information Networking and Applications Workshops (WAINA), IEEE 24th International Conference on* , vol., no., pp. 567,570, 20-23 April 2010
- [28] D. Zhou, et al., "Design of beam steering antenna array for RFID reader using fully controlled RF switches." *Proc. Progress In Electromagnetics Research Symp.* 2008.
- [29] A. K. M. Baki, N. C. Karmakar, U. W. Bandara, et. al. , "Beam Forming Algorithm with Different Power Distribution for RFID Reader", *Chipless and Conventional Radio Frequency Identification: Systems for Ubiquitous Tagging*. IGI Global, p.64-95. Web. 6 Jul. 2014
- [30] L. Wang, B. A. Norman, J. Rajgopal, "Placement of multiple RFID reader antennas to maximise portal read accuracy", *International Journal of Radio Frequency Identification Technology and Applications*, Vol. 1, No. 3. , 2007
- [31] P. Salonen, L. Sydanheimo, "A 2.45 GHz digital beam-forming antenna for RFID reader," *Vehicular Technology Conference, VTC Spring 2002. IEEE 55th* , vol.4, no., pp.1766,1770 vol.4, 2002
- [32] P. Salonen, M. Keskilammi, L. Sydanheimo, et.al., "An intelligent 2.45 GHz beam-scanning array for modern RFID reader," *Phased Array Systems and Technology*,. *Proceedings. 2000 IEEE International Conference on* , pp.407,410, 2000

- [33] W.-J. Liao, S.-H. Chang, Y.-C. Chu, et.al., "A Beam Scanning Phased Array for UHF RFID Readers with Circularly Polarized Patches", *Journal of Electromagnetic Waves and Applications*, Vol. 24, Iss. 17-18, 2010
- [34] K. O. C Saito, S. O. C. Okamura, T. O. C. Kawai, "RFID tag communication apparatus comprising a scanning beam antenna", US Patent, 2012
- [35] M. Schneider, "Automotive radar - status and trends," *Proceedings of the German Microwave Conference GeMiC 2005*, paper 5-3, 2005
- [36] B. Fuchs, O. Lafond, S. Rondineau, et.al., "Design and characterization of half Maxwell fish-eye lens antennas in millimeter waves", *Microwave Theory and Techniques, IEEE Transactions on* 54 (6), p. 2292–2300, 2006"
- [37] P. Wenig, R. Weigel, M. Schneider, "A dielectric lens antenna for digital beamforming and superresolution DOA estimation in 77 GHz automotive radar", *Smart Antennas, WSA 2008. International ITG Workshop on*, p. 184–189, 2008
- [38] L. Xue, V.F. Fusco, "24 GHz automotive radar planar Luneburg lens", *Microwaves, Antennas & Propagation, IET* 1 (3), S. 624–628, 2007
- [39] J. Butler, R. Lowe, Beam forming matrix simplifies design of electronically scanned antennas, *Electronic Design* 9, p 170–173, 1961
- [40] C. Dall'omo, "Contribution à l'étude d'antennes à pointage électronique en millimétrique: Conception et réalisation de différentes topologies de Matrices de Butler". Diss. University of Limoges, 2003.
- [41] H. Nord, "Implementation of 8x8-Butler Matrix in Microstrip", Royal Institute of Technology Stockholm, Diploma Thesis, 1997
- [42] P. Chen, W. Hong, et.al., "A Multibeam Antenna Based on Substrate Integrated Waveguide Technology for MIMO Wireless Communications", In: *Antennas and Propagation, IEEE Transactions on* 57 (6), S. 1813–1821, 2009

- [43] S. Yamamoto, J. Hirokawa, M. Ando, "A beam switching slot array with a 4-way Butler matrix installed in a single layer post-wall waveguide", Antennas and Propagation Society International Symposium, 2002. IEEE, Bd. 1, S. 138-141 vol.1, 2002
- [44] Ji-Xin Chen, W. Hong, Zhang-Cheng Hao, et.al. "Development of a low cost microwave mixer using a broad-band substrate integrated waveguide (SIW) coupler", Microwave and Wireless Components Letters, IEEE 16 (2), S. 84-86, 2006
- [45] J. Shelton, "Reduced sidelobes for Butler-matrix-fed linear arrays", Antennas and Propagation, IEEE Transactions on 17 (5), S. 645-647, 1969
- [46] T.T. Taylor, Design of Line-Source Antennas for Narrow Beamwidth and Low Sidelobes, IRE Transactions on Antennas and Propagation, Vol. AP-3, No. 1, pp. 16-28, 1955
- [47] H.J. Visser, Array and Phased Array Antenna Basics, John Wiley & Sons, 2006
- [48] B. Zheng, Z. Zhao, and D. Wu, "Millimeter wave beam tilting array for radar system", Intern. Conf. on Microwave and Millimeter Wave Technology (ICMMT), pp. 991-993, 2010
- [49] M. Tariq Rashid, "Design and modeling of a linear array of longitudinal slots on substrate integrated waveguide", Master Thesis, Concordia University, QC, Canada, 2006
- [50] Y. J. Cheng, "Millimeter-Wave Half Mode Substrate Integrated Waveguide Frequency Scanning Antenna with Quadri-Polarization. Antennas and Propagation, IEEE Transactions on. In: Antennas and Propagation, IEEE Transactions, p. 1-1, 2010
- [51] L. Chiu, W. Hong, Z. Kuai, "Substrate integrated waveguide slot array antenna with enhanced scanning range for automotive application", Microwave Conference, APMC, Asia Pacific, p. 1-4, 2009
- [52] F. Barnes, B. Colo, "Phased Array Antenna System Including a Coplanar Waveguide Feed Arrangement", US Patent 5,694,134, 1997
- [53] S.-G. Kim, K. Chang, "Low-cost monopulse antenna using bi-directionally-fed microstrip patch array," Electronics Letters, vol.39, no.20, pp. 1428- 1429, 2 Oct. 2003

- [54] L. Yan, W. Hong, K. Wu, "Simulation and experiment on substrate integrated monopulse antenna", Antennas and Propagation Society International Symposium, IEEE, p. 528-531 Vol. 1A, 2005
- [55] F. Kolak, C. Eswarappa, "A low profile 77 GHz three beam antenna for automotive radar," Microwave Symposium Digest, 2001 IEEE MTT-S International , vol.2, no., pp.1107-1110 vol.2, 2001
- [56] F. Kolak, Slot fed switch beam patch antenna", Tyco Electronics Corporation, US Patent 6313807 B1, 2001
- [57] D. Busuioc, S. Safavi-Naeini, M. Shahabadi, "High frequency integrated feed for front end circuitry and antenna arrays", International Journal of RF and Microwave Computer-Aided Engineering 19 (3), p. 380–388, 2009
- [58] A. Bakhtafrouz, A. Borji, D. Busuioc, et.al. , "Compact two-layer slot array antenna with SIW for 60GHz wireless applications", Antennas and Propagation Society International Symposium, AP-SURSI IEEE, p. 1–4, 2009
- [59] A. Bakhtafrouz, A. Borji, D. Busuioc, et.al. , "NOVEL TWO-LAYER MILLIMETER-WAVE SLOT ARRAY ANTENNAS BASED ON SUBSTRATE INTEGRATED WAVEGUIDES", Progress in Electromagnetic Research (PIER) (109), p. 475–497, 2010
- [60] S. R. Rengarajan, G.M. Shaw, "Accurate characterization of coupling junctions in waveguide-fed planar slot arrays", Microwave Theory and Techniques, IEEE Transactions on. In: Microwave Theory and Techniques, IEEE Transactions on, p. 2239–2248, 1994
- [61] A. Simmons, O. Giddings, M. Diamond, et.al., "A multiple-beam two-dimensional waveguide slot array", IRE International Convention Record. In: IRE International Convention Record DOI - 11, p. 56–69, 1963

CHAPTER 3

ENHANCED SLOTTED ELEMENTS IN SUBSTRATE INTEGRATED WAVEGUIDE

3.1. Introduction

This Chapter focuses on the study of *isolated* slotted SIW elements and their linearized characterization, before incorporating them into antenna arrays in the subsequent Chapter 4. The study is mainly based on the assumption of a *linear* element considered as a two-port system. To derive an alternative design concept with respect to the shortly outlined conventional design approaches in Chapter 2, the elements are enhanced by a couple of vias. The latter serve to alter the slotted element characteristics in a new way, applied subsequently in the proposed array design in Chapter 3.

3.2. Elementary Definitions of the Slot in the SIW

Throughout the text, the succeeding important expressions and definitions are used frequently.

3.2.1. Traveling-Wave Propagating Direction and Phase

The traveling-wave exciting the slotted elements is defined as a transverse electric (*TE*) wave, exhibiting the Poynting vector $\vec{S} = \vec{E} \times \vec{H}$ traveling from the input of a segment of any length to the terminated output. The latter ‘segment’ can be an array of similar elements or a single isolated element. For sake of convenience, the operational traveling-wave direction is described by *from left* to *right* and the Poynting vector indicates the dominant mode TE_{10} in the SIW. The traveling-wave may be altered by reflections and external contributions from mutual coupling that are treated in this work. However, it is still denoted as a *traveling-wave*.

In Figure 18, phase definitions are depicted by blue arrows. The resulting phase of the electric TE_{10} component in \vec{e}_z at the input of segment n carries the phase ϕE_z^n . If no reflection is scattered from a subsequent segment $n + 1$, the resulting phase equals the excitation phase. At the array’s input and

initial excitation point, ϕE_z^1 is per definition = 0° , thus, at all subsequent segments ϕS_{21}^n is accumulated to $\sum_1^n \phi S_{21}^n$ in the ideal traveling-wave case. The slot phase is ϕE_y , when excited from the left or right, and this with the index *left* and *right* for either side of excitation.

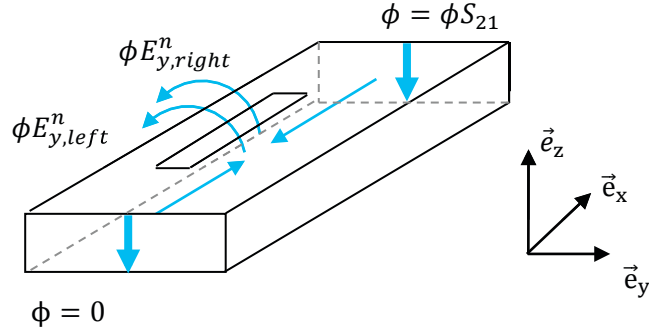


Figure 18 Definition and occurrence of the different phases

3.2.2. Radiated Power

The actual radiation coefficient c_0^n of an element n is derived by (15). The index '0' is auxiliary to distinguish between an *isolated* or mutually *coupled* element in an antenna array. If stated in the simple form of c_n , the coefficient of the mutually *coupled* element n is meant.

$$c_0^n = 1 - |S_{11}|^2 - |S_{21}|^2 \quad (15)$$

The radiated power P_{rad} or P_n at each element

$$P_{rad} = P_n = P_{in}^n c_0^n \quad (16)$$

is the product of input power and radiation coefficient. It is enhanced by ϕE_y which equals $\phi E_{y,left}$ if the element is fed solely from the left side. For convenience, the nomenclature of Figure 19 is applied for the input and output power as long as mutual coupling is not considered.

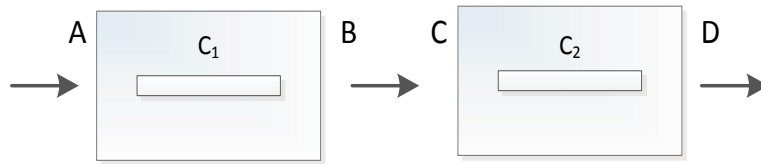


Figure 19 Input and output variables in the simple structure, (arrays are discussed in Chapter 4)

3.2.3. Additional Definitions

The input power is arbitrarily set to $P_{in} = A = 1$ and the remaining output power is called rP , i.e. D in Figure 19, at the end of a segment or array. In Figure 20, the electrical field in y-direction is depicted. Magnitude and phase are considered separately. A possible minor shift of the magnitude distribution is not taken into account, however, a phase divergence between a left or right fed element is fully considered. When validated with simulation software inside a long array, the radiated power P_n of a slotted segment is determined by *averaging* the electrical field above the slot, keeping the ratio between slots. This is in particular necessary for full wave simulations that typically generate spikes in the magnitude distribution that are most likely caused by meshing.

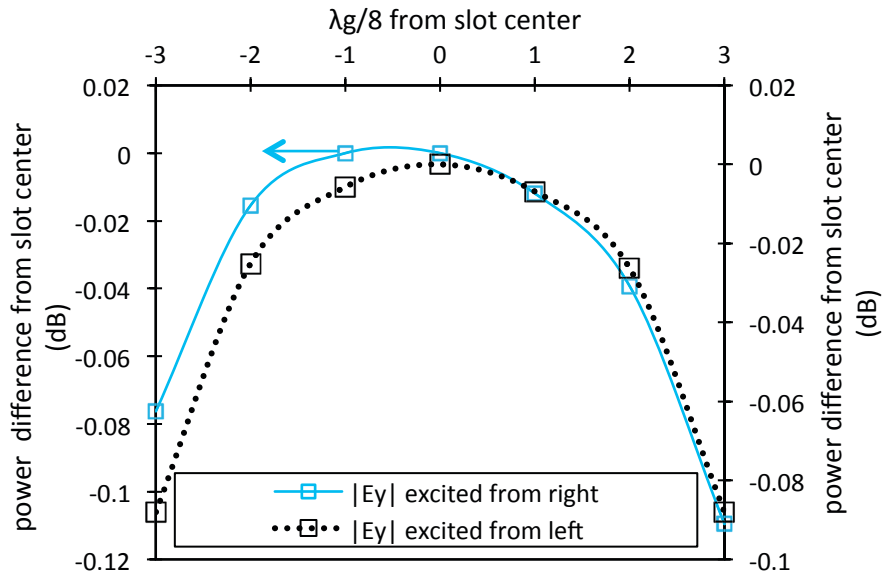


Figure 20 Y-component of the electrical field within the slot when excited from the left / right

3.3. Linearized Characterization of Isolated Off-Resonant Slots

A single slotted element may be considered as a two-port system of an input and output port with complex S-parameter results. The general behavior of a slot that is edged in a waveguide leading to linear polarization has been analyzed in the literature, see 2.3. It is common to embed the slot in an ideal segment of half λ_g or multiples for characterization purpose. Often, de-embedding is required to accurately obtain the transmission phase ϕS_{21} . This is displayed by the dashed line in Figure 21. The parameters l for the slot length and x for the slot offset are shown in the same way. The slot is of the width w . The SIW parameters are also defined in Figure 21, i.e. the width and the pitch.

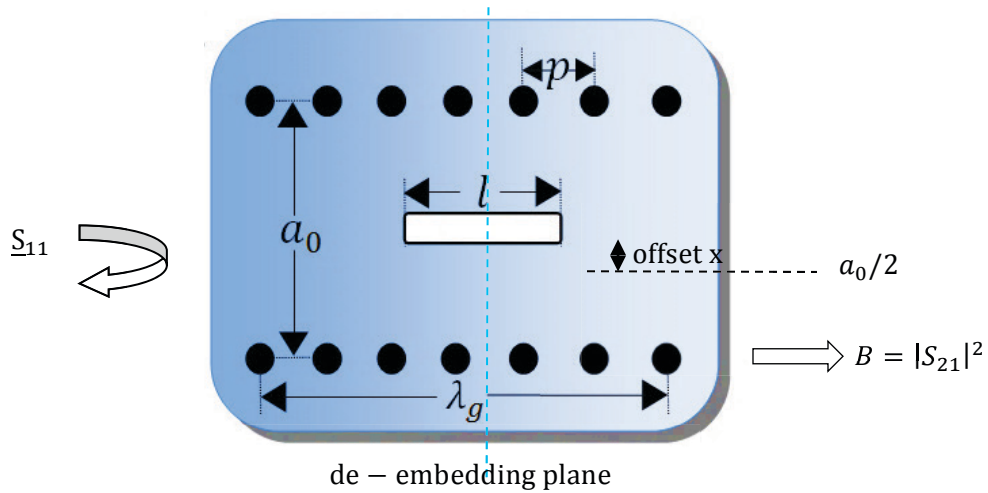


Figure 21 Common procedure of characterization for one radiating isolated slot in a SIW segment of the length λ_g , (if not stated otherwise)

3.3.1. Radiation, Transmission and Reflection

An element with the height h , the offset x and the slot length l has the following typical slot response, depicted in Figure 22. While radiation is constantly growing over slot length, reflection is increasing. The resonant length, *if* defined as the maximum radiation, is above half a guided wavelength. The typical radiation pattern of the slot is well-known from Chapter 2. In this work the focus is set on a reliable new design procedure while the gain discussion is of less importance since extensively discussed in the literature for longitudinal slots.

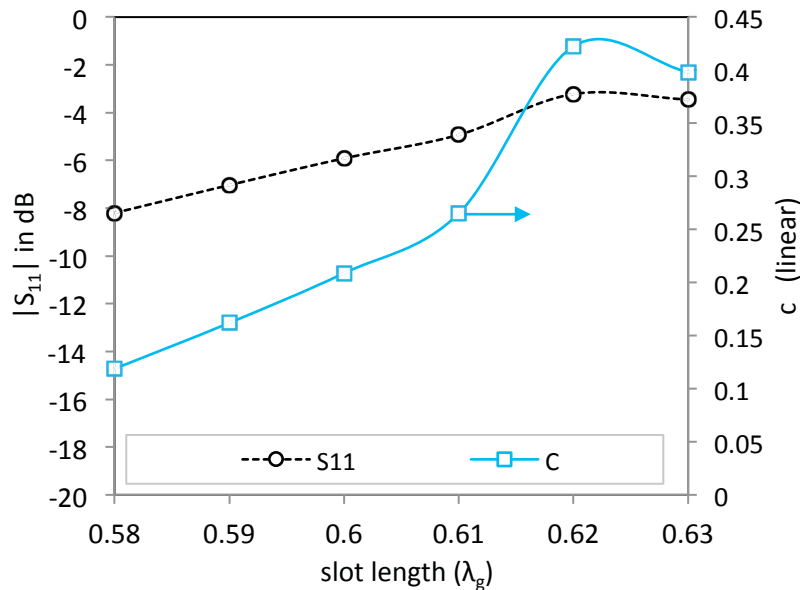


Figure 22 Basic linearized slot characterization

3.3.2. Offset and Slot Width

Next, slot characterization is presented with a parameter study over the range of the width w_x . The cut-off frequency and SIW general design rules have been respected by choosing $a_0 = 0.95 \text{ mm}$, $r = 0.5 \cdot 0.127 \text{ mm}$ and $p = 0.1905 \text{ mm}$ at 76.5 GHz for this example. Figure 23 shows the parameter sweep of the triplet (w_x, l, x) . While for each subfigure the range of (l, x) is the same, w_x varies from 0.14 mm to 0.19 mm . It is important to find a pair of the slot width and offset that generates sufficient radiating and suitable dependency of c . As a result, a value of $w_x = 1/10 l$ to $1/15 l$ is selected for this work. Similar results have been reported in [1]. Figure 23 reveals that for an increasing offset a longer slot is necessary to achieve similar radiation. This effect is described as the increasing resonant length of a slot, recall also 2.4. The slot is still off-resonant which will be shown further below.

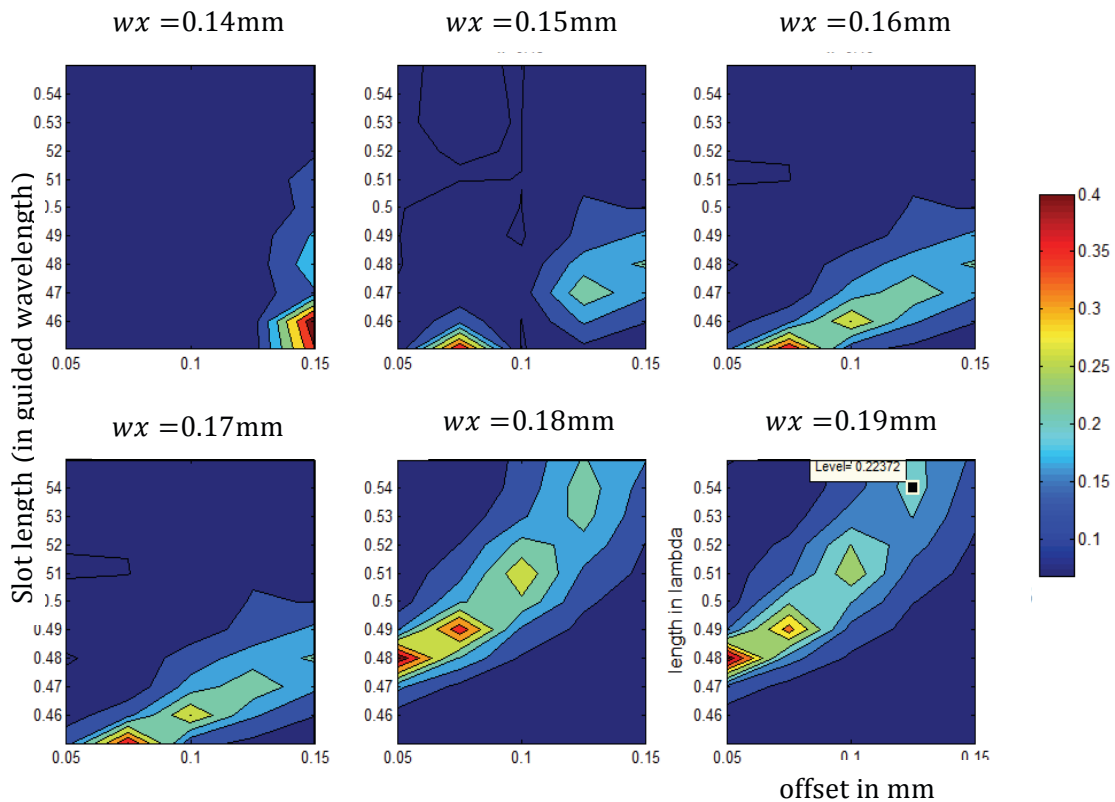


Figure 23 Parameter study on slot width influence. The six Figures depict the radiation coefficient for $w_x = 0.14 \text{ mm}$ to $= 0.19 \text{ mm}$, $CF=76.5 \text{ GHz}$

Resulting parametric studies for both $|S_{21}|$ and c_0 are provided in Figure 24 and Figure 25. Again it is observable that for higher offsets an increased slot length is required to achieve the same $|S_{21}|$. Figure 25 reveals that the highest radiation is obtained at a certain (l, x_0) due to a fixed width.

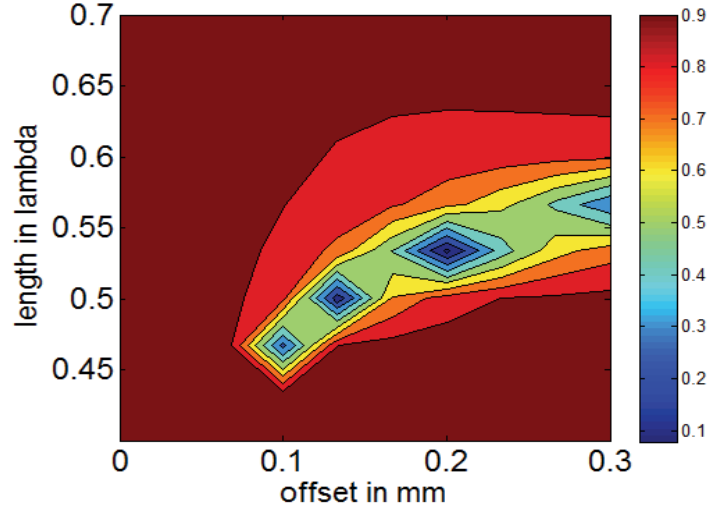


Figure 24 $|S_{21}|$ as a function of offset x and length l , peaks are due to the parameter sweep resolution and MATLAB function

3.3.3. Impact of the Substrate Height

The influence of the substrate thickness is determined by simulating the typical characterization sweep for two different substrates. Figure 26 represents the fundamental basic slot design data. With $x = constant$ and $wx = constant$, S_{11} , and S_{21} are shown in magnitude and phase as a function of l . The latter quantity is normalized to half of a guided wavelength. Additionally in Figure 26, c_0 is depicted. It is apparent that maximum radiation occurs at very different l for both substrates, i.e. the ‘resonant’ length l for this frequency and (small) x depends on h , though the wavenumber in theory does *not*. This is an important finding and underlines the unique character of an SIW slot.

Figure 26 reveals also again that the reflection increases significantly while radiation rises. A much smoother curve is seen for a two times thinner substrate. c_0 does not reach similar values as with the thicker substrate. Since altering l is the favored method to modify the radiated power, it is therefore preferable to use a thicker substrate since dc/dl is higher.

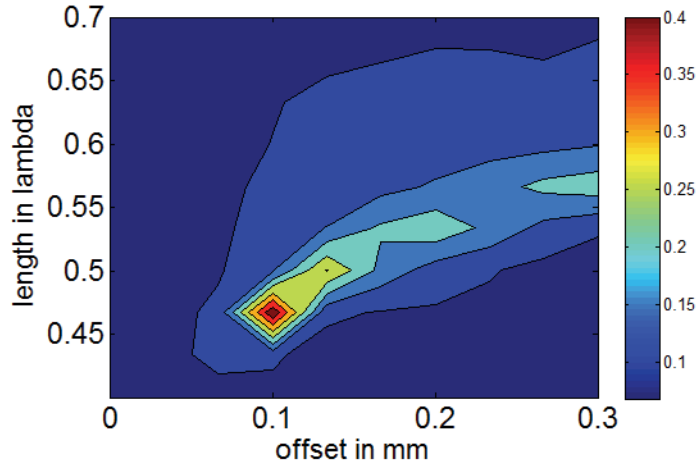


Figure 25 $|c_0|$ as a function of l and offset, there is only one maximum due to the fixed slot width and higher reflections for increased offset, (the dark region around the rising curve is a graphical error)

3.3.4. Phase of Reflection and Radiation

Figure 27 covers the phase relations. A slot reflection of 180° may be considered as resonance, since the wave travels along λ_g and is partially reflected by a real admittance. Contrarily to RWG slots, this ‘resonant’ length does *not* coincide with a real S_{21} . The equivalent model used for resonant arrays in conventional design procedures, as discussed in 2.4, is not applicable.

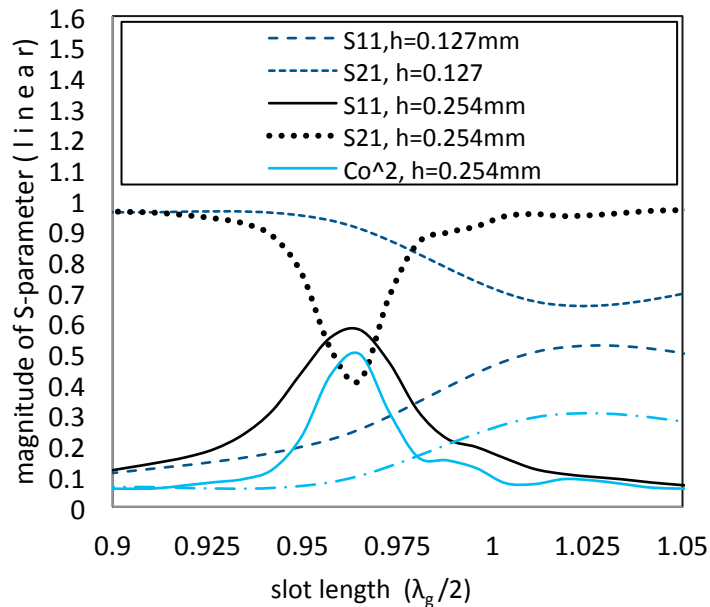


Figure 26 Slot characterization for $x = 0.05 \text{ mm}$, two different substrates at 76.5 GHz, (simulation: CST)

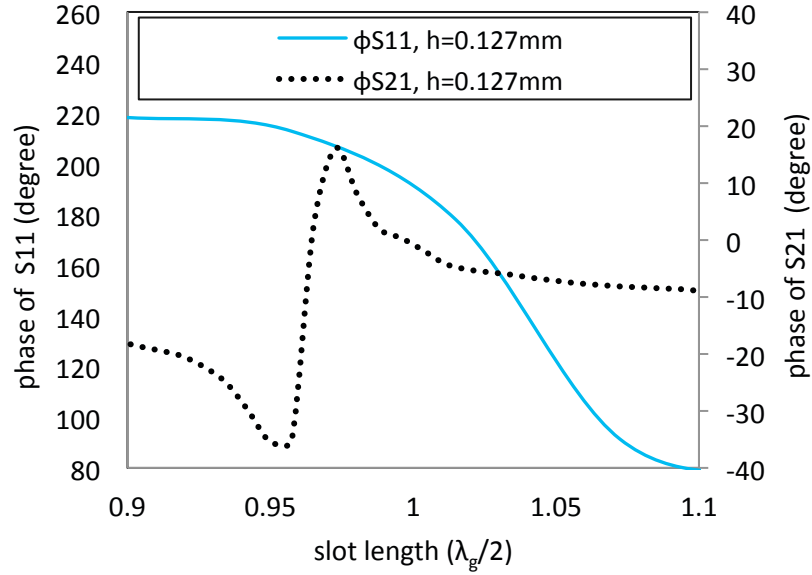


Figure 27 Phase Characterization of a single isolated slot, fixed offset x , (CST)

In the following, the field quantity ϕE_{y0}^n is discussed. Recall that this parameter has been defined previously in 3.2 Its value varies strongly with l , as shown Figure 28. The next Figure 29 demonstrates the phase gap between excitation from the left and right. This will be essential in the design of an array later in Chapter 4 where this effect is responsible for phase gaps.

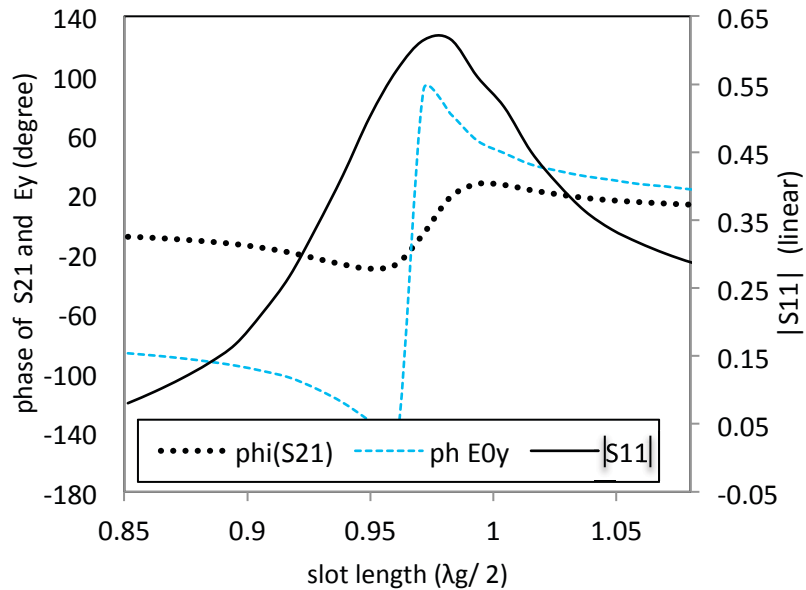


Figure 28 Phase of E-field ϕ , and reflection

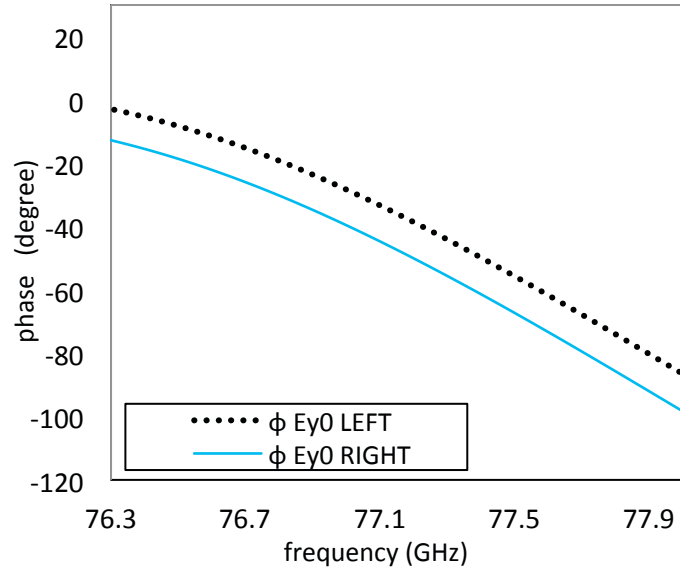


Figure 29 The E-field, excited from either side (for $x = 0.05, l = 0.486 \lambda_g$)

3.3.5. Discussion of Difficulties with the Linearized Longitudinal Slot

To wrap up 3.3, it is possible to conclude that a slot brought into the SIW conductive layer, in a position where displacement currents occur across the slot, takes a significant eigen-admittance. This causes mismatch and reflections. The closer l is to the maximum radiation, the higher is $|S_{11}|$ in general, and the closer is ϕS_{11} to 180° . However, the definition of a resonant length is critical and no longer plausible for SIW, since the transmission phase and reflected phase do not fit with the idea of a resonant thus non-complex equivalent admittance. For the use in a TWA, a reflection less slotted segment is to be designed. Equally, the effect of a non-zero transmission phase and E-field phase for off-resonant length slots excited from both sides needs to be taken into account.

3.4. Study of the Impact and Capabilities of Vias in the Slotted SIW

In the last section, a fundamental issue with the linearized slotted element has been observed, the reflection of reasonable radiating slots. Another important challenge is that the varying phase is not controlled but rather accepted as the result of the slot radiation.

All previous design procedures would compensate for this shift in an array by means that may degrade the results, or limit each slot to have very low radiation to avoid the outlined issues.

Conveniently, the LTCC technique of Chapter 7 allows cutting vias at arbitrary positions with few constraints, also listed in 7. It suggests itself to study the influence of a via in an SIW for the purpose of the TWA design. This was partly proposed e.g. by [2] but only for very narrow via radius and a single via close to the SIW wall without any involved slot. First of all, the influence of a via which is not connected to the surface, i.e. the conductive layer of the SIW, is simulated.

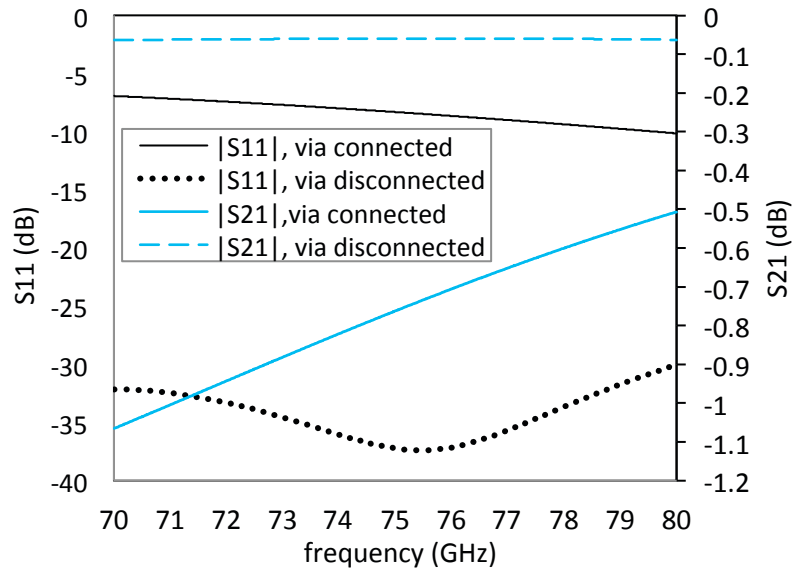


Figure 30 Effect of a via in the SIW

It is thinkable that for lower frequencies a via may be »switched« on or off by means of a diode, however, in millimeter bands, this is actually out of technical feasibility. Figure 30 and Figure 31 illustrate the general behavior of a via brought into the SIW. Two cases are considered. First, the via is *not* connected to the upper and lower conductive layers, and second, the via is a fully *ideal* via. Apparently, the via causes a high reflection when connected to the conductive layer, since only in this case a current on the via cylinder results in the equivalent inductance. On the other hand, a strong phase progression is observed, see also Figure 33 and Figure 34.

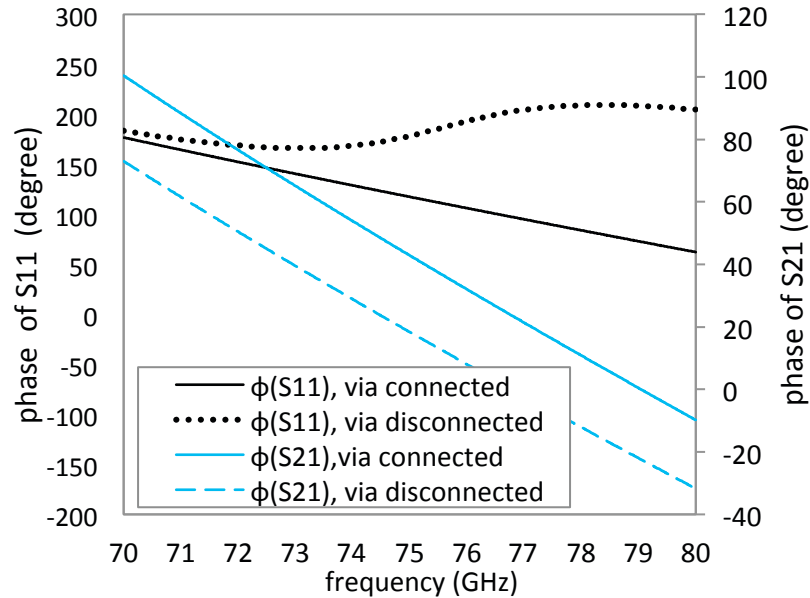


Figure 31 Effect of a via in the SIW, connected or not to the SIW conductive layer, (up) magnitude (below) phase

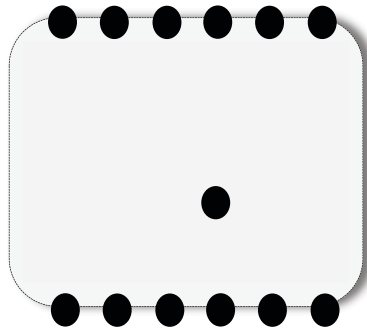


Figure 32 The single via in the SIW

Thus, vias may be used to alter the slot segment network behavior, i.e. its S-parameters. All required phase relations may be set by vias in order to overcome the general issue of phase gaps and provide freedom for further designs in Chapters 5 and 6.

3.4.1. Altering the Complex Transmission and Reflection of the Slot by Vias

The most important alteration is to minimize reflections of a segment. Furthermore, the complex effect of the via as in Figure 32 shall be exploited for the array design in general. It is assumed that a slotted SIW segment can be kept reflection-less although the via exhibits the same diameter as the SIW wall vias which is very convenient for production.

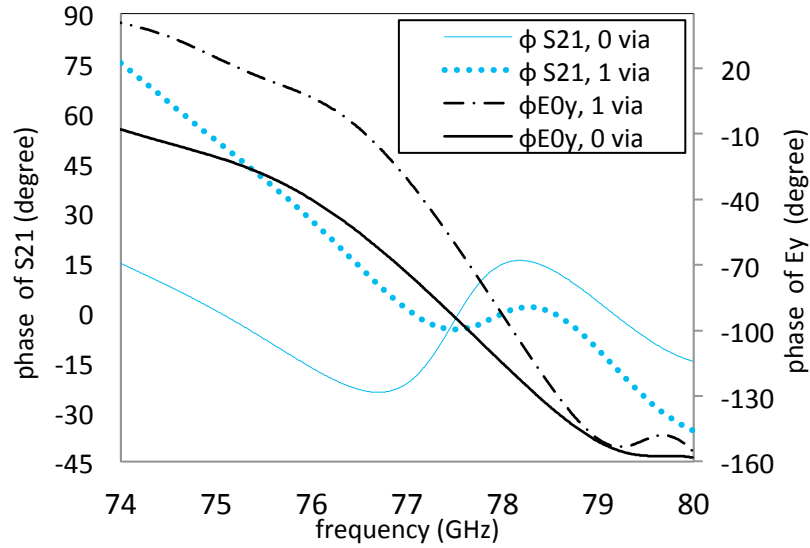


Figure 33 The effect of the additional via on $\phi_{S_{21}}$ and ϕ_{E_y} (at c_{max})

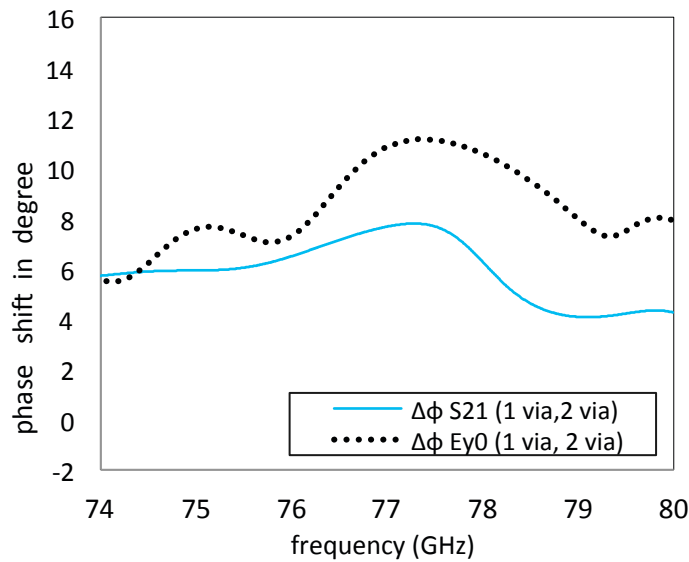


Figure 34 Effective shift of $\phi_{S_{21}}$ and ϕ_{E_y} as function of frequency

TWA design procedures mostly assume reflection-less elements [Chapter 4, ref. 8], i.e. slots and the entire antenna array are not considered as mismatched, due also to a matched termination. This is by default not the case for longitudinal slots as discussed, i.e. most of the TWA designs are written e.g. for circular matched slot pairs [6]. In order to overcome this issue with longitudinal slots, nulling the reflected wave is indispensable. Figure 30 and Figure 31 have shown the eligibility of the via for altering the transmission phase and reflection of a SIW segment. This has been partly done in

[3] for RWGs with a pit. [13] has achieved reflection cancelling in a comparable way but a precise discussion and look on the impacts in particular on the phase has not been accomplished.

Two classes of reflection cancelling methods can be figured out. The first uses an additional adjacent slot spaced $\lambda_g/4$ prior to the main slot in various orientations. The 180° phase difference of the reflected and incident waves lead to total cancelation. Principal work on this field is found in [5] [6] [7] [8]. For longitudinal slots edged in parallel to the wave propagation, these ideas have the disadvantage of very close slots.

The second class of reflection cancelling introduces reactance in form of steps [9] or posts, e.g. for a 45° slot in [10] or [11, 12]. The equivalent inductance of the via is a function of its position in the waveguide and its diameter [2]. The effort of [13], of purely simulated work, deals with a variable diameter in order to achieve reflection cancelling. However, in a realistic SIW scenario at this frequency, most labs impose a fixed diameter or, in best case, a choice of two different radii. It is preferable for low cost purposes to use one diameter for all vias of the SIW and reflection canceling. For this thesis, $|S_{11}|$, as a result of a mismatched capacitive slot, is minimized by a via underneath the slot. It is of a unique radius r , as depicted in Figure 35. Figure 36 allows to draw the conclusion that the input reflection can be kept very low, however, this is accompanied by an altered value of $|S_{21}|$.

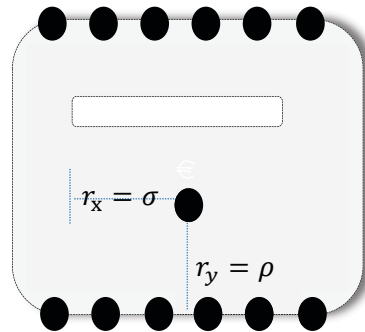


Figure 35 Reflection Cancelling Design for one slot, ($r_x = \sigma, r_y = \rho$, in some Figures)

The impact of the via on reflection and transmission is observable in Figure 36. The optimal position reveals a reflection coefficient of -50 dB. S_{21} attracts higher attention since the value increases significantly by several dB, together with a slight shift of l for maximum c_0 . Therefore, P_{rad} is impacted though no modification of l_n or x_n is done. For each slot length, the via position has to be readjusted, see the design curves in Figure 37 for 76.5 GHz and Figure 38 for 10 GHz.

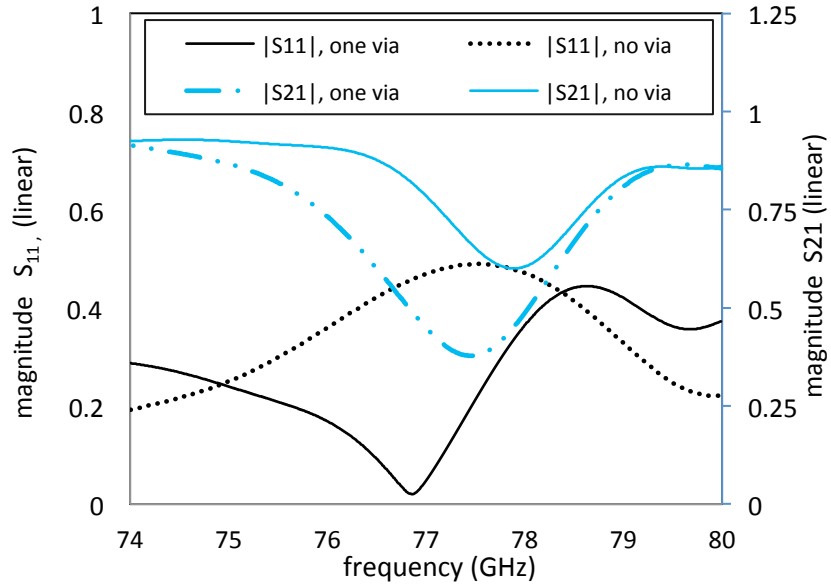


Figure 36 Influence of one and no via for reflection cancelling purpose

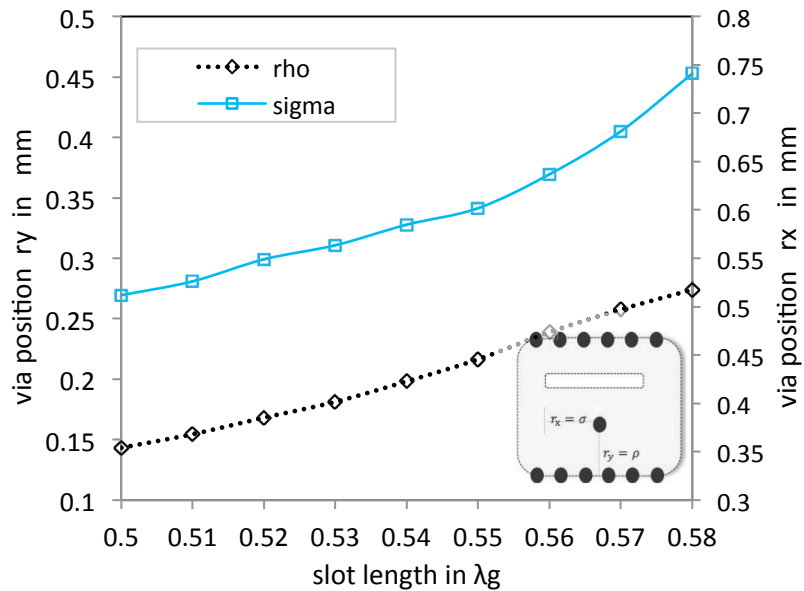


Figure 37 The linearized parameters for the reflection cancelling via for a 76.5 GHz element of $a_0 = 1.074 \text{ mm}$

Note that, the CF has been chosen to be 76.5 GHz in general, however, feasibility and simulation have also been carried out for 10 GHz as an asset for this project. For a few Figures, the 10 GHz graph is solely presented.

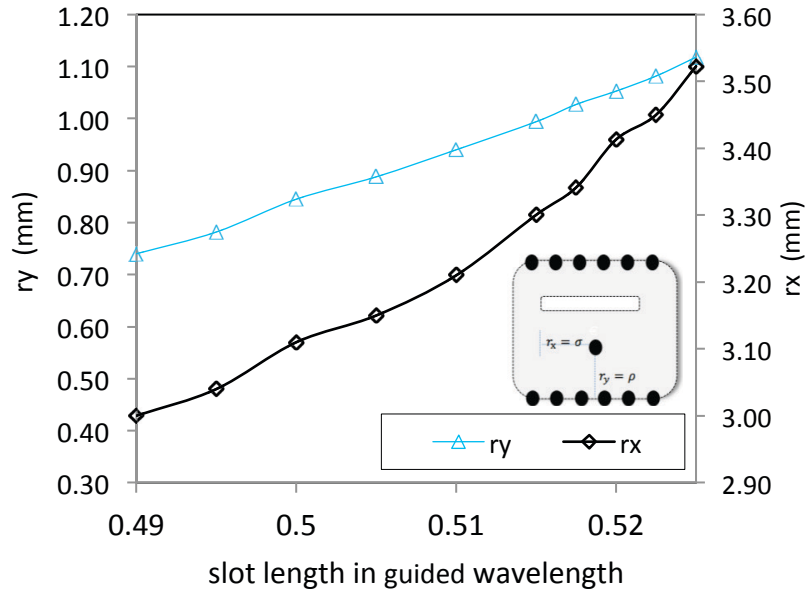


Figure 38 Reflection cancelling via position, at 10 GHz

In Figure 39, the slot phase is considered now for the reflection cancelled solution, as a function of l . Again, the gap between the left and right fed produced field is observable. This is due to the asymmetric nature of the element with multiple vias in an asymmetric configuration. At the same time ϕE_{y0} of the slot is altered. That means, the same segment with a triplet of (x_n, l_n, c_0^n) , obtains a new ϕE_{y0} and ϕS_{21} after optimizing its $r_{x,y}$.

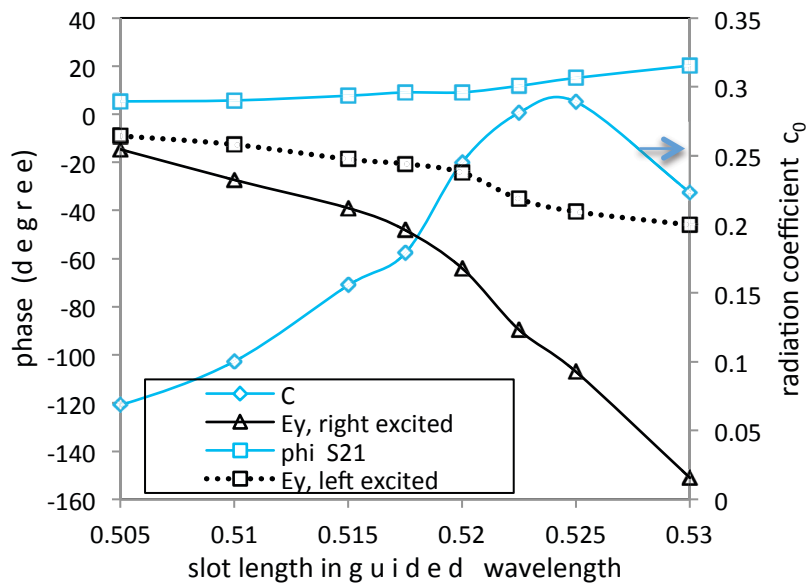


Figure 39 Impact of the reflection cancelling on the slot and segment phase

To sum up, the results of the parameter studies on the impact of the via are as following. Brought into the correct position underneath the slot, the via cancels the reflection efficiently. However, all parameters are very sensitive to the via position. Therefore, it has to be verified later by which criterion to optimize its position. The via reduces the radiation substantially, i.e. the slot length has to be increased. The inherent deviation from a zero phase of (ϕS_{21}) for a full element can be reduced. However, the gap between the slot phase when excited from left and right is substantial.

3.4.2. Approaches of Slot Phase Shifted Elements

An added via has been evaluated and found to be a good candidate also for SIW thin slotted waveguides to cancel the reflection with the result of lower $|S_{11}|$. However, a full control of the slot phase is not yet achieved. In Figure 35, the basic slotted element with one via is depicted. The first via reduces the reflection as shown in 3.4.1 and partly compensates the phase delay of the slot, though it does not allow adjusting equal phase between array elements.

A via close to the SIW wall has been proposed as a phase shifter in [14]. Unfortunately, the greater the phase is shifted, the greater is the reflection from the inductive via. Thus, this effect of the via has not been exploited with longitudinal mismatched slots. Hence, a particular via configuration with negligible reflections is suggested.

A variable phase shift is desired in between segments. In a TWA, each segment shows a different decreasing radiation coefficient c_0^n along the array which means on the other hand an individual $(\phi S_{21}^n, \phi E_{y0}^n)$ to each slot.

3.4.2..1. The Modified β -Shifter (#1)

Figure 40 shows a section of a modified width $a_0' < a_0$, prior to a slot section. Certainly, a_0' could also be $> a_0$. In this approach, the slot section is not altered, i.e. kept as in the isolated case. The segment of a_0' reveals a different propagation constant, thus two segments with different wave-numbers are cascaded. [15] has shown broad band shifting capabilities for approaches without slots.

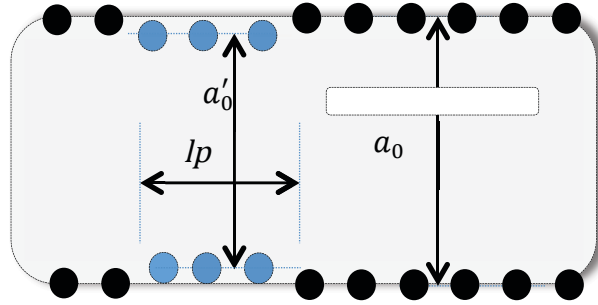


Figure 40 Section of modified propagation constant with a'_0 , see (17)

The analytical computation of the phase shift by taking into account β_0 and β_1 , see (17), does not count in nonlinear effects and the particular circumstance of the SIW wall.

$$\Delta\phi(l) = \begin{bmatrix} \sqrt{\left(\frac{2\pi}{\lambda_g}\right)^2 - \left(\frac{\pi}{a_0}\right)^2} \\ -\sqrt{\left(\frac{2\pi}{\lambda_g}\right)^2 - \left(\frac{\pi}{a'_0}\right)^2} \end{bmatrix} \times l_p \quad (17)$$

In fact, the effective phase shift $\Delta\phi$ is proportional to the length of the section l_p . But Figure 41 shows the divergence in simulated phase shift for the narrowed section of a'_0 , compared to the theoretical value. As an example, Figure 42 depicts a simulated phase shift of approx. $+80^\circ$ in the lower with respect to the upper SIW. Degradation in SWR of the incident wave is obvious.

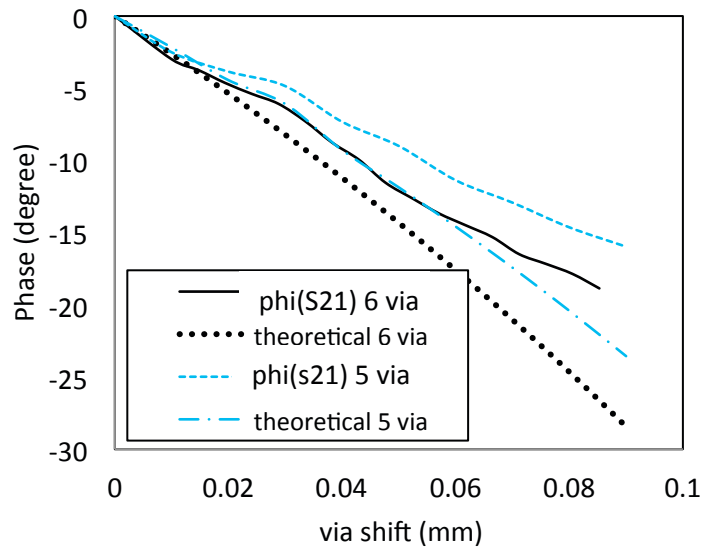


Figure 41 Simulated phase shift compared to the predicted one from (17)

Unfortunately, this solution has reflections in the range of -20 dB, see Figure 43, which has a severe impact on the slot radiation in antenna arrays. Recalling the motivation of this work that is limiting side lobes to a minimum, the approach is not versatile enough.

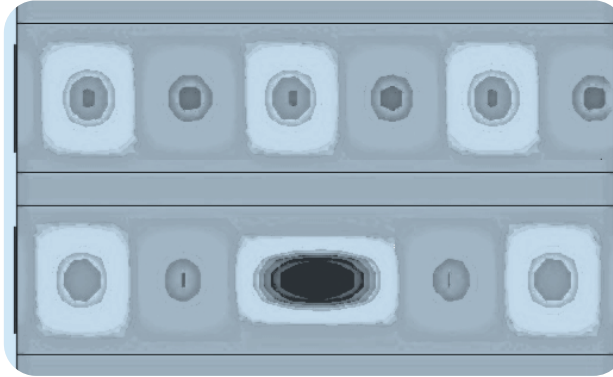


Figure 42 Effect of phase shifter with 6 vias in the lower part

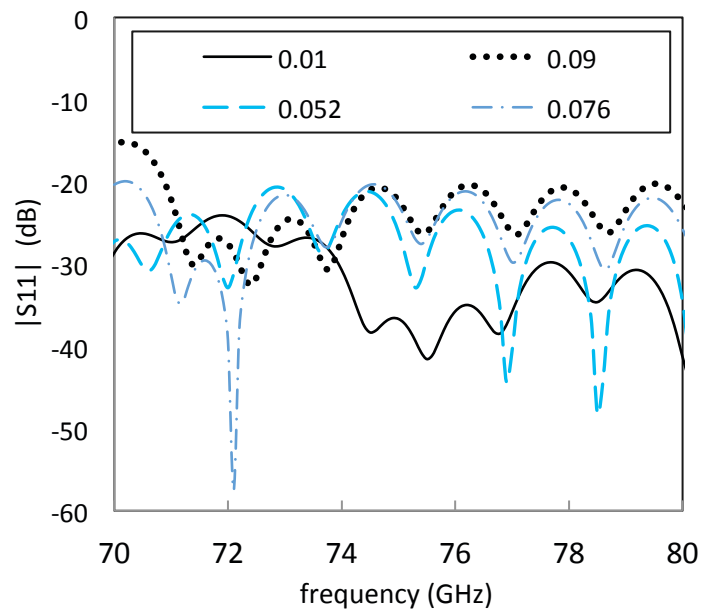


Figure 43 Input reflection of a 6 via shift with $(a_0 - a_0')/2$ from 0.01 to 0.076 mm at 76.5 GHz center frequency

3.4.2..2. The τ -Approach (#2)

The ensuing approach to enhance the element is by adding additional vias behind the first one, in the traveling-wave direction. Since the element is now detuned from its original $r_{x,y}$, the latter has to be re-adapted. The parameter τ is responsible for increased shift, but naturally, the minimum pitch p has to be respected. In the frequency domain, the effect is depicted in Figure 45, with the difference in phase between one and two vias.

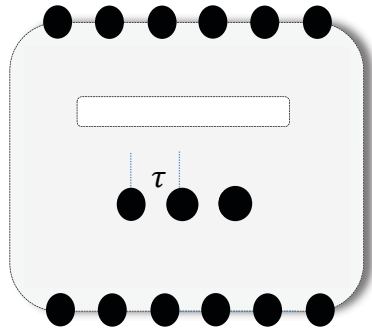


Figure 44 Additional via introduced after the reflection cancelling via

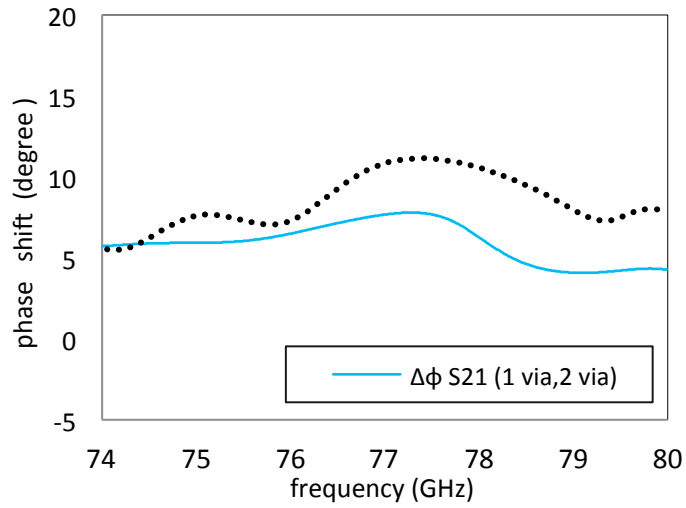


Figure 45 Effective shift of $\phi_{S_{21}}$ and ϕ_{E_y} as function of frequency

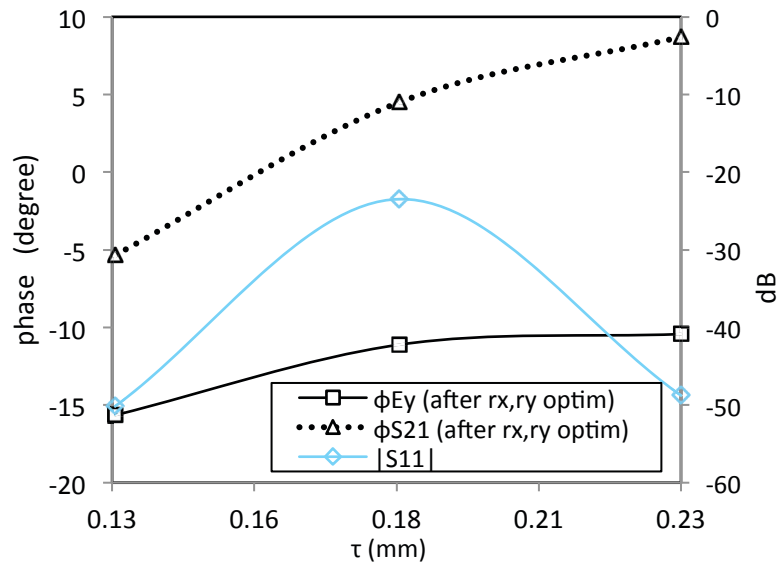


Figure 46 The τ -method, with two vias, approach #1

When considered at center frequency, the total capability of shifting both ϕE_y and ϕS_{21} is true but in a low range. The reflection can be kept very low, when optimized for each value of τ . Figure 47 and Figure 48 wrap up the impact of this method by showing results for no via, one via and one additionally placed via behind. (Note the slightly modified nomenclature in the caption).

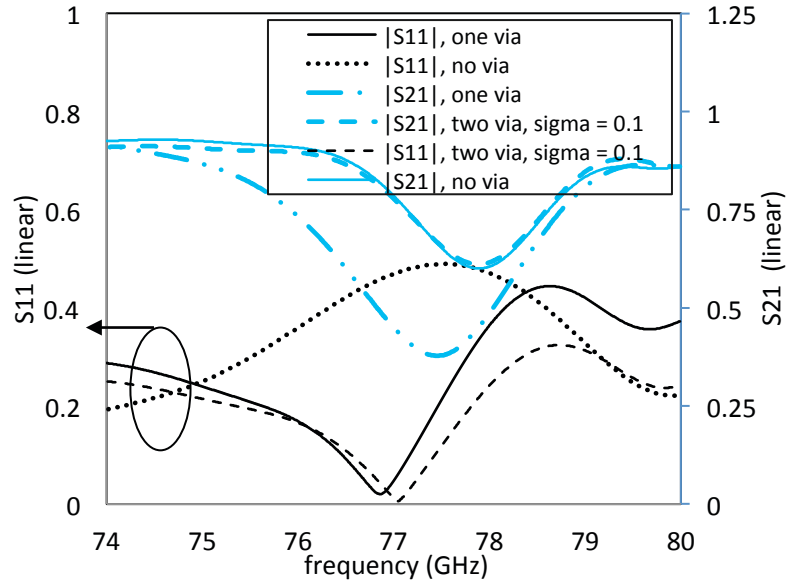


Figure 47 Influence of one, two, and no via, $\sigma=r_x$, $\rho=r_y$

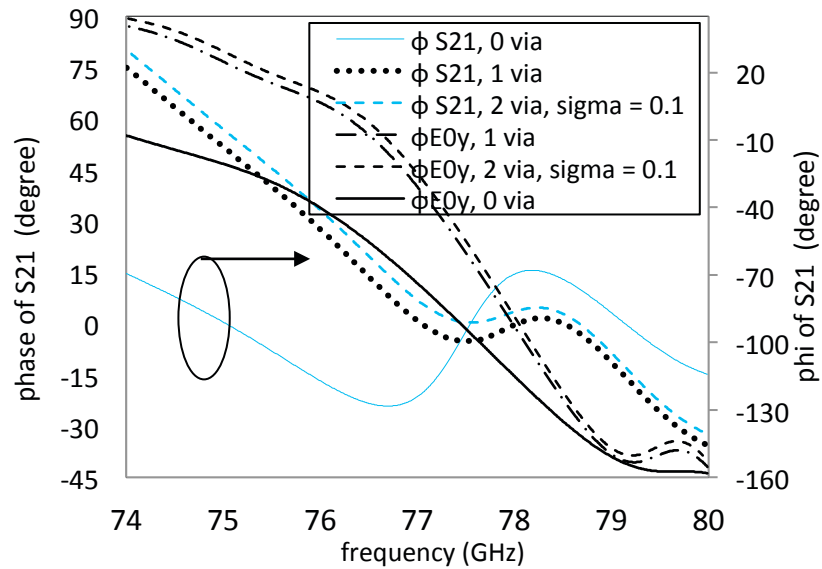


Figure 48 The effect of the additional via on ϕS_{21} and ϕE_y (at C_{max})

3.4.2..3. The v_y Narrower Approach (#3)

The approach discussed in the following uses up to four fifths of the via wall for shifting, see Figure 49. The most significant assumed disadvantage is the altered offset x , yielding a different radiation. Assumingly, the impact on ϕE_y^n will be equally high for the same reason of both x and modified TE mode propagation. Results are depicted in Figure 50. The reflection can be kept very low, best values are achieved for small v_y , since the ‘detuned’ couplet of x and $r_{x,y}$ is ‘retuned’ at this position.

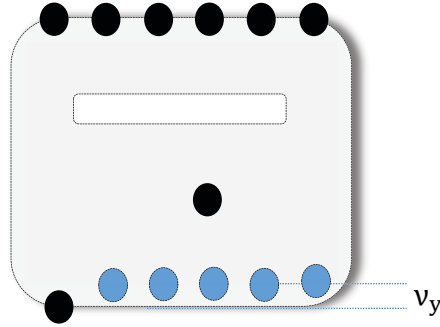


Figure 49 Approach #3

However, the issue with heavily varying $|S_{11}|$ as well as strongly impaired radiation due to the offset variation is a significant drawback compared to the small capability of adjusting the phase.

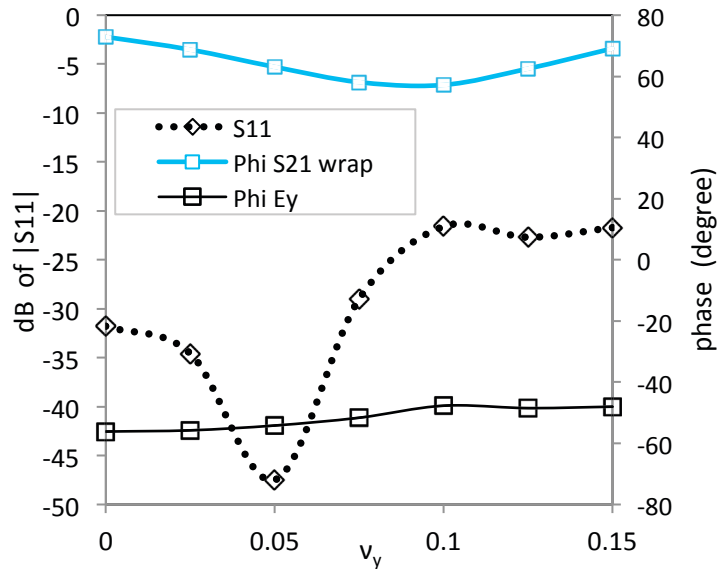


Figure 50 Approach #3, at 76.5GHz $a_0=1.074$ mm

3.4.2..4. Dual Close Via Narrower Approach, Behind (#4)

This method uses one via underneath and two vias narrowing the SIW at the end, see Figure 51. Naturally, the reflection cancelling via has to be adapted for each position of v_y . Thus, two relations for the via adjustment $r_x(v_y)$ and $r_y(v_y)$ are provided in Figure 53. The dependency is quite relaxed compared to subsequent approaches in 3.4.3.

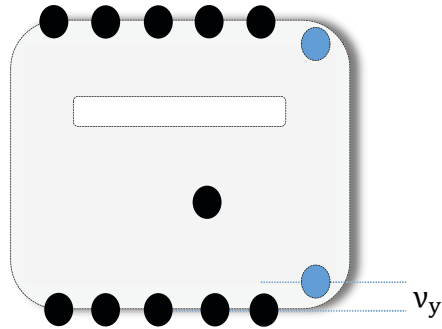


Figure 51 Approach #4

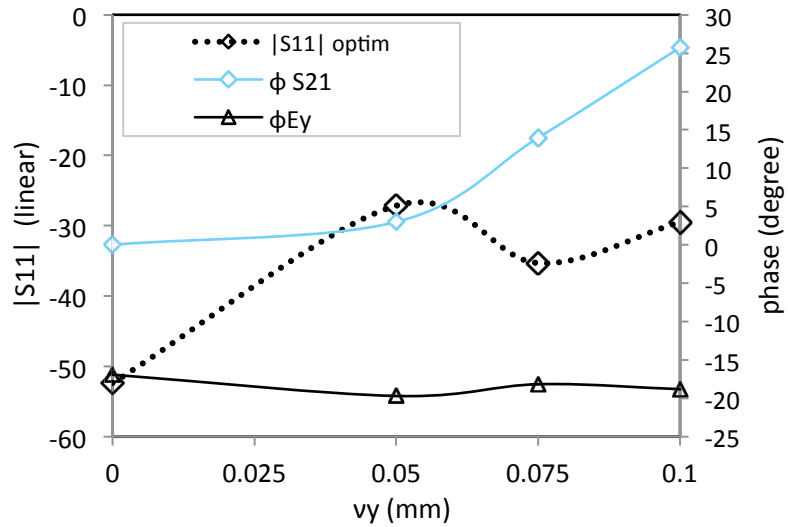


Figure 52 Results of approach #4

The good results and versatile use of the vias are however impaired by the degraded radiation, see Figure 54. This is caused by the small reflection of the additional shifted via which is out of phase with the dominant mode exciting the slot.

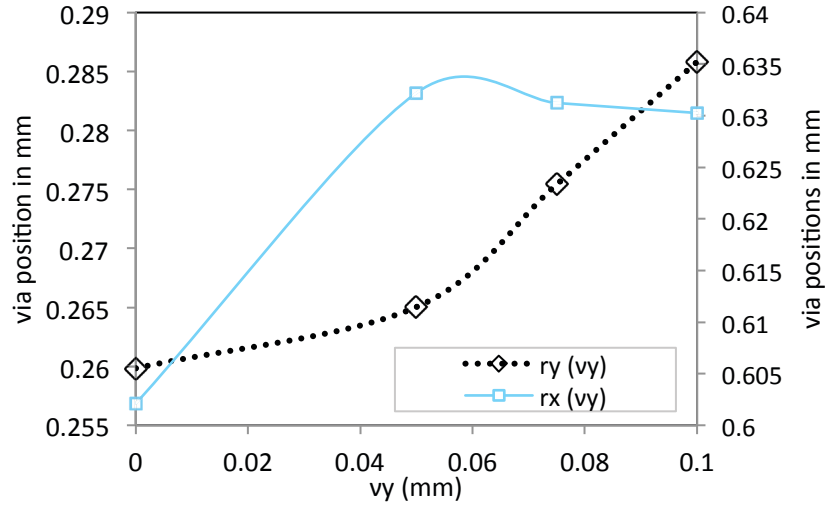


Figure 53 Approach #4, adjustments on first via position, at 76.5 GHz

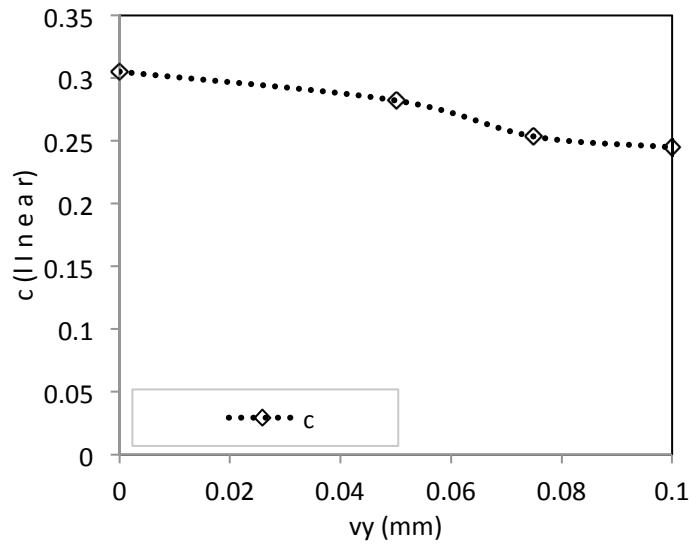


Figure 54 Radiation as a function of the via position

3.4.2..5. Dual Close Via Narrower Approach, in Front (#5)

The fifth approach uses one via underneath and a slightly modified widened respectively narrowed via section *just* before the slot, as indicated in Figure 55. Results prior to re-optimizing the reflection canceler are depicted in Figure 56. Prior to re-optimizing the reflection, this approach reveals a very linear and well sufficient shifting.

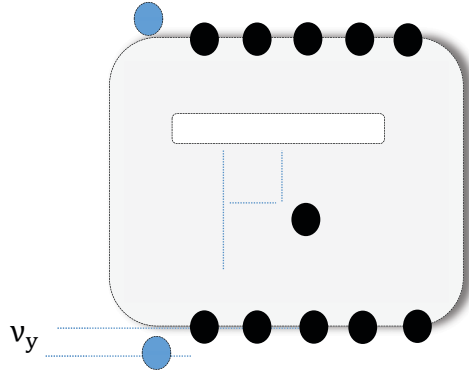


Figure 55 Approach #5, no particular distance to the slot position is considered

Nevertheless, the increased return loss makes it mandatory to re-optimize the via underneath the slot and this reduces the positive outcome of the method to a minimum, see Figure 57.

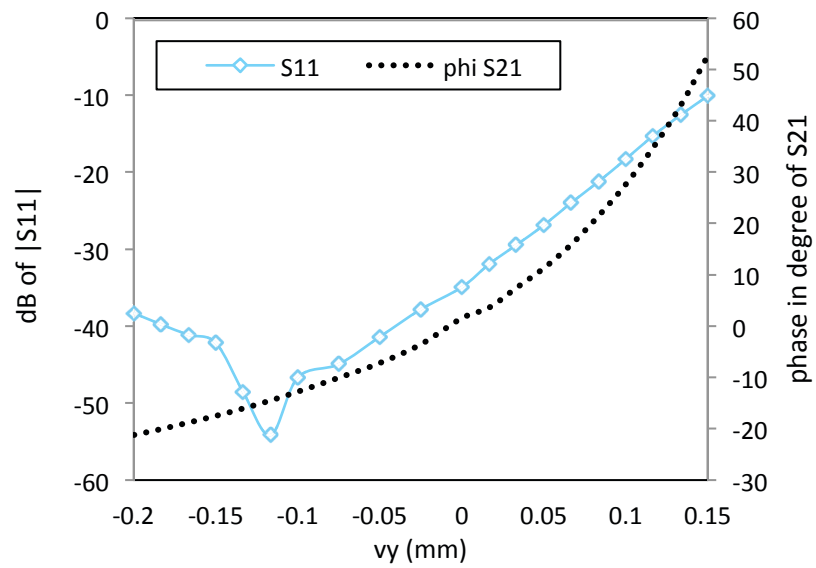


Figure 56 Transmission and reflection coefficient as a function of the via position

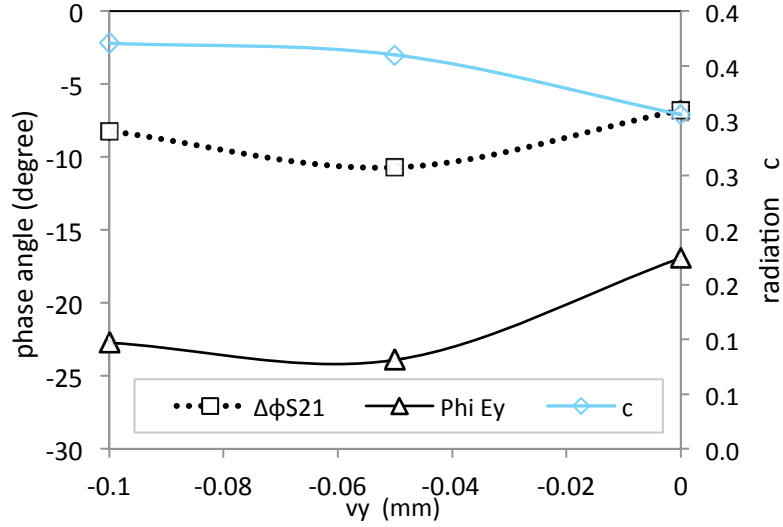


Figure 57 Results of Approach #5 after re-optimization of reflection

3.4.3. A Sophisticated Versatile Slot Phase Shifting Approach

With the observed issues and limitations in the previous section of simpler approaches with moving vias, a more sophisticated alternative concept is conceived. Figure 58 (a) depicts again the slotted element with one via and (b) with multiple vias in the 2nd case, but now with a different relation of the parameters $v_{x,y}$ that are defined with respect to the slot center and lower via wall center respectively.

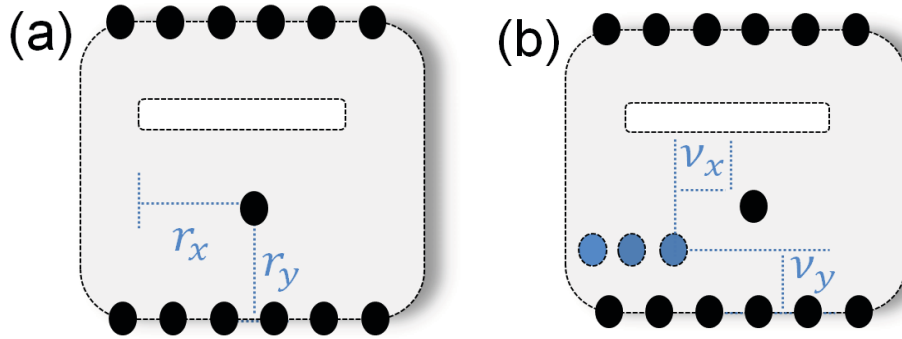


Figure 58 (a) Slotted SIW element with one via, (b) with four vias

Figure 58b with three additional vias is representative for the proposed element; more or less vias can be inserted depending on the required range of phase shift. The distance v_y of the vias, and the slot length l are basically free parameters. With respect to the transmission phase $\phi_{S_{21}}$ of the ele-

ment in Figure 58a, the effective transmission phase with additional vias is evidently a function of v_y in the first place. The radiation capability c , however, is varied solely by l .

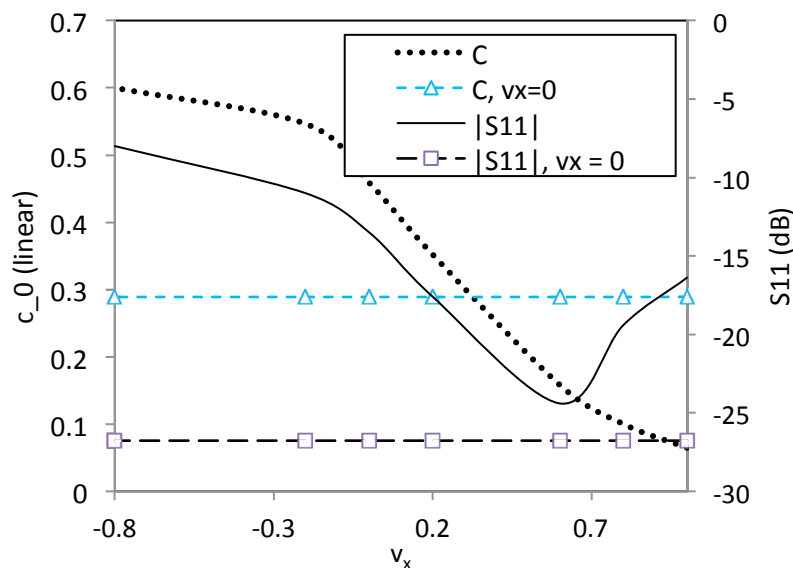


Figure 59 Impact of v_x on the radiation and reflection

To keep it manageable, the final design curves that link l with c_0 shall be bijective, while $|S_{11}|$ shall stay low, wherever the vias are actually placed. For this sake, over all l values, it is required to set a pair of $v_{x,y}$ that yields the same $c_0(l)$ as for $v_y = 0$, and to increase $r_{x,y}$ to limit reflections. This represents the main design effort and differs substantially from a pure slot related approach or a pure reflection cancelled slot. As a function of v_x , the strongly impacted radiation coefficient is depicted in Figure 59. While increasing the via position v_x , the radiation is impacted contrariwise. In order to obtain a c_0 equal to the default value, depicted as c_0 with $v_x = 0$, a different v_x is required.

In Figure 60, sample resulting design curves are depicted for $l = 0.5 \lambda_g$, $0.5175 \lambda_g$ and $0.52 \lambda_g$, yielding $c_0 = 0.05 \dots 0.25$ of the input power. (Note that for small values of v_y , the intersecting vias of the SIW wall are removed). In this way, the phase is shifted by 30° while $|S_{11}|$ stays below -30 dB and c_0 remains constant for one particular l_n . One may also consider the shift as $\pm 15^\circ$.

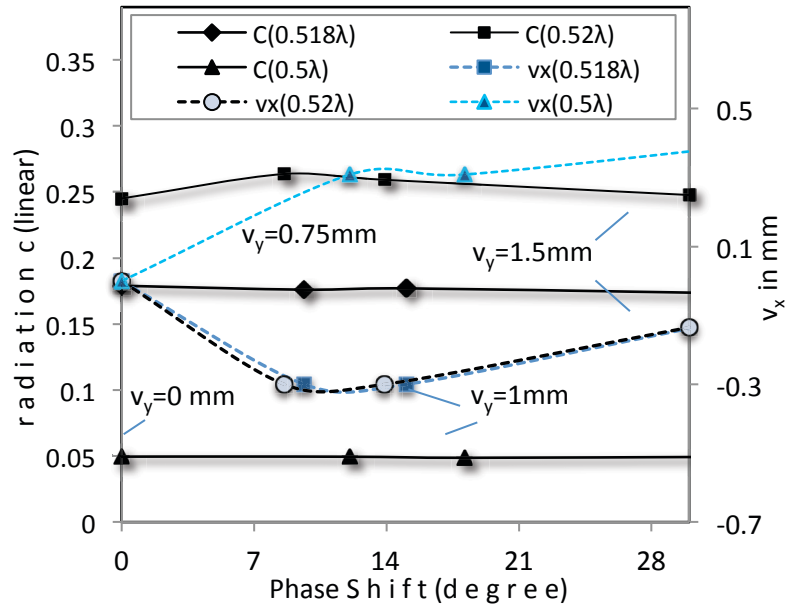


Figure 60 Characterization results of a single element with five vias, exemplarily shown for three slot lengths, the free parameter is v_y

A potential source of errors is $r_{x,y}$ for each of the required slot length samples for interpolation. If mistakenly the sole optimization criterion is a minimal $|S_{11}|$, all dependent parameters such as c_0 , ϕE_y , as well as the mutual coupling coefficients, become relatively nonlinear over the range of l . This results in a less accurate interpolation but especially hinders finding values for $v_{x,y}$ as described above. Therefore, as a general rule, instead of seeking an absolute minimum for $|S_{11}|$, it is preferable to produce $r_{x,y}(l)$, $\phi S_{21}(l)$ and $c_0(l)$, as well as the mutual coupling coefficients⁴, as linear as possible. This will cause $|S_{11}|$ slightly to increase over l , i.e. care should be taken to the maximum acceptable reflection which should match with the maximum required radiation. To illustrate this impact of $r_{x,y}$ and thus $|S_{11}|$ on the radiation, as an example for all other parameters, Figure 61 is provided. Although a good matching is already achieved in the first case, a pure optimization for reflections would yield -40 dB for $|S_{11}|$ at center frequency, however, with a decrease of radiation to 1/3.

⁴ Mutual coupling is treated in Chapter 4

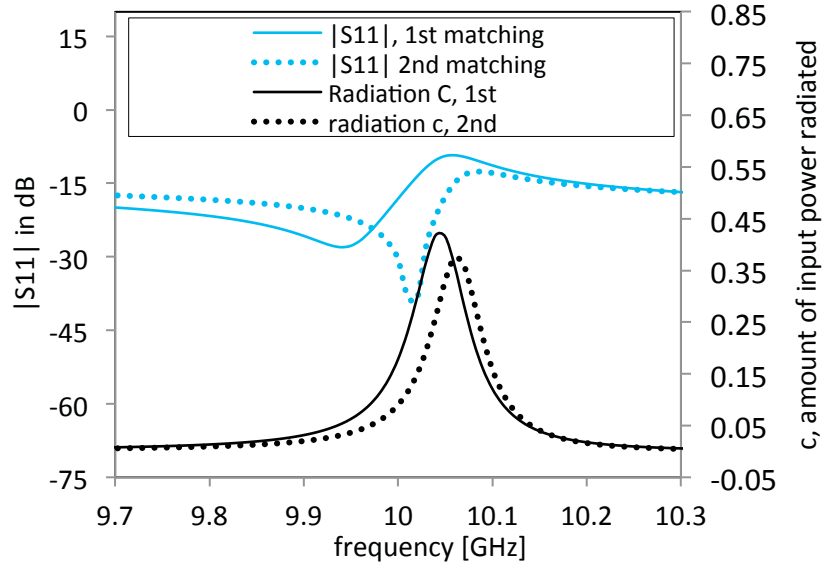


Figure 61 Impact of matching on radiation (as an example for all other dependent parameters), the results of two different pairs of $r_{x,y}$ are shown, slot l constant

Thus, the reflection can be kept very low, compared to the less sophisticated via movements of the previous Section 3.4.2. This is an essential advantage. The sensitivity or impact of the proposed matching is also observed on ϕS_{21} , depicted in Figure 62.

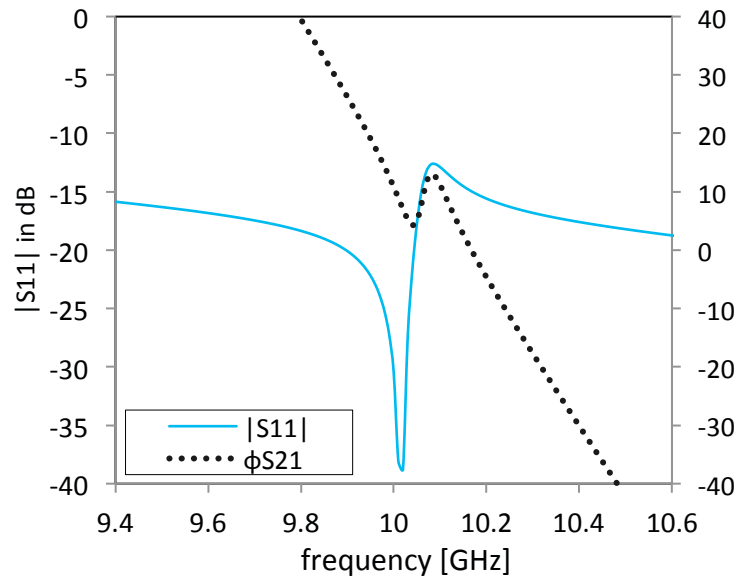


Figure 62 Impact of an inaccurate matching on the phase of the transmission

By the proposed means, an element becomes more versatile in terms of its radiation, transmission, and radiation phase. This technique has been published in parts under [16]. It can be applied in an antenna array designed by a revised TWA design procedure discussed in 4, if a couple of preconditions are verified in advance.

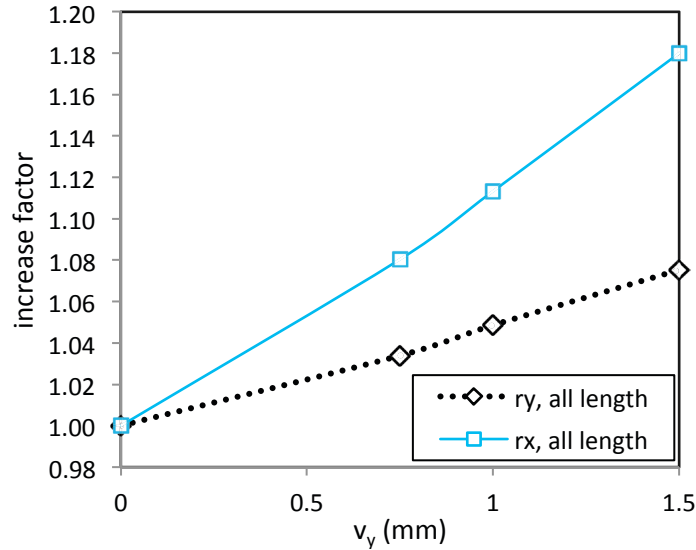


Figure 63 Factor for $r_{x,y}$ when phase shifting by v_y , shown at 10Ghz

3.5. Preconditions for the application of the designed elements in an array

In Sections 3.2 to 3.4, the isolated slotted element has been considered and its slot phase and S-parameter results have been manipulated. The challenges for applying these elements appropriately in traveling-wave antennas have been outlined as reflection, phase gaps, unequal ‘left’ and ‘right’ phase and high dependency of the matching mechanism on the radiation capability. The approach of 3.4 has solved most of these issues and allows conceiving a new way of designing TWAs. However, further substantial elementary requirements shall now be confirmed or disconfirmed prior to a potential application in antenna arrays.

3.5.1. SIW and RWG Equivalent Width

A very important consideration is the comparison of SIW and equivalent RWG S-parameter results. This equivalence is mainly checked for feasibility, since full wave simulation with all SIW vias is very time-consuming due to a high amount of mesh cells. Basically, results shall not vary significantly when (5) is applied for the equivalent width computation. In Figure 64, a short segment of

SIW is compared with the equivalent RWG. It depicts a shift of relative 0.5% in the resonance frequency, which is significant in low bandwidth 1% antenna array designs. Therefore, as a conclusion, wherever possible at least the isolated SIW structure is simulated with all vias without simplification. This will, nevertheless, yield a significantly increased simulation time.

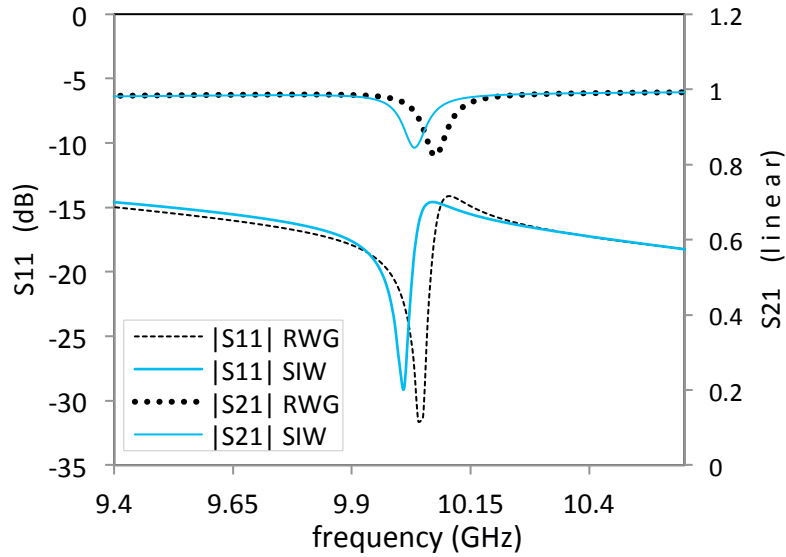


Figure 64 Comparison of SIW and RWG reflection and transmission coefficients; the conversion is based on (5)

3.5.2. Full Wave Analysis Evaluation

Performing a full wave 3D electromagnetic simulation has become straightforward with recent software packages from CST or Ansoft. In contrast to the isolated element, electrically large TWAs face the issue of very high mesh cell quantities. Typically, the criterion for converging for this thesis is a phase error $< 2^\circ$. It was observed that it becomes very difficult to de-embed the phase correctly to the center of a slot with CST. Phase errors of 20° or more occur even with very fine meshing. Therefore, the design procedure excludes the possibility of de-embedding and simulates all slots as segments of one entire guided wavelength λ_g , as the TWA is subsequently composed of λ_g segments due to the high value of $\epsilon_r > 7$. HFSS and CST show minor differences in magnitude in Figure 65.

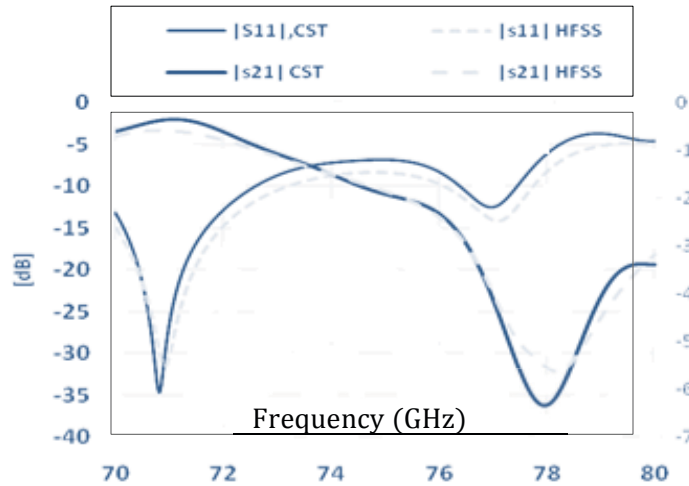


Figure 65 Comparison between CST and HFSS for an arbitrary SIW

3.5.3. Proof of Traveling-Wave Matched Slot

The elements designed in 3.4.3 are matched for the traveling-wave architecture. This implicitly means that the slot may be moved within a longer element without degrading the total reflection performance, in contrast to a mismatched or purely *resonant* element.

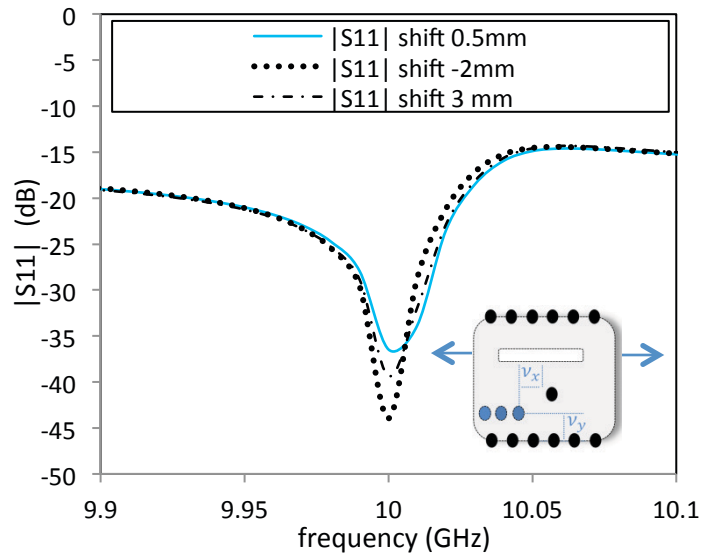


Figure 66 Proof of quasi traveling-wave condition

It is important to verify the correct design of the element by shifting the slot and via position slightly within the SIW, see Figure 66. $|S_{11}|$ stays the same with at the most -30 dB at a CF of 10 GHz. Note that this result is applicable for an *isolated* element only. Section 3.5.4 considers results for a SIW with multiple slots.

3.5.4. Dependency of Shifting Slotted Elements

The obvious and quite trivial solution to eliminate phase gaps may be to move elements within the array. In Figure 67, an array of four elements is treated this way. All four effective element phases are depicted. Only the third element is shifted. The free parameter is the shift in mm from the original position. It is seen that although solely one element is shifted, the impact on ϕE_y is more important than assumed from a linear perspective considering the dominant mode.

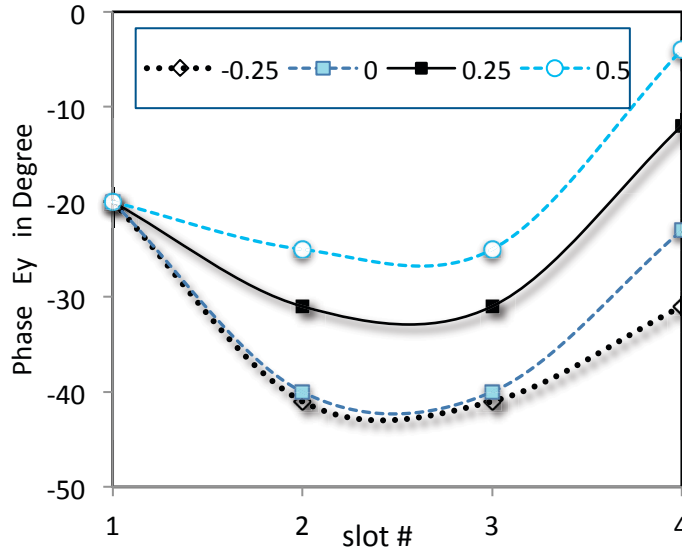


Figure 67 Shifting solely the third element, impact on ϕE_y , shift is in mm

As an important conclusion for this work, without evaluating the exact cause of the below depicted result at this moment⁵, a fixed position is the preferred approach for the new straightforward design procedure.

3.5.5. Slot Phase Linearity over Bandwidth of a Fabricated Circuit

The phase ϕS_{21} of a fabricated single element is measured over the entire bandwidth to confirm linearity. Figure 68 depicts the measured phase of a single element with one via for reflection cancelling, relative to a THRU element. For details on the THRU and the material see Chapter 7 .

⁵ Mutual coupling is one important effect, see Chapter 4

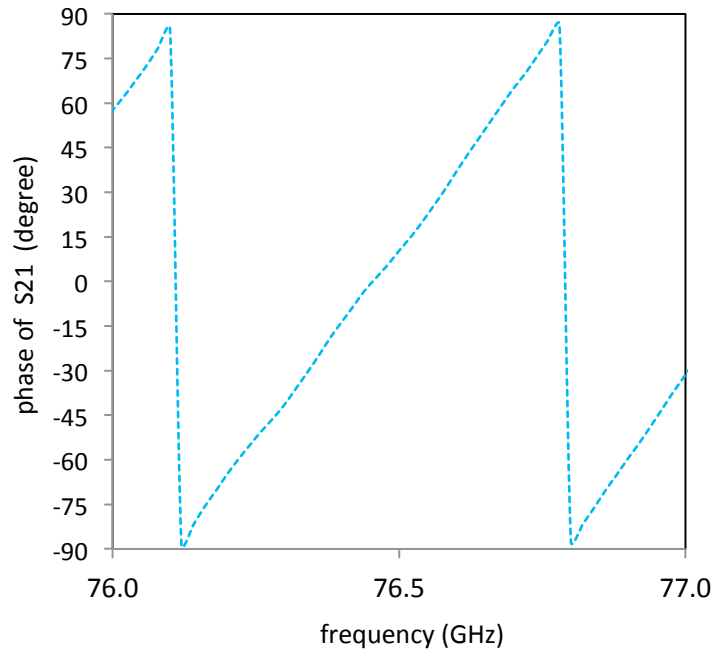


Figure 68 Measured phase of a single element

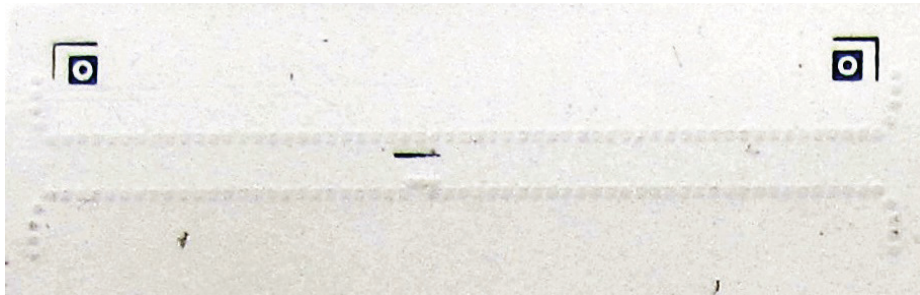


Figure 69 Measured phase of a single element

3.5.6. Simulation Stability of Dominant and 2nd Mode

A further basic requirement, the non-occurrence of higher modes, is shortly verified. Figure 70 depicts the propagation $|S_{21}|$ of the first and second mode when simulated with a full wave simulation program. It is obvious that although high density meshing is applied, some instability is artificially generated in the simulation at cut-off frequency. However, at CF, the basic requirement is fulfilled. As a conclusion, all simulations are mainly carried out with at least 15% margin from CF.

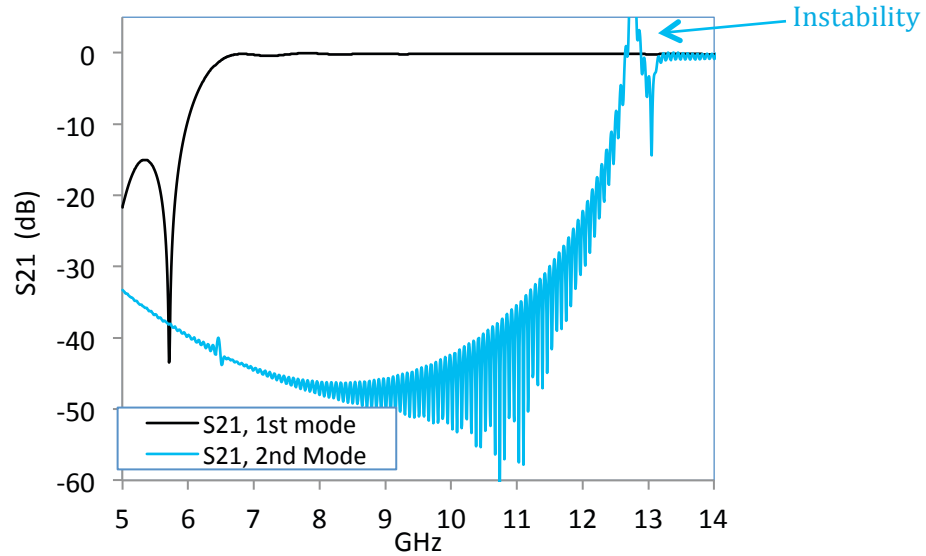


Figure 70 Propagation of first and second mode, the full wave simulation is instable around the transition from complex to real propagation constant

3.6. Conclusion

In this Chapter, longitudinally slotted elements that are mismatched have been discussed. The closer l is to the maximum radiation, the higher is $|S_{11}|$ in general, and the closer is ϕS_{11} to 180° . Since the definition of a resonant length is critical and no longer plausible for SIW, shown by the transmission phase, slots have been designed off-resonant. For the use in a TWA, a reflection less slotted segment has been designed. Equally, the effect of a non-zero transmission phase and E-field phase for off-resonant length slots excited from both sides has been taken into account. Fortunately, a configuration of vias within the element has been found that allows controlling the element and slot phase partially, allowing revising and simplifying the TWA design concept based on S-parameters of isolated slots. A couple of preconditions have been verified in order to perform the TWA composition in the next Chapter.

3.7. References

- [1] M. Henry, C. E. Free, et. al., "Millimeter Wave Substrate Integrated Waveguide Antennas: Design and Fabrication Analysis", *Advanced Packaging*, IEEE Transactions on., vol. 32, p. 93-100, 2009
- [2] K. Sellal, L. Talbi, T.A. Denidni, "Design of a Substrate Integrated Waveguide Phase Shifter", *Information and Communication Technologies*, ICTTA '06. 2nd, p. 2155–2160, 2006

- [3] J. Sato, J. Hirokawa, M. Ando, "Reflection-canceling of slotted waveguide antenna by using a circular pit", Antennas and Propagation Society International Symposium, vol. 3, p. 1706-1709, 1998
- [4] T. Suzuki, J. Hirokawa, M. Ando, "Analysis and Design of a Reflection-Cancelling Transverse Slot-Pair Array with Grating-Lobe Suppressing Baffles", IEICE Transactions on Communications E92.B (10), p. 3236–3242, 2009
- [5] J. Hirokawa, M. Ando, "45° linearly polarised post-wall waveguide-fed parallel-plate slot arrays", Microwaves, Antennas and Propagation, IEE Proceedings - 147 (6), p. 515–519, 2000
- [6] K. Sakakibara, J. Hirokawa, M. Ando, et.al., "A slotted waveguide array using reflection-cancelling slot pairs", Antennas and Propagation Society International Symposium, AP-S. vol.3, p 1570-1573, 1993
- [7] J. Hirokawa, M. Ando, "Efficiency of 76-GHz post-wall waveguide-fed parallel-plate slot arrays", Antennas and Propagation, IEEE Transactions on, vol. 48 (11), p. 1742–1745, 2000
- [8] J. Takeda, M. Ando, et. al., "Suppression of reflection from slots in a linearly-polarized radial line slot antenna", Antennas and Propagation Society International Symposium, vol. 3, p. 1342-1345, 1991
- [9] Y. Tsunemitsu, J. Hirokawa, M. Ando, et. al., "Single-layer slotted waveguide array with reflection canceling stairs", Antennas and Propagation Society International Symposium 2006, p. 3149–3152, 2006
- [10] S. Park; Y. Okajima, J. Hirokawa, et. al., "A slotted post-wall waveguide array with interdigital structure for 45° linear and dual polarization", Antennas and Propagation, IEEE Transactions on. Vol. 53 (9), p. 2865–2871, 2005
- [11] S.H. Park, et. al., "Analysis of a Waveguide Slot with a Reflection-Canceling Post", IEIC Technical Report, 102.232, p.31-36, 2002
- [12] P. Sanchez-Olivares, J.L. Masa-Campos, "Slot radiator with tuning vias for circularly polarized SIW linear array," Antennas and Propagation (EUCAP), 2012 6th European Conference on, vol., no., pp.3716, 3720, 26-30 March 2012

[13] Q. Zhang, L. Qingfeng; et. al. "Design of 45-degree Linearly Polarized Substrate Integrated Waveguide-fed Slot Array Antennas" International Journal of Infrared and Millimeter Waves vol. 29 (11), p. 1019–1027, 2008

[14] K. Sellal, et.al., "A New Substrate Integrated Waveguide Phase Shifter", 36th European Microwave Conference, pp. 72–75, 2006

[15] Yu Jian Cheng; Ke Wu; W., Hong "Substrate integrated waveguide (SIW) broadband compensating phase shifter", Microwave Symposium Digest, IEEE MTT-S International, p. 845–848, 2009

Published papers:

[16] F.D.L. Peters, S.O Tatu, T.A. Denidni, "Design of traveling-wave equidistant slot antennas for millimeter-wave applications," IEEE International Symposium on Antennas and Propagation (AP-SURSI), pp.3037-3040, 3-8 July 2011

CHAPTER 4

TWA DESIGN BY INTERNAL PHASE VARYING AND ENHANCED APPROPRIATE MODELING IN SIW

4.1. Introduction

While in Chapter 3 isolated slots have been considered with the goal of creating full antenna arrays, this Chapter proposes the steps and design rules to achieve this goal. An alternative new way of configuring and modeling traveling-wave antennas of this kind is set up in Sections 4.3 and 4.4 that allows considering the particularities of the elements treated in the previous Section. For convenience, an implementation in MATLAB is presented in Sections 4.5 along with the results in Sections 4.6 and 4.7.

4.2. Introductory Definitions and Thoughts on the Traveling-Wave Antenna

Traveling-wave slot antennas (TWA) stand out for their high gain, high aperture efficiency, and pure polarization. The TWA provides great freedom in the design of its aperture distribution. Implemented in rectangular waveguide (RWG), it has many field approved applications due to well-known design rules available for decades, recall 2.6.

A discrete traveling wave antenna array can be defined as a composition of discretely radiating elements which are fed by the same non-standing wave, i.e. by a wave which propagates along cascaded radiating elements [1, 2]. The alternative continuous way is not treated in this work.

Two TWA defining characteristics repeatedly given by the literature are worth to be reviewed.

First, the traveling wave antenna array may not be terminated with a matched resistance at the end of its physical structure and still be a TWA. Often, if the design is successful, the residual power (rP) at the end of the array is inconsiderable. If so, a badly or even not at all matched termination, e.g. a

short [3], causes a rather small reflection compared to the mostly neglected *internal* return loss. This is considered herein in the following.

The second property often attributed to discrete TWAs is the distance d in between radiating elements. Typically, a TWA provides unequal d between elements, and d is further unequal to the guided wavelength λ_g , whereas a resonant array locates the radiating elements exactly e.g. on maxima of the standing wave. This may result in $d \approx \lambda_g$ or $\lambda_g/2$ in case alternating offsets are used. Nevertheless, a TWA may be composed of any d , as long as the feeding wave continuously travels along the array, equal phase is guaranteed, and the slot distance avoids grating lobes. This in fact imposes dielectric loading. The very well elaborated thesis on dielectric loading of slotted waveguide⁶ states, that, *“in practice, this approach is rarely employed because several system-level penalties are incurred. First, manufacturing costs and weight are higher for a dielectrically loaded waveguide. Second, the broadwall width must decrease in order to maintain a common single-mode band of operation after the waveguide has been dielectrically loaded. This restricts the range of slot sizes (. . .). Because slot arrays are typically composed of resonant elements, the necessary $\lambda_0/2$ slot length will no longer fit within the dimensions of the broad wall. Dielectric loading also presents a problem in terms of increasing loss. (. . .), most practical dielectric materials suitable for loading a waveguide will increase the loss of the waveguide more than alternative passive phase shifter architectures.”*

That is, to sum up, three main penalties shall be solved prior to any use of dielectric loading. The first is effectively already resolved by the technique of SIW. The second issue of reduced free space in between slots may be circumvented with a $\approx \sim \lambda_g$ spaced slots. The third issue is resolved in the future by low loss green tapes from DuPont.

4.2.1. Slot Phase Consideration in the Reflection Cancelled Case

By 3.4, the phase relations are known for all slotted elements. From slot segment n to slot segment $n + 1$ the simple relation of (18) describes the slot phase gap within the TWA.

⁶ from L.M. Paulsen, “A Study of and Design Procedure for Dual Circularly Polarized Waveguide Slot Arrays”, DISSERTATION, MICHIGAN TECHNOLOGICAL UNIVERSITY 2006

$$\Psi = \Delta\phi = (\phi S_{21}^n + \Delta\phi E_y^{n+1,n}). \quad (18)$$

Note that the first summand in (18) depends exclusively on n due to the acquisition of ϕS_{21} from the entire segment. The summand $\Delta\phi E_y^{n+1,n}$ considers the difference from slot n to $n + 1$. To visualize the virtual phase gaps between isolated cascaded elements that are reflection cancelled, the parameter Ψ is defined. The available range of $c_0(l)$ is sampled by $m \approx 2N$ steps and typical gaps are computed for minor slot length differences by $k = 1$ and bigger ones with $k = 3$.

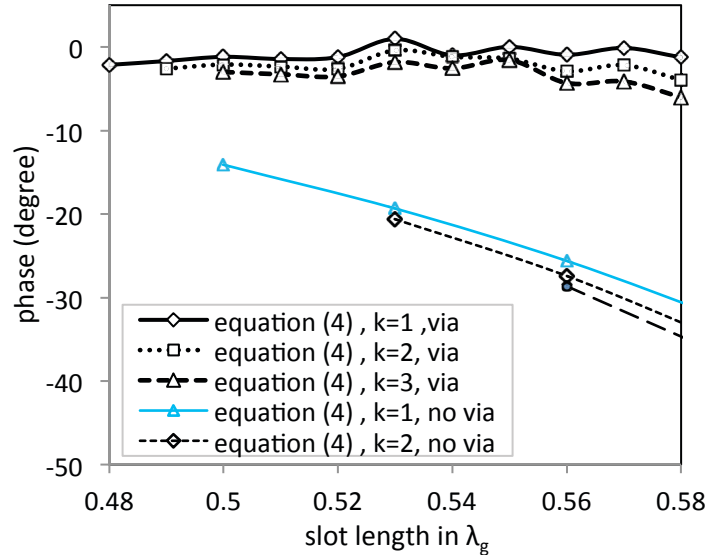


Figure 71 Equalized phase, estimation, k according to (19)

Then (19)

$$\Psi = \Delta\phi(m, k) = \Delta\phi S_{21}^{m-k} + (\phi E_{y0}^{m-k} - \phi E_{y0}^m), \quad (19)$$

results in a rather flat curve for the slot phase delta at least for $k = 1$ and 2, but even for $k=3$ the range is a few degree only, depicted in Figure 71. That is, yet with the single introduced via, the total phase gap persists but is reduced significantly when considered in the isolated case.

4.2.2. Radiation Coefficients Considering Losses

Losses in the TWA have to be reconsidered when segments of equal length but different c are applied. Each segment of a guided wavelength experiences the same decrease in power due to dielectric and SIW losses, see 2.2.2. However, the input power of each segment is *not* equal and not linearly decreasing in case of a non-uniform distribution. Thus, for each c , except for the first one, the loss

has to be considered separately. It is convenient to set up recursive equations describing the actual power ratios from one element to the adjacent one. With respect to the drawing in Figure 19,

$$\begin{aligned}
P_1 &= A C_1 = C_1, \quad \text{if } A = 1 \\
P_2 &= B C_2 = (1 - C_1)C_2 \\
P_3 &= C C_3 = (1 - P_1 - P_2)C_3 \\
&= (1 - C_1 - C_2(1 - C_1))C_3 \\
&= C_3(1 - C_1)(1 - C_2).
\end{aligned} \tag{20}$$

For P_4 , the same applies,

$$\begin{aligned}
P_4 &= C_4(1 - C_1 - (1 - C_1)C_2 - (1 - C_1)(1 - C_2)C_3) \\
&= C_4(1 - C_1)(1 - C_2)(1 - C_3).
\end{aligned} \tag{21}$$

In (22), the power ratio of the element n and $n + 1$ is called wR . Thus, the first slot has the relation

$$\frac{P_1}{P_2} = wR_1 = \frac{C_1}{\alpha_\lambda C_2(1 - C_1)} \tag{22}$$

in which $\alpha_\lambda = (k^2 \tan \delta / 2\beta) \lambda_g$ is the linear loss factor for each segment. For the second element, (23) applies and so on.

$$\frac{P_2}{P_3} = wR_2 = \frac{C_2(1 - C_1)\alpha_\lambda}{C_3(1 - C_1)(1 - C_2)\alpha_\lambda^2} = \frac{C_2}{\alpha_\lambda C_3(1 - C_2)} \tag{23}$$

Note that, in the mid-section of the array, from $n = N/2$ to N , the ratio wR_n becomes > 1 , except for uniform distribution. The generic equation is written for all $n = 1 \dots N$

$$wR_{n,n+1} = \frac{C_n}{\alpha_\lambda C_{n+1}(1 - C_n)}, \text{ for } P_{in} = 1. \tag{24}$$

In order to anticipate and/or set the correct rP , (24) shall be enhanced for a fixed value of rP . (See the ANNEX for the idea of an absorbing patch at the end). Another very important reason to set rP to a fixed value is to allow verifying the entire array behavior, i.e. especially the assumption of loss

and generated ϕS_{21} . It is not only easier to verify the magnitude against a fixed value of e.g. 0.1 than against zero, but it is virtually impossible to verify ϕ in case of an $rP \approx 0$. As a conclusion,

$$P_1 + P_2 + P_3 + \dots P_N + P_{loss} = 1 - rP. \quad (25)$$

In (25), all radiated power terms are independent from the loss which is compensated at all slots by increased radiation coefficients. However, the last slot still has a distance to the end of the array, therefore $\sqrt{\alpha_\lambda}$ is introduced for this sake, (since by definition, the first slot faces $P_{in} = 1$), so that

$$1 - C_1 - C_2(1 - C_1) - C_3(1 - C_1)(1 - C_2) - \dots = rP/\sqrt{\alpha_\lambda} \quad (26)$$

Conveniently, the complexity is reduced to the ratio of the last element P_8 and rP as wR_N . Since $AC_8 = P_8$ and $A - AC_8 = A(1 - C_8) = rP$, again this ratio is evidently independent from the input A , so that (27) applies.

$$wR_N = \frac{P_8}{rP} = C_8/(\alpha_\lambda(1 - C_8)). \quad (27)$$

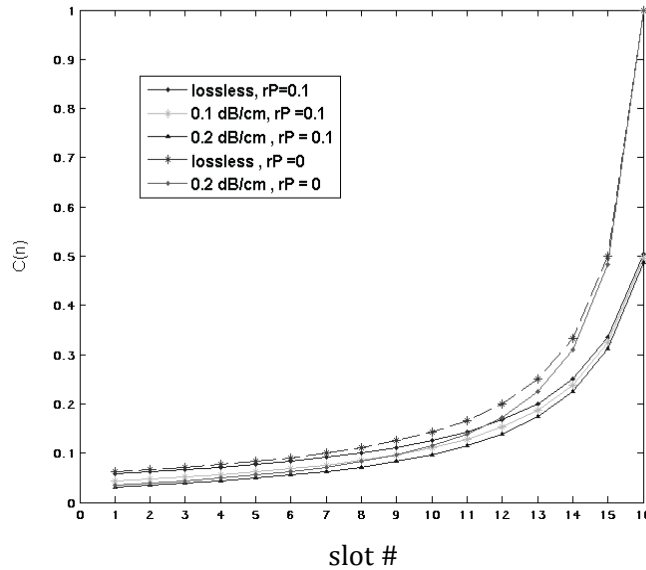


Figure 72 Radiation coefficients as a function of the slot n , parameterized for loss and rP

However, for $rP \rightarrow 0$, since $(1 - C_8)$ is in the denominator, the design procedure in MATLAB of 4.5, limits rP to a minimal value of 0.008. For $N = 16$, and with respect to (24) and (27), the results for a couple of different losses in dB/cm are depicted in Figure 72.

4.3. Alternative Configuration of the Slotted Radiating Elements in the TWA

The new alternative configuration of slotted radiating elements is based on a new way of computing P_{rad} in magnitude and phase. The magnitude is then optimized by altering solely the slot length, while the phase is readjusted as much as possible by means of vias as proposed in 3.4.2 and 3.4.3. Altering the phase by internal measures, instead of displacing slots, is very suitable for achieving a good side lobe performance and a broadside beam with less computational effort. For this sake, with respect to an initial setup in 4.4.1, a simplified yet bi-directional signal flow graph is drawn to back up the straightforward approach. Validation is carried out in 4.4 by comparing slot amplitudes of different arrays designed through different procedures with ideal desired values. Secondly, fabricated and simulated circuits are evaluated in terms of reflection and radiation performance in 4.7.

4.3.1. Design and Configuration

The TWA is traditionally designed through procedures that consider the slot as resonant. Yet, when slots are edged into substrate integrated waveguide (SIW), with a width-to-height ratio $wth \gg 1$, the slot has to be designed as off-resonant [4]. Thus, complex multi-port scattering parameters are required to describe the slotted element [5]. To some degree, design procedures that are based on 2-port S-parameters of the slotted waveguide can be applied [6, 7]. It is assumed therein that the TWA operates solely with forward traveling waves, which greatly simplifies the design procedure. However, this does not truly match the slot response for higher wth . Particularly, reflections from two or more slots that are slightly mismatched by mutual coupling (MC) are not covered.

Improvements to match the slot response for higher wth have been made in [8]. Yet, the latter relates to an antenna design with nearly standing waves, with virtually negligible phase gaps between elements. Thus, in [8], only one last element must be shifted in order to achieve equal slot excitation. Unfortunately, in the TWA, the required shift is inherently increased since slots are driven significantly off-resonant. This conventionally obliges to move the slots away from the standing wave position which implicates also deriving the mutual coupling coefficients for varying distances between elements. The entire array must be iteratively recomputed to optimize slot phases, as also in [6]. However, this approach must a priori assume pure forward traveling waves, and would lead to unreasonable computing efforts otherwise. Unsurprisingly, tested commercial antenna design software limits the complexity as well when it comes to the TWA [9].

In many cases, the resulting divergences of the State-of-the-Art with these limited models are small, e.g. amplitude errors in the range of a few dB. Often not verified or tolerated, they have been at times reported to be likely responsible for higher side lobes [10]. In contrast, the error increases in the particular case where cancelling of the individual slot reflection, e.g. by a via, is indispensable. The slot response is then in addition impacted by the asymmetric slot and via assembly. To design e.g. very low side lobes, a sophisticated algorithm must include this effect. For this sake, a different proposed matching may be applied [11], but equally necessitates moving elements and requires a very accurate matching to allow shifting slots without degradation. This might explain the results in [11], in which simply uniform aperture distribution is presented with amplitude ripples.

Thus, a more comprehensive yet simple design method for TWAs is surprisingly challenging. Mainly due to the internal slot phase delays, there is still a lack of a simple optimizable design approach for a TWA with high *wth* as well as both off-resonant and mismatched slots. Simple in the sense that it solely requires S-parameter input from one isolated and two typical mutually coupled slots, while considering reflections. Though, for the above listed reasons, this new approach can in no case be found without a greater control over the internal phase of the slotted SIW.

One previous solving approach by the authors has been to modify the phase constant β in between elements by widening and tapering the SIW, see also 3.4.2..1. However, this self-suggesting idea cannot be fully exploited due to reflections from the widened or tapered sections. Further matched slotted SIW elements offering superior freedom in the design of the complex transmission coefficient have been proposed consequently.

4.3.2. Typical Mutual Coupling in the Array and its Compensation

Unintentional mutual coupling (MC) of electromagnetic waves is present in all antenna array networks. It can be classified in external, i.e. free near field coupling, and internal feeding network coupling. In resonant slot antenna arrays the internal coupling is increased in case the alternate offset technique is used since the slot edges are closer than without alternating offsets. Elliot's design procedure for resonant arrays in [12] includes these effects in the improved version of [13].

Additionally, higher order modes caused by the excitation of the radiating slots may reach adjacent elements. One significant advantage of the proposed TWA structure is that the element distance is λ_g , thus very large, which reduces the internal coupling of higher order modes. The electrical length shall be in any case higher than the effective free wave desired distance of no more than $\lambda_g/2$, as for instance also in [14].

External coupling is influencing the effective radiation of each element. Each slot in the TWA receives power from adjacent slots and delivers this power to the left and right neighbored segments. For two elements, a typical pattern generated by MC between element $n + 1$ to n is depicted in Figure 73 and Figure 74. An MC model drawn in Figure 75 shows the four considered normalized MC waves. By superposition, these MC terms alter the isolated obtained slot S-parameters.

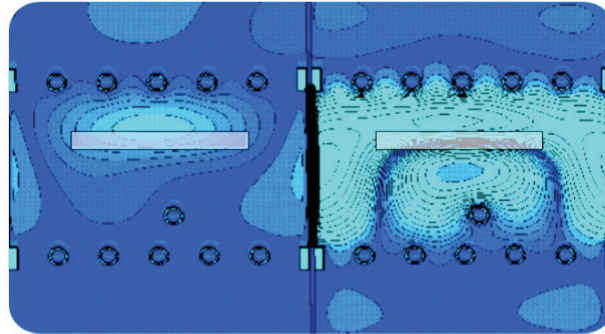


Figure 73 Typical SIW mutual coupling field produced in the first element by exciting the second

Figure 76 depicts the typical evaluated MC coefficients for the four possible combinations of minimal and maximal slot length when the via is included in the design. Unlike in [6], a strong impact of the 2nd slot length l_2 on the involved parameters is observed. While less influencing the magnitude, the phase is highly affected and thus, these MC contributions cannot be neglected.

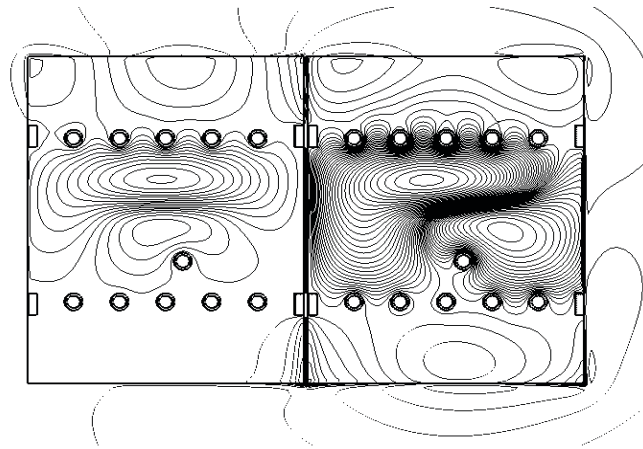


Figure 74 Mutual Coupling of two elements

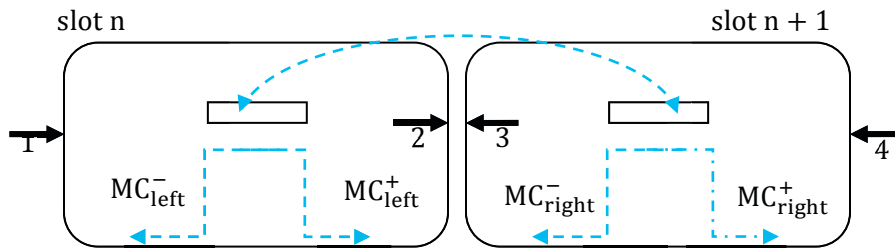


Figure 75 Mutual coupling characterization: model with 2 slots and 4 ports

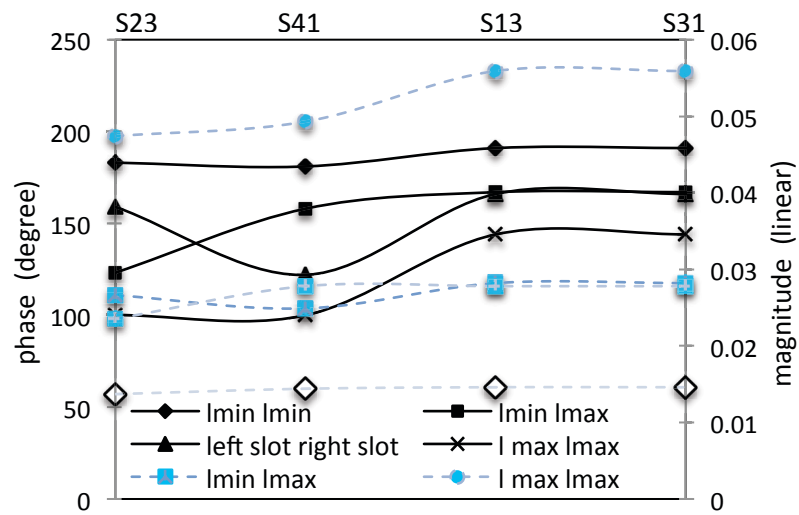


Figure 76 Mutual coupling coefficients for four different slots, (from left to right for each coefficient)

In the frequency domain, the drastic impact on one particular length of $\lambda_g = 0.5175$ with another slot of the same length with approximately $\lambda_0/2$ apart is depicted in Figure 77. Both bandwidth and

effective length of the slot are impacted. In the occurring case, the slot appears to be longer and compensation, if the impact is correctly determined, would be possible by choosing a *shorter* slot.

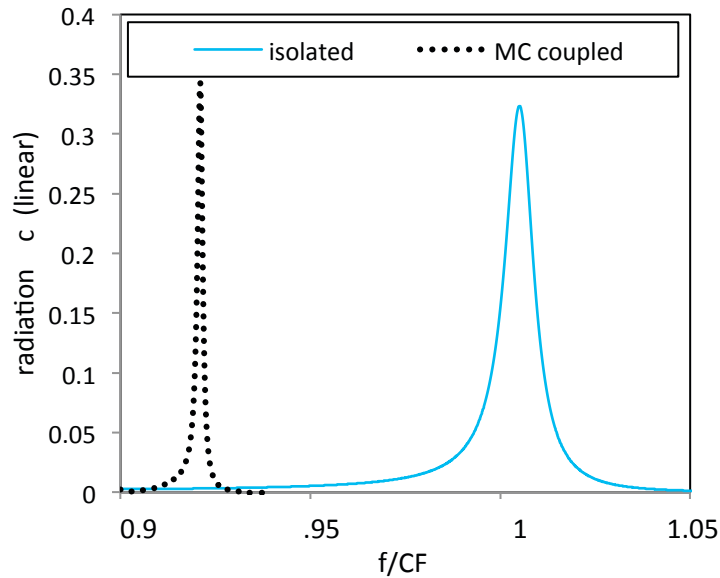


Figure 77 Impact of mutual coupling in the frequency domain

Fortunately, the interpolation of MC for different slot lengths becomes very accurate due to a quite predictable result when using *equidistant* slots. This advantage is essential. If the interval of l is carefully chosen to be below maximum radiation, the use of interpolation is sufficiently precise.

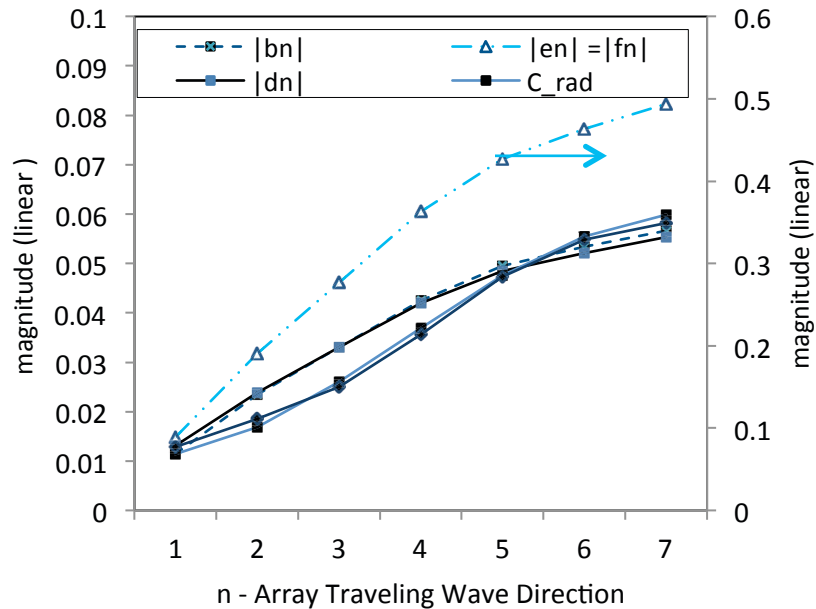


Figure 78 Mutual Coupling and S_{22} along the array, magnitude

For instance, the MATLAB function `interp2()` can be used in order to interpolate all length constellations in the interval of the minimal and maximal length. The magnitude of the MC for different lengths along a typical TWA is depicted in Figure 78. The phase is shown in Figure 79.

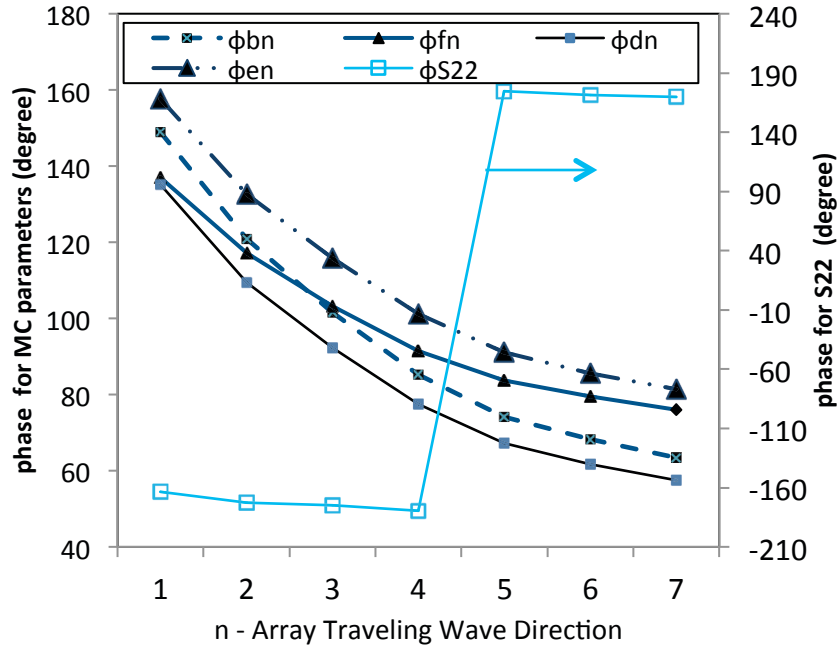


Figure 79 Mutual Coupling and S_{22} along the array, phase.

4.3.3. Dual Excitation of the Slotted Element

The coupling causes backward and forward contributing waves. A model for a TWA shall be enhanced by this excitation from both sides of an element.

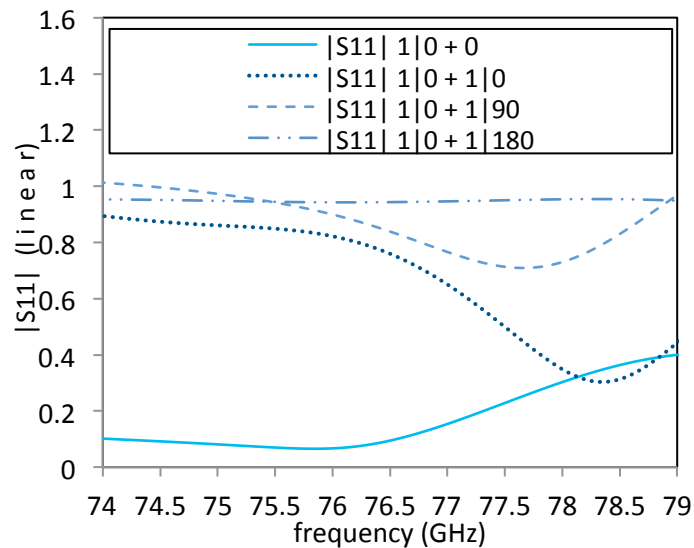


Figure 80 One enhanced element excited from either side, $|S_{11}|$

To quantify the impact of the dual excitation, Figure 80 depicts the result for $|S_{11}|$ for different sums of excitation, respectively $A = 1, B = 0$, $A = 1, B = 1$, $A = 1, B = 1j$ and $A = 1, B = -1$ with respect to Figure 19.

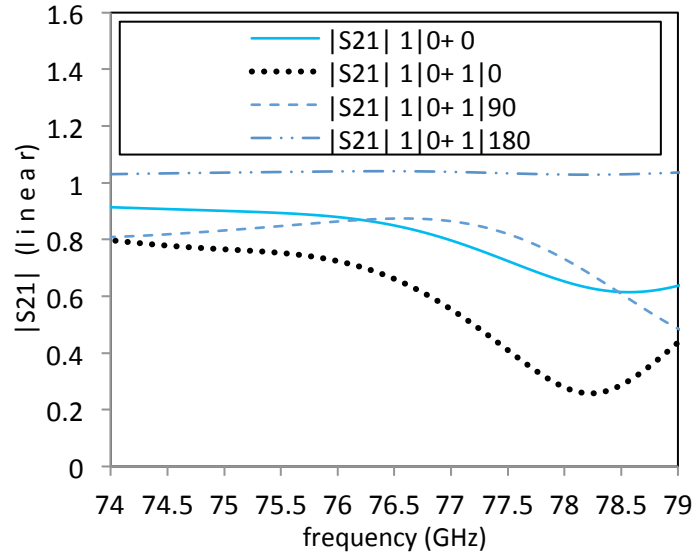


Figure 81 One element excited from both sides, transmission coefficient

It is obvious, in particular from Figure 81 where S_{21} is depicted, that excitation cancels out for opposite phase, and vice versa. More important is the impact on ϕE_y which is shown in Figure 82.

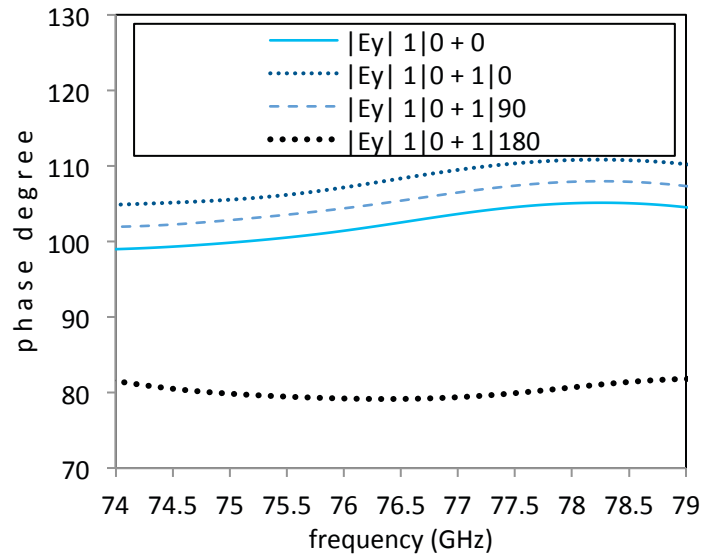


Figure 82 One element excited from both sides, slot phase

To conclude, the excitation from backwards traveling waves may alter the result and is mandatory to be considered in the following.

4.4. Modeling of the New TWA Configuration Applying an SFG

4.4.1. Sequential Linear Full Model of the TWA (Rule of Mason)

When modeling two port linear networks, a signal flow graph is straightforwardly drawn, i.e. can be considered as a direct mapping of the transmission line theory with ingoing and out coming normalized waves represented by arrows of an input and output direction. Nodes represent sums. Pure reflections that add up to the their original node are depicted as loops.

The Signal Flow Graph (SFG) is not a comprehensive replacement of the complex normalized wave theory. In order to determine the power absorbed by a port, or to derive the standing wave ratio at a certain position, multiple nodes have to be evaluated together. For instance, the S-parameter S_{11} is derived from the signal at the reflected node divided by the fed incident wave, i.e. node.

An SFG is applied in lieu of the full mathematical expressions where a wider cascaded or otherwise widespread network of different sub-elements has to be evaluated. It is thus necessary to have a closed form procedure to derive all considered nodes, mostly the input and output ports. These rules have been described and setup by Mason in [15].

In Figure 83, a five node signal flow chart for one *isolated* slot segment is drawn. The transmission line in between elements for this TWA is represented by 1 since $d = \text{constant}$ at this design. Segments are cascaded in a row in order to form an array. Applying the rule of Mason, the transfer function from the input node to every other node can be computed. The sink represents radiation.

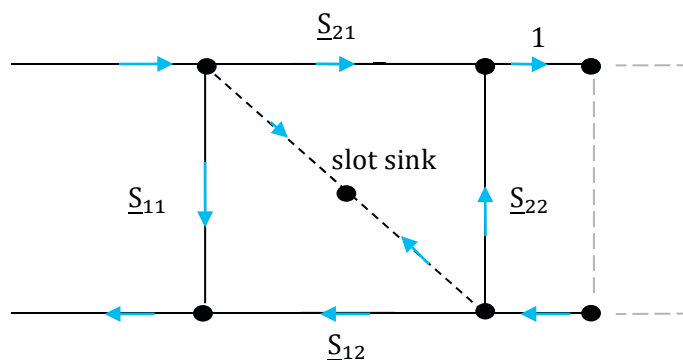


Figure 83 A single isolated slot signal flow chart

The model includes recursive paths yielding a quotient as transfer function which is, however, still computable for $N = 8$. The input reflection for $N = 4$ is e.g. computed by (28) if the simplifications $S_{11} = S_{22}$, $S_{21} = S_{12}$ are made.

$$\Gamma_{in} = \frac{S_{11}(S_{11}^2 - S_{21}^2 - 1)(S_{11}^4 + S_{21}^4 - 2S_{11}^2 - 2S_{21}^2 S_{11}^2 + 1)}{(S_{11}^3 - S_{21}^2 S_{11} - S_{11}^2 - S_{11} + 1)(S_{11}^3 - S_{21}^2 S_{11} - S_{11} + S_{11}^2 - 1)} \quad (28)$$

The residual power at the end of the SIW would be

$$S_{21} = \frac{S_{21}^4}{1 - S_{11}^6 + S_{11}^4(2S_{21}^2 + 3) - S_{11}^2(+2S_{21}^2 + S_{21}^4 + 3)} \quad (29)$$

However, the above outlined SFG lacks the MC relation and cannot consider any interaction between elements. The next Section revises this SFG and proposes an enhanced format for the TWA.

4.4.2. Enhanced Antenna Array Design

To model the antenna array, a cascaded SFG that considers external mutual coupling from two adjacent elements is drawn in Figure 84. Since S_{11}^0 can be kept very low due to the procedure and rules of 3.4.1, it can be neglected in the first place. S_{22} on the other hand is of substantially higher values,

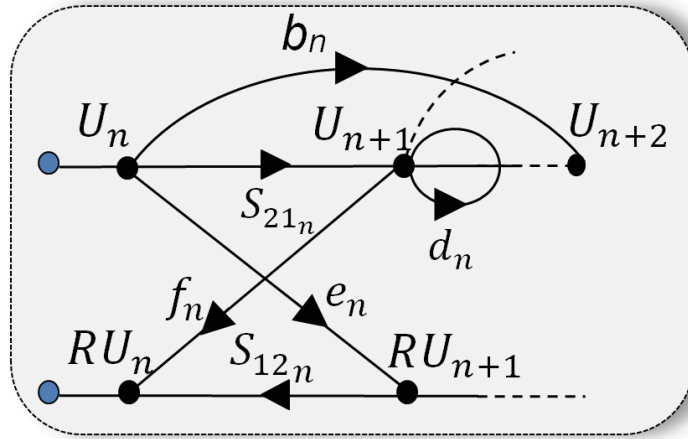


Figure 84 Signal flow graph for the antenna array design, the parameters are defined in Figure 85, $S_{12/21}$ are based on the isolated slot characterization

but the reflected waves that occur at the output port are much below the input power, thus, it is neglected equally. The coupling factors are termed b_n, d_n, e_n and f_n and are defined in Figure 85, each for a pair of two slot lengths from the origin to the sink. To better demonstrate the relation between n and $n + 1$, the parameters are substituted by (30),

$$\begin{aligned}
 f_n &= S_{13}^{n+1 \rightarrow n} \\
 e_n &= S_{31}^{n \rightarrow n+1} \\
 b_n &= S_{41}^{n \rightarrow n+1} \\
 d_n &= S_{23}^{n+1 \rightarrow n},
 \end{aligned}
 \tag{30}$$

with the coupling direction in superscript. However, care should be taken to the correct order of the elements when deriving (30) numerically. Note that in Figure 85, for better readability, the arrows are not fully drawn back to the source, but are in all cases originated in the next adjacent slot.

All other internal and external coupling is neglected. The coefficients are numerically obtained from two-slot characterization with a couple of typical slot lengths for the 1st and 2nd element. The results are interpolated; see also 4.5. In general, coupling coefficients of two adjacent slots may be derived as in [16] where the real and imaginary parts of the coupling coefficient is depicted.

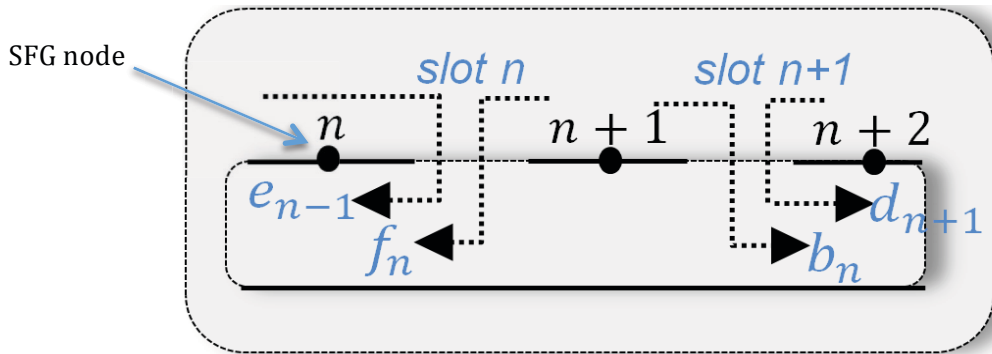


Figure 85 Definition of mutual coupling coefficients b_n, d_n, e_n and f_n , as also used in the MATLAB script (see the ANNEX)

In the SFG, each slot n holds input and output nodes, and a pair of excitation nodes U_n and RU_{n+1} to derive the total sum of radiation, which is the product of accumulated feeding and the radiation coefficient. Notably, backwards traveling waves RU_n are contributing differently to the slot as dis-

cussed earlier and must be considered in detail. The inherent slot phase ϕE_y^n , i.e. the phase between the feeding SIW dominant mode and the perpendicular electrical field in the slot n , differs for either side of excitation. In particular, for longer slots $> 0.55\lambda_g$, the difference between left and right excitation $\left| \phi E_{y, left}^n - \phi E_{y, right}^n \right|$ is well $> 20^\circ$ as depicted beforehand in Figure 39. For superposition, both U_n and RU_{n+1} have to be ‘delayed’ by the appropriate ϕE_y , and weighted with (the same) c_0^n to obtain the sum of radiation.

Up to this point, the signal flow graph considers mutual coupling solely as a contribution to the input and output nodes. This is where the direct impact on the in-coupled slot shall be also counted in, unlike [6], where the slot phase is cut down to a fixed relation with the effective radiation coefficient c . For instance, the path b_n in Figure 85 couples through slot $n + 1$ and contributes to node $n + 2$, but also impacts slot $n + 1$ itself. To derive this additional slot ‘excitation’, the b_n path obtained at $n + 2$ needs to be de-embedded to $n + 1$. Since $\phi E_{y, right}^{n+1}$ and c_{n+1} of the isolated slot are known, this is approximately feasible.

Once solved, the SFG aids to optimize the array by varying l_n (see MATLAB script) until sufficient match with the desired amplitude is accomplished. Next, phase delays are reset as proposed.

4.4.3. The Approximate Solution of the Signal Flow Chart

The *forward* path, carrying the incident traveling wave, receives coupling from adjacent elements by b_n and d_n , which also travel in positive direction. However, a backward traveling path accumulates the negative traveling coupling terms f_n and e_n . The occurring reflection from each element is solely fed by MC, since the isolated S_{11}^0 is very low.

As a result of the presence of the backward path, the model can handle partly non-matched constellations in the element. Referring to Figure 84, a (typical) ratio of $RU_n/U_n > 0.3$ can be assumed, and this for perfectly matched elements when isolated.

Circumventing the self-loop (d_n) in the SFG forward path is advantageous, so that the transmission coefficient becomes

$$x_n = \frac{S_{21}^n}{1 - d_n}, \text{ without loss} \quad (31)$$

$$x_n = \alpha \frac{S_{21}^n}{1 - d_n}, \text{ where } \alpha \text{ is the loss,}$$

For sake of optimization, a forward node transfer function U_n , can be defined by

$$U_n = \begin{cases} 1, & \text{for } n = 1 \\ x_1, & \text{for } n = 2 \\ (U_{n-1})x_{n-1} + b_{n-2}U_{n-2}, & \text{for } n \geq 3 \end{cases} . \quad (32)$$

The backward path function is composed by starting from the end of the array, i.e. $n = N + 1$. Backscattering into the last element is zero, thus the node function at the end is

$$RU \equiv 0., \quad (33)$$

Alternatively, a small realistic reflection S_{11} absorber can be allowed. Next, the most adjacent element $n = N$ is described recursively from the forward string as

$$U_{N-1}e_{N-1}, \quad (34)$$

since this node is fed solely from right coupling e_{N-1} . Remember that U_{N-1} is entirely known from (32). For all following nodes towards $n = 1$, the right and left contributing branches are added,

$$U_{n-1}e_{n-1} + U_{n+1}f_n + S_{12}^n RU_{n+1}. \quad (35)$$

Written in one expression,

$$RU_n = \begin{cases} 0, & \text{for } n = N + 1, (\text{matched}) \\ S_{11}^{absorber}, & \text{for } n = N + 1 (\text{unmatched}) \\ U_{N-1}e_{N-1}, & \text{for } n = N \\ U_{n-1}e_{n-1} + U_{n+1}f_n + S_{12}^n RU_{n+1}, & 1 < n < N \\ U_{n+1}f_n + S_{12}^n RU_{n+1}, & \text{for } n = 1 \end{cases} \quad (36)$$

Nevertheless, S_{22} is yet unconsidered. Based on experience, a criterion for neglecting S_{22} of $|S_{22}|^2 > 0.1$ may be useful, its consideration is part of the future work.

Straightforwardly, the reflection of the array can be estimated from computing the ratio of $RU_1/U_1 = S_{11}$, as well as for the $rP = S_{21} = U_N/U_1$. For each element n , there is a pair of excitation nodes, U_n and RU_{n+1} . Thus, the slot excitation signal depends on

$$V_{TE}^n = U_n e^{j\phi E_{yleft}^n} - RU_{n+1} e^{j\phi E_{yright}^n}. \quad (37)$$

As stated earlier, in case $|S_{22}|$ becomes significantly higher than $|S_{11}^0|$, RU is slightly altered and the reflected wave might be subtracted from RU_{n+1} , which is future work. However, its influence stays small in off-resonant conditions.

RU_n depends strongly on n and does not decrease in the same way U_n decreases. Thus, a different fraction of the supposed incident power is even accepted at each element. The phase alteration caused by the backscattered wave RU_n varies as well over n .

Equation (38) defines the intermediate power as radiated by the slot, based on U_n and RU_{n+1} .

$$P_{TE}^n = C_0^n |V_{TE}^n|^2 e^{j\phi(V_{TE}^n)} \quad (38)$$

Subsequently, the two remaining nodes of the actual element, U_{n+1} and RU_n , are considered. They depend on the in element n received MC. De-embedding is carried out to the position of the slot. Moreover, in order to solely account for the energy received at the actual element n , one earlier node is subtracted in the definition of the slot excitation.

$$\begin{aligned} V_{MC^-}^n &= (RU_n - RU_{n+1} S_{21}^n) \cdot e^{-j\phi E_{yleft}^n} \\ V_{MC^+}^n &= (U_{n+1} - U_n S_{21}^n) \cdot e^{-j\phi E_{yright}^n} \end{aligned} \quad (39)$$

Without the radiation coefficient c , $P_{MC^\pm} = |V_{MC^\pm}|^2 e^{j\phi V_{MC^\pm}}$, and thus the sum of all three is the actual radiated power, as

$$P_{rad}^n = |P_{TE_{10}}^n + P_{MC^-}^n + P_{MC^+}^n|, \quad (40)$$

whereas the actual phase is directly derived, (due to the definition of ϕE_y), from

$$\phi P_{rad}^n = \phi(V_{TE_{10}}^n + V_{MC^-}^n + V_{MC^+}^n). \quad (41)$$

The relevant phase relations in the previous equations are now illustrated for better understanding in Figure 86. The nomenclature of Figure 86 is the following: The black variables describe the inner phase delays of the dominant mode propagation. The blue arrows describe the free wave delays. ‘*in*’ describes the input phase of element one, ‘*slot*’ is the actual phase at the 2nd slot and ‘*out*’ the output phase. The left Figure depicts the case of two adjacent elements of two *different* lengths whereas the right Figure describes the equal slot length case. It is obvious that *out* in the first case differs from *out* in the 2nd case.

The coupling receives the phase delay ϕE_y from free wave to guided wave indeed two times, at $(n - 1)$ and (n) , depending on the length of both involved slots. The incident dominant mode also experiences this phase when the slot (n) is excited. The relevant phase relation is visualized as the delta between the *slot* and the TE_{10} arrow. ϕS_{21} is not considered in the Figure, but the shift of X° stands for additional accumulated shifts considered in the model of Figure 85.

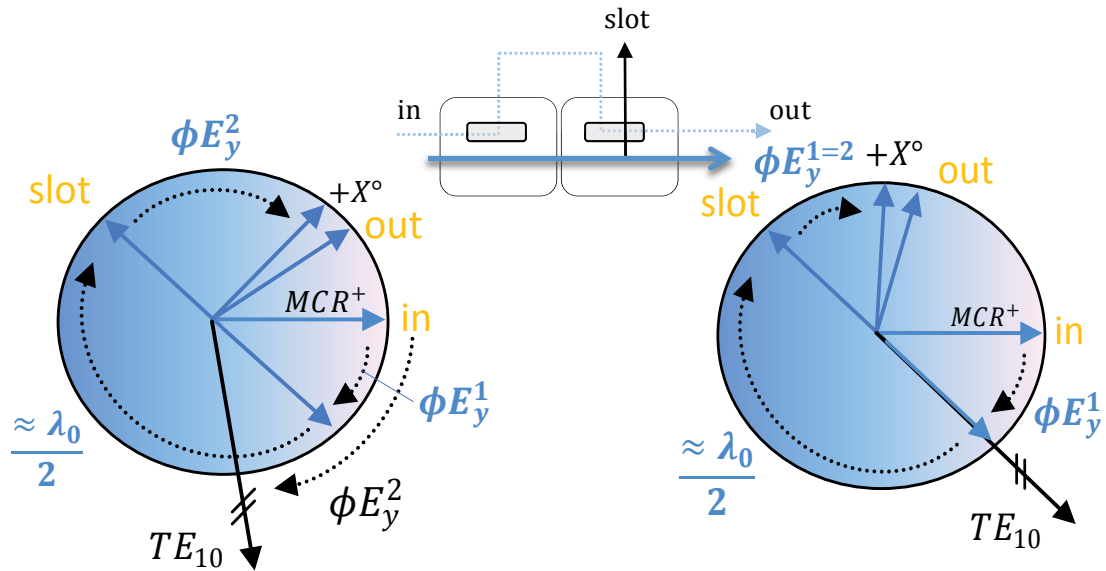


Figure 86 Phase relation for (left) unequal slot lengths, (right) equal slot lengths

4.4.4. Simplifications of the TWA Model and their Limitations

The proposed SFG is a compromise to a full S-parameter network and certainly contains limitations. The simplifications are mainly the consideration of coupling from only *two* adjacent slots, and reflections that are solely mutual coupling based. It has its limits where a) mutual coupling from two

slots apart is significant. Thus, in all cases a high ϵ_r in combination with a long segment of about λ_g is preferred to reduce MC. It is further b) neglecting the 2nd reflection at the output port of each segment and c) not taking into account that remaining S_{11} can occur from the isolated element, too.

Although the proposed model is simplified and partly sequential, it yields a much higher precision compared to a full negligence of the negative traveling terms. The necessary condition, however, is a very low S_{11}^0 , i.e. care should be taken to the thoughts of 3.4 on the matching procedure.

4.4.5. Validation

Beside radiation pattern, the straightforward concept shall be validated in terms of divergence between the effective and desired amplitude aperture distribution. For this sake, an array with $N = 4$ is designed in three different ways with the common goal of defined 'ideal' slot amplitudes. The resulting slot lengths are used for simulation in HFSS. In Figure 87, the effective simulated power at each slot center is compared to the desired 'ideal' one. The simplest design procedure called 'initial' disregards all mutual coupling entirely, i.e., derives the effective slot radiation from the isolated slot. This leads, unsurprisingly, to a bad result compared to the desired 'ideal'. On the other hand, the two key central slots radiate as desired, i.e. equal, when designed as 'proposed', but differ noticeably by 2 dB with latterly discussed simplified presumptions of other 2-port models, see 'forward'. This is mainly related to the neglected strong alteration by mutual coupling based reflections. One small remaining issue with all approaches is a slightly too high slot #1 power due to the neglected minor S_{11} after reflection cancelling.

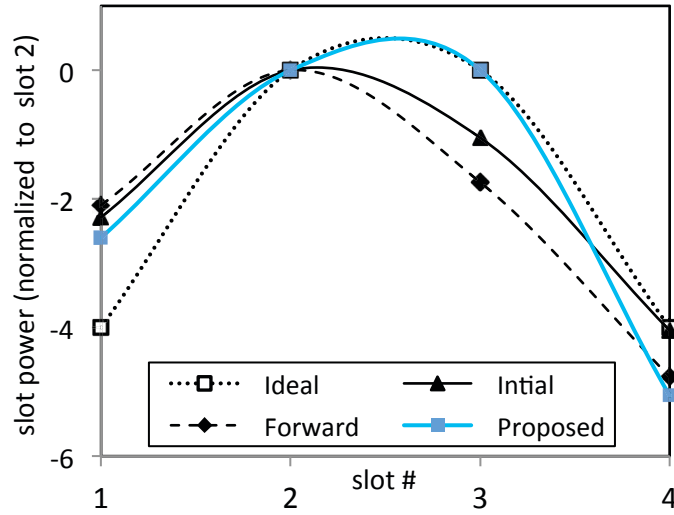


Figure 87 Model validation in terms of divergence from the ideal slot amplitudes

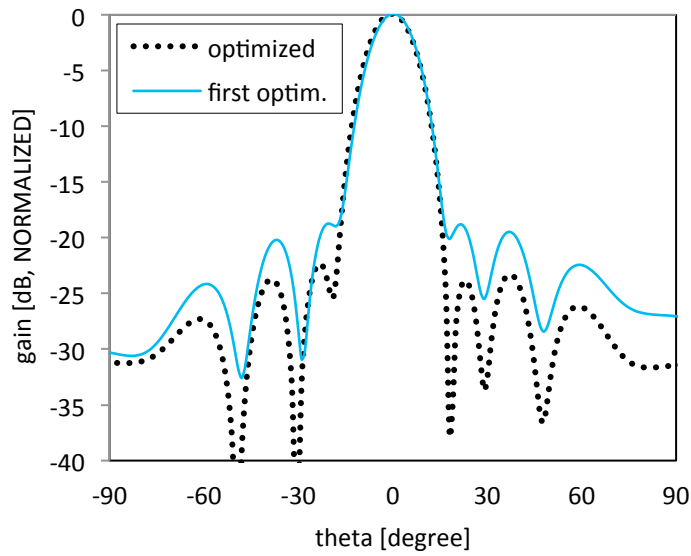


Figure 88 Validation #2 optimized pattern side lobes

A simpler validation is presented in Figure 88 where side lobe levels are depicted substantially lower if the level of optimization is increased; see 4.5.1 for a typical optimizer run. The ‘first optim.’ is achieved early in the optimization procedure.

4.5. Matlab Application with Graphical User Interface

To comprise all design procedure steps including the solution of the SFG of the previous Subsections, a script has been written in the commercially available mathematical language MATLAB [17] and fully published in [19].

4.5.1. Concept and Implemented Flow Chart

The MATLAB implementation allows designing traveling-wave antennas via the novel procedures proposed in 3 and 4. Based on the provided slot characterization results, it computes all necessary steps including the optimization. The flow chart in Figure 89 outlines the main functions of the script. Further details on functions that are not listed be found in the ANNEX where the full script is provided. In the latter flow chart, the isolated and two coupled slot S-parameter and coupling coefficients, as defined in 3 and 4, serve as the starting point. Subsequent to computing an initial guess of slot magnitudes and slot phases, the deviations to the ideal values are computed and iteratively optimized.

4.5.1. The Optimizer Function

The optimizing function eliminates the impact of reflections and mutual coupling. Its basic error criterion is linked to the ideal values, stored in w , by (42).

$$\text{err} = \text{abs}((1 - (\text{xcorr}(\text{rad_pow}, w, \text{'coeff'})))) \quad (42)$$

The total computed radiated power rad_pow is cross correlated with the ideal amplitudes of w , the optional `'coeff'` is enabled in order to receive the result in the range of 0 and 1. Thus, (42) yields zero for no deviation from the ideal amplitudes. The MATLAB function `fmincon()`, part of the `optimizer toolbox` [18] has been selected to minimize err . The latter function has the advantage of an arbitrary number of iterations, variables and flexible boundary conditions.

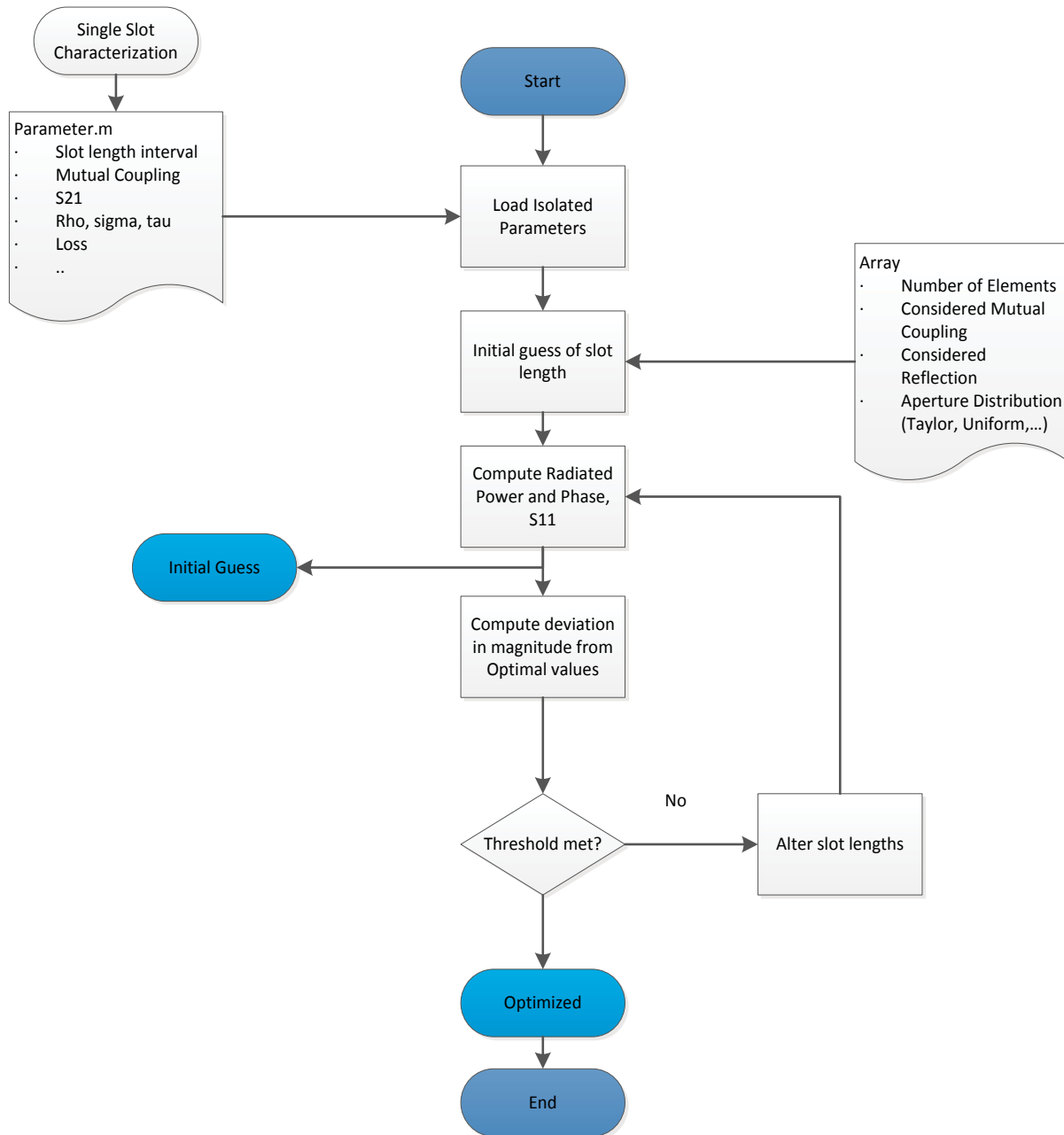


Figure 89 Flow chart of the MATLAB script

It is called with a mandatory `start` value, which is conveniently taken from the initially derived ‘initial guess’ slot lengths before considering MC. The total call is documented in (43).

```
fmincon(@pow_err, start, A, b, [], [], [], [], [], options) (43)
```

A typical output of the optimizing function is depicted in Figure 90. A moving average filter for sake of filtering spikes is applied. These spikes are generated by arbitrary alterations of the slot length. The function approaches the final result within about $N \cdot 30$ runs. It is advantageous to multiply the output of the cross correlation (42) by a factor in order to benefit from an increased dynamic.

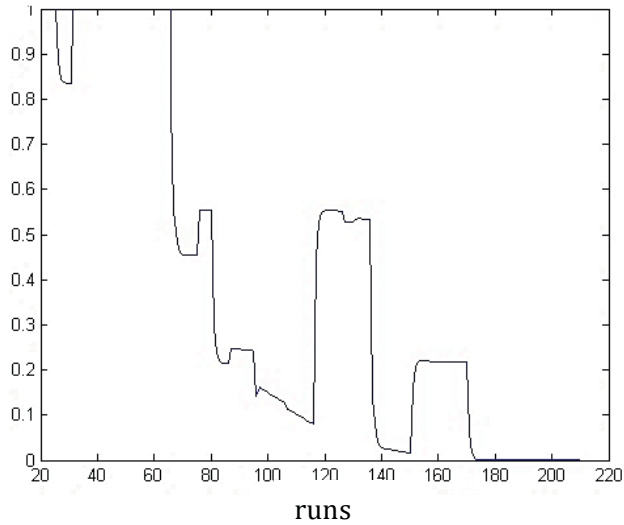


Figure 90 A typical optimization procedure for $N = 4$, y-axis depicts the deviation from the optimum, ('noise' of the function suppressed)

4.5.1. Parameter File and Data Structure

Table 1 lists the relevant parameters that are used in the structured matrix called `parameters` in the script. It is loaded by `loadParameter()`. One field has been reserved for future use.

Table 1 Parameter Matrix Order

1	2	3	4	5	6	7	8	9	10	11	12
ϕE_y^{left}	ϕE_y^{right}	S_{11}	S_{21}	S_{22}	b_n	d_n	e_n	f_n	x	C_0	<i>R.F.U</i>

4.5.2. Graphical User Interface

A graphical user interface is added for convenience, depicted in Figure 91. The tool provides a rough estimation of the compared radiation pattern, generated by the `ffit()`, see Figure 92.

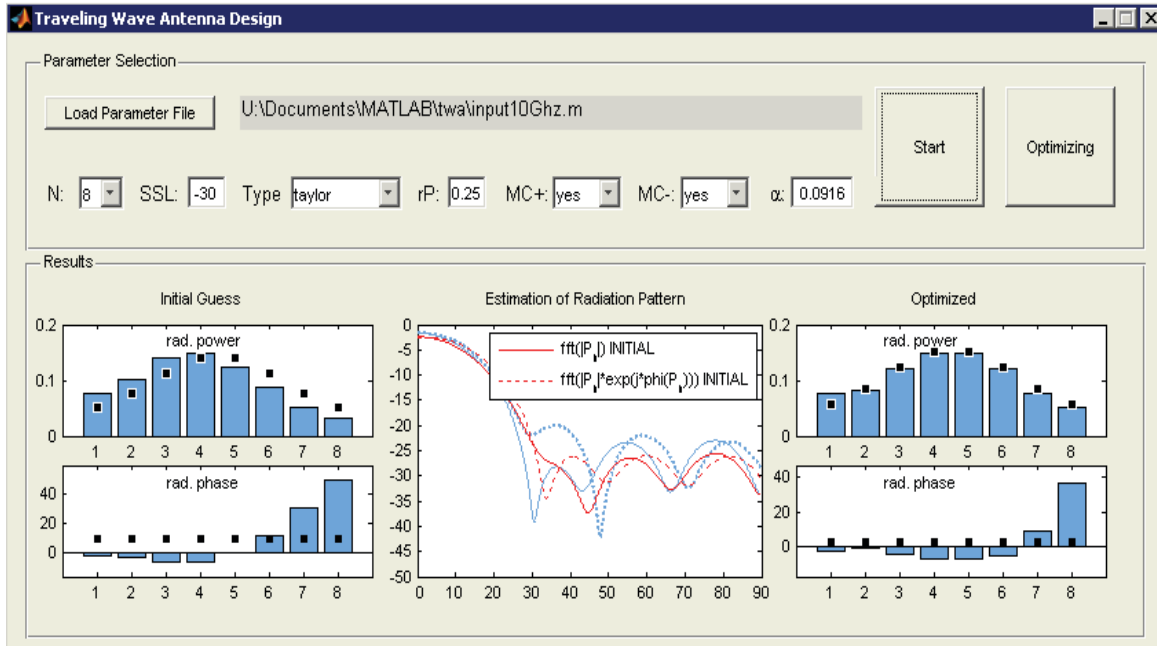


Figure 91 GUI of the Matlab Script

4.5.1. Design Example

In order to run a full design with this script, preparations and steps to be carried out are: First, a simulation of a single slot shall be done within a reasonable range of two slot lengths. Secondly, these two slot lengths min and max are both applied in the two slot characterization, generating the MC coefficients for all four possible constellations min/min , max/max , min/max and max/min . These results are stored in the format provided in the HELP text as a .txt file and loaded into the GUI. Next, the aperture distribution and losses in dB/cm are selected in the GUI and finally the optimization is enabled if desired. This is sufficient to start the script with the button `start`.

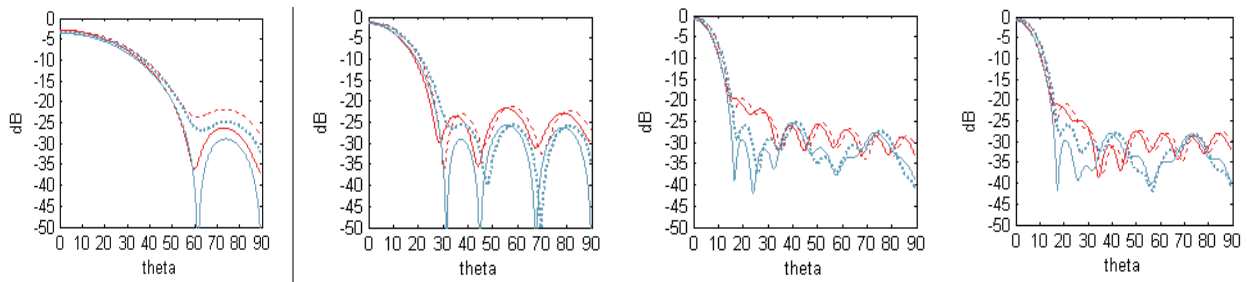


Figure 92 Typical result of the tool with comparable curves before and after optimization

4.6. TWA Radiation Pattern Measurement Setups

4.6.1. Impressions from the First Setup

The setup has been prepared for radiation pattern measurements applying the transition described later in Chapter 7. It is connected by WR12 adapters. Impressions are provided in Figure 93.

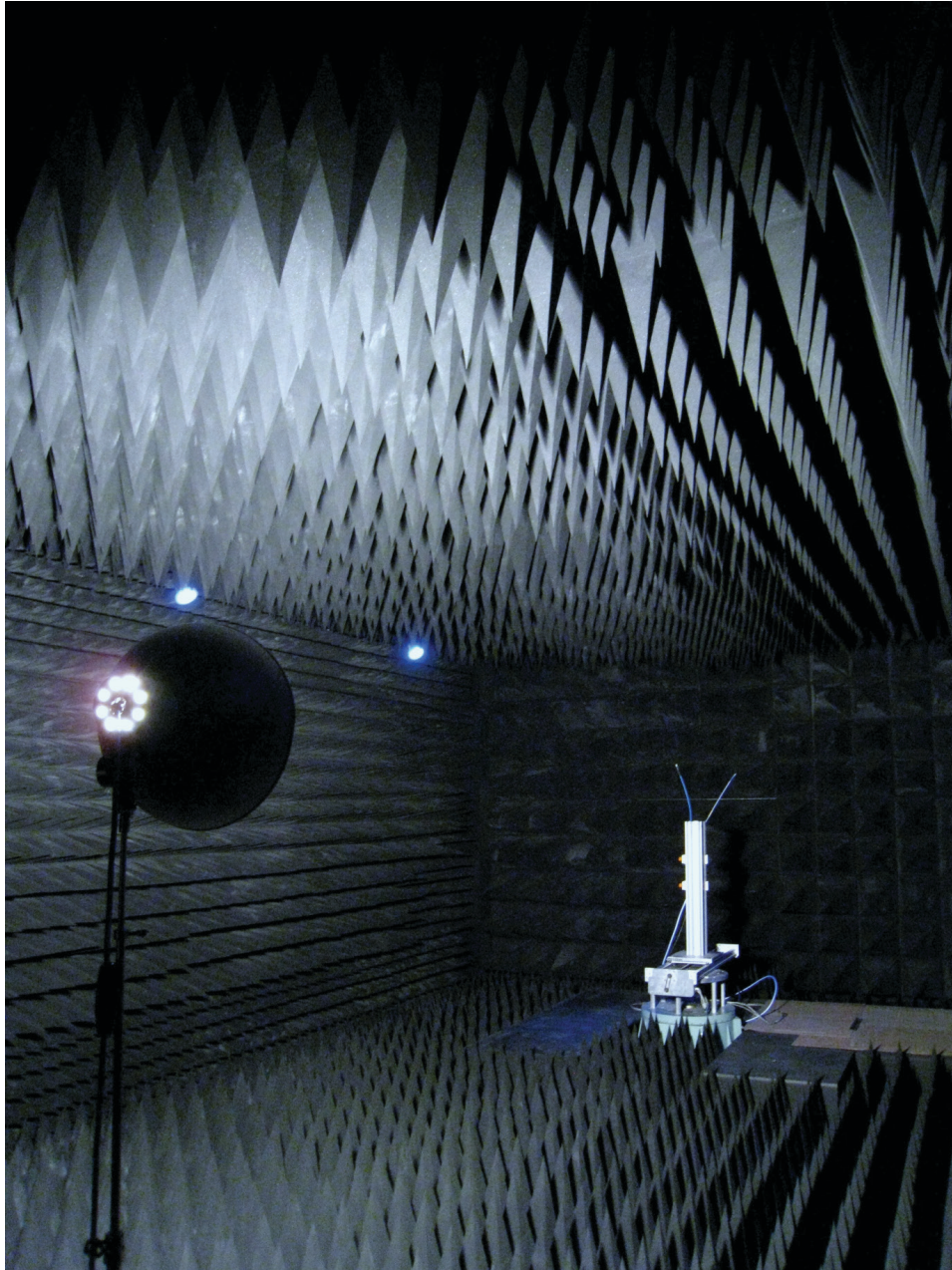


Figure 93 Radiation pattern measurement in the anechoic chamber

4.6.2. Second Setup using Power Diodes

In addition, a 2nd measurement setup has been prepared for millimeter wave measurements with power diodes and a horn antenna. The second setup has been partly constructed for this thesis⁷. It is schematically depicted in Figure 94, a picture is given in Figure 97. It is limited, however, in its adjustable angle, unfortunately.

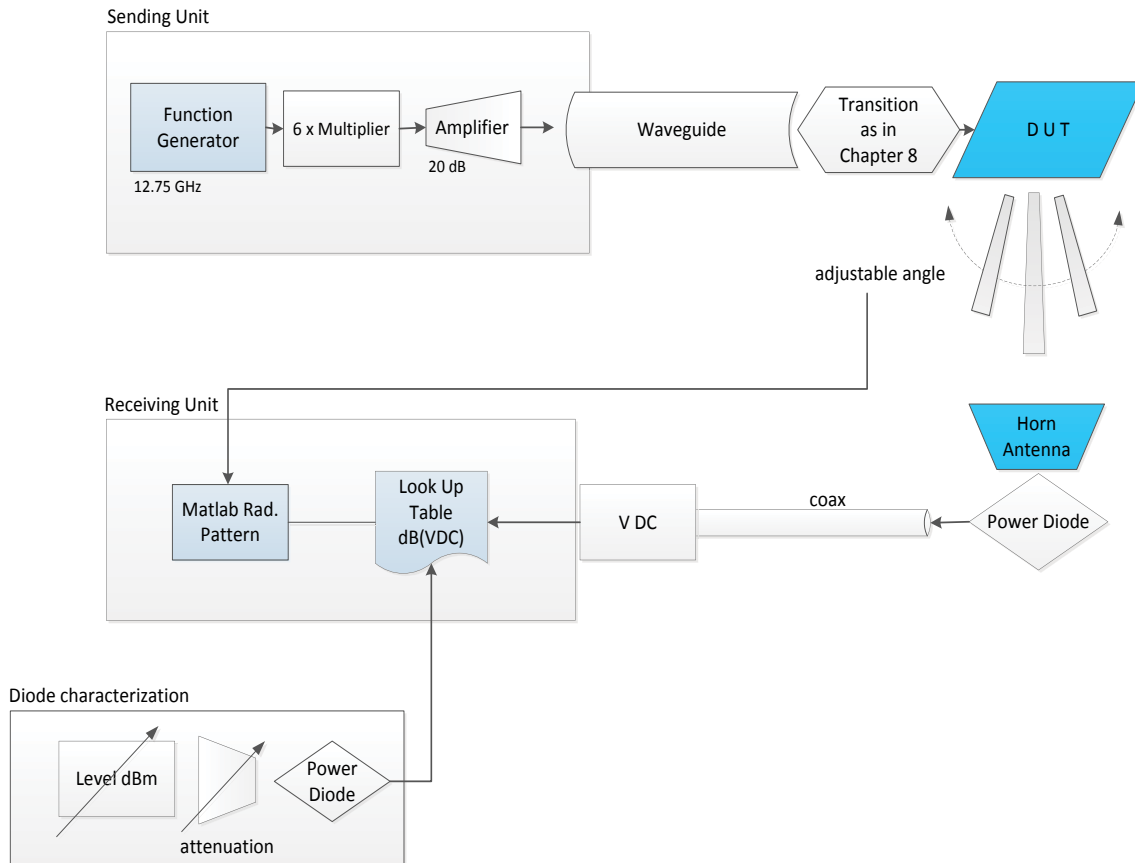


Figure 94 Self-made radiation pattern measurement set up at the EMT-INRS

4.6.3. Power Level Diode Characterization Curves

The power diode characterization, (see Figure 94 for the diode purpose), has been done for two diodes to derive the actual power level at the receiving port. First, the diode with the Serial Number #2k804109 has been characterized. It shows the behavior for low power, see Figure 95. For future

⁷ based on work of Alexandre Perron, PhD

use, Figure 96 depicts in addition the full range of the diode S/N #2k804111. Matlab functions as look up tables have been written in `DiodeLev()`.

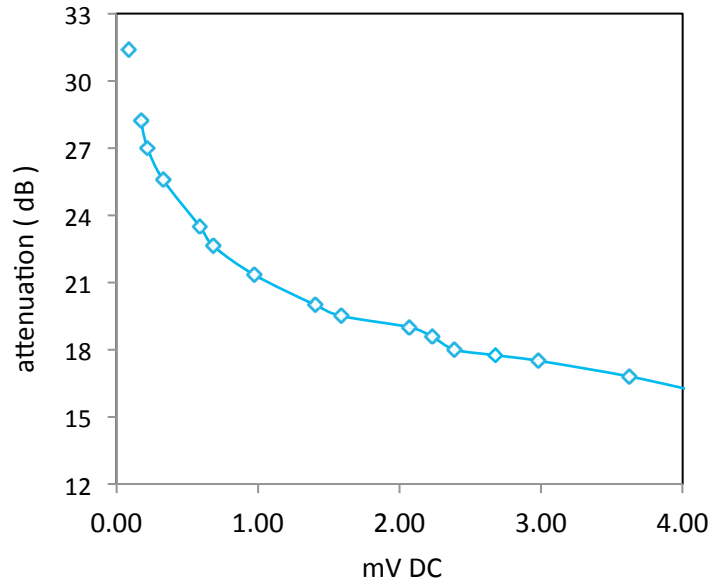


Figure 95 Low Power Curve for Diode #2k804109

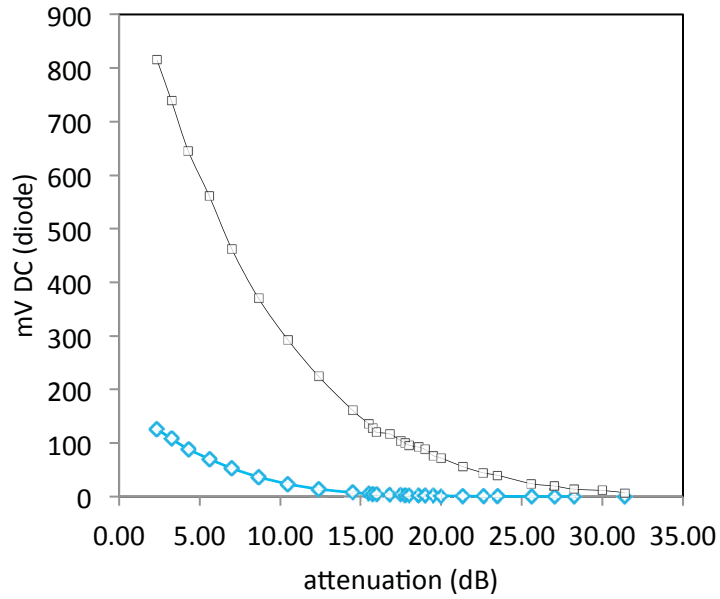


Figure 96 Full range, diode #2k804111 and #2k804109 (blue)



Figure 97 Entire setup with excitation and reception



Figure 98 Fixation holding the antenna, surrounded by absorber material

4.7. Results and Discussion

To prove the concept and feasibility of the proposed design procedure, antenna array circuits for the 77 GHz millimeter-wave band have been fabricated, see Figure 99 and Figure 100, and measured with a transition to waveguides and a mechanical fixture, proposed further below in Chapter 7. The general circuit parameters for Dupont 951 are SIW width $a_0 = 1.235 \text{ mm}$, height =

0.21 mm, $\epsilon_r = 6.8$, (this value is differing from the nominal value, the observed 'dispersion' is derived in Chapter 7 by measurements), via radius $r = 0.075$ mm and pitch $p = 0.326$ mm, with $N = 4$ and 8 slotted elements. Due to the individual element optimization, the total performance in terms of $|S_{11}|$ for the $N = 4$ is very good, despite many introduced additional vias, which is presented in Figure 101, in which simulation and measurement well agree. ($N = 8$ unfortunately had mechanical issues.)

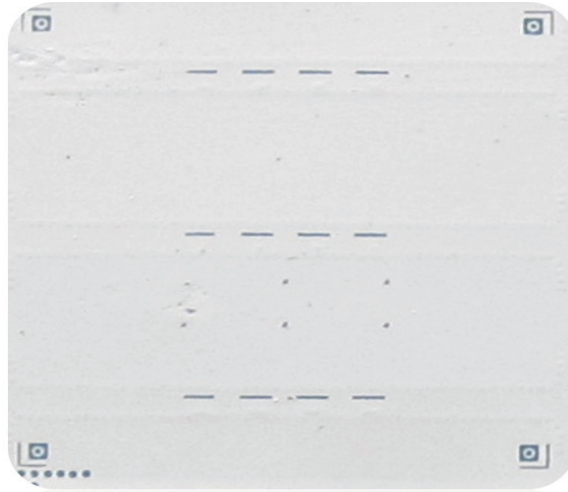


Figure 99 Produced slot antenna array with $N = 4$, the transition conceived in Chapter 7 is applied on both sides

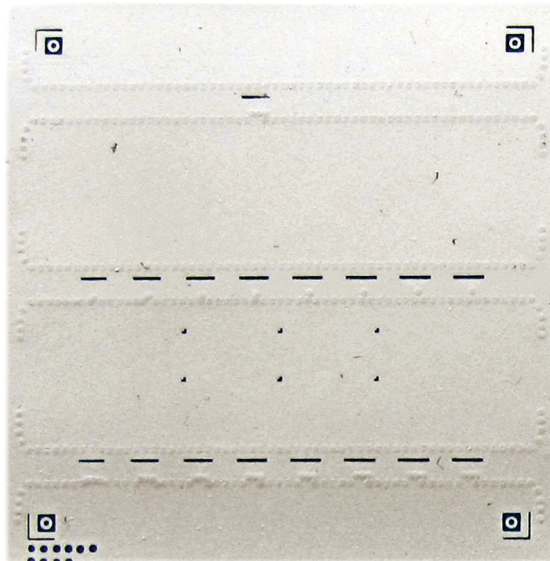


Figure 100 Produced slot antenna array with $N = 8$, the transition conceived in Chapter 7 is applied on both sides

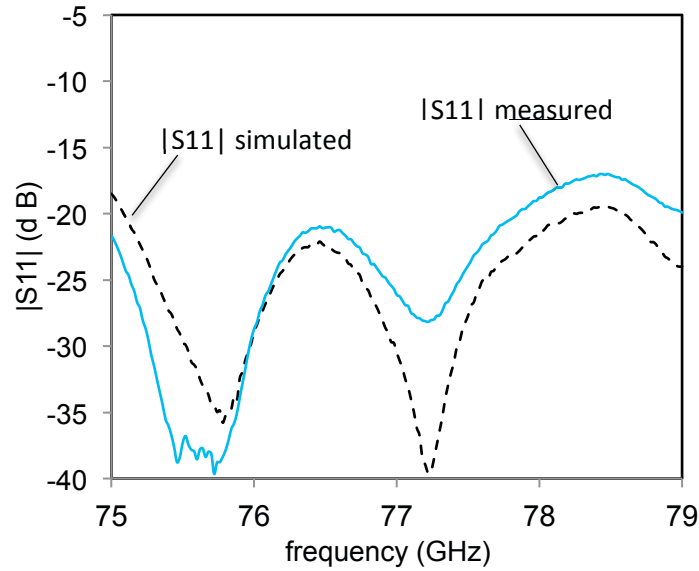


Figure 101 Reflection coefficient $|S_{11}|$ of the fabricated circuit ($N = 4$), measurement and simulation

The measured and simulated radiation pattern results are depicted in Figure 102 $N = 4$ and Figure 103, $N = 8$, for the H-Plane. The principal aim of adjusting and equalizing the beam direction has been well achieved. Recall that without an appropriate method, the main beam would be tilted due to the inherent slot phase gap between elements with different slot lengths.

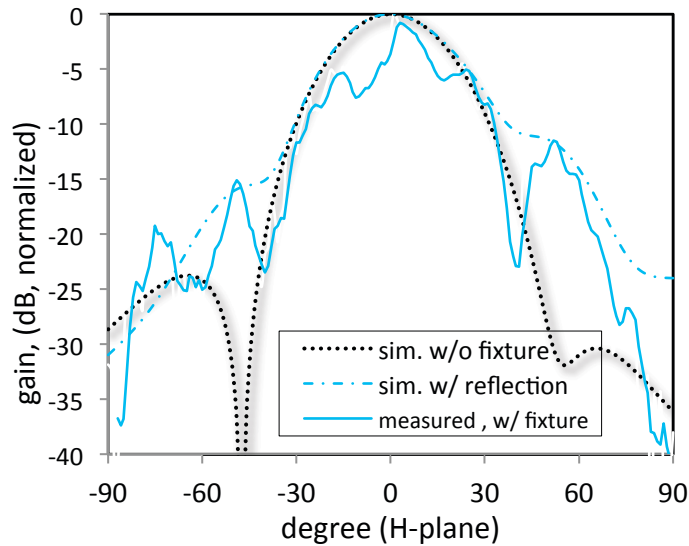


Figure 102 Radiation pattern of fabricated circuit ($N = 4$) within transition and fixture proposed in Chapter 7

However, after intense search, mechanical issues with the fixture and waveguide have been identified as responsible for the modest result in terms of measured side lobes. Although the waveguide

is terminated with a matched absorber at the very end, reflections are documented, partly depending on the torque of fixture screws. This is a frequently faced issue in millimeter-wave bands. Although these reflections are in a low range of approx. -15 dB, (this is shown later) the remaining amount at the end of the array is still significant. For comparison, the highest mutual coupling coefficients in the TWA, e.g. b_n , are in the same range as the reflections from the end, but their severe impact has been very well compensated in the design process, as seen in the simulation in Figure 102. Unfortunately, the reflections from the long milled and screwed waveguide cannot be circumvented by a perfect SIW match, due to the lack of an absorber directly implementable in SIW. We take this issue as future work. In order to verify our assumptions, a simulation introducing the small reflection at the end of the array has been added, see also Figure 102. The results including this error then match the side lobe levels of the measured radiation pattern very well.

For $N = 8$, the max. gain reveals to be about 14 dB at CF, see Figure 103.

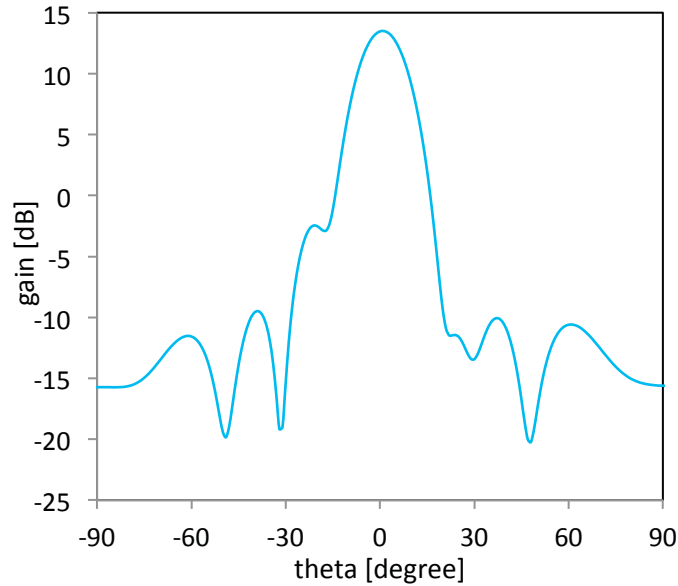


Figure 103 Simulated gain of $N = 8$

Another array of $N = 8$ is simulated and S_{11} and rP are visualized in Figure 104. The rP does not decrease < 0.1 and $|S_{11}|$ stays above $-15dB$ at CF which is typical for the proposed antenna since the MC based reflection is not fully eliminated though counted in. Co-polarized far field results in H-plane and E-plane are depicted in Figure 105.

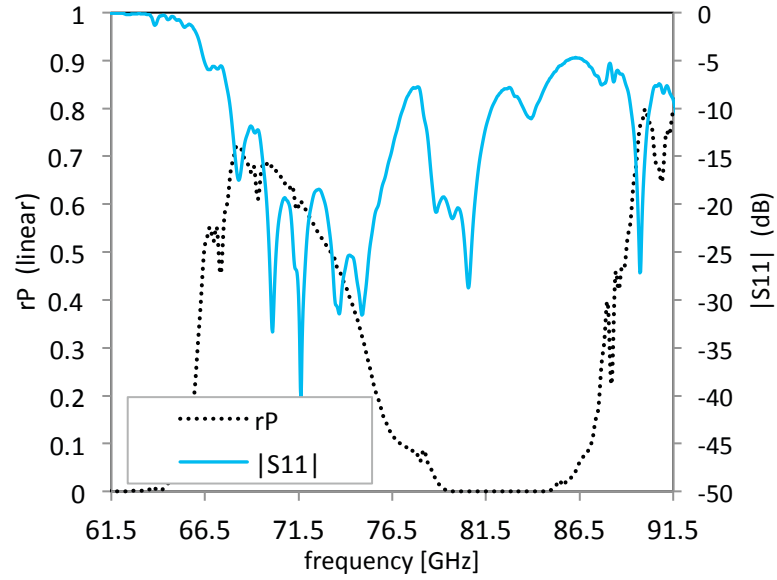


Figure 104 Reflection and residual power

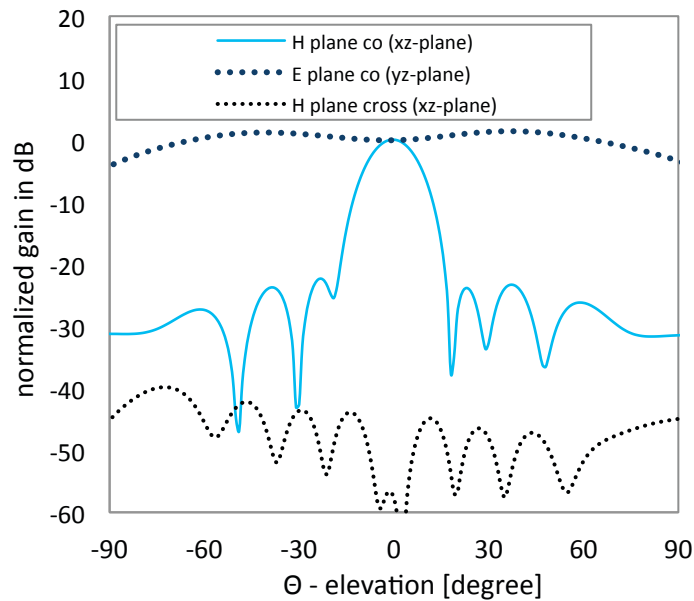


Figure 105 Radiation pattern of fabricated circuit ($N = 8$), (simulated)

In this case, the maximum (IEEE) gain is 13.75 dB, simulated without infinite ground plane. Low SLL of -22.4 dB and less are observable. The HPBW accounts for approximately 15° . The simulated efficiency is above 80%. Also visualized, the cross polarized radiation is very low.

Further, a third full wave simulation assuming an *ideal* matched termination at the end of the array, has been carried out especially to compare the results with conventional approaches. This design

for a 10 GHz center frequency and $N = 4$ on RO3010 is summarized in Table 2, with an SIW width of 7.39 mm and a slot offset of $x = 0.5$ mm.

Table 2 List of all slotted element parameters

<i>slot</i>	<i>length in $\lambda_g^{(*)}$</i>	<i>r_x in mm</i>	<i>r_y in mm</i>	<i>v_x in mm</i>	<i>v_y in mm</i>
#1	0.5	0.85	3.11	n/a	0
#2	0.519	1.05	3.38	6.5p+0.3	0.11
#3	0.523	1.11	3.60	6.5p-0.135	0.6
#4	0.518	1.05	3.38	6.5p-0.3	-0.1

(*) at center frequency of 10 GHz for nominal ϵ_r , (†) the pitch p is defined in the text

Again, butterfly and grating lobes are avoided by a positive equal offset and high ϵ_r . The via radius is $r = 0.375$ mm for the wall and 1.11·times r for all additional vias, with a via pitch of $p = 1.2$ mm. Recall that for validation and design, the reader may also visit the MATLAB Exchange website to fully download the provided test script and to load the results of own slot characterization from full wave simulations [19].

Radiation patterns are depicted in Figure 106. Once more, the ‘initial’ and pure ‘forward’ (without moving d) are included. Before any optimization, (e.g. to match the effective β in the SIW), the proposed concept yields a very good SLL. For the chosen aperture distribution, it would require a further small negative phase shift to eliminate the presumed cause of the slightly asymmetric SL. In Figure 107, $|S_{11}|$ for the circuit at 10 GHz is depicted. To see the effect of the vias, $v_y = 0$ mm serves as reference; the best result of -30 dB at center frequency is achieved *with* all vias and $v_y \neq 0$. This good result is related to the partly resonant optimization of $v_{x,y}$ for each c .

Recall that each element has been modified by at least one via and the impact on the total reflection is minimized. Though the total mutual coupling caused RU is considered and taken into account for P_n , there is no measure to minimize the total $|S_{11}|$.

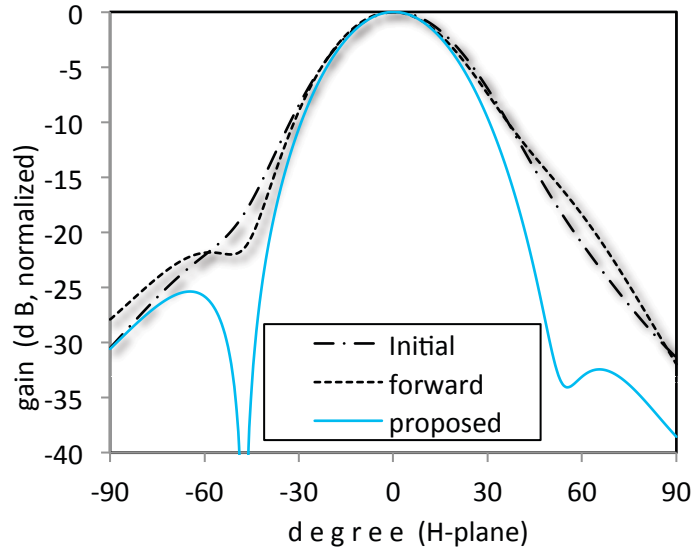


Figure 106 Rad. pattern comparisons at 10 GHz, 'initial' is the design approach neglecting MC, 'forward' assumes forward trav. waves only according to [6]

This does explain the remaining RL of about 10 dB, as also predicted by the model in that range. The general TWA character is underlined by the lack of a strong resonance in the range of CF, (below at about 9.3 GHz a resonance is most likely caused by the vias). Now when the vias are inserted, the total S_{11} becomes slightly better. At CF, the curve agrees almost exactly with the non-modified TWA. This is due to the initial boundary condition of the constant radiation coefficient set in 3.4.3. However, slightly above CF, the element exhibits resonant behavior and thus the total element *may* be considered as partly resonant, caused by the additional vias.

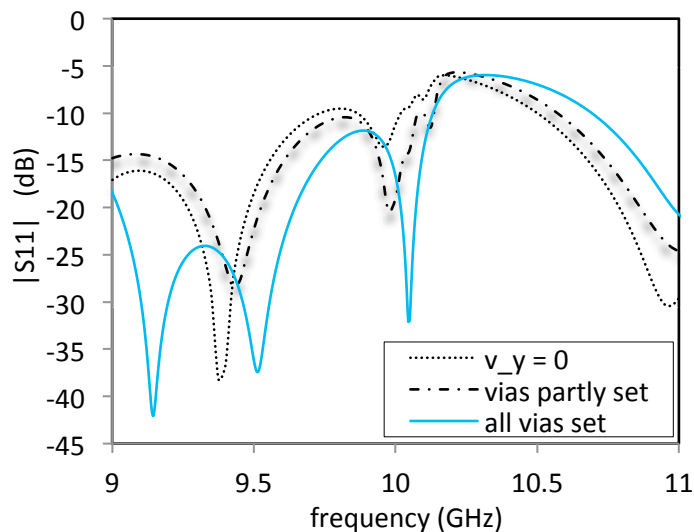


Figure 107 Result of simulated $|S_{11}|$ with and without additional vias

4.8. Conclusion

In summary, in this Chapter, a way of configuring slotted elements that allows shifting the phase by $>30^\circ$ has been presented. For a slot antenna array, phase gaps between slots have been adjusted internally, i.e. without impacting the slot itself or displacing it. Due to this advantage, a straightforward design method that includes slot excitation from either side could be proposed. Validation against FEM software has proven a good agreement with the desired amplitudes and reveals a radiation pattern with low SLL of -27 dB before other means of optimization. Measurements of a fabricated circuit have proven that a zero degree broadside beam can be successfully achieved with this approach. The antenna array yields a low $|S_{11}|$ at CF in particular, proven by measurements.

However, the project has revealed that an SIW absorber has to be developed as a future work since reflections from the applied transition and fixture at the end of the array degrade the results. In summary, the proposed design methods and slotted element configuration is very convenient and efficient, which has been further confirmed with a MATLAB script, see the ANNEX and [19]. The proposed method is very useful specifically for traveling-wave antennas in SIW with high width-to-height ratios as well as both off-resonant and mismatched slots, where other conventional methods have been shown to be less performing.

The good results in terms of simulation particularly demonstrate that this alternative way to configure a slot antenna in traveling-wave architecture is a very good candidate in particular for low-effort applications. The work has been published under [19] and [20].

4.9. References

- [1] C. A. Balanis, "Antenna Theory, Analysis and Design", 2. ed. Wiley, NY, 1997
- [2] Johnson, R. Clayton; et.al. "Antenna engineering handbook". 3rd ed. , McGraw-Hill, NYC, 1993
- [3] S. Park; Y. Okajima, et. al., "A slotted post-wall waveguide array with inter-digital structure for 45-deg linear and dual polarization", Antennas and Propagation Society International Symposium, Vol.3, p. 2368-2371, 2004

- [4] J.C. Coetzee, et.al. , “Analysis procedure for arrays of waveguide slot doublets based on the full T-network equivalent circuit representation of radiators”, IEE Proc. on Microw. Ant. a. Propag., pp. 173–178, 2000
- [5] J. Hirokawa, “A study of slotted waveguide array antennas”, PhD Thesis, Tokyo Institute of Technology, Nov. 1993
- [6] G. Montisci, “Design of circularly Polarized Waveguide Slot Antennas”, IEEE Trans o. Ant. a. Prop., Vol. 54, pp. 3025–3029, 2006
- [7] J. Hirokawa et al., “A single-layer slotted leaky waveguide array antenna for mobile reception of direct broadcast from satellite”, Vehicular Technology, IEEE Trans.on, vol.44.4, pp.749-755, 1995
- [8] S. Costanzo, “Synthesis of Slot Arrays on Integrated Wave-guides”, IEEE Ant. a. Wirel. Propag. Letters, vol. 9, pp. 962-965, 2010
- [9] Commercial Antenna Software “*Antenna Magus*”, Version 4.1, 2012
- [10] S. Park,Y. Okojima, et.al., “A Slotted Post-Wall Waveguide Array With Interdigital Structure for 45 Linear and Dual Polarization”, IEEE Trans o. Ant. a. Propagation,vol.53, pp.2865-2871, 2005
- [11] Q. Zhang, Y. Lu., “45° Linearly Polarized Substrate Integrated Waveguide-Fed Slot Array Antennas”, ICMMT, vol.3,pp.1214, 2008
- [12] R. Elliott, W. O’Loughlin, “The design of slot arrays including internal mutual coupling”, Antennas and Propagation, IEEE Transactions on, vol. 34, pp. 1149–1154, 1983
- [13] R. Elliott, “An improved design procedure for small arrays of shunt slots”, Antennas and Propagation, IEEE Transactions on, Vol. 31, pp. 48–53, 1983
- [14] L. Chiu, W. Hong, et. al., “Substrate integrated waveguide slot array antenna with enhanced scanning range for automotive application”, Microwave Conference, Asia Pacific, pp 1–4, 2009
- [15] S. J. Mason, “Feedback theory—Further properties of signal flow graphs,” Proc. IRE, vol. 44, pp. 920–926, Jul. 1956

[16] G. Mazzarella, G. Panariello, "On the evaluation of mutual coupling between slots", *Antennas and Propagation, IEEE Transactions on*, pp. 1289–1293, 1987

[17] MATHWORKS, "MATLAB R2014", www.mathworks.com ,

[18] MATHWORKS, "Matlab Optimization Toolbox"
www.mathworks.de/de/help/optim/ug/fmincon.html

Published work:

[19] F.D.L. Peters, "Traveling Wave Antenna Design", MATLAB File Exchange Website, 2013

[20] F.D.L. Peters, T.A. Denidni and S.O. Tatu, "Internal Slot Phase Varying in Traveling-Wave SIW Slot Antennas and Appropriate Modeling", *Wiley Microwave and Optical Technology Letters*, Volume 56, Issue 6, pages 1303–1307, June 2014

CHAPTER 5

FURTHER PHASE VARYING FOR MULTIPLE ARBITRARY BEAMS IN A QUASI-TWA ARCHITECTURE

5.1. Introduction

The latter Sections have revealed a linear simple approach of the design of traveling-wave antennas with multiple vias. Since the vias in Chapters 3 and 4 are inserted to allow shifting the phase in between elements, further shifting beyond the necessary is thinkable. In the first place, the results of 3.4 are available and used. This provides a solution of beam forming arrays that would have the substantial advantage of a fine control on the beam angle without losing the effortful computed mutual coupling compensation.

5.2. Attraction and Challenge of Extending the TWA for Arbitrary Beams

The need for beam forming approaches in the millimeter bands is expressed in [1]. There is virtually no completed work on beam forming of longitudinal slotted SIW TWA that does not use frequency scanning or modified element distance [Chapter 2, ref. 7]. The reason is a very high computational effort for each segment [2] when it is off-resonant and mismatched. Recall also the very unsatisfactory results for shifting elements in 3.5.4. However, trials of designing a TWA with versatile reconfigurable beams have been carried out for microstrip and SIW, nevertheless, with bad results, in particular SLL, as shown in [48, 49] of Chapter 2.

The approach to use the shifter elements might not be as appealing as a matrix based solution in the first place. However, millimeter waves are short. Electrically large circuits are producible on one waver and of low cost. Once millimeter waveband switching is available, multiple beams may be realized by copying reconfigurable structures for each beam. The advantages of this solution are

numerous: a high isolation between channels, arbitrary configuration of each beam, and space as the only limitation for the number of beams. Thus, the approach applied in the following can be used to derive single beam shaped SIWs that can be switched for instance with RF MEMS [3]. See also the future work in 8.3.

5.3. Enhanced Phase Shifting with Additional Vias

In 3.4.2 to 3.4.3, the best method to phase shift the slotted element ϕE_y without impacting radiation and reflection has been studied. With these measures, additional phase shift might be inserted while still keeping good characteristics as discussed.

5.4. Experimental Results and Discussion

The most important parameters are listed in Table 3.

Table 3 Parameters of the N=4

<i>slot</i>	<i>l/λg</i>	<i>slot</i>	<i>l/λg</i>	<i>slot</i>	<i>l/λg</i>	<i>slot</i>	<i>l/λg</i>
#1	.655	#2	.675	#3	.675	#4	.655

5.4.1. Phase Shifting in the TWA

Arrays are designed for three different beams. The total phase at the end of the array ϕS_{21} over all elements is compared. The zero beam antenna shall have an equalized phase distribution and thus reveal roughly *zero* degree shift (compared with THRU), when measured in the transition later reported. Note that the phase of a pure THRU line, also reported in Chapter 7, is subtracted from the result. Figure 108 depicts the three different phase delays. The zero beam has a negligible value whereas the two-via approach has 30° and the three via approach has approximately 90° at CF.

Thus, the general idea is proven. The mid-channel reveals almost the lowest phase shift, both additional antenna arrays reveal a shift of about 30° and 90°.

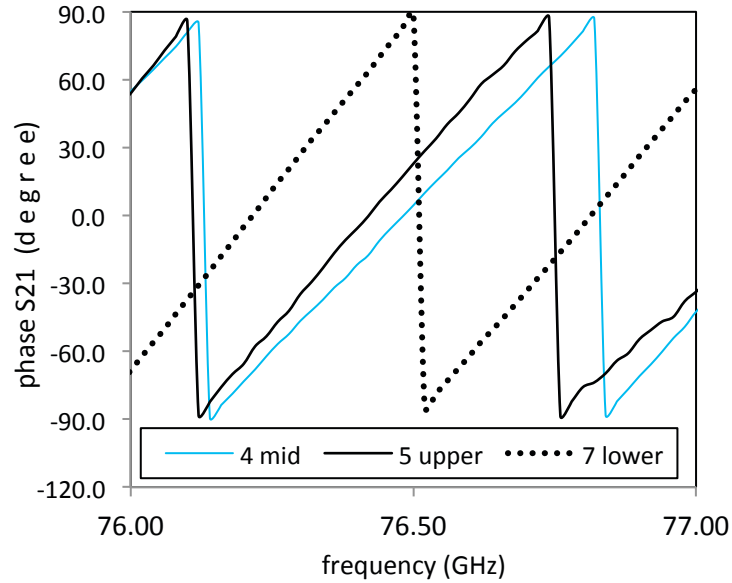


Figure 108 ϕS_{21} , Phase shifting entity, proof of feasibility (measured)

5.4.2. Isolation between Channels

It is important to confirm a high isolation between channels in order to exclude SIW leakage issues. Since the arrays are intended to be very close to each other on the circuit for low space requirements, the isolation is crucial. Results are depicted in Figure 109. Unfortunately, the transmission exceeds also partially the typical MC values and thus will degrade the actual measurements. Future work shall use EBG or supplementary SIW walls to reduce this effect. Dupont 951 has been applied.

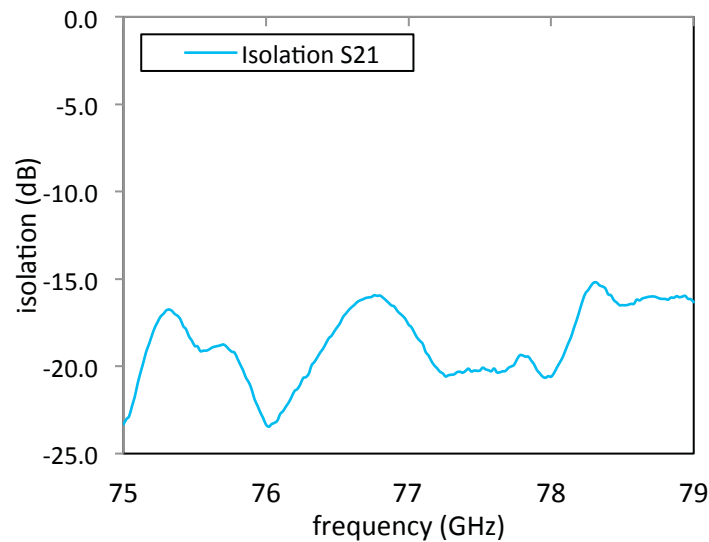


Figure 109 Measured isolation between two beam channels

5.4.3. Reflection Coefficient and Pictures

The reflection and transmission of an array of $N = 8$ within the fixture is provided in Figure 110.

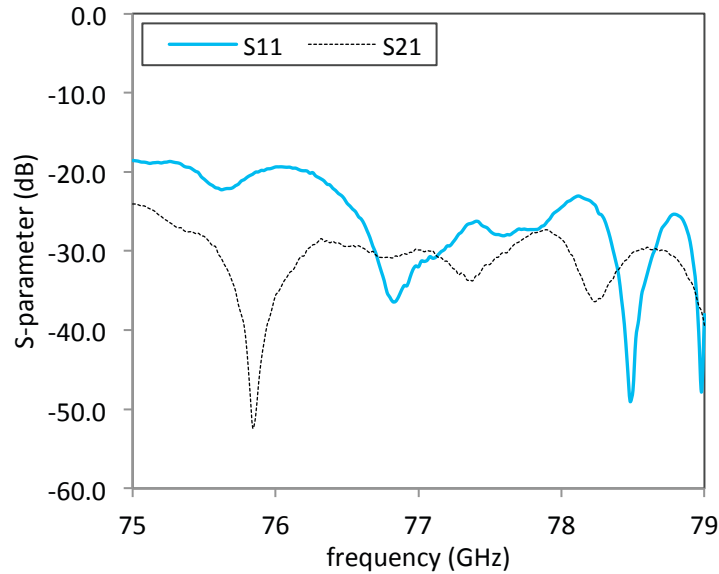


Figure 110 Reflection of the array, $N = 8$

A picture of a zero degree beam is depicted in Figure 111.

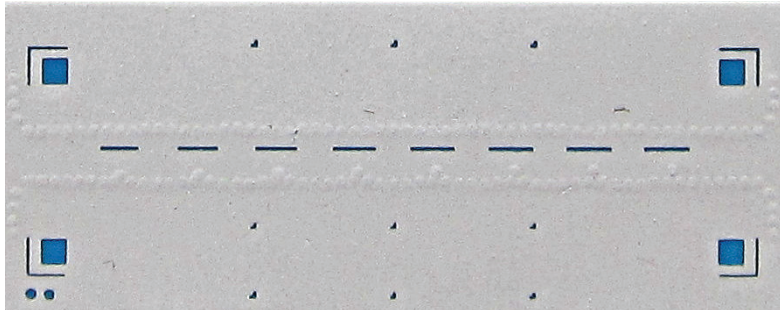


Figure 111 Fabricated circuit (0° beam)

5.4.4. Radiation Pattern

First, results of simulating three beams with arbitrary beam angles are shown in Figure 112. For the first time, to the best of the author's knowledge, a passive beam shaping without modifying the distance, for longitudinal slots in this form factor has been shown. The side lobe levels stay inferior to -20 dB which is a good result and substantially better than e.g. shown in [48, 49] of Chapter 2.

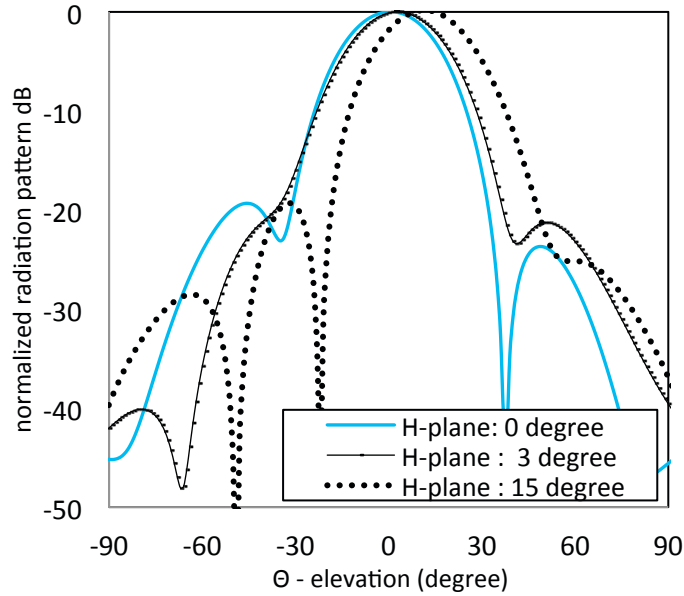


Figure 112 Radiation pattern, 3 beams, simulated

However, fabrication of this antenna type has not brought the desired values; nevertheless, a feasibility proof of concept is manifested in a straight beam of similar HPBW than the simulated one. In Figure 113 results of measurements using the setup of 4.6.2 for the main beam are depicted. A general shift of the relative permittivity has been expected and determined by measurements in Chapter 7, however, the tolerance of the measurement is either not enough, or the fabrication tolerances itself are too high. The main beam is shifted from its initial angle in this production.

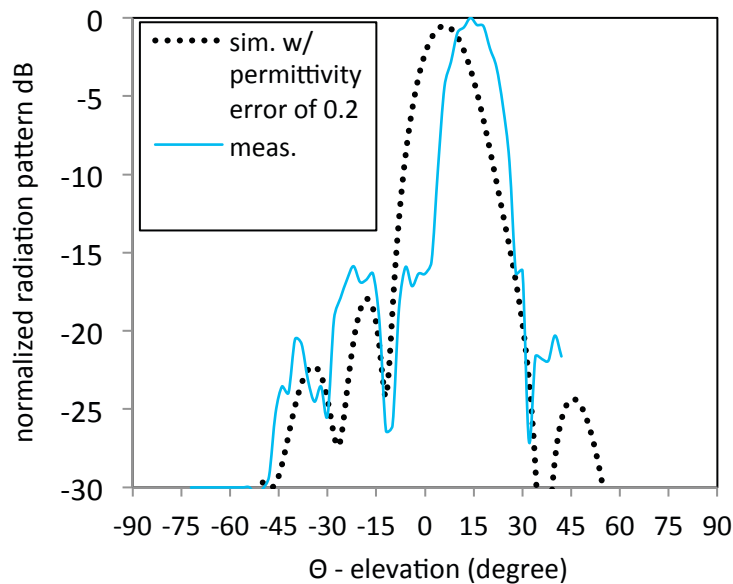


Figure 113 Radiation Pattern of zero degree, slightly erroneous ϵ_r

Unfortunately, other antenna circuits with further beam degrees have been unable to measure correctly. Either the power was not sufficiently transmitted at the entry port or reflected inside the array to a high degree. This issue has several assumed causes, see also 5.5 and Annex A 2 for a discussion.

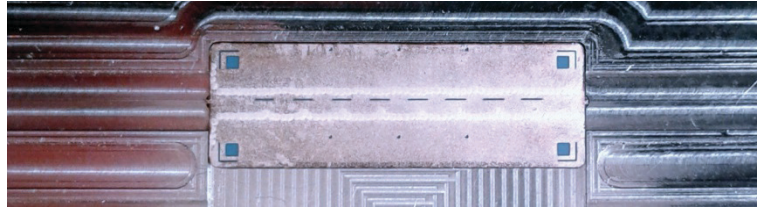


Figure 114 Photograph of the 8-element fabricated applying the transition reported in Chapter 7

5.5. Fabricating Efforts and Issues

Some other issues have been seen in this production, which are presented in Figure 115 and Figure 116. They are mainly impacting the slot shape.



Figure 115 Issues with this technique demonstrated with a slot

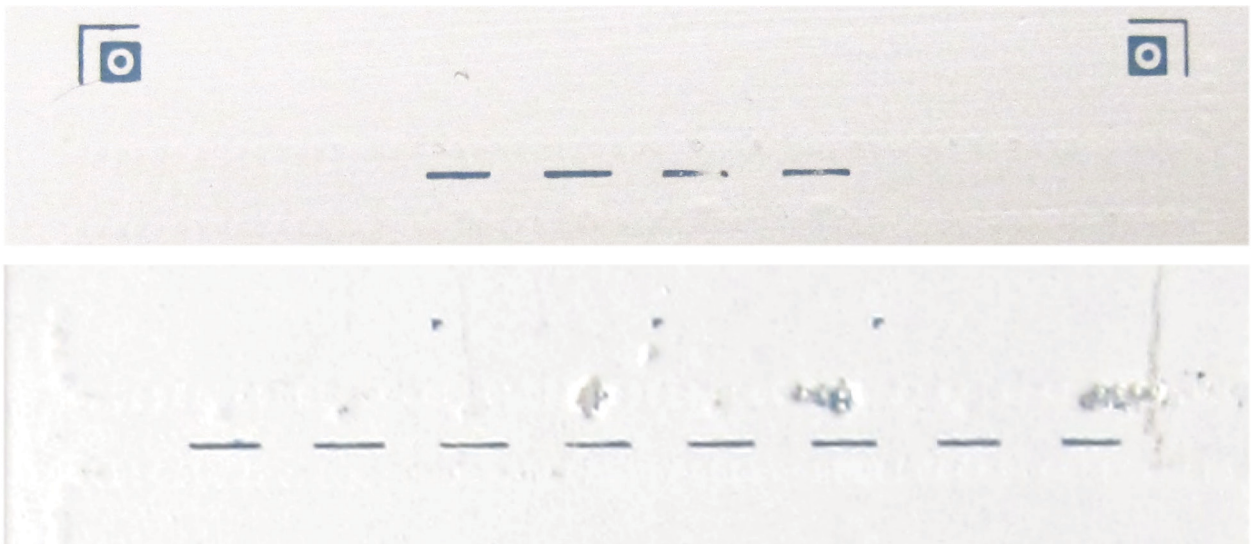


Figure 116 Issues on some LTCC circuits

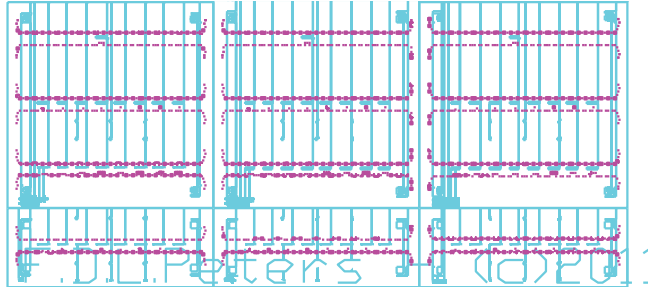


Figure 117 Fabricated board of SIWs

5.6. Conclusion

In this Chapter, an approach of using vias in the TWA as an asset to the technique in Chapter 4, has been presented. Two positive things can be seen. First, the shifted beams are in the same range of beam width as the initial beam. Second, the side lobe level can be kept in the same range as the unshifted beam. The heavy time consuming computation of all parameters can be avoided by this approach since elements are not modified except by the via positions.

In addition, this Section shows the general feasibility of the antenna in terms of its radiation pattern. To the best of the author's knowledge, a novel way to reconfigure arbitrary beams has been presented for the first time without any modification of the distance. However, substantial issues of fabrication, partially with the material characteristics have degraded or destroyed the manufactured results. This has to be improved.

Recall that *all* design steps have to be carried out for one permittivity and then to be finished for a particular shrinkage effect. In fact, the measurements later in 7.6 reveal a relative permittivity close to the designed one; however, the impact of the small error seems to be too high at this time of production, unfortunately.

5.7. References

- [1] M. Schneider, "Automotive radar - status and trends," Proceedings of the German Microwave Conference GeMiC, paper 5-3, 2005
- [2] B. Macintosh-Hobson, "Slotted Substrate Integrated Waveguide Array Antenna & Feed System", Master Dissertation, Concordia, Montreal, 2008

[3] J. Schoebel, T. Buck, M. Reimann, M. Ulm, M. Schneider, et. al., Design considerations and technology assessment of phased-array antenna systems with RF MEMS for automotive radar applications, *IEEE Transactions on Microwave Theory and Techniques*, Vol. 6, pp. 1968–1975, 2005

CHAPTER 6

A TWO LAYER TWA FED FOUR-BEAM SLOT ANTENNA IN RESONANT ARCHITECTURE

6.1. Introduction

While the TWA on one layer designed in the previous Chapters is radiating into *free* space, the approach of this Section comprises a two layer layout where an SIW in traveling-wave mode is used for feeding a 2nd layer. The latter contains itself a 90° turned resonant slotted antenna array (RESA). It consists of an SIW and is based on common architectures outlined in 2.4. The entire structure of a TWA Fed Antenna is called TWAFa in the following.

The antenna has four distinct beams over a range of 40 degrees generated by four different exciting traveling-waves in the two SIWs underneath. It is designed for two LTCC layers. The general architecture is proposed in 6.3, the design procedure and resulting parameter values are presented in 6.4, and the results in 6.5.

The TWAFa may be used for instance in millimeter-wave bands at 77 GHz. The proposed solution can also be used as a monopulse antenna of four ports in radar applications, which is shown in 6.5.

6.2. Background and Context of the TWAFa

The background has been shown in 2.7.

6.3. General Antenna Architecture and its Preparation for Beam-forming

The beam forming feature is accomplished by designing a feeding architecture with two different SIW widths a_0 . This allows two *unequal* propagation constants $\beta_{1/2}$ in each of the two feeding SIW. In this way, the required $\Delta\phi$ for each desired beam tilt is created in between elements. Since each

feeding SIW has one width a_0 , the coupler slot offsets and lengths need to be found iteratively to achieve equal $\Delta\phi$ for the same β .

The top layer is composed of four resonant slot arrays. Each of them is fed from either side by a coupling slot, as depicted in Figure 118. This slot is edged perpendicularly to the slot orientation in the top-layer. The total antenna architecture is depicted in Figure 118. The resonant architecture is designed from the bottom to the top whereas from the left to the right a traveling-wave feeding is designed. The distance between the feeding couplers is constant and slightly below $\lambda/2$. Vias are used to reduce the coupler reflections from either side as in 3.4.1.

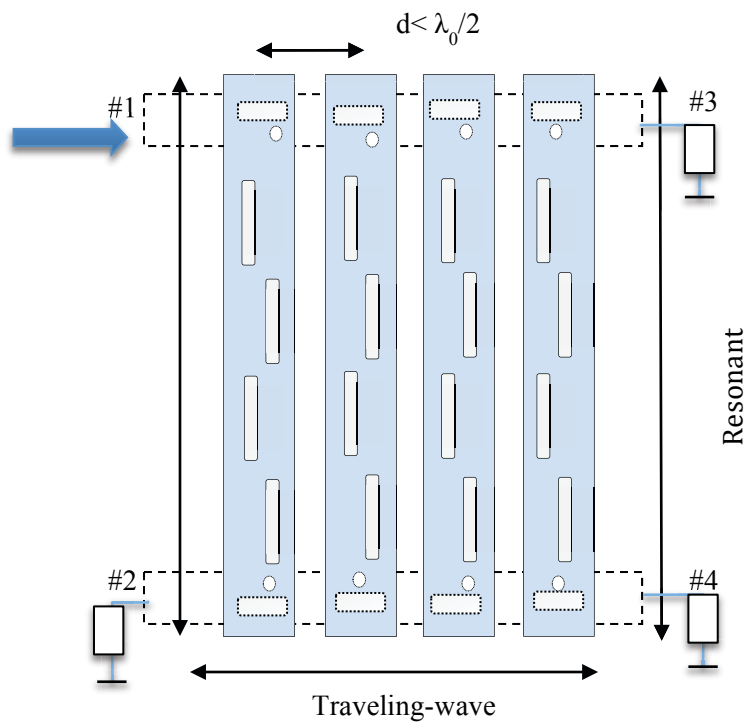


Figure 118 Traveling-wave fed four beam scanning antenna, architecture, example: port #1 is excited, ports #2,#3,#4 have to be matched

6.4. Design Procedure

6.4.1. Radiating Top Layer

On top, a resonant architecture is designed. Conventional design approaches [1, 2] are applied. Mutual coupling is not considered in this case due to a lower targeted side lobe level performance. The top layer parameter values are wrapped up in Table 4.

Table 4 Parameters of the designed top layer antenna

<i>slot</i>	l/λ_g	<i>Slot</i>	l/λ_g	<i>slot</i>	l/λ_g	<i>Slot</i>	l/λ_g
#1	0.612	#2	0.63	#3	0.63	#4	0.612

6.4.2. Design of the Four Port Feeding Network and Transverse Couplers

The design challenge lies in the proper selection of the SIW length of the upper layer in combination with the coupler positions. For all four ports of excitation, equal electrical length must be achieved. Since the coupler is impacting the effective electrical length, the upper SIW cannot be simply designed with $N \cdot \lambda_g$, with λ_g being the wavelength without couplers.

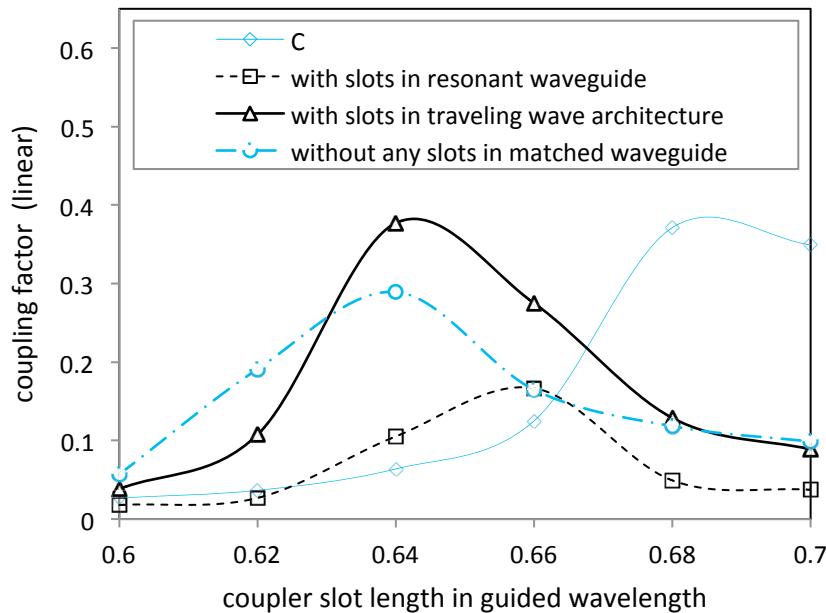


Figure 119 Slot coupler design curves of coupling

Conventional RWG may be coupled in a way proposed by [3], however, this contains only resonant feeding slots and arrays. SIW power coupling curves are therefore derived and depicted in Figure 119 where the impact of the 2nd fed layer is shown.

The impact of the coupler on the wavenumber in the top layer is shortly shown for a failed design in Figure 120 and Figure 121. Excitation is performed in the upper left and lower left port afterwards. Obvious at the 1st and 4th slot, the coupler position causes both slots to be $> 90^\circ$ different in phase with respect to the other slots. The solution for this issue are asymmetrically placed couplers that are optimized in their positions. With respect to Figure 122, the resulting d_{up} and d_{down} are wrapped up further below in Table 5 together with other general parameters.

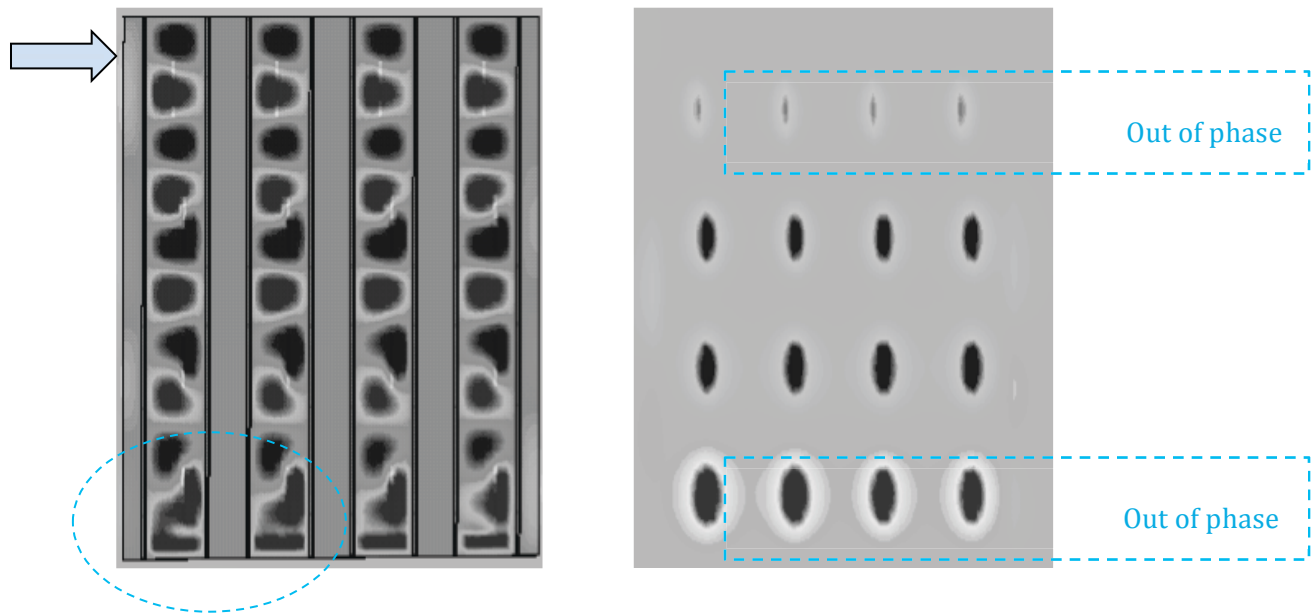


Figure 120 Excitation of the resonant layer from left up and (right) near field result on top layer, slots out of phase are marked

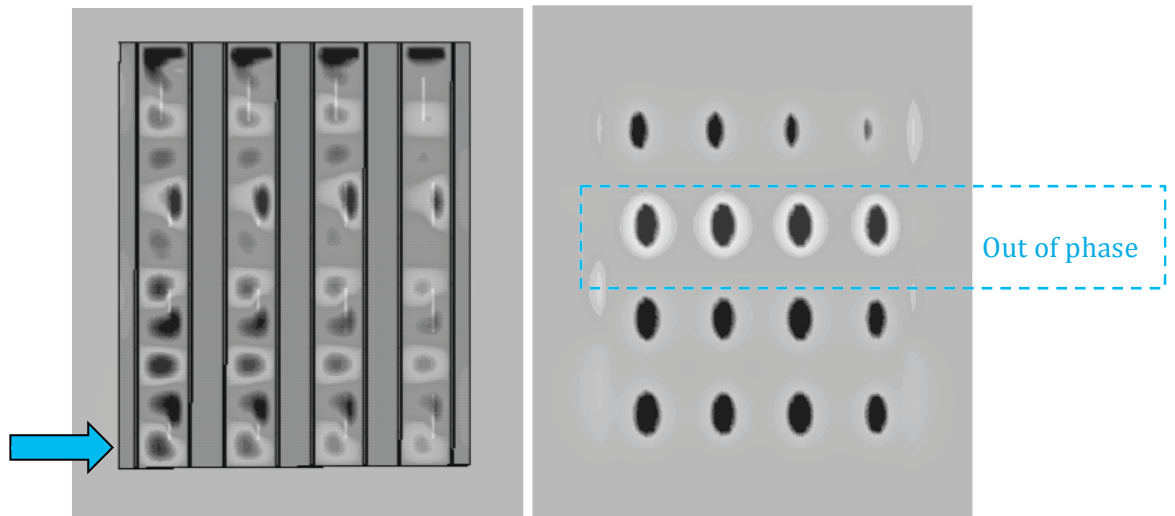


Figure 121 Excitation from down left port #1 (see arrow), result dark = in phase, light = out of phase

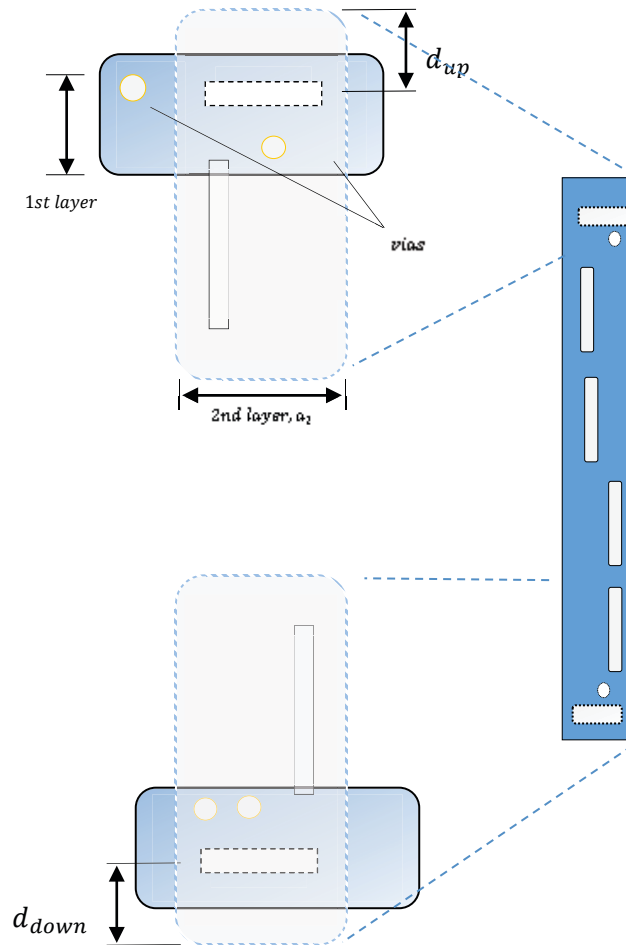


Figure 122 Coupling challenges and parameters

Figure 123 shows again excitation from up-left. At this time, all four slots from top to down in the resonant architecture are in phase due to the asymmetrically set d_{up} and d_{down} .

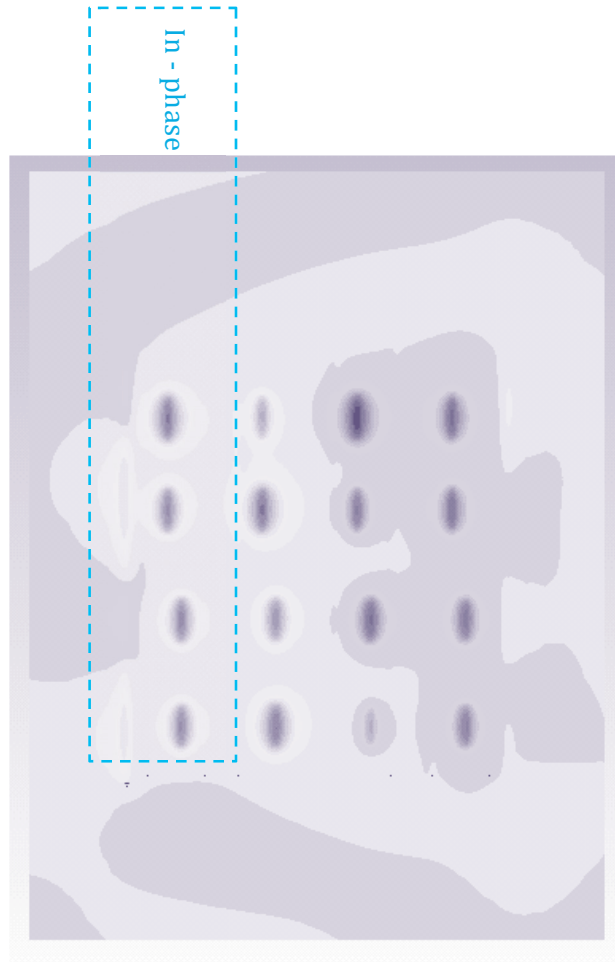


Figure 123 Near field result for a four-beam Design, all slots are in phase

As the design has a *symmetric* aperture distribution, solely two coupling factors, C_1 and C_2 are required, however, each coupler needs to provide the desired C_1 and C_2 , *and* equal inherent phase for all couplings, (recall that the distance is fixed), and low reflection. The lower couplers are designed in a mirrored orientation, see Figure 122.

The proposed transition from SIW to the 2nd SIW for the two layer concept is based on the assumption that the electrical slot field will excite the TE_{01} mode in the upper layer in both directions, see Figure 124. Further optimization is applied to ensure minimal reflection by setting a via, and secondly by choosing the best ratio between the upper and lower a_0 , since the maximum length for $C_{r_{max}}$ shall not touch the boundaries of the SIW.

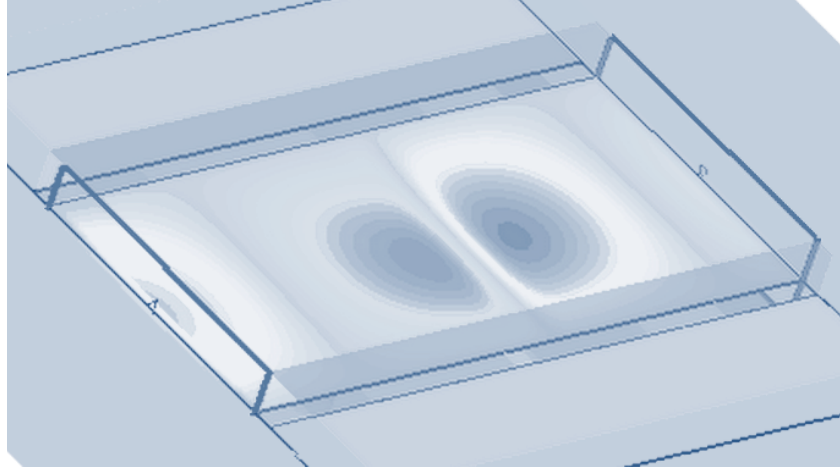


Figure 124 Resulting TE mode in upper SIW, simulation

Note that, both SIW do not share the same propagation constant, to allow for beamforming. This requires that the coupler is designed with the *same* coupling factor for a *different* β .

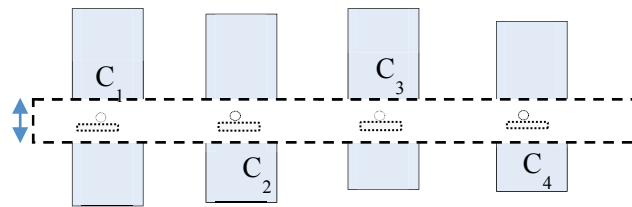


Figure 125 The feeding coefficients, (shown for one side only)

The ratio of the outer to the inner coupling factors $C_r = C_2/C_1$ is evidently responsible for the side lobe performance. Both mid couplers shall provide the same coupling since excitation is expected to be possible from either side. Figure 126 depicts the trade-off for in total 8 different configurations i.e. four different C_r and two efficiencies each, η low and high.

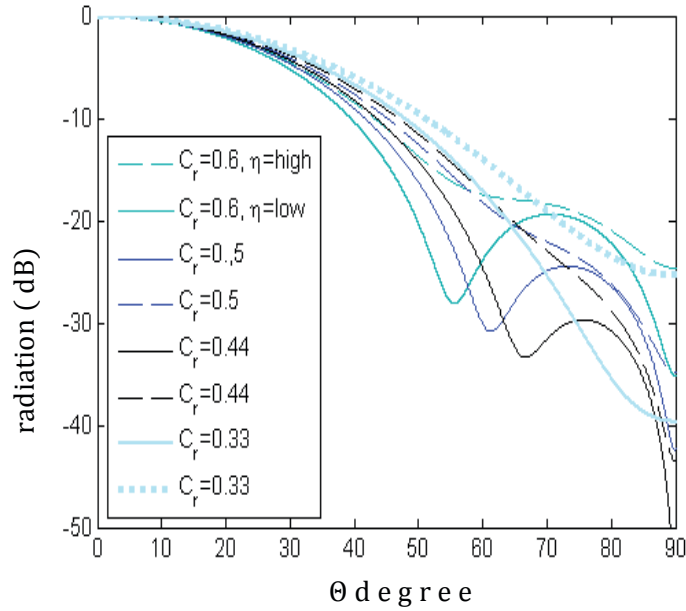


Figure 126 Estimated radiation pattern, as a function of different coupling factors C_r , each for high (dotted) and low efficiency (not dotted)

6.5. Results and Discussion

The proposed antenna array is designed and simulated for four sub-arrays with four slots each. Optimization is carried out with the equivalent SIW to RWG conversion known from [4]. With $\epsilon_r = 9.9$, $\tan\delta = 0.001$ and a substrate thickness of 0.254 mm, results are shown in the following for all four excitation ports. All actually not excited ports are terminated with matched absorbers. Either port cannot be equally well matched due to the forced asymmetry in the via positions. Nevertheless, a good compromise has been found. In fact, S_{11} and S_{44} share a similar response while S_{22} and S_{33} are quite equal too.

Table 5 Other general parameter values of the TWAFAs⁸

<i>parameter</i>	<i>value</i>	<i>parameter</i>	<i>value</i>
a_0 top layer	.915mm	radius via	.127*.5 mm

⁸ The results of this configuration are presented in section 6.5

<i>parameter</i>	<i>value</i>	<i>parameter</i>	<i>value</i>
<i>height</i>	<i>.254 mm</i>	<i>pitch</i>	<i>.1905 mm</i>
ϵ_r	<i>see 7.6.1</i>	<i>x</i>	<i>$\pm .129$ mm</i>
d_{up}	<i>4 mm</i>	d_{down}	<i>-3.7mm</i>

S-Parameters for one optimized antenna configuration of the conceived TWFA are depicted in Figure 127. This Figure combines the reflection of each feeding port and in the isolation between ports. With respect to the nomenclature of Figure 118, the isolation is plotted for S_{34} and S_{23} in the same plot Figure 127. The isolation to the non-excited ports stays > 15 dB.

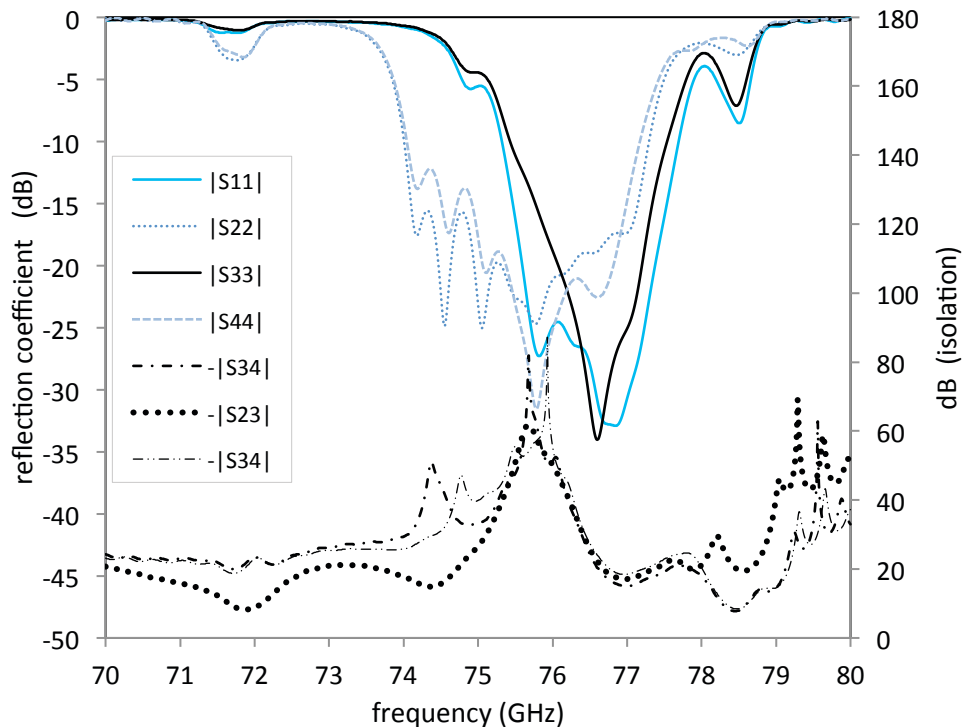


Figure 127 S-parameters for all four input ports, the isolation between fed and not fed ports is also depicted

All ports are well matched with $S_{nn} < -10$ dB at CF. A minor drawback of the asymmetric matching is the small impedance BW, which is $\sim 2.3\%$ but cannot reach significantly higher values over all ports equally.

The radiation pattern for all four ports #1 to #4 is depicted in Figure 128 at 77 GHz. The achieved scanned angle range is -20° to $+20^\circ$. Beam angles are #1 and #3 $= \pm 22^\circ$ and for #2 and #4 $= \pm 12^\circ$. A maximal directivity of 15.3 dBi is obtained. Neglecting the non-radiated residual power, the efficiency is around 70 %.

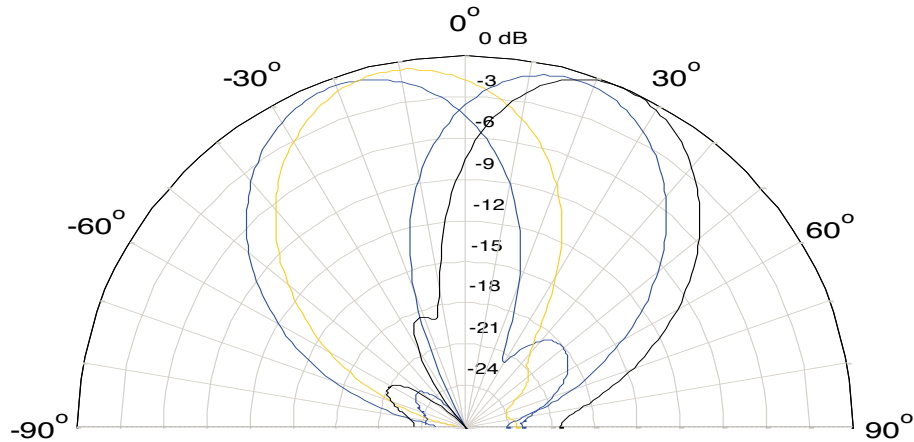


Figure 128 Rad. pattern, normalized directivity in E-plane, from left to right: port #3, #2, #4, #1

In the next Figure 129, all four ports are shown in H-plane. The result slightly differs for each port, however, a zero degree main lobe is achieved.

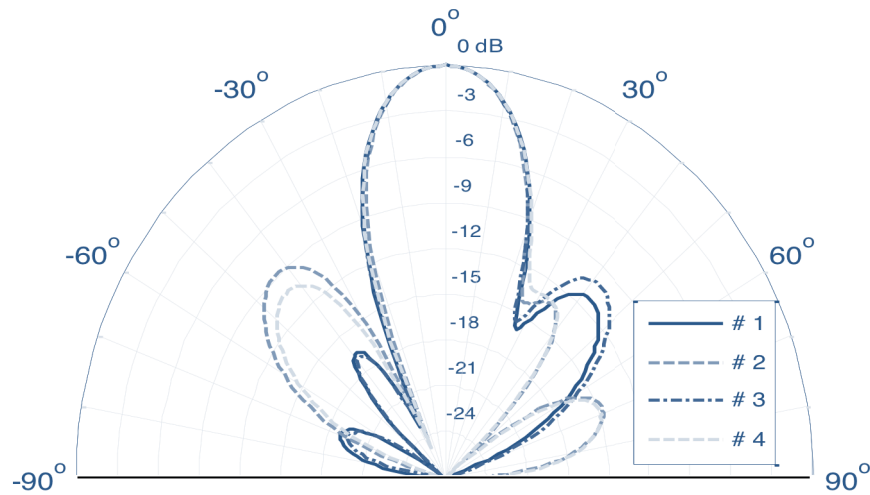


Figure 129 Radiation pattern, normalized directivity in H-plane

It is important to check the directivity for each port to not differ substantially. The directivity over all four ports is depicted in Figure 130. It counts for 16 dB with at least 60% efficiency, recall also Figure 126 for the estimation of efficiency if taking the residual power at the end into account.

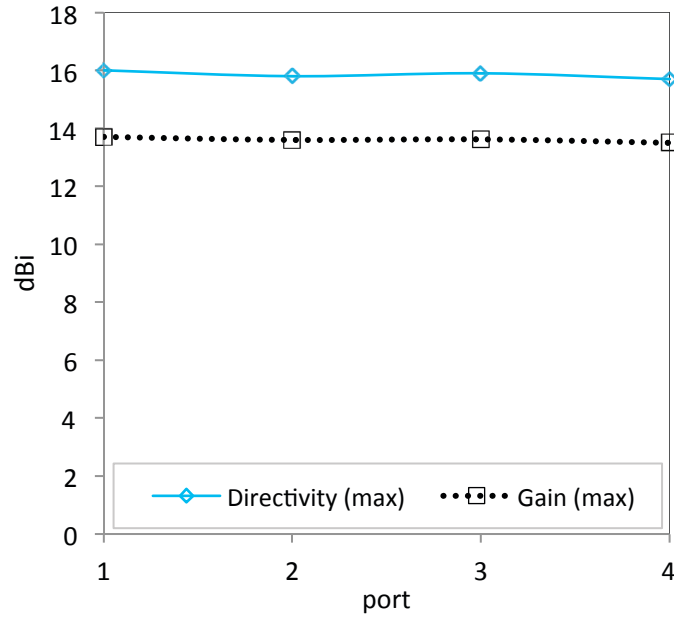


Figure 130 Gain and Directivity over all ports, i.e. beams

Subsequently, the initial motivation to design a monopulse antenna is reiterated and the designed TWFAFA is applied in that way. For this sake, entry signals are shifted by 180 degree as previously shown in the literature, Figure 15. Recall, that one initial goal of the design concept was to increase the number of beams for monopulse antennas. In Figure 132, the sum and differences are depicted of #1 and #3 as well. The result is excellent.

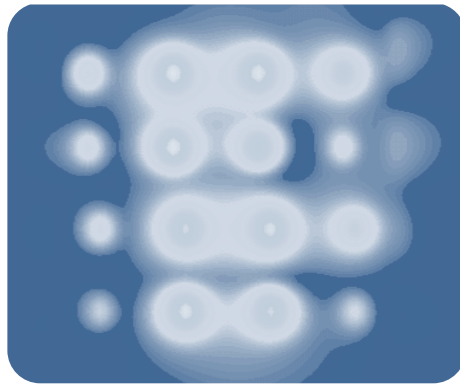


Figure 131 Aperture Distribution

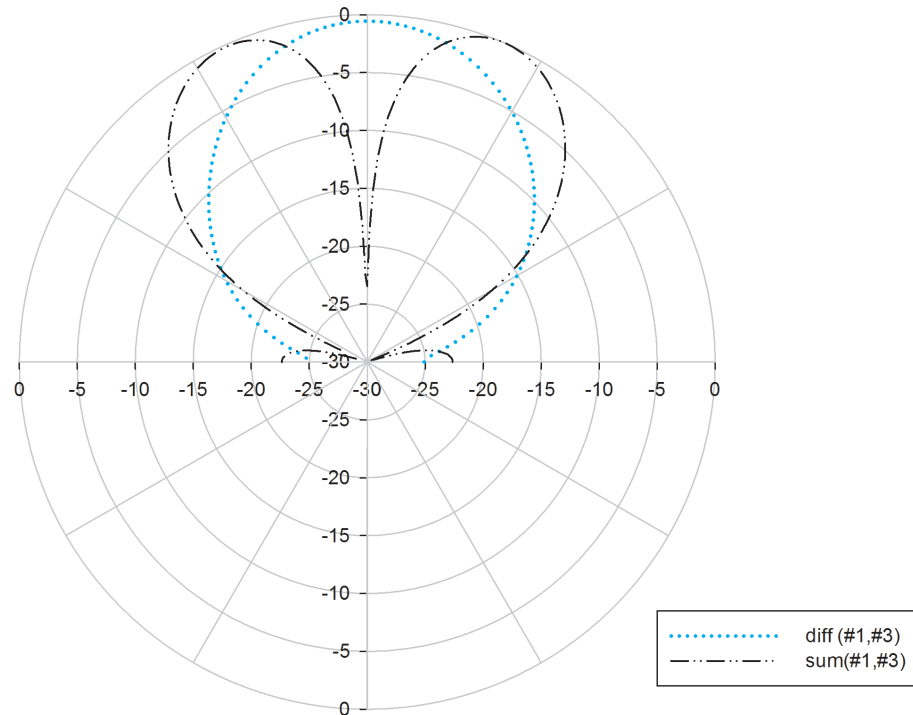


Figure 132 Monopulse radiation pattern for difference of #1 and #3 and sum of 1# and #3

6.6. Conclusion

To sum up the solution of this Chapter, slot antenna sub-arrays have been excited from either side by two SIWs of different widths located underneath. This approach yields four different beam angles. Slot couplers have been designed for minimal reflection and equal phase shifts by means of additional inductive posts. Since the resonant length of the sub-array and the isolation between input ports depend on the coupling slot position, a tradeoff between radiation pattern performance in the H-plane and isolation is unavoidable.

Four particular beams from -20° to $+20^\circ$ - have been designed. The TWFA can be designed for arbitrary beam angles by modifying the width of the feeding SIW. For instance, a broadside pair of beams and two off-broadside arbitrary angles can be designed without redesigning the top layer. Good matching of better -10 dB reflection has been obtained for all ports at CF. The isolation between exciting ports could be kept above 15 dB by placing the coupling slots unequally in the lower and upper end. Simulation results show a max. directivity of about 16 dBi and efficiency near 70 %

with actual available substrates. This antenna is therefore an ideal candidate for integration into multiple layer radar sensor projects. A monopulse application has been shown.

Obviously, an absorber used at the four ports is necessary since the SIWs provide residual power $\neq 0$. For this sake, a new two layer planar LTCC transition is necessary which is solved in Chapter 7. The work has been published under [12].

6.7. References

[1] L. Josefsson, "Analysis of longitudinal slots in rectangular waveguides", Antennas and Propagation, IEEE Transactions on, vol. 35 (12), p. 1351-1357, 1987

[2] G. Stern, R. Elliott, "Resonant length of longitudinal slots and validity of circuit representation: Theory and experiment", Antennas and Propagation, IEEE Transactions on, vol. 33 (11), p. 1264-1271, 1985

[3] S.R. Rengarajan, G.M. Shaw, "Accurate characterization of coupling junctions in waveguide-fed planar slot arrays," Microwave Theory and Techniques, IEEE Trans. on , vol.42, no.12, pp. 2239-2248, Dec 1994

[4] F. Taringou, J. Bornemann, "Return-loss investigation of the equivalent width of substrate-integrated waveguide circuits," Microwave Workshop Series on Millimeter Wave Integration Technologies (IMWS), IEEE MTT-S International, pp.140-143, 15-16 Sep. 2011

Published papers:

[5] F.D.L. Peters, S.O. Tatu, T.A. Tayeb, "Design of beamforming slot antenna arrays using substrate integrated waveguide", Antennas and Propagation Society International Symposium (AP-SURSI), IEEE 2012

CHAPTER 7

TWO LAYER PLANAR LTCC TRANSITION AND ITS APPLICATION FOR LTCC CHARACTERIZATION

7.1. Introduction

In the previous Chapters, single and double layer circuits have been developed and their feasibility has been proven by both simulation and partly measurements. Though the SIW antenna array of 4 is primarily conceived for one layer, it has been manufactured in LTCC technique likewise, with the aim to master all processes of this technique and to use it in the double layer projects. LTCC requires at least two layers for stability reasons. This implies a new challenge if a conventional RWG of another height shall be connected exclusively to one SIW on the top layer, without any transition to microstrip. Existing approaches applying planar transmission lines shall be circumvented. Microstrip has the disadvantage of necessitating both effective *and* relative permittivity, which is emphasized later in this Section. An accurate waveguide transition for pure TE-mode coupling from SIW to RWG is therefore required. This main task is solved in this Chapter.

In addition, the relative permittivity, loss and shrinkage (while firing) of the applied LTCC substrates, called *tapes*, are not yet fully described by the literature for this frequency. A short investigation on these parameters is covered as well in this Chapter as the 2nd topic.

Furthermore, both the antenna arrays of 4, 5 and 6, and the required calibration and LTCC circuits to determine the material parameters, require a mechanical structure for measuring S-parameters and radiation pattern. A metallic fixture is proposed for all this tasks that allows measuring *three* channels with equal electrical length. *Three* waveguides become obligatory for the calibration process of THRU-REFLECT-LINE(TRL) since replacing the circuit a couple of times would degrade the final result substantially, shown in the following Sections by analyzing air gaps in the transition.

Overall, in this Chapter, a new transition is designed and LTCC material is characterized with valuable information about loss and permittivity. In addition, shrinking behavior is studied. Moreover, a mechanical fixture is presented that serves as a very useful tool for performing all measurements.

7.2. Motivation for a Planar Solution and Mechanical Constraints

The basic concept provides three channels in conventional waveguide architecture, connected to SIW on LTCC circuits via the new transition. It is drawn in Figure 133.

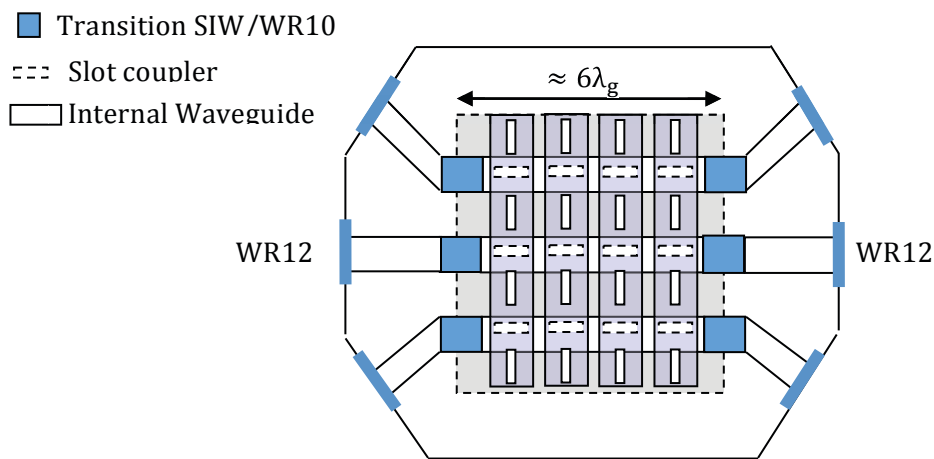


Figure 133 Front view of the fixture holding the novel transition designed in this Chapter (slots shown exemplarily)

As a single WR12 connector requires a certain distance to the adjacent WR12 flunch as a result of screws and supporting wholes, an octagonal-shaped fixture is preferred. Note that in Figure 133, the actual width of the RWG is naturally *not* equal to the SIW width a_0 but the conventional standard WR12 width. When viewed from side, Figure 134 reveals an important detail. The clearance θ_{max} should be designed sufficiently large, at least for including both major side lobes of the most left and the most right beam of the antenna array. Otherwise, reflections from the side walls impact the near field. In fact, reflections cannot be fully avoided but the previous Sections have shown that very low side lobes of $< 30 \text{ dB}$ are achieved with the proposed procedures.

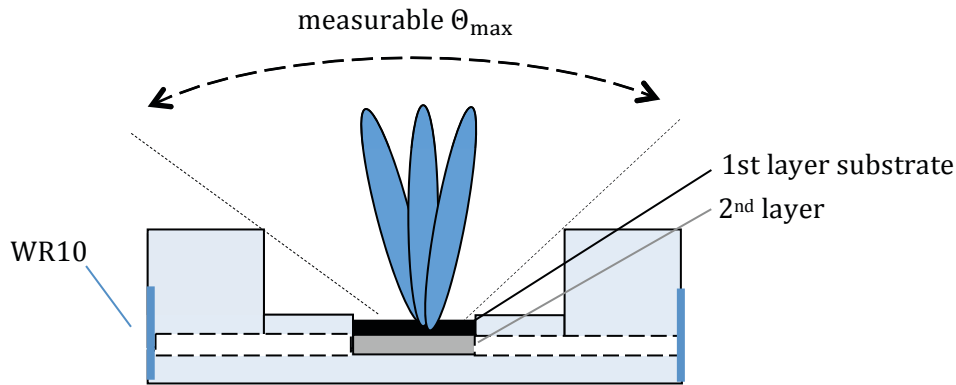


Figure 134 Mechanical Model with one layer TWA

7.3. The LTCC Technique and the Need for Investigating its Properties

The designed antennas and circuits of 3, 4, 5, and 6, are developed for the Low Temperature Cofired Ceramic (LTCC) technique. Details on the LTCC technique are provided in [1] and [2] where it is compared with conventional PCB techniques and proposed as a reliable multiple layer technology. In [4] it was shown how useful LTCC multiple layers may be for fulfilling e.g. the automotive radar requirements. The main advantages are the virtually unlimited number of layers, typically 64, that can be stocked, and the freedom of placing virtually unlimited vias on all layers since vias are drilled in the flexible *unfired* tape. All rules for the LTCC production at the ETS laboratories are found in [3]. However, though for lower frequencies up to 10 GHz production tolerances and margins are well predictable, for millimeter wave bands these tolerances become very important with respect to the guided wavelength. Recall e.g. Figure 23, where the importance of the slot width has been exposed. For the envisaged transition, this issue is as severe as for the slots. Relative to the wavelength, the shrinkage tolerances and uncertainty of the permittivity ϵ_r become a key parameter in the design. In particular, since the guided wavelength is a function of ϵ_r as well.

Therefore, in order to master the LTCC technique, and in particular to derive the loss, permittivity and shrinkage, a characterization circuit shall be manufactured mainly for obtaining the actual propagation constant β which serves as basic parameter to derive ϵ_r . Optical shrinkage measurements are performed on the same circuit, which shall apply the novel transition designed in the following.

7.4. Design of the Novel Two Layer SIW to RWG Transition

In this Section, the novel practical approach for designing a millimeter-wave transition at 76.5 GHz, from *one* SIW line on *two* LTCC layers to a rectangular waveguide, is presented in detail. To the best of the author's knowledge, this is the first feasible planar solution to couple a top-layer SIW exclusively. For this sake, a very small probe is cut in both layers and inserted into a milled clearance in the metallic RWG. Shrinkage tolerance is addressed in particular in the design procedure in 7.6.1.

7.4.1. Background and Context of this Transition

In contrast to radio frequency bands, measurement devices for millimeter-wave bands, such as network analyzers, currently rely virtually all on RWG technique. Consequently, to measure the SIW circuits e.g. designed in 4, robust transitions to interconnect the SIW with conventional millimeter-wave band RWG standards – such as WR12 – are required.

Available solutions that are based on 90°-vertically slot coupled RWGs or superposed patch antennas [5, 6] are less suited for antenna arrays, which require a wide angle of free sight. Moreover, to keep the fabrication effort low, horizontal waveguides are preferred since they are straightforwardly milled into the lower and upper half of a metallic fixture. For this sake, the SIW is connected congruently with zero distance to the RWG by widening its width appropriately [7]. In practice, it is indispensable to insert the substrate into the RWG to avoid leaked waves. However, due to the different dielectric constant, a perfect impedance and mechanical match are not feasible by this technique. Thus, for one layer, probes of the equivalent RWG width have been proposed, which achieves increased E-field coupling [8].

Recently, the general feasibility of Low Temperature Co-fired Ceramics (LTCC) for millimeter-wave bands has been demonstrated [9, 10]. In combination with SIW, LTCC allows an exceptionally high integration of all modules of the circuit, even providing a varying relative permittivity among layers if required. However, the current trade-off at millimeter-wave frequencies above 60 GHz is the few work on LTCC material characterization. In addition, the application of the latter reviewed transitions for multilayer LTCC requires solving two particular issues. First, the probe can be only cut in all layers simultaneously. However, sandwiching multiple layers in the RWG, as mentioned above, increases the RWG height. This leads to significant decrease in coupling to the aimed layer while all others are spuriously excited at the same time.

Secondly, LTCC requires the consideration of its particular attribute of the unpredictable effective planar shrinkage. This is mainly true for back-to-back and multi-port projects. An imprecise substrate length cannot be corrected by moving the circuit away or towards the transition, at least not equally at all ports.

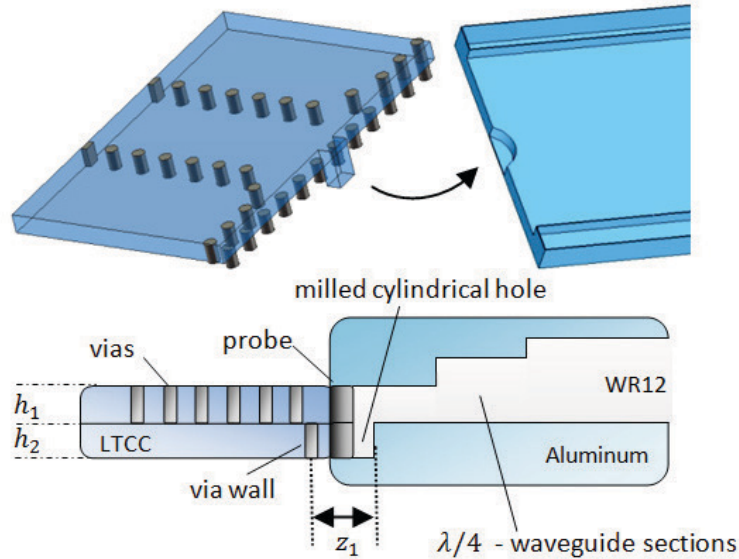


Figure 135 Substrate integrated waveguide including probe and rectangular waveguide, side view

Recently, beyond the known average shrinkage, empirical studies have tried to better anticipate the size reduction [11]. It is therein considered as a function of the metalized surface and lamination pressure. However, even including those new findings, shrinkage uncertainties in the range of 0.25 % (with respect to the unfired LTCC) are common, corresponding to approximately 1/8 of the maximum shrinkage range (1-2 %) typically specified by laboratories. In case of electrically large substrates, these variations become crucial. The larger the substrate, the more the proportions are impacted within the transition. For this thesis, the envisaged substrate length was at least $10\lambda_g$. Therefore, a novel design for two layers should be also robust against shrinkage tolerances of the above mentioned span. This minimizes the very laborious work of optical shrinkage measurement and post-production trimming.

To overcome the LTCC shrinkage issue, a designed gap between both waveguides is inevitable. Moreover, to minimize the excitation of the 2nd layer, a cylindrical hole is milled into the level of the metallic RWG fixture where – on the LTCC side – no excitation is desired. See Figure 135 for a

side view of this idea. The design procedure in 7.4.2 discusses the SIW, the probe size and the position in the hole, as well as the RWG layout. Shrinkage and LTCC characterization are discussed in 7.6.1. Afterwards, results of a full back-to-back implementation are presented.

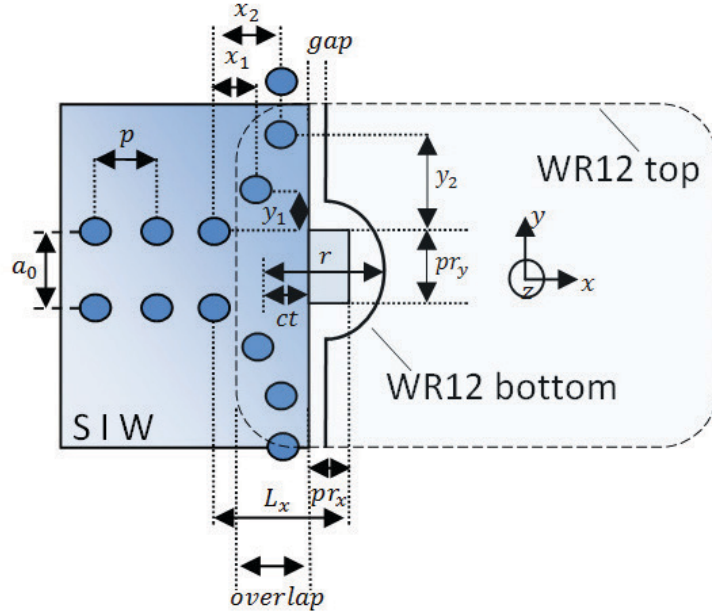


Figure 136 SIW to WR12 transition overview, ct is defined for the default gap

7.4.2. Via Configuration and Cylindrical Hole Design in the RWG

On the 1st LTCC layer, the SIW in question is widened to approach the WR12 width, i.e. two vias in its wall are moved outwards, as seen in Figure 136. Subsequently, a rectangular probe of the size $pr_x \times pr_y$ is cut in the edge of the substrate by means of laser, at this step, only in the first layer. Contrary to earlier referred one layer solutions, the probe width pr_y is kept very small to about 1/10 of the equivalent RWG width a_{RWG} derived via (5). Neglecting the second layer at this step, $y_{1,2}$, pr_x , pr_y and roughly $x_{1,2}$ are then optimized for the center frequency, by solely exciting one layer with both SIW and RWG congruently placed at a minimum distance.

Nevertheless in fabrication, all superposed layers are cut likewise as a mechanical constraint. A small cylindrical hole of the height h' , (arbitrarily $h' = h_1$) and the radius r is consequently milled into the metallic fixture underneath the waveguide to receive the probe partly, see Figure 135 and Figure 136. Its center has a distance of ct from the edge. Thus, the inserted probe faces metal on the lower level from $-h'$ to 0 and the free waveguide on the upper level, from 0 to h_1 . The radius is cho-

sen in line with the probe size, i.e. guaranteeing sufficient space for vertical and horizontal shrinkage deviance, while minimizing the 2nd layer excitation. See Table 6 for a full list of all parameters. To complete the list, the SIW width a_0 is 1.2353 mm, which results in a guided wavelength of λ_g of 1.96 mm for the derived minimal ϵ_r , hence the pitch p is well $< 1/5 \lambda_g$ see also Table 6. Note that we are dealing with remarkable small cutting-edge dimensions regarding the hole, see Table 6.

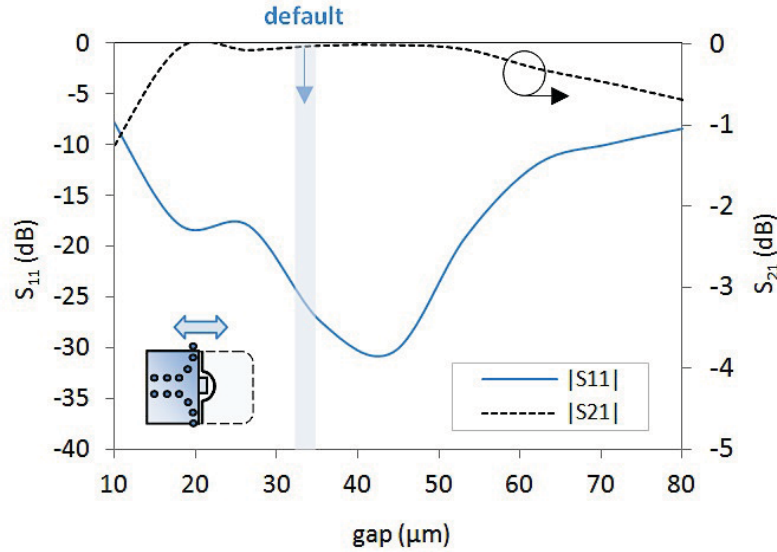


Figure 137 Input reflection and transmission as a function of the air gap, at CF, simulated with CST

Next, in order to enhance the isolation between the 1st and the 2nd layer, a via wall of the same pitch p is designed on the 2nd layer. As an initial position, it should be placed under the last via of the first layer. Yet, the final distance from the via center to the cylindrical hole wall, z_1 in Figure 136, must be optimized again as the last step of the design.

Subsequently, to raise the robustness against LTCC shrinkage issues, a gap is introduced e.g. corresponding to the known shrinkage standard deviation. The latter basically depends on the reproducibility of the lamination temperature curve and pressure. Alternatively, if unknown and for prototypes, the half of the expected reduced tolerance is chosen, (plus a very small margin for mechanical reasons). This gap is set to 0.0333 mm for this study. The parameters L_1 , L_x , ct , z_1 , r , and $x_{1,2}$ are optimized such that optimal coupling is achieved with the kept gap. The initial length for L_1 can be set slightly below $1/4 \lambda_g$ in the RWG, whereas the initial value of L_x is $\lambda_g/4 + pr_x$ in the SIW. Since L_1 and L_x form mainly the frequency response around the CF, the two resonances allow to increase the BW if designed to be at about the limits of the envisaged band (compare later with

Figure 149). The gap must be covered by a small overlapping RWG top cover. It carries a length named *overlap* in Figure 136. Recall that all parameter values are listed in Table 6.

Table 6 Transition Parameters

<i>Symbol</i>	<i>Value in mm</i>	<i>in λ_g(*)</i>	<i>Symbol</i>	<i>Value in mm</i>	<i>in λ_g(*)</i>
$\mathbf{a_0}$	1.235	n/a	$\mathbf{L_x}$	0.661	0.3379
$\mathbf{a_{WR12}}$	3.0988	n/a	$\mathbf{L_1}$	1.049	0.2073†
\mathbf{p}	0.326	$\approx 1/6$	$\mathbf{L_2}$	1.277	0.2319†
$\mathbf{x_1}$	0.286	0.146	\mathbf{R}	0.397	0.2029†
$\mathbf{y_1}$	0.286	0.146	\mathbf{Ct}	0.203	0.1037
$\mathbf{x_2}$	0.384	0.197	$\mathbf{h_1}$	0.210	n/a
$\mathbf{y_2}$	0.652	1/3	$\mathbf{h'}$	0.210	n/a
$\mathbf{pr_x}$	0.162	0.0828	$\mathbf{h_2}$	0.775	n/a
$\mathbf{pr_y}$	0.263	0.1346	$\mathbf{h_{WR12}}$	1.55	n/a
<i>Overlap</i>	0.133	0.0679	<i>gap</i>	0.033	0.017
$\mathbf{z_1}$	0.328	0.164	<i>average shrinkage (planar) = 12.7%</i>		

(*) for the minimum value of the obtained ϵ_r , † guided wavelength in WR12

To test the robustness against shrinkage issues, a parametric study with a variable gap, depicted in Figure 137, is carried out. In a range of about $\pm 40 \mu\text{m}$, reflection and insertion loss perform well, with an insertion loss $< 0.5 \text{ dB}$ for a single transition, and return loss $> 10 \text{ dB}$.

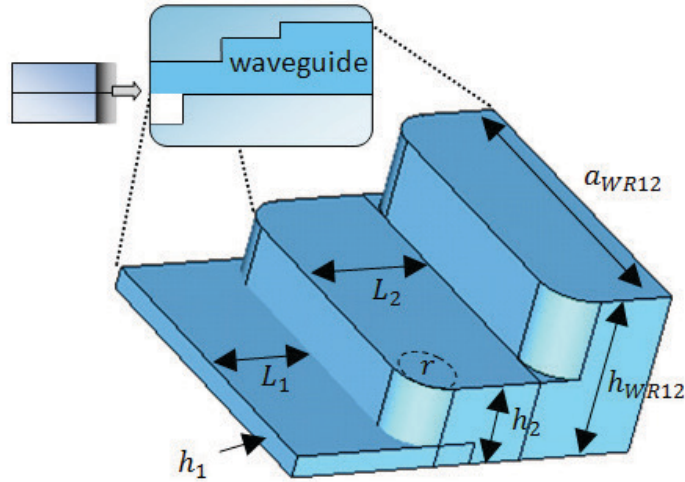


Figure 138 Three step waveguide impedance transformer

The remaining section of a joined air-filled RWG in Figure 138 is designed in a two-step architecture. It is implemented by a top and a bottom part made of Aluminum. The first section of length L_1 provides the same height as the excited LTCC layer, i.e. $h_1 = h_{SIW}$. It is underlined that, in contrast to [7], L_1 plays a substantial role in the design. As seen previously in Table 6, L_1 is significantly below $\lambda_g/4$ due to the gap and probe. The mid-section is outlined by L_2 , and $h_2 = h_{WR12}/2$, whereas the final section consists of a regular WR12.

7.5. Design of a Three Channel Fixture Comprising the New Transition

The fixture itself comprises the transition and the three step waveguide impedance transformer of Figure 138. Three back-to-back waveguide channels are designed. WR12 flunches, see also drawings in the ANNEX, are designed at each of the six in and output ports. All three channels yield equal ϕS_{21} as one major boundary condition for the design, this is depicted in Figure 139. The effort to design three instead of one complete channel is justified by the highly increased precision of the material study, later discussed in the result Section 7.6.1. THRU and LINE calibration is therein not measured with the same RWG. Due to the gap which has a severe impact on the results, it is important that for each channel, the same gap is applied which impacts the measurement equally. This has been shown previously in Figure 137.

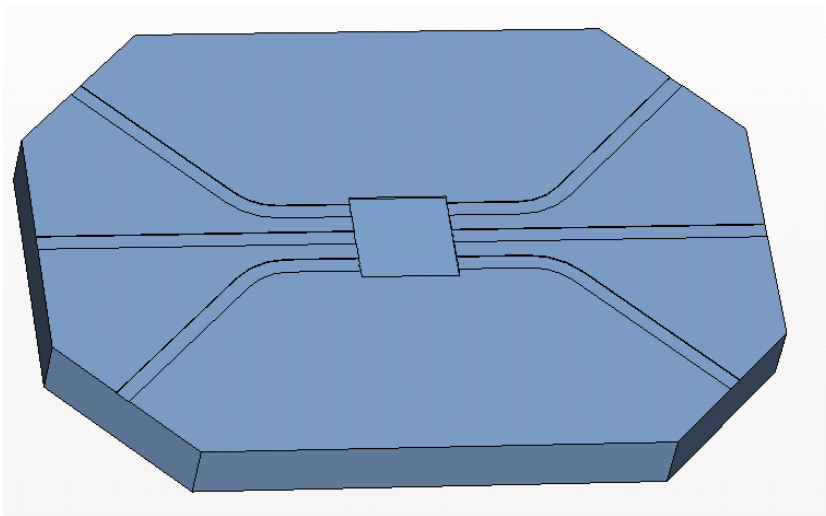


Figure 139 Horizontal cut through the fixture

If for each measurement the circuit was replaced, an unknown effective relative position to the walls would yield a degraded measurement. Only by this approach the total LTCC characteristics are obtained. In addition, two further beams for concepts of 5 and 6 can be produced at the same time.

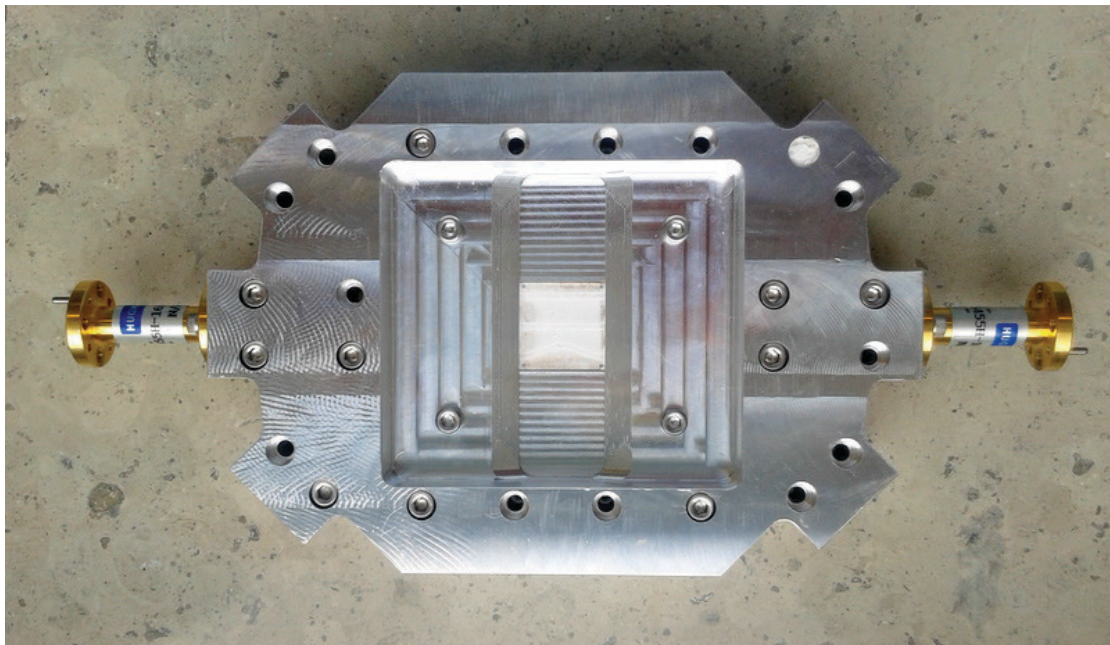


Figure 140 The fixture

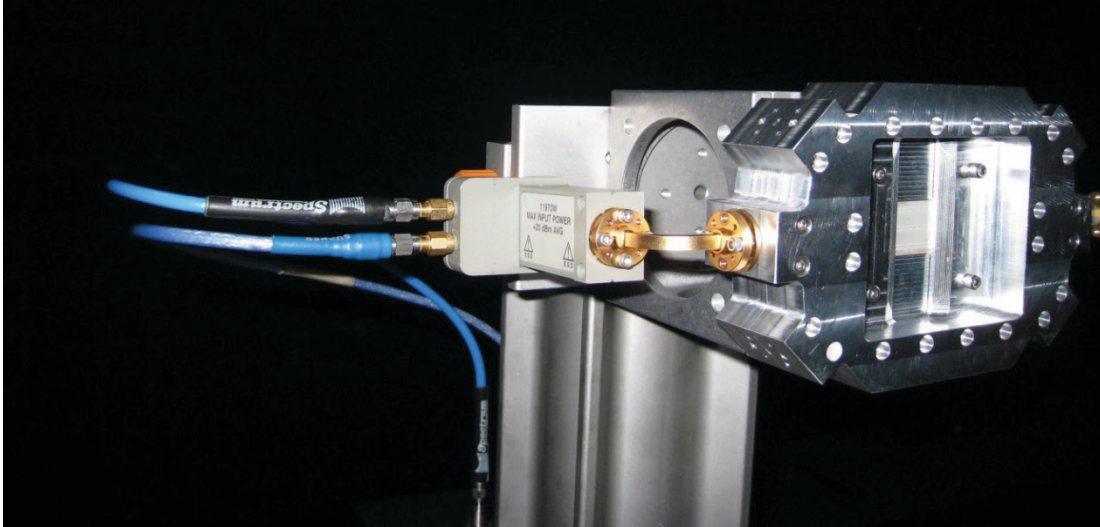


Figure 141 Fixture applied in anechoic chamber

A picture of the fixture including the calibration and material characterization circuit is depicted in Figure 140. Figure 141 depicts its use in an anechoic chamber respectively, with a matched absorber, at the *University of Bremen, Germany*.

7.6. Circuit Fabrication a. LTCC Characterization Applying the Conceived Fixture

The ceramic tape DuPont951 of a nominal $\epsilon_r = 7.8$ is used for simulation and fabrication of the proposed idea. This tape was previously assumed to undergo a significant dispersion in millimeter-wave bands [9, 10]. This is one important proposition to be verified in this Section. The expected default shrinkage is 13 %, i.e. 0.87 times the unfired dimensions. The thickness of either layer is 0.2096 mm, after firing the LTCC.

7.6.1. Shrinkage Measurements of Micrographed LTCC circuits

Fabricated prototypes of LTCC circuits have been micrographed and analyzed by optical measuring methods. An average shrinkage of 0.873 was expected. The distance between on-board designed donut marks, see Figure 142, Figure 144, and Figure 145, was measured and the shrinkage was found to be 0.8696, i.e. 13.04 % diminished instead of 12.7 %, again with respect to the unfired LTCC. Hence, with respect to the expected shrinkage, the substrate shows a fault length on either side. In our design, this error equals to $-34 \pm 2 \mu\text{m}$. Figure 142 depicts the cut substrate in the waveguide. Figure 143 shows the probe and vias in a vertical cut. Note that after laser cutting, the residues of the cutting process have been removed by sandpaper.

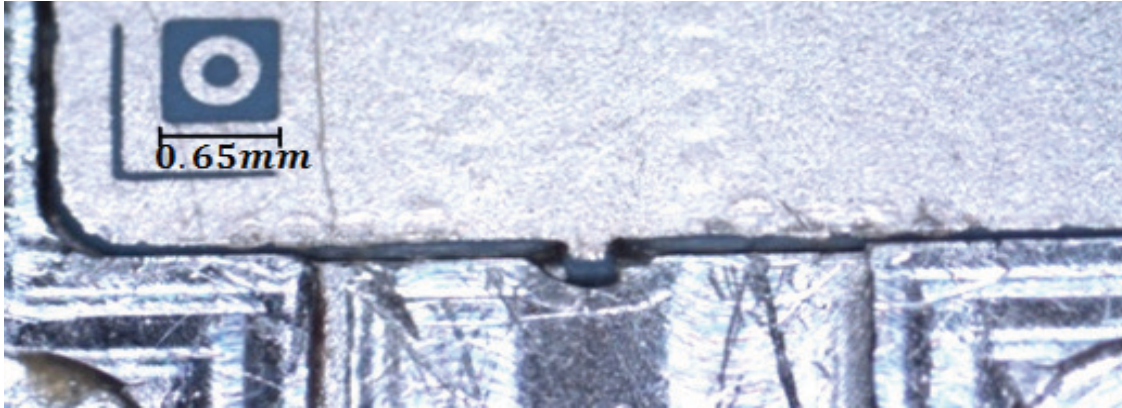


Figure 142 Probe in waveguide cylindrical hole and optical calibration donut mark

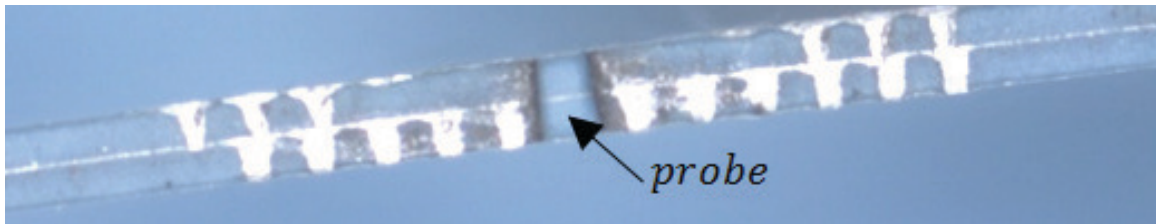


Figure 143 Laser cut through two layer LTCC, probe and slightly impaired vias

7.6.1. Material Study on LTCC

In order to experimentally prove the concept and usefulness, back-to-back WR12-SIW-WR12 transitions are fabricated and measured. In the first place, they were applied to obtain the unknown dielectric loss and relative permittivity of the substrate at CF by means of THRU (T) and LINE (L) measurements of the circuit depicted in Figure 146. In [9], the range of ϵ_r has been determined to be $\approx 7-7.4$ at 60 GHz.

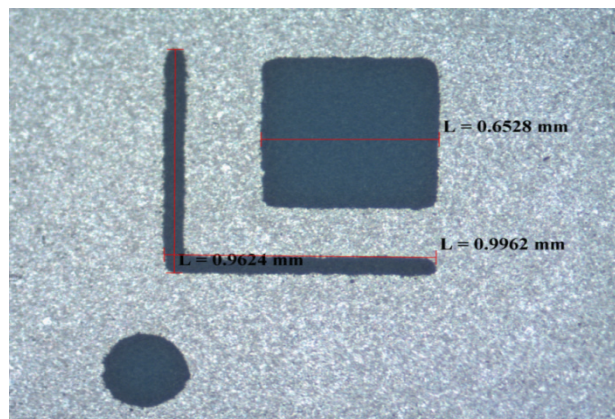


Figure 144 Optical Measurement of LTCC shrinkage

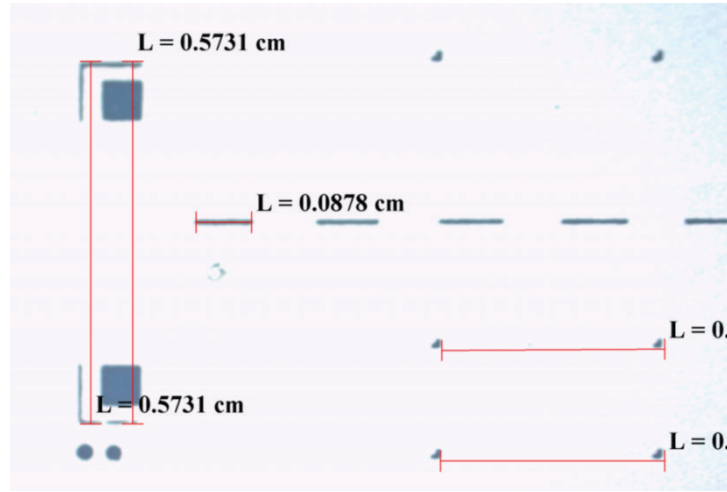


Figure 145 Optical measurements of LTCC shrinkage result

In contrast to a planar microstrip or CPW experiment, this waveguide approach has the advantage to solely consider the *relative* and not the *effective* permittivity, including the calibration. This avoids questioning the result of ϵ_r derived from the measured ϵ_{eff} at these frequencies by (44).

$$\epsilon_{eff} = \frac{\epsilon_r + 1}{2} + \frac{\epsilon_r - 1}{2} \left(1 + 12 \left(\frac{h}{W} \right) \right)^{-0.5}, \quad (44)$$

with h being the microstrip substrate height and W the width. In order to further enhance the quality of the characterization, special attention was paid not to alter the results by falsely measuring T and L with a different gap. For this sake, the same substrate carries T and L , which are quantified in a fixture containing three back-to-back transitions, see Figure 146 as well. The LTCC $\tan\delta$ was found to be about 0.009-0.01, which is slightly higher than the range in [9] but below some values for lower frequencies, provided by the manufacturer [12].

The permittivity is now determined by means of comparing $\Delta\phi_{S_{21}}$ and $\Delta length$ of T and L , applying a_{RWG} as the common known width [13]. That is, with the measured $\Delta\phi_{S_{21}}$, (45) is solved for ϵ_r , which yields 6.8-7.0 at CF. The length difference is determined by optical measurements similar to Figure 144. Note that, to obtain the permittivity from (45), the waveguide width a_{RWG} has to be known.

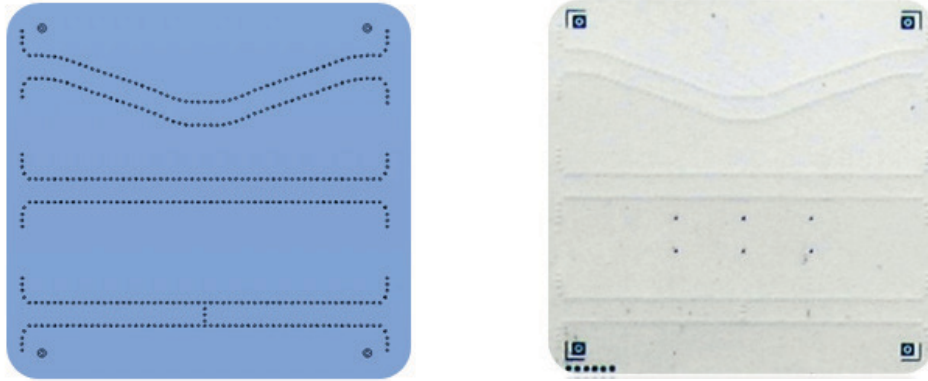


Figure 146 TRL measurement, (left) drawn circuit (right) photographed circuit

Measurements are depicted in Figure 147. Here, the equivalent waveguide based on relation (5) is used, corrected with the effective shrinkage factor. The interval of ϵ_r provided earlier (6.8 - 7.0) reflects the tolerances in the measurement of $\Delta\phi$ and exact determination of the relevant $\Delta length$ of the bent SIW. Also, a general distribution range of ± 0.2 given by the manufacturer must be considered [12]. These experiments equally discovered the loss of the (very spacious, see Figure 140) fixture due to mechanical miss-alignment of the walls and flanges. It is quantified by shortening the waveguide before the transition. It is discovered to be ≈ 1.5 dB, yet, this also includes the theoretical waveguide loss of 0.2 dB for the 13 cm Al-WR12 section at CF.

$$\Delta\phi = \Delta l \sqrt{\left(2\pi f \sqrt{\frac{1}{\epsilon_r c^2}}\right)^2 - \left(\frac{\pi}{a_{RWG}}\right)^2} \quad (45)$$

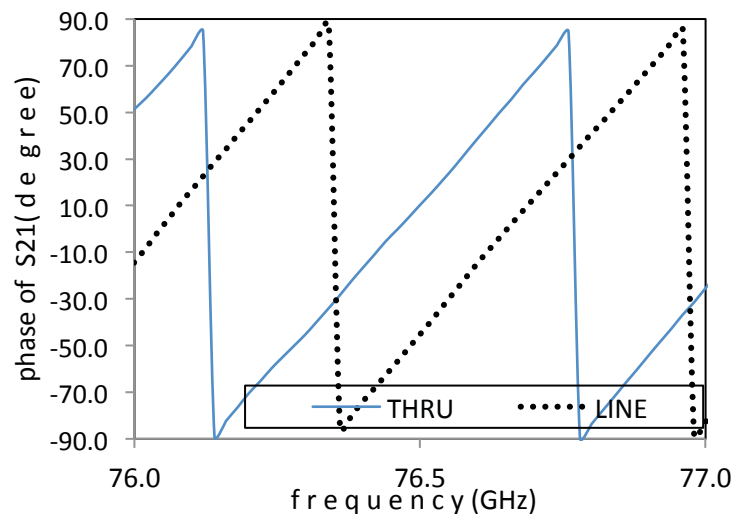


Figure 147 Comparing $\Delta\phi S_{21}$ measurements of THRU and LINE

7.7. Experimental Results and Discussion

In the first place, a back-to-back SIW–WR12–SIW transition has been simulated *without* LTCC losses and with an *expected* degree of shrinkage. Figure 148 depicts the S–parameter results. Two resonances at the CF of 76.5 GHz and above ensure a relatively wide 10 dB impedance BW of 9 % as well as virtually no insertion loss in the envisaged band, which is 1 GHz for radar applications [14]. Insertion loss would be for instance caused by spurious excitation of the 2nd layer. Leakage and reflection are both very low for this default case without considering a possible deviation from the expected shrinkage.

Secondly, the measurement results of a fabricated back-to-back WR12–SIW–WR12 are shown in Figure 149, therein the simulation was carried out with the minimal $\epsilon_r = 6.8$. The RWG is air-filled and of aluminum, and the appropriate LTCC loss $k^2 \tan \delta / 2\beta$ was subtracted appropriately, in addition to the fixture loss. It is assumed again that a_{RWG} is well known from a_0 by (5). While $|S_{21}|$ shows some ripples, it stays nevertheless in a good agreement with the simulation. Insertion loss for the single transition is better than 0.7 dB at CF. Recalling Figure 137, for this gap, a small loss of about this value is expected.

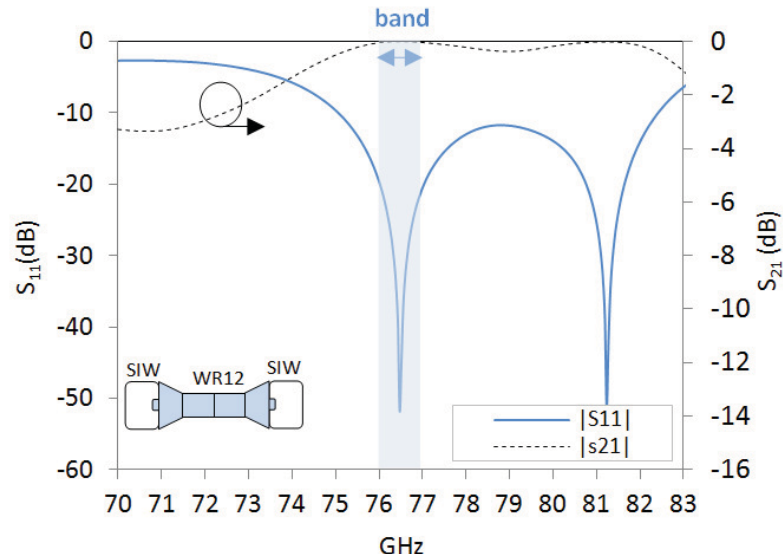


Figure 148 Lossless results of back-to-back SIW-WR12-SIW trans., gap=0.033 mm

Recall that the shrinkage absolute tolerance of about 1-2 % commonly specified by laboratories has been reduced to about a quarter by taking into account [11]. However, the fabricated circuit has

entirely exhausted the envisaged range. Yet, the insertion loss is still very good. Within the envisaged band, the reflection coefficient remains < -10 dB for 74.5 GHz. Above at 77.5 GHz, very good values are achieved as well. Beyond these frequencies, S_{11} reveals differences between simulation and measurements. Two reasons are most likely responsible: The 2nd layer is to some extent more excited than in simulation, due to unfortunately slightly impaired vias (by the laser cutting process), seen in the micrograph Figure 143. The second reason is the influence of the screwing of top and bottom RWG. At these frequencies, screwing produces some unavoidable non-alignment of the walls which causes some loss but also shows a slightly shifted S_{11} result each time the RWG top and bottom parts are screwed together.

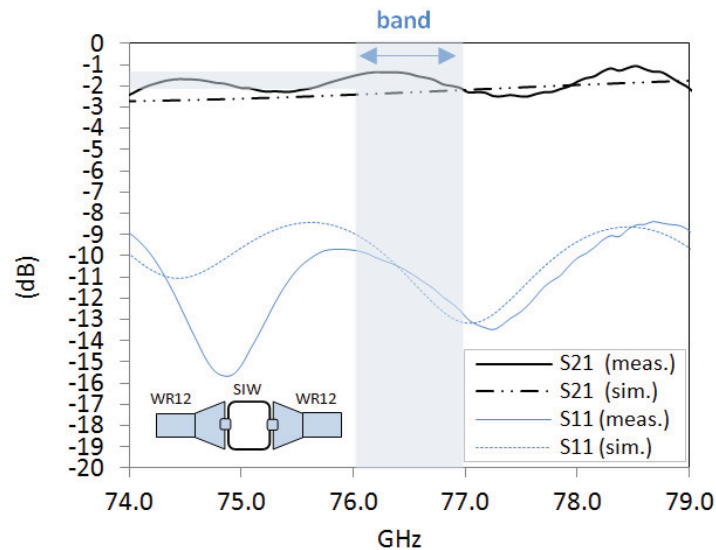


Figure 149 Measured and simulated reflection and transmission, with a shrinkage error of $\approx -34 \mu\text{m}$, WR12-SIW-WR12 section, (see text for loss, ϵ_r , etc.)

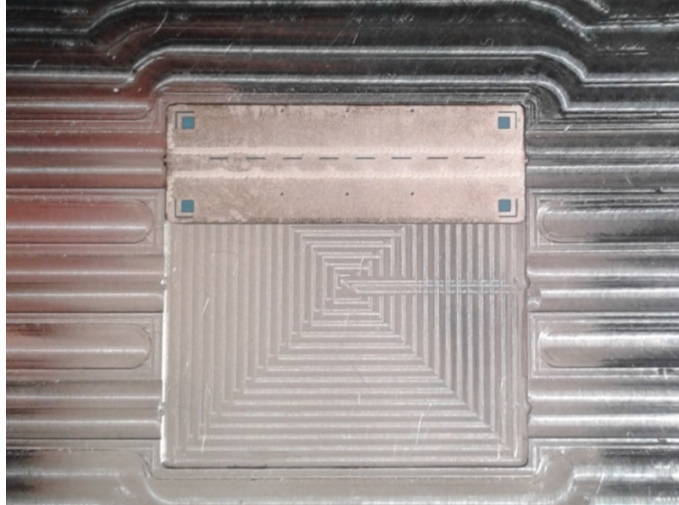


Figure 150 Circuit in Fixture with transition

7.8. Conclusion

To sum up, a new very practical millimeter-wave transition for joining an RWG with the 1st layer SIW of a two layer LTCC has been proposed in this Chapter. It addresses both the shrinkage tolerances typically seen with this material, as well as the avoidance of a 2nd layer excitation. The LTCC $\tan\delta$ and ϵ_r have been determined through a LINE and THRU measurement to distinguish the transition loss from the actual transmission line loss.

These novel purely intra-substrate experiments further confirm the strong dispersion of the LTCC. These experiments allow avoiding the uncertainties that occur when the relation of (44) is used to derive the relative permittivity from the effective one of a microstrip.

Simulations, with and without a varying gap, as well as the measurements on the fabricated back-to-back transition prove the concept of transition and fixture. Fabricated LTCC circuits have been analyzed optically and even exceeded the total estimated shrinkage range. However, the transition shows good insertion loss < 0.7 dB and a good matching with RL < 10 dB in the envisaged band. These results allow recommending this transition for two layer LTCC SIW projects up to an approximate circuit length of $12 \lambda_g$ in comparable environments. Thus, this transition and fixture is eligible for measurements on all other circuits on CF as e.g. shown in 4, and exemplarily depicted in Figure 150 holding an antenna array. The completed material study of LTCC allows anticipating shrinkage and permittivity sufficiently. This project has been a first and pioneering LTCC lab project in millimeter bands at the ETS de Montréal, which has been published in [15, 16].

7.9. References

- [1] I. Wolff, "Design and Technology of Microwave and Millimeterwave LTCC Circuits and Systems," Signals, Systems and Electronics, 2007. ISSSE '07. International Symposium on , vol. no., pp.505,512, July 30 2007-Aug. 2 2007
- [2] R. Kulke, M. Rittweger et. al., "LTCC - Multilayer Ceramic for Wireless and Sensor Applications", Hg. v. IMST GmbH. <http://www.seaceramics.com/Download/Papers/doc-plus-01-engl.pdf>
- [3] N. Gravel, "Aperçu des règles de conception LTCC. École de technologie supérieure ", ÉTS, Montreal, QC, Canada, 2010
- [4] P. Uhlig; C. Günner; S. Holzwarth; J. Kassner; R. Kulke; A. Lauer; M. Rittweger , "LTCC Short Range Radar Sensor for Automotive Applications at 24 GHz", IMST GmbH, Kamp-Lintford, Germany, 2004
- [5] Q. Zhang and Y. Lu, "E-band T shape transitions between substrate integrated waveguide and standard waveguide", Microwave Conference, APMC, pp. 1–4, 2008
- [6] J. J. Lee, K. C. Eun, D. Y. Jung, et.al. , "A Novel GCPW to Rectangular Waveguide Transition for 60 GHz Applications", Microwave and Wireless Components Lett., IEEE, Vol. 19, No. 2, pp. 80–82, 2009
- [7] B. Boukari, E. Moldovan, S. Affes, K. Wu, R. G. Bosisio, and S. O. Tatu, "Robust Microstrip-to-Waveguide Transitions for Millimeter-Wave Radar Sensor Applications", Antennas and Wireless Propagation Letters, IEEE, Vol. 8, pp. 759–762, 2009
- [8] E. Moldovan, R. G. Bosisio and K. Wu, "W-band multiport substrate-integrated waveguide circuits", Microwave Theory and Techniques, IEEE Trans., Vol. 54, No. 2, pp. 625–632, 2006
- [9] T. Baras and A. Jacob, "Manufacturing Reliability of LTCC Millimeter-Wave Passive Components", IEEE Trans. on Microwave Theory a. Techniques, Vol. 56, No. 11, pp. 2574–2581, 2008
- [10] S. Adhikari, A. Stelzer, et. al., "Characterization of LTCC substrate up to 100 GHz", International Conference on Microwave and Millimeter Wave Technology, Vol. 4, pp. 1776–1779, 2008

[11] M. Girardi, "Response Predicting LTCC Firing Shrinkage: A Response Surface Analysis Study", Journal of Microelectronics and Electronic Packaging, Vol. 6, No. 2, 2009

[12] DuPont, Green Tape - Low Temperature Co-fired Ceramic system, Guidelines, http://www2.dupont.com/MCM/en_US/assets/downloads/prodinfo/GreenTape_Design_Layout_Guidelines.pdf

[13] M. D Janezic, J. A. Jargon, "Complex permittivity determination from propagation constant measurements", IEEE Microwave and Guided Wave Letters, pp. 76-78, 1999

[14] Federal Communications Commission FCC 11-79, 2011

http://hraunfoss.fcc.gov/edocs_public/attachmatch/FCC-11-79A1.pdf

Published papers:

[15] F.D.L. Peters, T.A. Denidni and S.O. Tatu, "Two Layer LTCC Substrate Integrated to Rectangular Waveguide Transition and its Application for Millimeter-Wave LTCC Characterization", Microwave Opt. Technol. Letters, vol.54, pp 2675-2679, 2012

[16] F.D.L. Peters, "LTCC Millimeter Wave Applications: Transitions and Antennas with SIW", LTCC Workshop, Ecole Supérieure de Technologie, Montreal, QC, Canada, 2011

CHAPTER 8

CONCLUSIONS AND OUTLOOK

8.1. Conclusions

This work has elaborated slotted waveguides in three different arrangements. It has been based on complex S-parameter values of slotted elements, rather than resonant admittances, in combination with a traveling-wave approach. Based on parametric studies with an isolated slot in thin SIW, it has been confirmed that a pure resonant conductor does no longer occur. Since the reflection of longitudinal slots is high for reasonably radiating slots, a via has been added. The latter led to a discovery of the altered slot phase of the modified element. In fact, the via increases the transmission phase due to its inductance, hence, multiple via configurations have been studied to allow for internal phase shifting in the TWA other than by shifting elements.

Among the studied via configurations there is solely one partly resonant solution appropriate for the imagined purpose. The derived case provides at least 30 degrees of freedom in the slot phase design and keeps radiation constant. A very low reflection of $< -30\text{dB}$ has been obtained. Yet, it was shown that it is very important to monitor and keep a linear dependence of the radiation coefficient and the slot length rather than to minimize the return loss. Obtaining the design curves for these altered elements is not straightforward but interpolation can be applied upon three sampled slot lengths. The latter is feasible due to a fixed space between elements in the envisaged antenna array.

Resulting a consideration of the State-of-Art in the TWA design of longitudinal slots, three inconveniences can be emphasized. First, slot radiation is often kept artificially low, i.e. well below the physical possible coupling in order to avoid reflections. Secondly, a simplification considers the TWA as a purely forward traveling-wave even in the case of strong mutual coupling. Thirdly, the phase computation has been somewhat disregarded due to computational efforts. These three restrictions inconveniently brought together lead to poor side lobe performance. With the proposed combination of slotted elements and a signal flow graph, the issue has been resolved to a good de-

gree. Note that a signal flow graph becomes possible due to the assumed a priori condition of unchanged spacing between elements. Thus, the mutual coupling coefficients of the unmoved slots are known precisely from full wave simulation. The new approach still simplifies modeling with respect to a fully reverse signal flow graph. Nevertheless, it does not neglect backwards traveling-wave parts considered as mismatched elements of shown -10 dB. Comparing with the simplified computation of radiated power, the model is 1 to 3 dB closer to the desired ideal amplitudes.

Results of the 1st arrangement of antenna arrays are in general very good while measurements are ambiguous. The radiation pattern delivers low SLL of -27 dB before any other means of optimization. The impedance bandwidth is >10%, however, the array yields a low $|S_{11}|$ at CF in particular. The vias decrease the bandwidth slightly.

In the 2nd arrangement, beam forming has been envisaged by means of the derived elements while keeping a good control over the side lobes. The results are better than every other outcome of the literature where TWAs designed for broadside are modified for beam forming. The concept has been proven with three slightly shifted beams and side lobes <-20dB. However, to manage the same low SLL than for a broad side beam, future work with newer slot phase results is necessary.

In a 3rd arrangement, a slot antenna composed by four resonant sub-arrays been excited from either side by two SIWs of different widths located underneath, is presented. This approach yields four different beam angles. It was found that the slot coupling over two layers has a sever impact on the effective electrical length of the upper SIW resonant length. Four particular beams from -20° to $+20^\circ$ - have been designed. Arbitrary beam angles are possible by modifying the width of the feeding SIW. Good matching of -10 dB and better has been obtained for all ports at CF. The isolation between exciting ports could be kept above 15 dB and the maximum directivity is about 16 dBi and efficiency near 70 %. Therefore, this antenna is an ideal candidate for integration into multiple layer radar sensor projects. A monopulse application has been shown.

Regarding the project in general, faced challenges in terms of experimental circuits persist. This is admittedly based on the choice of LTCC. This technique turns out to be a good candidate for microwave and millimeter-wave bands for its undisputed ease of via drilling. However, a disproportionately long time had to be spent on studying the shrinkage factors and studying the SIW propagation constant. In addition, designing a new transition for two layers was indispensable due a minimum of

two layers in LTCC. This has been underestimated. Furthermore, the slot shape, the cutting residues and many broken circuits have earned us setbacks.

More severe difficulties have occurred with measured circuits that are based on uncontrollable small reflections caused by the mismatched termination at the end of the TWA. In fact, the screwing and aligning of the RWG did cause higher reflected power values than expected. Fortunately, this effect could be emulated also in simulations so that the total conclusion of the proposed solution is still positive. The lack of sound experience with this technique has been an inevitable challenge.

On the other hand, a sound transition has been the fruitful finding of the material choice. The outcome from the material study provided valuable empirical values for the LTCC technique.⁹ The observed effective shrinkage will help other projects to come up with closer results. It was revealed to be in the range of the anticipated value of 12.7%-13.3% but effectively 13.04 %. Dispersion was confirmed, the relative dielectricity differs by >20% from the nominal value. Instead of being 7.8, it was measured for the first time in a fully waveguide tool to be $\epsilon_r = 6.8 - 7.0$ at 76.5 GHz. Still, this tolerance of 0.2 is unsatisfactory too high for the envisaged very small relative via positions. The LTCC $\tan\delta$ was found 0.009-0.01, which is higher than expected. The new green tapes from DuPont with lower loss tangents are ready to use in future work with the same designed fixture.

The transition itself is based on the widened SIW on the surface with a small cylindrical probe in a half cylindrical hole in the other waveguide. The transition shows good insertion loss < 0.7 dB and a good matching with RL < 10 dB in the envisaged band. These results allow recommending this transition for two layer LTCC SIW projects up to an approximate circuit length of $12\lambda_g$.

To sum up, the present results confirm the initial hypotheses of a possible slight enhancement in the design of the TWA. It may be very helpful in all industrial applications where a fast procedure is required that allows to be applied solely based on once obtained S-parameter results for a couple of two slot simulations. The industry can rely on this proposed procedure.

⁹ and to the manufacturer of the GreenTape

8.2. Main Contributions of this Thesis

The main contributions of this thesis are:

- An enhanced traveling-wave slot antenna concept with a linearized straightforward model, configurable for particular beams,
- A MATLAB implementation with graphical user interface
- A planar LTCC to SIW two layer waveguide transition, that allows quantifying material characteristics, independently from microstrip,
- Characterization of LTCC material applying this transition,
- A new two layer 4-beam antenna with low space requirements,
- A new SIW antenna patch absorber with slight microstrip patch matching (ANNEX).

8.3. Outlook and Future Work

The faced issues in ANNEX A 2 require a solution. In particular, the waveguide or microstrip termination has been determined to be crucial for high side lobe performance.

To sum up the further future work to be accomplished:

- Multiple beam approach needs to be further exploited. The need for more precise phase equalization is evident to reduce further the SLL,
- SIW absorber shall be developed, i.e. inside the SIW material instead of a matched termination outside,
- Switches that are based on MEMS may be developed to switch between the beam formed arrays of Chapter 5 once the latter are improved,
- Remaining minor reflection of each *isolated* element shall be taken into account,
- Using more recent green tapes of DuPont in the fixture to reduce losses to a minimum.

ANNEXES

A 1 MICROSTRIP PATCH ANTENNA MATCHING BY PARASITICALLY COUPLED MICROSTRIPS

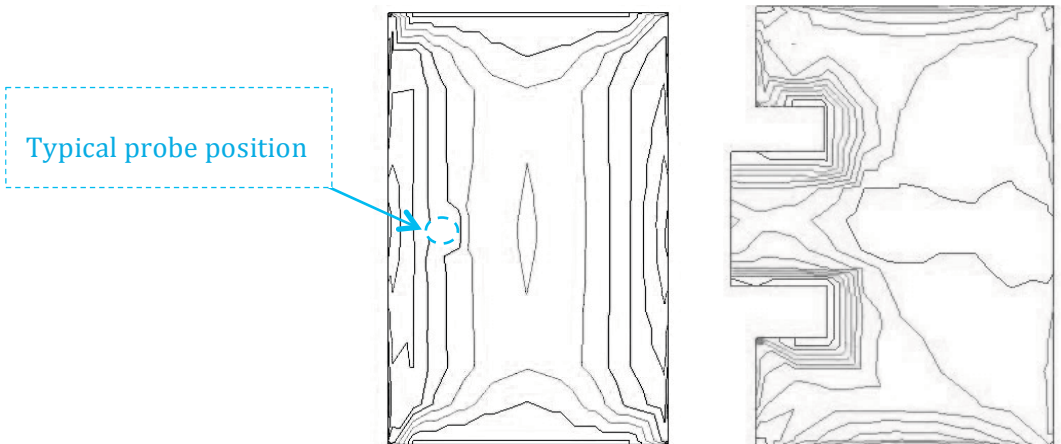
Introduction

In Section 3 and 4, a traveling wave antenna has been conceived that requires a termination to absorb the power rP that is residual at the very end i.e. after the last slot. For measurement purposes, a waveguide section is used that represents an absorber at the measured frequency. For this sake, a robust transition is developed in 7. However, some issues have been seen, see A 2 as well. As an auxiliary tool and probable solution for *real* applications, a second alternative shall be shortly described in this Chapter. It proposes the use of a matched microstrip patch at the end of the TWA that entirely overcomes the need of waveguide technology by absorbing otherwise lost rP .

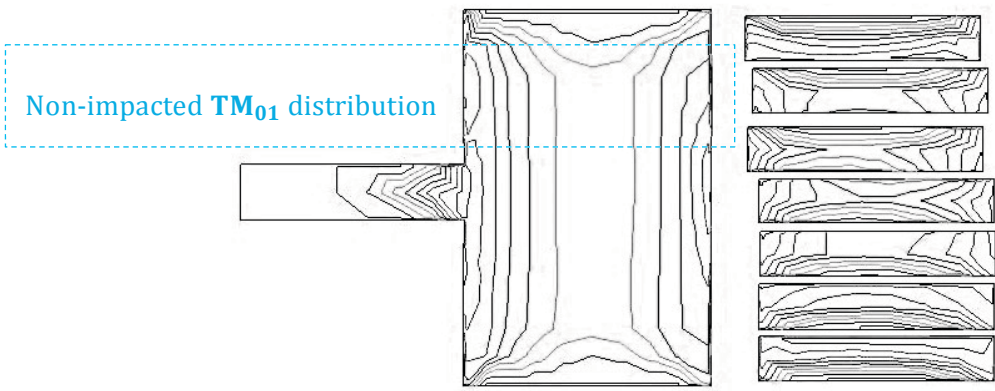
A microstrip patch antenna may be matched by the inset fed technique. However, the particular effect of the microstrip was not taken into account until recently [1-3] discussed these differences especially for the inset fed method. In particular, for some very large MS feds compared to the MS patch antenna width, no matching is achievable by this technique.

The Problem of Impedance Matching of Patch Antennas

Generally discussed in [4] and [5], the return loss of a mismatched microstrip fed antenna can be decreased significantly by an accompanying gap coupled microstrip element. This has been done for probe fed patches [6] and for a second patch [7]. Gap coupling for lower frequency bands is summarized e.g. in [8] and [9] which describe mostly probe fed constellations. Exciting multiple different resonance frequencies lead to broader impedance bandwidth and to improved gain when losses are low. This effect is applied and visualized in the following Figures.

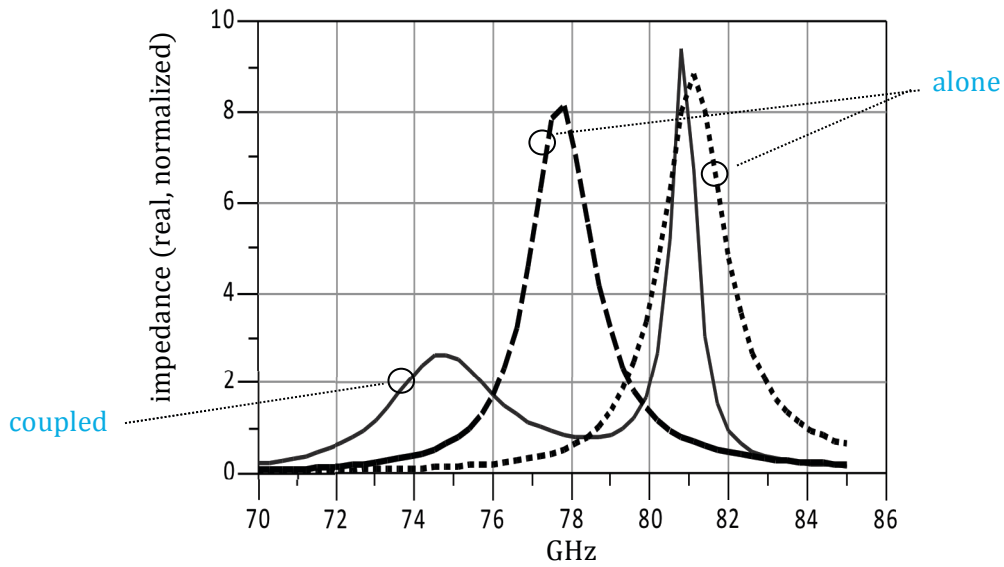


ANNEX - Figure 1 (left) Ideal current distribution of a probe fed patch, (right) inset fed patch with strong perturbation of ideal current

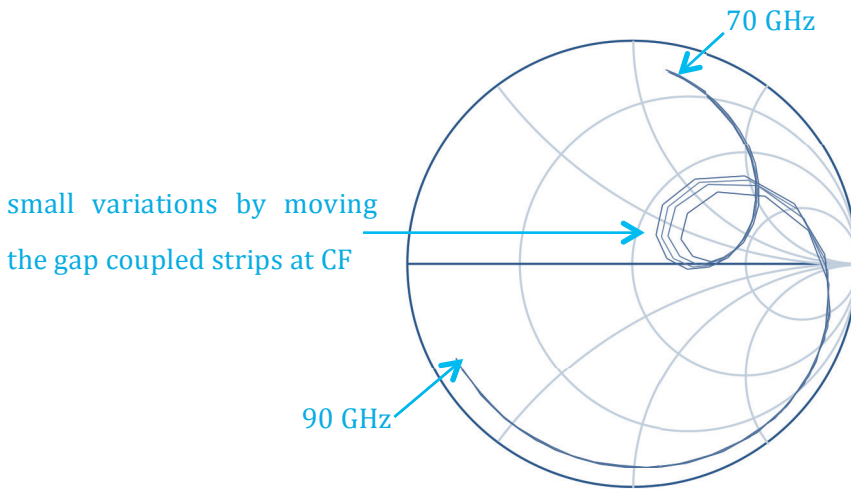


ANNEX - Figure 2 Homogenous field along y-axis in a wide zone, $\lambda/2$ variation over x-axis

The main basic patch is gap coupled to 5-7 individual microstrips of a different or equal length in ANNEX - Figure 2. Both, the main patch as well as the parasitic microstrips provide real impedance at resonance when observed independently. Brought together, the second parasitic resonance circuit is transformed into the input impedance. It is obvious that the length of both the patch and the small parasitic strips are independently defining the eigenfrequency.

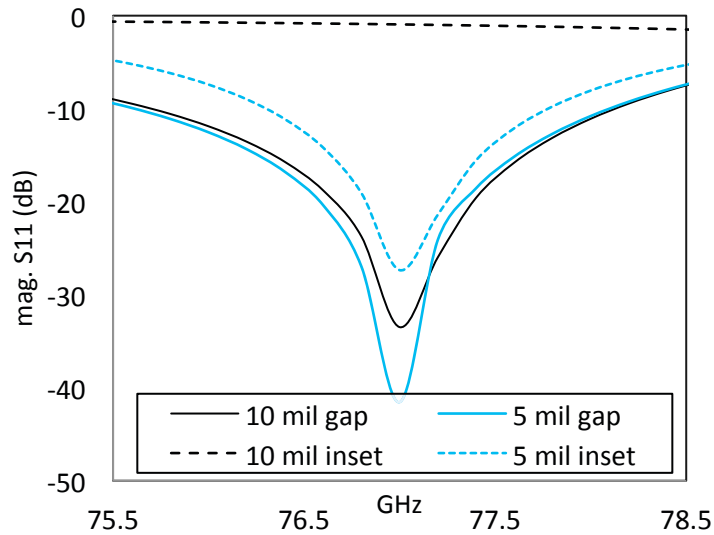


ANNEX - Figure 3 Real part of impedance shows two maxima caused by two eigen-frequencies



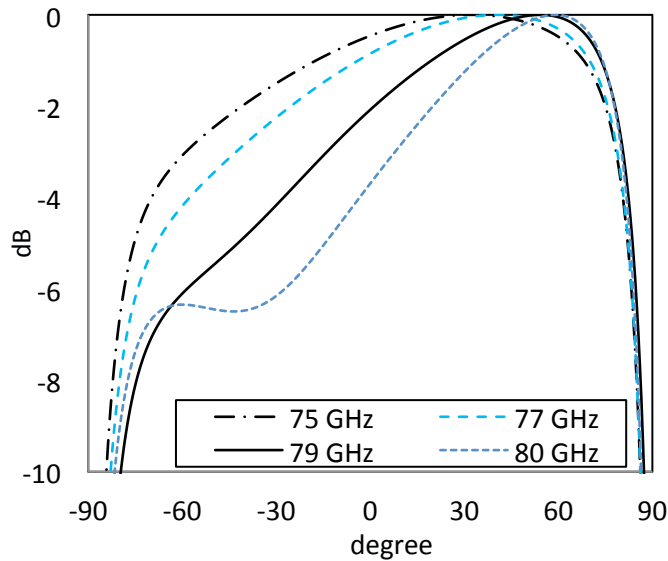
ANNEX - Figure 4 Due to the small narrow slots the »coupling loop« can be modified accurately

By manually increasing or decreasing the individual gap between the strip and the main patch, the loop size can be modified very precisely to achieve a perfect match at CF.

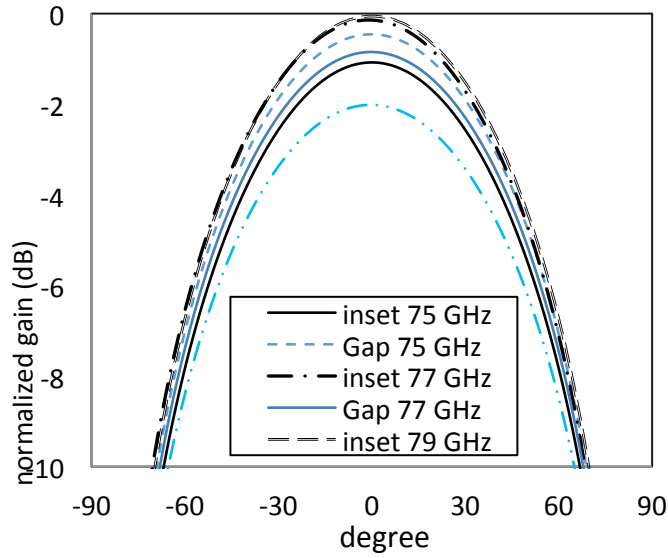


ANNEX - Figure 5 |S₁₁| comparison of both patch antenna matching methods for 10 and 5 microstrip widths

In ANNEX - Figure 5, conventional inset fed patches with 5 mil, resp. 10 mil = 0.254mm, are compared to the gap coupled equivalents. As discussed, no matching can be achieved with inset fed and 10 mil. In contrast, with gap coupling, bandwidth and matching are very good.

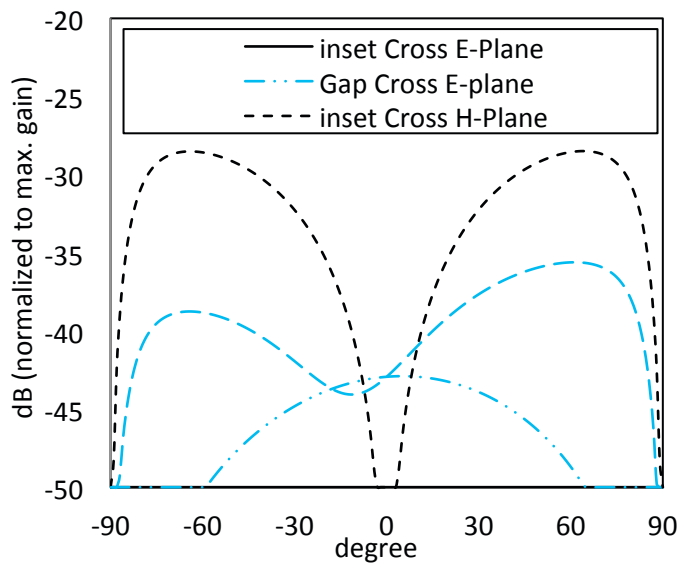


ANNEX - Figure 6 Gain of gap coupled patch with shifted radiation in E-Plane, (75-80 GHz)



ANNEX - Figure 7 Comparison of gain for inset and gap coupling matching at three frequencies, in H-plane, normalized

The effect on cross polarization is depicted in ANNEX - Figure 8. The parasitic microstrips introduce cross polarized radiation considered from E-Plane, on the other hand, in H-Plane, less cross polarization is observed than with the inset fed.



ANNEX - Figure 8 Cross polarization in H-Plane and in E-Plane

Table 7 Parameter Values for the patch termination of the hybrid antenna, $\epsilon_r = 9.8$

<i>width of MS</i>	<i>length coupled patch</i>	<i>length main patch</i>	<i>gap between</i>	<i>width of both patches</i>
<i>0.5mm</i>	<i>3.97 mm</i>	<i>4.34 mm</i>	<i>0.1 mm</i>	<i>8mm</i>

Conclusion

To sum up, limitations of the inset fed matching method have been outlined. A simple idea of several small microstrip lines which can be moved separately has been presented and implemented which allows increasing the bandwidth and to match with the feeding microstrip. Degradations in the radiation pattern are small. While the gain decreases slightly, bandwidth increases and the current distribution on the main patch shows a TM_{10} mode. This method has been studied as a potential candidate to match patches that may be used as a termination for other antennas like e.g. SIW slot antennas with residual power at the end.

References

- [1] M. Ramesh, Y.I.P. KB, and P. Motorola, "Design Formula for Inset Fed Microstrip Patch Antenna", Journal of Microwaves and Optoelectronics, vol. 3, no. 3, p. 5
- [2] L.I. Basilio, M.A. Khayat, J.T. Williams, et.al., "The dependence of the input impedance on feed position of probe and microstrip line-fed patch antennas", Antennas and Propagation, IEEE Transactions on, vol. 49, no. 1, pp. 45–47.
- [3] Ying Hu, D.R. Jackson, J.T. Williams, S.A. Long, and V.R. Komanduri, "Characterization of the Input Impedance of the Inset-Fed Rectangular Microstrip Antenna", Antennas and Propagation, IEEE Transactions on, vol. 56, no. 10, pp. 3314–3318.

- [4] Qing Song, and Xue-Xia Zhang, "A study on wideband gap-coupled micro-strip antenna arrays", *Antennas and Propagation, IEEE Transactions on*, vol. 43, no. 3, pp. 313–317
- [5] C.S. Lee, and V. Nalbandian, "Impedance matching of a dual-frequency microstrip antenna with an air gap", *Antennas and Propagation, IEEE Transactions on*, vol. 41, no. 5, pp. 680–682
- [6] Lee, C. S.; Nalbandian, V. (1993): Impedance matching of a dual-frequency microstrip antenna with an air gap. In: *Antennas and Propagation, IEEE Transactions on* 41 (5), S. 680–682.
- [7] Qing Song; Xue-Xia Zhang (): A study on wideband gap-coupled microstrip antenna arrays. In: *Antennas and Propagation, IEEE Transactions on* 43 (3), S. 313–317, 1995
- [8] G. Kumar, *Broadband microstrip antennas*. Boston Mass. u.a.: Artech House, 2003
- [9] S.Ghosh and K. Nirmala K. P. Ray, "Compact Broadband Gap-Coupled Microstrip Antennas", vol. 2006,

Published papers:

- [10] F.D.L. Peters, S.O. Tatu, and T.A. Denidni, "77 GHz Microstrip Antenna With Gap Coupled Elements for Impedance Matching", *Progress In Electromagnetics Research C*, Vol.9, pp. 35–45, 2009
Available at doi:10.2528/PIERC09060908

A 2 FACED ISSUES AND SOLUTIONS

Laser Cutting Impact and Handling of Residues

Cutting of the millimeter wave band circuits in LTCC has been performed by a laser. In general, the laser is the appropriate tool to cut edges in the range of 0.0254 mm. Thus, very fine lines especially around the waveguide probe of the transition developed and applied in 7.3 have been able to cut.

However, laser cutting has been discovered to be responsible for two accompanying drawbacks compared to mechanical cutting. The first minor drawback is a small margin to be added to cutting lines. About 1 mil of the material vanishes.

Second, this process causes a substantially thick residue of assumed ceramic oxide. The vertical view in Figure 143 reveals a black layer of oxide on the surface. The impact of this issue is low for microstrip technology. However, for the SIW transition of 7.3, this has been a huge issue. The solution was not as simple as sandpapering the waveguide face. It was important to limit polishing to a minimum reduction of the waveguide length, which is of high importance in the design. A couple of trials have been necessary to discover the best way to avoid destruction.

Waveguide Alignment Issues with Pins and Screws

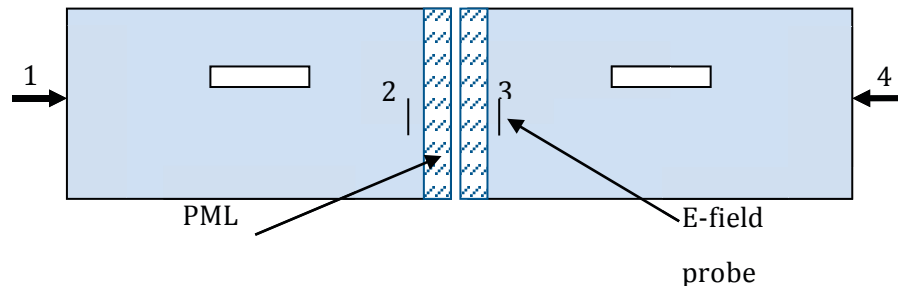
A critical feature and key part of the fixture are the alignment pins. In order to align, find and hold the correct position and relation of upper and lower part of the fixture, mechanical alignment holes have been produced on each side. The impact of this technique on measurement results is however significant. Although waveguide walls have been produced with an artificially raised up 'wall', the alignment does however play an important role in how to bring both walls together. Unfortunately, when the fixture of 7.3 has been measured, both the alignment pins and screws caused differing results from time to time screwed together. This was only mostly resolved by screwing and reassembling the fixture many times to find the perfect alignment

Limitations of Phase Measurements

While designing the THRU and LINE circuit entirely designed in LTCC in 7.6.1, a phase gap of about 45 degrees has been determined to be possible to achieve. The LINE curve could not be designed with a higher angle since reflections would become significantly different from THRU to LINE and thus Z_0 would not be equal. Consequently, to determine the material characteristics, the phase needs to be measured with a very high accuracy which is very difficult with the fixture, for the above mentioned reasons.

Simulation of the Mutual Coupling with HFSS

A simulation model in HFSS for the determination of the mutual coupling parameters of 4.3.2 is not straightforward to set up. Unfortunately, internal waveguide ports are not permitted with HFSS and lumped elements provide less accuracy. A different approach has been applied and drawn in ANNEX - Figure 9. Instead of a wave port, a perfect matched layer (PML) absorbs the traveling wave of the SIW. This PML is defined as 'continuous waveguide', i.e. it imitates a perfectly matched waveguide. It is important to provide HFSS with the desired propagation constant β of this layer. In order to obtain the desired power value and calculate the MC terms, E-field probes are placed close to the PML sections.



ANNEX - Figure 9 HFSS Simulation of mutual coupling

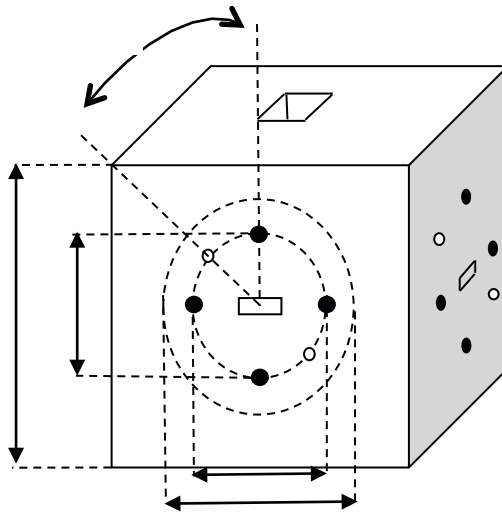
For some reasons, this does not give satisfying results. The input reflection differs significantly, i.e. higher than the MC may cause, from the isolated wave port terminated model. For that reason, CST and HFSS results differ in this matter and CST results have been taken in the first place.

Complex Termination and Transition Reflection

By far the most important issue is the complex reflection from the transition used to terminate the arrays. Due to a limitation of the surface, we had to terminate with a 50 Ohm resistance that allows the traveling wave concept to work. The assumption of no reflection was an essential boundary condition when the research objectives were defined. During the thesis we have derived that the mutual coupling coefficients are very important even with very small values. Unfortunately, the state of the art transitions and our own designed solution do definitely have reflections that are higher than the mutual coupling between elements. That is, the effect cannot be neglected when designing smaller arrays of $N = 4$ or $N = 8$. This issue was not resolved for conventional designs.

A 3 WAVEGUIDE WR12/WR10 FLUNCH

The flunch applied in the fixture is based on a standardized WR12 connector. The design is standardized such that the fabrication is done by standard milling tools. The following ANNEX - Figure 10 depicts this flunch and the surrounding holes for documentation.



ANNEX - Figure 10 RWG Flunch

A 4 COMPREHENSIVE LIST OF MATLAB FUNCTION CALLS

All Matlab Function Definitions ('calls') are provided herein for documentation.

Important Note:

All functions and scripts have been written by the author of this thesis, except for the commonly available MATLAB internal functions. These functions have been incorporated in the script without particular comments, these are for instance `fmincon()`, `xcorr()`, `filter()`, and other standard functions.

calc_TWA_interpol()

```
% ===== Traveling Wave Antenna Computation =====
% ===== (c) Florian D L Peters, University of Quebec, 2012-2014, =====
% ===== peters@emt.inrs.ca =====
%
% For full documentation refere to the article:
%
% " Internal Slot Phase Varying in Traveling-Wave SIW Slot Antennas and Appropriate Modeling "
%
% or visit the webpage:
% MATLAB FILE EXCHANGE:
% Manual:
function finish=calc_TWA_interpol(parameterfile,hN,hSSL,hrP,hType,hMC,hMC_neg,hloss)
```

GUI ()

```
function GUI()
```

Find_C_param()

```
% ===== Traveling Wave Antenna Computation =====
% ===== (c) Florian D L Peters, University of Quebec, 2012-2014 =====
% ===== peters@emt.inrs.ca =====
%
% function C= find_C_param(N,SSL,rP,type,loss_lin)
%
% This function derives the required radiation coefficients.
% It considers:
%     N = the number of elements = 2,4,8,16
%     SSL = the side lobe level (negativ!)
%     rP = the residual power, linear, e.g. 0.1=10%
%     type =
%         'cheb' : chebychef
%         'tay'  : taylor
%         'uniform' : uniform
```

```

%         loss_lin = power loss per lambda segment, linear factor!
%         e.g. 0dB, no loss means loss_lin = 1.
function C= find_C_param(N,SSL,rP,type,loss_lin) %#ok<INUSD>

```

find_length()

```

% ===== Traveling Wave Antenna Computation =====
% ===== (c) Florian D L Peters, University of Quebec, 2012-2014=====
% ===== peters@emt.inrs.ca =====
%
% function des_length = find_length(C,N);
%
% This file finds the initially best fitting slot lengths
% without considering mutual coupling.
%
% It considers:
%     C = radiation coefficients
%     N = number of elements

function des_length = find_length(C,N);

```

Initialisiere.m

```

%% ===== Traveling Wave Antenna Computation =====
% ===== (c) Florian D L Peters, University of Quebec, 2012-2014=====
% ===== peters@emt.inrs.ca =====

set(0,'DefaultFigureWindowStyle','normal')

```

Optimize()

```

%% ===== START OF OPTIMIZATION LOOP ( if optim =yes' ) =====
function finish=optimize(x,y)

```

Pow_err()

```

% ===== Traveling Wave Antenna Computation =====
% ===== (c) Florian D L Peters, University of Quebec, 2012-2014=====
% ===== peters@emt.inrs.ca =====
%
% function [amp_err,rad_pow,rad_ang,S11] = pow_err(l_initial)
%
% This core function computes the following results
%
% amp_err = criterion for amplitude precision
% rad_pow = the estimated radiated amplitudes
% rad_ang = the estimated phases
% S11 = estimation of S11 based on Mutual Coupling
%
% It requires solely input of the slot lengths of the array,
% but loads global variables from the Excel Input .m file.

```

```
function [amp_err,rad_pow,rad_ang,S11] = pow_err(l_initial,DPhifix)
```

Results.m

```
% ===== Traveling Wave Antenna Computation =====
% ===== (c) Florian D L Peters, University of Quebec, 2012-2014-=====
% ===== peters@emt.inrs.ca =====
%
% This script plots and displays results only.

global w;
global a;
global b;
global angD;
```

Calc_GUI()

```
function varargout = calc_GUI(varargin)
% CALC_GUI M-file for calc_GUI.fig
%   CALC_GUI, by itself, creates a new CALC_GUI or raises the existing
%   singleton*.
%
%   H = CALC_GUI returns the handle to a new CALC_GUI or the handle to
%   the existing singleton*.
%
%   CALC_GUI('CALLBACK',hObject,eventData,handles,...) calls the local
%   function named CALLBACK in CALC_GUI.M with the given input arguments.
%
%   CALC_GUI('Property','Value',...) creates a new CALC_GUI or raises the
%   existing singleton*. Starting from the left, property value pairs are
%   applied to the GUI before calc_GUI_OpeningFcn gets called. An
%   unrecognized property name or invalid value makes property application
%   stop. All inputs are passed to calc_GUI_OpeningFcn via varargin.
%
%   *See GUI Options on GUIDE's Tools menu. Choose "GUI allows only one
%   instance to run (singleton)".
%
% See also: GUIDE, GUIDATA, GUIHANDLES
```

CompNodes()

```
%
%   --- function [nod] = CompNodes(param) ---
%
% =====
% =====
% This function computes the node values as indicated in [2]
% in the main function
%
% input: parameter matrix
% output: node values
%
%  $\ddot{U}_n = \{ 1, \text{for } n = 1$ 
```

```

% = { x1, for n = 2
% = {(Ün-1)(xn-1)+(bn-2)(Ün-2), for n>=3
%
% RÜn = { 0, for n = N+1 (matched)
% = { S11_absorber for n = N+1 (unmatched)
% = { (ÜN-1)(eN-1) , for n=N
% = { (Ün-1)(en-1)+(Ün+1)fn+S12_n(RÜn+1), for 1<n< N
% = { (Ün+1)fn+S12_n(RÜn+1), for n=1
%

```

cc.m

```
close all;clear
```

optimZ()

```

% ===== Traveling Wave Antenna Computation =====
% ===== (c) Florian D L Peters, University of Quebec, 2012-2014-=====
% ===== peters@emt.inrs.ca =====
%
% function [X] = optimZ(l_initial)
%
% This optimizer function uses the slot length input in order to find
% the optimum slot length X which has the highest correlation with the
% distribution type set in 'type' prior to this function call. It does NOT
% consider phase.
%
% Its global variables are set in the initialisieren.m but should in
% general NOT be modified. The process of optimizing is monitored at
% the end in a separate figure called Iteration Process. A value of 0
% is the optimum. Values >> 1 are observable when the optimizer
% alters the slot length heavily. IN fact, it finds the optimal
% values by about 10 heavy alterations of slot length, which can be
% observed in the figure.
%
%
function [X] = optimZ(l_initial,DPhifix)

```

slotPow()

```

% --- function [rad_pow] = slotPow(nod) ---
%
=====
=====
% This function computes the slot radiated power
%
% input: node values
% output: radiated powers
%
% =====(c) FDL Peters Univ.du.QC 2012-2014=====
function [rad_pow,rad_ang] = slotPow(nod,param)

```

Example data

```
%
% ===== Traveling Wave Antenna Computation =====
% ===== (c) Florian D L Peters, University of Quebec, 2012-2014-=====
% ===== peters@emt.inrs.ca =====
%
%
% FILE ID : 10 GHZ - 4-8 elements
%
% This file receives your prerequired simulation results.
% Your input should be in the following format:
%
% global 'length';          % slot range declaration
% 'length'=[0.49:0.01:0.59]; % min, max and step size
%
% then all other parameters are the results for ALL steps declared in
% 'length'
%
% Example:
% -----
%
% global rho_excel;
% length=[0.49:0.1:0.51];
% rho_excel = [0.135 .22. 34 ];
%
% ..defines and assigns a value to the variable rho_excel for the
% length 0.49, 0.5 and 0.51. All other required steps are interpolated.
%
% MANUAL:
% -----
%
% Input in (1) the selection of length in guided wavelength @ CF,
% suitable for your array.
%
% Insert in (2) the rho and sigma values for at least the same number of
% steps you have provided in (1). [ units not relevant]
% rho := distance of via center from the lower SIW via wall center
% sigma := distance from left slot edge (centered)
%
% Insert in (3) the S21 magnitude and phase, lossless !
%
% Insert in (5) the vertical (e_y) component phase of the electrical
% field within the slot
%
% Insert in (6) the appropriate mutual coupling, accord to [1], for
% three constellations, for each constellation 4 slot length cases are
% required:
%
% the length constellations are: =
%
%                [min\max max\max
%
%                min\min max\min];
% where the first slot length is left in the MC simulation.
```

```

%
% Insert in (7) the S22 magnitude and phase, lossless !
%
% (8), (9), (10) R.F.U.

```

phiEyinterp()

```

% Function to obtain the interpolated values for right phi Ey (length)
% Call:
%     function des_phiEy = phiEyinterp(length)
function des_phiEy = RphiEyinterp(length)

```

Ph_fehler()

```

% ===== Traveling Wave Antenna Computation =====
% ===== (c) Florian D L Peters, University of Quebec, 2012-2014-=====
% ===== peters@emt.inrs.ca =====
%
% function pherr = ph_fehler(rad_ang)
%
% This function gives a feedback regarding the phase error.
% It takes the element which is the closes to the average phase as the
% reference.
function pherr = ph_fehler(rad_ang)

```

Example data

```

%
% ===== Traveling Wave Antenna Computation =====
% ===== (c) Florian D L Peters, University of Quebec, 2012-2014-=====
% ===== peters@emt.inrs.ca =====
%
% This file receives your prrequired simulation results.
% Your input should be in the following format:
%
% global 'length';           % slot range declaration
% 'length'=[0.49:0.01:0.59]; % min, max and step size
%
% then all other parameters are the results for ALL steps declared in
% 'length'
%
% Example:
% -----
%
% global rho_excel;
% length=[0.49:0.1:0.51];
% rho_excel = [0.135 .22. 34 ];
%
% ..defines and assigns a value to the variable rho_excel for the
% length 0.49, 0.5 and 0.51. All other required steps are interpolated.
%
%

```

```

% Input in (1) the selection of length in guided wavelength @ CF,
% suitable for your array.
%
% Insert in (2) the rho and sigma values for at least the same number of
% steps you have provided in (1). [ units not relevant]
% rho := distance of via center from the lower SIW via wall center
% sigma := distance from left slot edge (centered)
%
% Insert in (3) the S21 magnitude and phase, lossless !
%
% Insert in (5) the vertical (e_y) component phase of the electrical
% field within the slot
%
% Insert in (6) the appropriate mutual coupling, accord to [1], for
% three constellations, for each constellation 4 slot length cases are
% required:
%
% the length constellations are: =
%           [min\max max\max
%           min\min max\min];
% where the first slot length is left in the MC simulation.
%
% Insert in (7) the S22 magnitude and phase, lossless !
%
% (8), (9), (10) R.F.U.
%
=====
help end

```

refCanc_interp()

```

% ===== Traveling Wave Antenna Computation =====
% ===== (c) Florian D L Peters, University of Quebec, 2012-2014-=====
% ===== peters@emt.inrs.ca =====
%
% function [des_rho,des_sigma] = refCanc_interp(length)
%
% This function gives back the interpolated results for canceling the
% reflection with a via, placed at the position RHO and SIGMA as defined
% in
%   FDL Peters, et. al. , "Design of traveling-wave equidistant slot antennas for
%   millimeter-wave applications", IEEE APS 2011.
%
%
function [des_rho,des_sigma] = refCanc_interp(length)

```

avMean()

```

% ===== Traveling Wave Antenna Computation =====
% ===== (c) Florian D L Peters, University of Quebec, 2012-2014-=====
%
% ===== peters@emt.inrs.ca =====
% TOOL : Average Mean Filtering

```

```
function res = avMean(signal)
```

Plotheader.m

```
%% ===== Traveling Wave Antenna Computation =====  
% ===== (c) Florian D L Peters, University of Quebec, 2012-2014-=====  
% ===== peters@emt.inrs.ca =====  
%  
% PURELY COSMETIC FILE : Plotheader
```

Amp_error()

```
% function des_err= amp_error(rad_pow,type,N,SSL,rP)  
%  
% computes the amplitude error of the initial guess of slot length  
% compared to the desired distribution, previously set in 'type'  
%  
% NOTES:  
%  
% + The function considers  
%   = rP (residual power)  
%   = effective S11  
%   = dielectric losses  
% by simply renormalizing the references  
function des_err= amp_error(rad_pow,type,N,SSL,rP,S11)
```

Repet()

```
function res = repet(N,arg)
```

Ex()

```
function res = ex(degree)
```

phiS22interp()

```
function des_phiS22 = phiS22interp(length)
```

S22interp()

```
function des_S22 = S22interp(length)
```

right_neg_PhiMCinterp()

```
function des_MC = right_neg_PhiMCinterp(l1,l2)
```

left_neg_PhiMCinterp()

```
function des_MC = left_neg_PhiMCinterp(l1,l2)
```

leftMC_neg_interp()

```
function des_MC = leftMC_neg_interp(l1,l2)
```

rightMC_neg_interp()

```
function des_MC = rightMC_neg_interp(l1,l2)
```

Step78interp()

```
function des_deltaphi = step78interp(v1)
```

Outfun()

```
function stop = outfun(X, optimValues, state)
```

leftMCinterp()

```
function des_MC = leftMCinterp(l1,l2)
```

phiS21interp()

```
function des_phiS21 = phiS21interp(length)
```

rightMCinterp()

```
function des_MC = rightMCinterp(l1,l2)
```

rightPhiMCinterp()

```
function des_MC = rightPhiMCinterp(l1,l2)
```

S21interp()

```
function des_S21 = S21interp(length)
```

Cinterp()

```
function des_C0 = Cinterp(length)
```

phiEyinterp()

```
% Function to obtain the interpolated values for phi Ey (length)
```

```
% Call:
```

```
%     function des_phiEy = phiEyinterp(length)
```

```
function des_phiEy = phiEyinterp(length)
```

leftPhiMinterp()

```
function des_MC = leftPhiMinterp(l1,l2)
```

Deg()

```
function degree=deg(rad)
```

Rad()

```
function res = rad(angle)
```

This Function was written by Gerald Dalley (dalleyg@mit.edu), 2004

```
function printf(varargin)
%printf(varargin)
% Same as fprintf, but outputs to stdout
%Example:
% >> printf('foo %d\n', 10);
% foo 10
% >>
%Written by Gerald Dalley (dalleyg@mit.edu), 2004
```